Doctoral Thesis

A Search For Neutral Gas Outflows In Nearby Luminous Star-Forming Galaxies

Universidad Autónoma
de Madrid
Facultad de Ciencias
Departamento de Física Teórica

Consejo Superior
de Investigaciones Científicas
Centro de Astrobiología
Departamento de Astrofísica

Author:

Sara Cazzoli

Supervisor:

Prof. Santiago Arribas Mocoroa

Co-Supervisor:

Prof. Roberto Maiolino

A thesis submitted in fulfilment of the requirements
for the degree of Doctor of Philosophy

Madrid, May 2016

Dedicato alla nonna Gina
e alla mia famiglia

Acknowledgements

"...E la luna é una palla ed il cielo un biliardo
quante stelle nei flipper sono piú di un miliardo..."
L. Dalla

I would like to thank Santiago Arribas, for his investment of time, thoughts, and energy in mentoring me in these years and for making this PhD possible. I also thank him for allowed me to join the ELIXIR international team. I am grateful to Roberto Maiolino for the guidance throughout my 15 months in Cambridge and for giving me the opportunity to meet (and work with) important scientists. I would like also to thank Luis Colina for revising my papers and for all the precious advice.
I also owe my gratitude to my colleagues in Madrid and Cambridge who helped me for in tough moments and for being with me in my successes. I am grateful to Enrica for the uncountable good memories and for kindly providing me the Hα maps shown in the Appendix. A particular thanks goes to Javier, Miguel and Bruno who helped me with some parts of this thesis. Javier and Miguel, it has been a pleasure to share the office with you and thanks for all the "hitchhiking trip". Thanks also to JuanJo, Alvaro, Guilherme, Natacha, Dani, Ruyman, and Fabian. Luciano, Michela and Paola & Luca thank you for the support and all the laughs. I would like to thank the extragalactic group in Cambridge (in particular Claudia, Francesco, Stefano, Becky, Matt B. and Ying-jie) as well as Marina, Ciro, Alberto, Matt A. and Bethan, for the enjoyable discussions we had during the coffee breaks and before/after the daily talks. Other astronomy folks that I would like to thank are the other ELIXIR-students, especially Jacopo and Camilla.
I would like to thank the people who made this all possible, my parents and my sister. I thank you for your support and for being understanding of my choice to start my academic career within Spain and UK (I realize it is not ideal to have a daughter/sister living more than 1200 km away!).
Alessio, Andrea, Anna, Anita, Aurora, Bea, Cecilia, Erika, Gianluca, Greta, Irene, Luca, Lucia, Manuel, Ricky, Tasso, Veronica and Wally, thanks for maintaining our (priceless) friendship throughout the years and for being available every times I was back home.
Nuria, Jose, Santi, Ale, Julia, Oliva, Juanito, Cris and CO, I am extraordinarily grateful to all of you. You have helped me build my life in Madrid with intercambios, travels, dinners and bingos.
Tommaso, you have been on this journey with me since 2012. You have been a friend, a colleague, a partner in travels, runs, concerts and much more. Thank you for encouraging me when I needed it most.

This thesis was funded by the Marie Curie Initial Training Network ELIXIR (PI: Stéphane Charlot) of the European Commission under contract PITN- GA-2008-214227 and the grants AYA2010-21161-C02-01 and AYA2012-32295 by the Spanish Ministry of Science and Innovation (MICINN). S.C. gratefully acknowledges the logistic and financial support provided by the Cavendish Laboratory (Cambridge, UK).

Abstract

In the last decade, our understanding of the formation and evolution of galaxies over cosmic time has been significantly enhanced by large scale galaxy surveys. These surveys have drawn a detailed picture of the global properties of the galaxies, establishing the galaxy stellar mass function and scaling relations (e.g., mass-metallicity).

Galaxy evolution models attempt to reproduce the properties of the galaxies and those of the surrounding InterGalactic Medium (IGM) invoking the need of feedback mechanisms from starbursts or Active Galactic Nuclei (AGN). In fact, models of galaxy evolution without a strong (stellar or AGN) feedback, lead galaxies to have much higher Star Forming Rates (SFR) and larger stellar masses than observed. Outflows regulate Star Formation (SF) and AGN activity, and they are also considered the primary mechanism by which dust and metals are redistributed over large scales in the InterStellar Medium (ISM), or even expelled outside the galaxy into the IGM. In addition, it has been recently proposed that outflows can undergo vigorous SF. In this context, the study of the of feedback mechanisms is of critical importance to trace the build-up of stellar mass and evolution of galaxies in the Universe.

Multiphase outflows are ubiquitous at any redshift. Although the bulk of the black hole growth, SF, and galaxy mergers are believed to occur at z $\sim$ 1-3, studies of outflows in nearby galaxies offer detailed insights into feedback phenomena as one of the primary drivers of galaxy evolution. In this context, local Luminous and Ultra-Luminous Infrared Galaxies ((U)LIRGs) are particularly interesting populations. On the one hand these objects show the most conspicuous cases for outflows in the local Universe. On the other hand, local (U)LIRGs have a SF-activity similar to that found for "normal" (i.e., main-sequence) high-z star forming galaxies, and share with distant galaxies some other basic structural and kinematical properties. Therefore, local (U)LIRGs allow us to study the outflow phenomenon at environments similar to those observed at high-z, but with a much higher signal-to-noise and spatial resolution. The large majority of previous outflow studies are based on long slit observations giving only a partial description of the outflow phenomenon. However, Integral Field Spectroscopy (IFS) is well suited for the spectroscopic measurement of large areas of e.g., interstellar (outflowing) gas and therefore allows to study its 2D structure.

In the present work we search for outflows in a sample of 38 local (U)LIRG systems (51 individual galaxies) with $z < 0.09$ observed with the VIMOS and SINFONI Integral Field Units (IFUs) of the Very Large Telescope of ESO. This allows us to extend the census of the 2D mapping of neutral winds in local (U)LIRGs, covering the less studied LIRG luminosity range. In fact, previous IFS studies are

limited to a small number of extreme objects, mainly major-mergers. We exploit these optical and near-IR IFS-observations to make a significant step forwards in understanding the outflow properties such as their geometry and their connection/feedback with those of the host galaxy.
As first step in our analysis, we extract the ISM and stellar kinematics using Gaussian-fits and a maximum penalized likelihood approach, respectively (Chapter 3). In Chapter 4, we study the multiphase outflow in the prototype LIRG IRAS F11506-3851 and in Chapter 5 we expand the search of neutral outflows to all the VIMOS/IFS sample, looking also for scaling relations within outflows and galaxy properties. Finally, in Chapter 6, we investigate the occurrence of SF in the outflow of the ULIRG IRAS F05189-3851, exploiting near-IR SINFONI IFS data. The main results and conclusions of this thesis can be summarized as follows:

Spatially resolved kinematics, galactic wind, and quenching of SF in the LIRG F11506-3851.
We have accomplished a multiwavelength-IFS study for the nearby LIRG IRAS F11506-3851. The morphology and the 2D kinematics of the gaseous (neutral and ionized) and stellar components have been mapped in the central regions (< 3 kpc) using the NaD absorption doublet, the Hα emission line, and the near-IR CO(2-0) λ 2.29 μm and CO(3-1) λ 2.32 μm absorption bands. The kinematics of the ionized gas and the stars are dominated by rotation, with large observed velocity amplitudes and centrally peaked dispersion maps. In contrast, we have found that the ISM-NaD absorption shows a complex kinematic structure dominated by two main components. On the one hand, we observe an irregular slowly rotating thick disk which lags significantly compared to the ionized gas and stars. On the other hand, we find a kpc-scale outflow perpendicular to the disk, which is ejecting a significant amount of gas (3×10^8 M$_\odot$) from the central regions at a rate of 1.4 times larger than the ongoing SF. The relatively strong emission by SNe in the central regions as traced by the [Fe II] λ 1.65 μm emission, indicates a recent ($\sim$ 7 Myr ago) episode of SF. These results strongly suggest that we are witnessing (nuclear) quenching due to SF feedback in IRAS F11506-3851. However, the relatively large mass of molecular gas detected in the nuclear region via the H_2(1-0)S(1) line suggests that further episodes of SF may take place again.

Neutral gas outflow in nearby (U)LIRGs via optical NaD feature.
In addition to the detailed study of IRAS F11506-3851, we have studied the properties of the neutral gas in the whole sample of 38 (U)LIRGs. On the basis of spatially integrated, as well as the spatially resolved IFS-spectra of the NaD feature obtained with the VLT/VIMOS-IFU, we have found that neutral outflows are frequent (71 % and 55 % detection rate for the integrated and spatially resolved analyses, respectively). Outflow (integrated) velocities, V, are in the range: 65-260 kms^{-1} and these scale with the SFR as $V \propto SFR^{0.15}$ (excluding AGNs), in rather good agreement with previous results. The spatially resolved analysis could be performed for 40 galaxies. In a minor but significant fraction (11 targets) we found disk-rotation signatures, whereas for more than half of the cases (22 targets) the neutral gas velocity fields are dominated by non-circular motions with signatures of cone-like winds. Based on a simple model, we have found that the wind mass ranges from 0.4 to 7.5×10^8 M$_\odot$, reaching up to $\sim$ 3% of the dynamical mass of the host. The mass rates are typically only $\sim$ 0.2-0.4 times the

corresponding global SFR indicating that, in general, the mass-loss is small for slowing down significantly the SF. In the majority of the cases, the velocity of the outflowing gas is not enough to escape the host potential well and, therefore, most of it will rain-back into the galaxy disk. On average V/v_{esc} is higher in less massive galaxies, confirming that the galaxy mass has a primary role in shaping the recycling of gas and metals. The comparison between the wind power and the kinetic power of the starburst associated to SNe indicates that only the starburst could drive the outflow in nearly all the (U)LIRGs galaxies, as the wind power is generally lower than the 20% of the kinetic power supplied by the starburst. Only in two cases the contribution of the AGN is, in principle, significant.

Investigating positive feedback in the ULIRG IRAS F05189-2524.

In order to investigate if the multiphase AGN-driven outflow in the ULIRG IRAS F05189-2524 is able to undergo vigorous SF (as expected by some models) we have studied a set of near-IR emission lines: [Fe II], Paα, H_2 1-0 S(1) and Brγ with integral-field and integrated spectroscopy in the H and K bands, using the SINFONI instrument of the VLT. The multi-component decomposition of the near-IR emission lines has shown that an extended broad and outflowing component is present at velocities in the range 60-120 kms^{-1} (except some regions) and with a large velocity dispersion ($\sim$ 325 kms^{-1}, on average) in partial agreement with previous works. On the basis of near-IR diagnostic diagrams we discriminate the dominant source of ionization of the two kinematic components used to model emission lines. We have found that the mechanism of excitation of both narrow and broad components is AGN-photonization. This excludes ionization from young ionizing stars expected in case of positive feedback. By using two different diagnostic near-IR diagrams we have found that our measurements indicate that this galaxy has either an [Fe II] emission deficit or an H_2 excess, which will be investigate in the future.

Resumen

En la última década, nuestra comprensión de la formación y evolución de las galaxias ha mejorado considerablemente gracias a observaciones de grandes muestras de galaxias. Estos estudios han proporcionado una visión detallada de las propiedades globales de las galaxias, estableciendo relaciones de escala entre muchas de sus propiedades, como la relación masa-metalicidad.

Los modelos de evolución de galaxias tratan de reproducir tanto las propiedades observadas de estos objetos como las del medio intergaláctico, introduciendo los *outflows* (en inglés, a veces traducido como "supervientos") como mecanismos de regulación de los brotes de formación estelar y de la actividad de los núcleos galácticos (AGN, por sus siglas en inglés). Sin embargo, aquellos modelos de evolución de galaxias que no incluyen estos mecanismos de regulación, reproducen galaxias con tasas de formación estelar (SFR, por sus siglas en inglés) y masas estelares mucho mayores de las observadas. El fenómeno de los *outflows* es considerado también como el mecanismo primario por el cual el polvo y los metales se redistribuyen en el medio interestelar a grandes escalas, pudiendo ser incluso expulsados de la propia galaxia al medio intergaláctico. Asimismo, trabajos recientes han propuesto que estos *outflows* también pueden ser los responsables de activar procesos de formación estelar en las galaxias. En este contexto, la comprensión de estos mecanismos que regulan la formación estelar y la actividad nuclear tiene gran importancia para entender la evolución de las galaxias a lo largo de la historia del Universo.

Los *outflows* se han observado de forma simultánea en diferentes fases del medio interestelar en cualquier época cósmica. Aunque el máximo de actividad en términos de crecimiento de la masa estelar y de la de los agujeros negros centrales, así como la tasa de interacción entre galaxias, ocurre en torno a $z \sim 1$-3, los estudios de *outflows* en galaxias cercanas permiten investigar con detalle estos fenómenos de regulación. En particular, las galaxias luminosas y ultraluminosas en el infrarrojo (LIRGs y ULIRGs, por sus siglas en inglés) locales son poblaciones especialmente adecuadas para estudiar estos procesos. Por un lado, es en estos objetos donde los *outflows* se han observado con mayor frecuencia en el Universo local. Por otro lado, las (U)LIRGs comparten muchas propiedades estructurales y cinemáticas con galaxias lejanas con tasas normales de formación estelar (i.e., galaxias en la "secuencia principal"). Por tanto, las (U)LIRGs locales, permiten estudiar los mecanismos de regulación en entornos similares a aquellos observados en galaxias lejanas, con la ventaja de poder alcanzar una relación señal-ruido y una resolución espacial mucho más altas.

La gran mayoría de estudios estudios anteriores sobre *outflows* se basan en observaciones espectroscópicas de rendija. Estas observaciones proporcionan información parcial e incompleta de los *outflows* y de los fenómenos de regulación asociados al carecer de información espacial en 2D. Sin embargo, la espectroscopía de campo integral, está optimizada para los estudios espectroscopicos de regiones espacialmente extensas y permite estudiar en detalle la estructura 2D del gas en los *outflows*. En el presente trabajo, se ha analizado una muestra de 38 (U)LIRGs locales (51 galaxias individuales) a $z < 0.09$, observada con las unidades de campo integral de los instrumentos VIMOS y SINFONI en los telescopio VLT (Very Large Telescope, en inglés). De este modo, se ha podido ampliar el censo de *outflows* de gas neutro espacialmente resueltos (2D) en (U)LIRGs locales, cubriendo el rango de luminosidad menos estudiado, correspondiente a las LIRGs. En este contexto, el estudio simultáneo en estos objetos de los rangos óptico e infrarrojo cercano permite dar un paso significativo hacia la comprensión de las propiedades de estos *outflows*, como su geometría, así como su influencia en la galaxia anfitriona mediante los procesos de regulación de la formación estelar y/o de la actividad del agujero negro central.

En este estudio, como primer paso, se ha extraído la cinemática del medio interestelar y de las estrellas utilizando diferentes técnicas (Capítulo 3). En el Capítulo 4, se ha estudiado la presencia de *outflows* en diferentes fases del medio interestelar en un prototipo de LIRG, IRAS F11506-3851, mientras que en el Capítulo 5, se ha extendido el análisis de los *outflows* en el gas neutro a toda la muestra de objetos observados con VLT/VIMOS, estudiando las posibles relaciones entre las propiedades de los mismos y las características globales de la galaxia anfitriona. En el Capítulo 6, se ha investigado la posible presencia de formación estelar en el *outflow* de la ULIRG IRAS F05189-3851, mediante observaciones realizadas con VLT/SINFONI en el rango del infrarrojo cercano. Los principales resultados y las conclusiones de esta tesis son las siguientes:

Cinemática espacialmente resuelta, *outflows* y supresión de la formación estelar en la LIRG IRAS F11506-385.

Se ha realizado un estudio basado en datos de espectroscopía de campo integral a diferentes longitudes de onda de la LIRG local IRAS F11506-3851. A partir de estos datos, se ha obtenido la morfología y la cinemática bidimensional de las componentes neutras e ionizadas del gas, así como de la componente estelar, para las regiones centrales (~ 3 kpc) del objeto. Para ello, se han utilizando como trazadores el doblete de absorción del NaD, la línea de emisión Hα, y las bandas de absorción del CO(2-0) $\lambda\,2.29\,\mu$m y CO(3-1) $\lambda\,2.32\,\mu$m en el infrarrojo cercano. Los campos de velocidad del gas ionizado y de las estrellas están dominados por rotación, con una amplitud de velocidad elevada y mapas de dispersión de velocidades cuyo máximo se encuentra en el núcleo. Por el contrario, la fase neutra del gas, trazada con el NaD, presenta una cinemática más compleja, dominada por dos componentes. Por un lado, se observa un disco grueso irregular que rota significativamente más despacio que el gas ionizado y las estrellas. Por otro lado, se encuentra una componente asociada a un *outflow* de gas neutro, originado en el núcleo y perpendicular al disco de la galaxia, que expulsa una cantidad significativa de gas (3×10^8 M$_\odot$) de las regiones centrales, con una tasa 1.4 veces mayor que la SFR observada. La emisión debido a supernovas es relativamente fuerte en las regiones centrales, tal y como se deduce de la linea

de emisión [Fe II], e indica un reciente (~ 7 Myr) episodio de formación estelar. Estos resultados sugieren que la formación estelar en las regiones centrales de IRAS F11506-3851 está siendo suprimida por la acción del *outflow*. No obstante, la masa relativamente alta de gas molecular que se observa en las regiones centrales de la galaxia, trazada con la línea de emisión de [Fe II] $\lambda\,1.65\,\mu$m, hace pensar que estos episodios de formación estelar puedan volver a repetirse.

Supervientos de gas neutro en (U)LIRGs locales trazados con NaD.
Junto con el estudio detallado de IRAS F11506-3851, se han analizado las propiedades del gas neutro en la muestra total de 38 (U)LIRGs locales. El análisis se ha basado en el estudio del NaD en espectros integrados, así como en espectros espacialmente resueltos, obtenidos con VLT/VIMOS. Se ha encontrado que los *outflows* en el gas neutro son frecuentes (71% y 55% de detecciones en los espectros integrados y en los espacialmente resueltos, respectivamente). Las velocidades integradas de estos *outflows* se encuentran en el rango 65-260 kms^{-1}, y escalan con la SFR como $V \propto SFR^{0.15}$ (excluyendo los AGNs), tal y como mostraban estudios anteriores. El análisis de los datos con resolución espacial pudo llevarse a cabo en 40 galaxias. En una pequeña, aunque significativa, fracción de fuentes (11 objetos), encontramos evidencias de discos en rotación, mientras que en más de la mitad de los casos (22 objetos), el campo de velocidad del gas neutro aparece dominado por movimientos no circulares con características propias de vientos con estructura cónica. Basando el análisis en un modelo sencillo, se encuentra que las masas implicadas en los vientos abarcan un rango entre las 0.4 y las 7.5×10^8 M$_\odot$, lo que corresponde, en unos casos, a un ~ 3% de la masa dinámica total de la galaxia anfitriona. Las tasas con las que la masa es expulsada en los vientos son típicamente entre 0.2 y 0.4 veces la correspondiente a la tasa de formación estelar global, lo que indica que, en general, la pérdida de masa es pequeña como para poder frenar de forma significativa la formación estelar. En la mayoría de los casos, la velocidad del gas en los vientos no es suficiente como para escapar del potencial gravitatorio de la galaxia y, por tanto, su mayor parte terminará cayendo de nuevo al disco galáctico. En promedio, los valores V/v_{esc} son mayores en aquellas galaxias menos masivas, confirmando que la masa de la galaxia juega un papel principal en la redistribución y reciclaje del gas y de los metales. La comparación entre la energía del viento y la energía cinética de los brotes de formación estelar asociados a las supernovas indican que únicamente estos brotes de formación estelar tienen suficiente energía como para producir los *outflows* en prácticamente todas las (U)LIRGs. Esto se demuestra teniendo en cuenta que la energía asociada al viento es generalmente menor que el 20% de la energía cinética asociada a los brotes de formación estelar. En únicamente dos casos se encuentra que el efecto del AGN es, en principio, significativo.

Investigacion de la la regulación positiva en la ULIRG IRAS F05189-2524. Para estudiar si los *outflows* asociados al AGN en diferentes fases del gas en la ULIRG IRAS F05189-2524 son capaces de inducir formación estelar de forma significativa (como predicen algunos modelos), se ha estudiado un conjunto de líneas de emisión en el infrarrojo cercano ([Fe II], Paα, $H_2$1-0 S(1) y Brγ) empleando técnicas de espectroscopía de campo integral en las bandas H y K, utilizando el instrumento VLT/SINFONI. La descomposición en múltiples componentes de las líneas de emisión infrarrojas ha revelado la presencia de una componente ancha y extensa, asociada a *outflows*, con velocidades en el rango

60-120 kms^{-1} (excepto en ciertas regiones) y con elevada dispersión de velocidades (~ 325 kms^{-1}, en promedio). Estos resultados están en acuerdo parcial con otros trabajos previos. Mediante diagramas de diagnóstico en el infrarrojo cercano, ha sido posible discriminar la fuente dominante de ionización de cada una de las componentes cinemáticas empleadas para modelar las líneas de emisión. Encontramos que el mecanismo de excitación en ambas componentes, ancha y estrecha, se corresponde con fotoionización debido al AGN. Esto excluye los procesos de ionización como los debidos a estrellas jóvenes ionizantes, que son los esperados en caso de regulación positiva debido a formación estelar. Utilizando dos diagramas de diagnóstico diferentes en el infrarrojo, nuestras medidas indican que o bien esta galaxia presenta un déficit de emisión de [Fe II] o bien un exceso de emisión en la línea de H_2. Este resultado será estudiado con mayor profundidad en el futuro.

Contents

Acronyms

AO	Adaptive Optics
ACS	Advanced Camera for Surveys
AGN	Active Galatic Nucleus
ALMA	Atacama Large Millimeter/submillimeter Array
BGS	Bright Galaxy Sample
CALIFA	Calar Alto Legacy Integral Field Area Survey
CNM	Cold Neutral Medium
DM	Dark Matter
ESO	European Organisation for Astronomical Research in the Southern Hemisphere
EsoRex	ESO Recipe Execution Tool
EW	Equivalent Width
FoV	Field of View
FSC	Faint Source Catalogue
FWHM	Full Width Half Maximuum
FMR	Fundamental Metallicity Relation
GHASP	Gassendi HAlpha survey of SPirals
GNIRS	Gemini Near InfraRed Spectrograph
GW	Galactic Wind
HIM	Hot Ionized Medium
HR	High Resolution
HST	Hubble Space Telescope
HVC	HighVelocity Cloud
IDL	Interactive Data Analysis
IFS	Integral Field Spectroscopy
IFU	Integral Field Unit
IGM	Inter Galactic Medium
IRAF	Image Reduction and Analysis Facility
IR	InfraRed

IRAM	Institut de Radioastronomie Millimétrique
IRAS	InfraRed Astronomical Satellite
ISM	Inter Stellar Medium
IVC	Intermediate Velocity Cloud
JWST	James Webb Space Telescope
KMOS	K-band Multi Object Spectrograph
MAMBO	Max-Planck Millimetre Bolometer Array
LBG	Lyman Break Galaxy
LINER	Low-Ionization Nuclear Emission-line Region
LIRG	Luminous Infrared Galaxy
LOSVD	Line Of Sight Velocity Distribution
LGS	Laser Star Guide
LR	Low Resolution
MaNGA	Mapping Nearby Galaxies at Apache point observatory
MOS	Multi Object Spectrograph
MR	Medium Resolution
MS	Main Sequence
MUSE	Multi Unit Spectroscopic Explorer
MW	Milky Way
MZ	Mass Metallicity Relation
NASA	National Aeronautics and Space Administration
NED	NASA/IPAC Extragalactic Database
NGS	Natural Star Guide
NICMOS	Near Infrared Camera and Multi-Object Spectrometer
NICS	Near Infrared Camera Spectrometer
PA	Position Angle
PAH	PolyAromatic Hydrocarbons
PdBI	Plateau de Bure Interferometer (IRAM)
PV	Position Velocity Diagram
pPXF	Penalized Pixel-Fitting
PSC	Point Source Catalogue
QSO	Quasi Stellar Object
RBGS	Revised Bright Galaxy Sample
RD	Rotating Disk
SAMI	Sydney-Australian-Astronomical-Observatory Multi-object Integral-Field Spectrograph
SDSS	Sloan Digital Sky Survey
SED	Spectral Energy Distribution

SINFONI	Spectrograph for INtegral Field Observations in the Near Infrared
Sy	Seyfert
SF	Star Formation
SFG	Star Forming Galaxy
SFH	Star Formation History
SFR	Star Formation Rate
SMG	Sub-Millimiter Galaxy
SNe	Supernovae
Sub-mm	Sub-MilliMeter
S/N	Signal to Noise
ULIRG	UltraLuminous InfraRed Galaxy
UV	UltraViolet
VIMOS	VIsible MultiObject Spectrograph
VLT	Very Large Telescope
WFPC	Wide Field and Planetary Camera
WIM	Warm Ionized Medium
WNM	Warm Neutral Medium

Chapter 1

Introduction

The reservoirs of gas, dust, and stars in galaxies are in constant interplay. In particular, the cold gas (the fuel from which stars are formed) could be heated, accelerated and removed from its situ by SuperNovae and Active Galactic Nuclei feedback via outflows. The fate of such gas is then to either escape the gravitational well of the host (polluting the Inter Galactic Medium) or, to rain back to the central region (being available again for the Star Formation). Investigating the regulation of Star Formation in local luminous Star Forming Galaxies - the aim of this thesis - is critical to understand how galaxies evolve over time.

1.1 Outflows and feedback in the context of formation and evolution of galaxies

The modern galaxy formation theory is set within the cold Dark Matter (DM) cosmological model and proceeds via a fundamentally hierarchical paradigm. In this (standard) framework, the formation of an individual galaxy involves the following processes: the collapse and virialization of DM-halos, the cooling and condensation of gas within the halo, and the conversion of cold gas into stars and in a central supermassive black hole. Therefore, galaxy properties, such as luminosity or stellar mass ($M_\star$), are expected to be tightly coupled to the depth of the halo potential and thus to the halo mass.
However, such picture is met with problems. The process of galaxy formation is not 100% efficient at getting gas into galaxies as supported by observations of nearby and distant galaxies. Indeed, the galaxy stellar mass function does not follow the halo mass function at both low- and high- mass ends ($M_\star < 10^8\,M_\odot$ and $M_\star > 10^{11}\,M_\odot$). In these regimes, halos have a significantly lower value of stellar masses than predicted (Somerville et al. 2008; Moster et al. 2010). The break-down of the prevision of the hierarchical formation scenario is evident in Fig. 1.1 which shows the comparison of the galaxy baryonic mass function and the mass spectrum of cold DM-halos from numerical simulations. Additionally, this scenario leeds to the "overcooling problem": too many big galaxies in the nearby Universe, too few massive galaxies at high redshift, and too many baryons (in the form stars + gas) within the galaxy halos (by a factor four) are predicted but not observed (Rasera & Teyssier 2006).

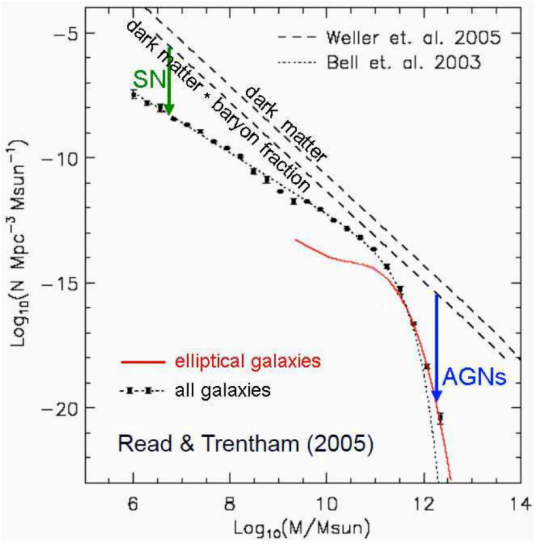

FIGURE 1.1: The galaxy baryonic mass function (black points) and Schechter (1976) function fit (Bell et al. 2003, dotted curve). These are compared to the mass spectrum of cold DM halos from numerical simulations by Weller et al. (2005) and to the DM mass function (multiplied by the universal baryon fraction of 0.163, Hinshaw et al. 2013, lower dashed curve). Green and blue lines arrows indicate the reduction of efficiency at getting gas into galaxies, likely due to the effect of supernovae and AGN feedback, respectively (see Sect. 1.1.1 for details). Figure from Kormendy & Ho (2013).

Other chronic issues refer to the observed disk angular momentum (Sect. 1.1.1), the halo density profiles and the dark satellites. We refer to Silk & Mamon (2012) for a review about outstanding problems in the galaxy formation theory.

To reconcile galaxy formation and evolution models and observations, a physical process able to prevent the gas from cooling efficiently, or reheat it, has become necessary, and should be take place at $z \sim 2$ already (Silk 2001).

Essentially, the solution to all of these difficulties might lie in the feedback from Star Formation (SF) and/or Active Galactic Nuclei (AGN). In fact, they are believed to be the processes able provide the required feedback by driving hot, warm and cold outflows (i.e., gas flowing observed outwards from galaxies, on various scales). Outflows were first discovery in the early 1960s (Lynd & Sandage 1963; Burke 1968) and provide a direct way of connecting the small spatial scales of sources to the surrounding environment (on kpc scales).

Outflows and feedback represent a complex phenomena which is not univocally defined, but has various aspects. The outflow feedback is addressed as the mechanism capable of depleting gas reservoirs, limiting black hole and spheroid growth (Veilleux et al. 2005, Sect. 1.1.1) or of triggering SF in the host galaxy through enhanced gas pressure in the InterStellar Medium (ISM) (Zubovas et al. 2013, Sect. 1.1.2). In addition, outflows can be defined as the process which favor the transport of metals either from the host galaxy into the InterGalactic Medium (IGM) or from the innermost to the external regions of the galaxy (Sect. 1.1.3). Therefore, for these various aspects of the feedback, the study of the physical properties of outflows is of particular importance for understanding of galaxy evolution. We will return to these important aspects of the feedback many times in the body of this thesis.

The basic quantities that we need to know to asses whether or not these outflows can have an impact on the host galaxy properties are: velocities, mass, mass outflow rate, energy and power, as long as their occurrence and structural properties (e.g., their gas-phase composition). In this sense, it is challenging to obtain accurate observational signatures and estimates for these quantities, but this work address this problematic.

1.1.1 Negative feedback

As mentioned in the previous section, the current galaxy formation scenario postulates that the intense SF in massive, high-redshift galaxies during their major period of growth[1] ($z \sim 1$-3) was truncated likely by the occurrence of outflows (as consequence of the strong nuclear activity). The straightforward consequence is the self-regulation (quenching) of the SF and the AGN activity by ejecting gas from the host and/or heating it up. This is called "negative feedback", it has been discussed by a number of authors (see Veilleux et al. 2005 for a review) and is now part of many galaxy evolution models (e.g., Somerville et al. 2008; Somerville & Davé 2015). A schematic view of the negative feedback is displayed in Fig. 1.2.

The negative feedback is invoked to explain both the low- and high- mass ends of the baryonic mass function of galaxies (Fig. 1.1). Specifically, smaller galaxies are thought to miss progressively more baryons because they were ejected by Super Novae (SNe) -driven outflows (Kormendy & Ho 2013). While, in halos that are much more massive than $M_{crit} = M_{DM} \sim 10^{12}\,M_{\odot}$, the AGN feedback efficiently suppress the cooling of hot gas which could in turn control the levels of future SF and black hole growth. The differences between SNe- and AGN- driven outflows are discussed in Sect. 1.2.

A strong negative feedback is also necessary to reproduce the structural properties of disk galaxies. Indeed, simulations with only modest feedback effects suffer from the so-called angular momentum problem: simulated disk galaxies have too low angular momentum, thereby being more compact and denser than the observed ones (e.g., Navarro & Steinmetz 2000). Recent high-resolution hydrodynamical simulations taking into account stronger feedback effects (based on more realistic physical background) have partially resolved such problem (Toyouchi & Chiba 2015 and reference therein).

Outflows might also imprint the mass-metallicity relation (as discussed in Tremonti et al. 2004, see also Sections 1.1.3 and 1.4.2) and cause color transformation of spiral galaxies into passive ellipticals caused by gas exhaustion (e.g., Weiner 2009).

The negative feedback has been observed in local galaxies (e.g., Heckman et al. 2000; Martin 2005; Rupke et al. 2005a,b), as well as those at high-z (e.g., Narayanan et al. 2004; Pettini et al. 2002; Shapley et al. 2003) by way of absorption and emission lines spectroscopy (see Sect. 1.3).

1.1.2 Positive feedback

During the past decade many theoretical and observational activities have focused on the understanding of the negative feedback mechanism responsible for self-regulating SF and AGN activity in galaxies. However, an additional aspect of outflow's feedback to consider has been proposed recently by several authors as Ishibashi & Fabian (2012) and Zubovas et al. (2013). They have proposed that the outflow feedback may not only consist of removing/heating the gas of their host galaxy but also able to form stars under certain conditions. Indeed, the compression of the cold gas induced by the passage of the outflow may cause local density enhancements, and hence the gas may undergo vigorous SF (Ishibashi & Fabian 2012). Such positive feedback takes preferentially place in AGN-driven outflows rather than in those driven by the SNe (Ishibashi & Fabian 2012; Zubovas et al. 2013). Indeed, the induced SF is

[1] The quoted redshift range has been derived from detailed studies of the cosmic SF based on optical and InfraRed (IR) deep surveys. It is often referred as the "epoch of mass assembly", as roughly half of today's stellar mass was formed during such period.

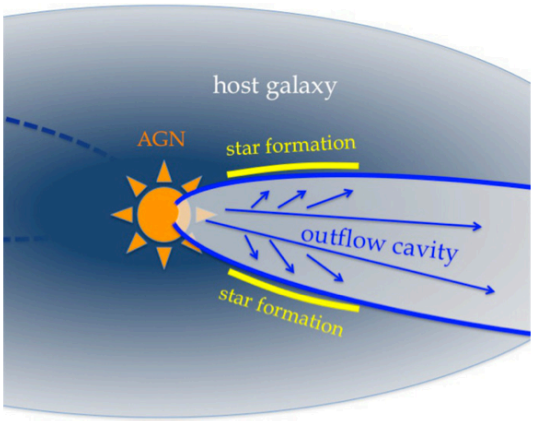

FIGURE 1.2: Schematic view of negative and positive feedback in an AGN-outflow. The outflow is sweeping out the gas creating a cavity and suppressing SF (negative feedback, Sect. 1.1.1), but also triggering SF as consequence of induced pressure at its edges (positive feedback, Sect. 1.1.2). Figure from Cresci et al. (2015)

achieved, since AGN-outflows are launched with high momentum (up to the Eddington limited photon momentum) and hence are able to reach large velocities. Then, an important outstanding question is, the estimation of the relevance of Star Formation Rate (SFR) in outflows and its relative importance with respect to the negative feedback. A schematic view of the positive feedback is displayed in Fig. 1.2.

Observational evidence of SF in outflows are still scarce. The difficulties in disentangling the SF occurring in the galaxy disk to the fraction taking place in the outflow, lead the positive feedback challenging to test. In 2015, Cresci and its collaborators (Cresci et al. 2015) attempt to provide the first evidence of SF in the outflow of a $z \sim 1.6$ radio-quiet QSO (Quasi Stellar Object). They showed that the QSO is in a significant outflowing phase via the Integral Field Spectroscopy (IFS) of the [O III] λ 5007 emission line. The fast ($v > 1500\,\mathrm{kms}^{-1}$) kpc-scale outflow lies in the center of a cavity in the star forming regions of the host galaxy (Fig. 1.2), as seen in the Hα λ 6563 line map and the rest frame U-band HST-ACS (Hubble Space Telescope and Advanced Camera for Surveys, respectively) imaging.

In the local Universe, the richness of diagnostics in the near-IR range allows to probe such positive feedback. A way to test the scenario in which SF occur in AGN-driven outflows, is to study and spatially resolve the SF activity by using the Paα λ 1.876 μm emission line as a (nearly) extinction-free SFR-indicator (Chapter 6).

This would be a new mode of SF in galaxies, which, if properly observationally probed, should be incorporated within the two SF-modes known. These are: the "quiescent mode " and "starburst mode". The first, which depends linearly on the mass and surface density of cold gas (usually traced by CO rotational transitions), is likely happening in giant molecular clouds of normal (i.e., star forming) galaxies on long dynamical timescale ($\tau_{\mathrm{dyn}} \sim 10^9$ yr). While, the second is a dynamically driven mode (relevant to mergers, spiral arms and bars) which also scales linearly with surface density of cold gas but has a shorter rate: up to 20 times faster than the quiescent mode.

1.1.3 Recycling of metals: ISM and IGM enrichment

Depending on the amount and concentration of energy that is injected by the power source, the gas and metals transported by outflows can be either escape or re-captured by the gravitational potential (falling back onto the disk) of the host. Therefore, outflows represent an "enrichment phenomenon", since a metal rich outflow can pollute with a substantial fraction of metals and heat the ISM/IGM (Aguirre

et al. 2001 and reference therein).
In general, the impact of such feedback on the host galaxy evolution is sensitive to three main factors: outflow velocity, entrainment fraction[2] and gravity. The formers are likely related to the outflow power source while the latter determines the mass range of galaxies from which outflows can escape. In particular, the trend for which the enrichment mechanism increases with galaxy mass has been well established in the literature: the "mass-metallicity relationship" which is observed at any redshift (Tremonti et al. 2004; Brooks et al. 2006).
The ejection of metals caused by outflows is invoked to explain unforeseen[3] IGM regions with metallicity larger than 0.1 % $Z_{\odot}$ observed, for example, via the study of metal lines in distant Lyα λ 1216 Å absorption systems (e.g., Cowie et al. 1995; Garzilli et al. 2015). The outflow IGM-pollution is taken into account in cosmological simulations (see also Sect. 1.3.4) since the it can have also an impact on the cosmic medium from which galaxies form (Barai et al. 2015; Taylor & Kobayashi 2015).
In the so called "fountain-scenario", the outflow in its expansion may fragments (due to the occurrence of Rayleigh-Taylor instabilities, Sect. 1.2) resulting in Intermediate and High Velocity Clouds (IVCs and HVCs, respectively) which may rain back to the disk. This mechanism is, however, challenging to catch in act. It has been mainly addressed by studying neutral hydrogen H I chimneys and clouds in the halo of the Milky Way (MW) (e.g., Marasco et al. 2012) and in other Star Forming Galaxies (SFGs) (e.g., Boomsma et al. 2005, Melioli et al. 2008 and references therein). Nowadays, IFS-observations allow to probe spatially resolved metal-variations (i.e., the amount of metals lost/gained), as a direct measure of the effects of metal-rich outflows during the evolution of galaxies (e.g., Belfiore et al. 2015).
The information about gas flows in galaxies both from inside (gas fountains) and outside (gas inflows), is highly valuable in the context of cosmological simulations and semi-analytic models of galaxy evolution (Sect. 1.3.4 and Sánchez Almeida et al. 2014, for a review). In particular, high-z fountains by ejecting material from the galaxy's disk, can strongly regulate the early-times SF, and, at the same time, provide, a gas reservoir that can fuel SF at late/present times. Therefore, increased SF and inflows at low redshift can be interpreted as feature of high redshift outflows whose material fell back onto the galactic disk within a Hubble time (Keller et al. 2015). This scenario is supported by Hα and UBV measurement of 210 nearby Sa-Irr galaxies by Kennicutt et al. (1994). They found that the recycling of stellar ejecta can extend the lifetimes of gaseous disks by factors of 1.5-4, enabling them to sustain their ongoing SFRs for periods comparable to the Hubble time (see also Sandage 1986).

1.2 Structure and power sources

Outflows are usually classified accordingly to their power source which is generally either SNe (resulting from the starburst) or AGN. Both SNe and AGN inject energy into the ISM, leading to the formation of a bubble of hot gas that expands and drives the shocks into the rest of the gaseous medium. SNe are active powering outflows, as long as new stars continue to form, whereas the AGN boost tends to last only a short fraction of time (Hill & Zakamska 2014). However, the instantaneous energy injection by the AGN may be higher, leading to large outflow velocities ($> 1000\,\mathrm{km s^{-1}}$, Narayanan et al. 2008).

[2]The fraction of the ambient material entrained by the outflow in its propagation (Aguirre & Schaye 2007).
[3]In the standard cosmology heavy elements (metals) form in stars and are stored in galaxies (closed box systems).

If the central engine is the starburst, the input power that generate the outflow is the radiation and the kinetic energy liberated by the sequential explosions of core-collapse SNe. These SNe events (of about 10^{51} erg each explosion, Smartt 2009) are likely to spatially and temporally clustered since they are related to the end stages in the evolution of massive stars which in turn form in OB associations (Vasiliev et al. 2015).

In this case, theoretical models and simulations (Chevalier & Clegg 1985; Heckman et al. 1990 and reference therein) state that outflows can be described with two main evolutionary stages: the radiative (also called break-out) and the blow-out phases. During the radiative phase the outflow forms its characteristic "snowplow" structure. At this time, the snowplow is arranged in essentially four regions. These are: free wind, shocked wind, shocked ambient medium and undisturbed ambient medium, respectively moving radially outward from the centre. Specifically, in its evolution, the hot gas thermalized by SNe (wind fluid), expands outwards and cools as a free wind, until passes through an inner shock. The shock driven by the expanding bubble (shocked wind), sweeps out the ambient gas (shocked ambient medium) which cools radiately into a thin shell. Afterwards, the snowplow evolves into the blowout phase, which can propagate out reaching the IGM. At the blowout phase the snowplow structure remains until the shell fragments via Rayleigh-Taylor instabilities. These occur at an interface between two fluids having different densities in a gravitational field or, equivalently, in case of acceleration. In this case, if the direction of the acceleration points from the heavy to the light fluid, the interface between the two fluids became unstable. The instability causes the two fluids to penetrate each other with "fingers " or "mushroom-caps" of gas, mixing the fluids and breaking up the interface (i.e., the shell). Figure 1.3, illustrates the vertical mass density distribution of a simulated SNe-driven outflow during its expansion (time-evolution).

In this framework, SNe are assumed to be very efficient in heating the gas up to X-ray temperatures (i.e., $> 10^6$ K) and in order to fill the volume of the central region of the starburst with such hot gas. However, it has been shown that this is not always the case. For example, large heating efficiency and filling factor should be assumed in order to explain the hot-gas outflow in M 82 (Chevalier & Clegg 1985) but, are not observed (Strickland & Heckman 2009). This indicates that the wind dynamics (e.g., morphology and X-ray emission) is sensitive to other factors such ISM distribution of the host galaxy (Sect. 5.6).

It has to be noted that not all the episodes of SF leads to the formation of an outflow. In the local Universe, SNe-driven outflows (also named Galactic Winds, GW) have been found in galaxies undergoing intense and spatially concentrated SF, in which the star formation rate per unit area ($\Sigma_{\rm SFR}$) exceeds the "Heckman limit":

$$\Sigma_{\rm SFR} \geq 10^{-1} M_{\odot} yr^{-1} kpc^{-2} \tag{1.1}$$

Most if not all starbursts (e.g., Heckman 2002; Chen et al. 2010) and dwarfs (e.g., Schwartz & Martin 2004) in the local Universe, has been found to fulfill this threshold (Sect. 1.3).

A sub-classification of outflows driven by the starburst are the stellar winds. These are gaseous outflows from stellar atmospheres of OB and Wolf Rayet stars. The corresponding mass loss affect the star's evolutionary track by producing changes in mass and in the time-scale of thermonuclear reactions. However, only in certain cases, in which the starburst gives very massive ($> 60\,M_{\odot}$), young ($< 10^7$ years), and metal-rich ($Z > Z_{\odot}$) stars, do stellar winds play a significant role in launching galactic outflows (Veilleux et al. 2005).

If the central engine is the AGN, outflows are powered by the energy and momentum released by accretion onto the central black hole. The AGN-driven outflow can be divided into four distinct regions as for SNe-driven outflows.

Interactions between AGN-outflows and the ISM were at first investigated in order to explain the emission lines and kinematics of broad and narrow line region clouds in quasars (Wagner et al. 2015 and reference therein). However, nowadays the most foremost implication of the ubiquitous detection of AGN outflows (e.g., Sturm et al. 2011; Cicone et al. 2014; Villar Martín et al. 2014 and Sect. 1.3) is that they offer a plausible physical origin for the connection between the central black hole to its host galaxy first formulated by Silk & Rees (1998). They proposed that the AGN provides a source of negative feedback: clearing gas from the host galaxy and inhibiting further SF and AGN activity. The so called: "M_{BH}-σ" (observational) relation (Kormendy & Ho 2013 and reference therein) is hence established. However, as mentioned in Sections 1.1.1 and 1.1.2, the feedback from AGN has also been invoked to reproduce the bright-end of the extragalactic luminosity function (e.g., Hopkins et al. 2006) and to trigger SF (Ishibashi & Fabian 2012; Zubovas et al. 2013).

There are two modes of AGN feedback: "quasar-mode" and "radio-mode" (c.f., "maintenance-mode"). The quasar-mode feedback occurs in high redshift quasars when the AGN is very luminous (close to the Eddington limit), the outflow is driven by the radiation from the accretion disk or young jets which heat the gas on kpc-scale (regulating the overall black hole mass budget). Similarly, the radio-mode feedback is the result of hot gas accretion onto a central black hole but it is active only in massive objects at late times of their evolution (i.e., after the principal growth phase, Croton et al. 2006). This feedback becomes important at low redshifts and on Mpc-scales. The outflow by heating the IGM prevents the growth of massive galaxies steepening the luminosity function at high mass (Fig. 1.1). There are other differences between the two type of outflows, among these: the role of energy and momentum input from the AGN in driving such outflows. This will be discussed in detail in the next section (Sect. 1.2.1). We refer to Fabian 2012 for a review about observational evidence of both modes of AGN feedback. A schematic view of how these feedback works is given in Fig. 1.4 (left).

One of the main goals of this thesis is to attempt to use observational evidence to determine which is the central engine of outflows found in our galaxy sample: the AGN or starbursts? This issue is addressed in Sections 4.7 and 5.7.

1.2.1 Momentum vs. energy driven outflows

As mentioned in Sect. 1.2, the formation of a shell is occurring during the time-evolution of the outflow's bubble. Such shell is basically the interface of the bubble and the ambient medium. Considering how the shock cools behind the shell settles if the outflow is either momentum or energy driven. In case of momentum driven outflow, the shock cool efficiently. The bubble collides with the ISM transferring its momentum in the interaction. Instead, if the shock is unable to radiate away its thermal energy, the shell is driven by the adiabatic expansion of the shocked (hot) wind. Therefore, no substantial cooling losses are sustained and the energy injected by the expanding bubble is fully conserved. In Fig. 1.4 (right) results from simulations of momentum and energy-driven outflows are shown. For a detailed description of these models (and the physics behind of such outflows) we refer to Costa et al. (2014) and Murray et al. (2007).

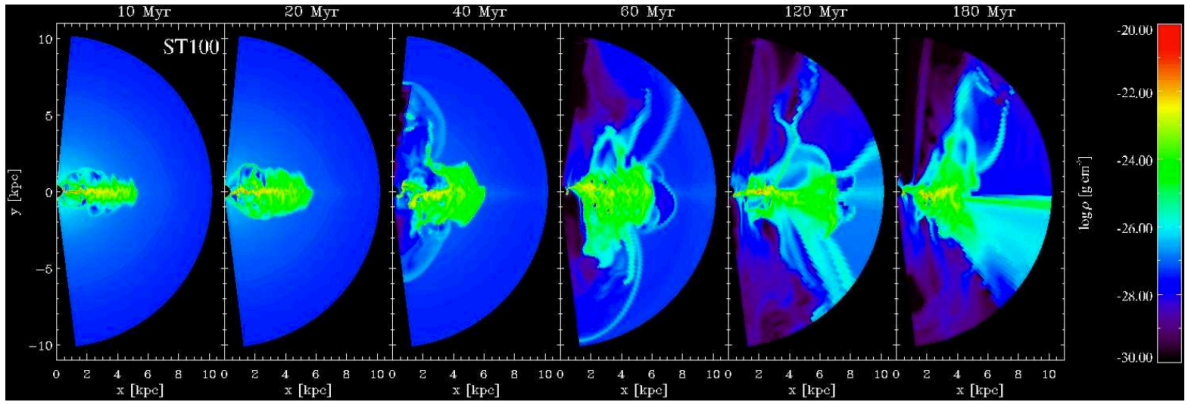

FIGURE 1.3: Snapshots of the mass density distribution at different times from the simulation of a SNe driven outflow. In this simulation each SNe release 4.0×10^{50} erg and 6.0×10^{50} erg as a kinetic and thermal energy, respectively. The elapsed time is marked above each snapshot. At 40 Myr, individual bubbles inside a 3 kpc merge and are fed sufficiently to prevent them falling back to the disk. While, in the outer part bubbles collapse back to the disk. At 60-120 Myr is notable a funnel (close to the axis of symmetry of the flow) which represent the path of the least resistance, surrounded by a conical structure. Figure from von Glasow et al. (2013).

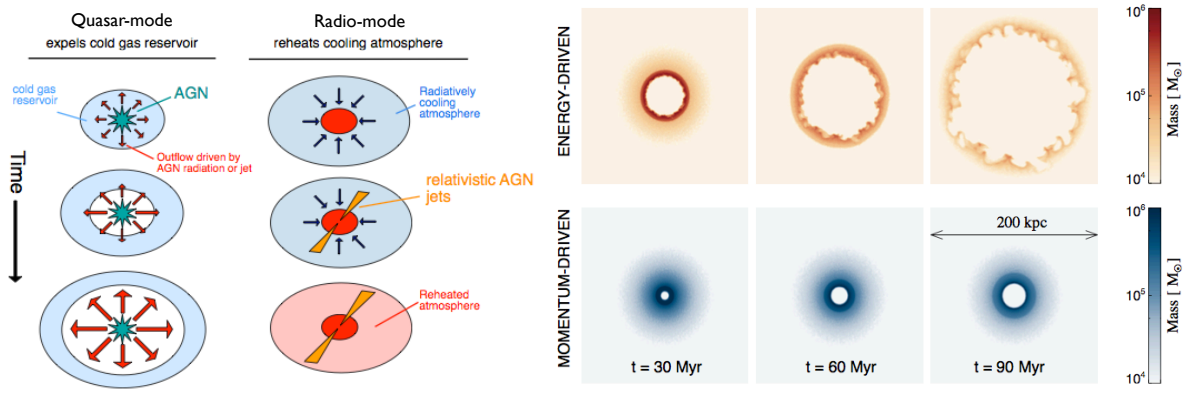

FIGURE 1.4: *Left:* Schematic diagrams to illustrate the two main modes of AGN-outflows (i.e., quasar and radio modes). Figure adapted from Alexander & Hickox (2012). *Right:* Snapshots of energy- and momentum- driven outflow models, top and bottom row, respectively. The different snapshots show the projection of gas mass along a slab of thickness = 10 kpc and length = 200 kpc for a black hole of mass: 10^8 $M_\odot$, emitting at Eddington Luminosity. The elapsed time is marked above each snapshot. Energy driven outflows form ripples due to the development of Rayleigh-Taylor instabilities. Figure from Costa et al. (2014).

Such detailed explanation is usually made for describing AGN-outflows. In pure starburst galaxies (i.e., without AGN detection), outflows are commonly associated either to the energy injected into the ISM by SNe explosions or by the radiation pressure young stellar population on dusty clouds (energy and momentum driven, respectively, see Cicone et al. 2014 and reference therein). Observationally, the investigation of the outflow momentum rate provides an important indicator to distinguish among outflow models. For example, Cicone et al. (2014) compare the outflow momentum rate with the photon momentum output of the AGN (L_{AGN}/c) obtained via CO emission measurements for a sample of 19 nearby galaxies. They found that outflows in AGN-host galaxies are typically energy-conserving, while in pure starbursts outflows are probably momentum-driven.

The mass loading factor ($\eta = \dot{M}_w/\mathrm{SFR}$) is the main outflow parameter incorporated in any model of galaxy evolution (Martin et al. 2013). It scales inversely with the halo velocity dispersion (σ_{halo}) for momentum-driven outflows, but for energy-driven outflows the relation steepens to $\eta \propto {\sigma_{halo}}^{-2}$ (Martin

et al. 2013). These dependencies affect the faint-end of the galaxy mass function (Creasey et al. 2013) and well as the slope of the mass-metallicity relation (Davé et al. 2012).

1.3 Observations of outflows

In this ection, we briefly review the increasing observational evidence probing SNe- and AGN- driven outflows. These observations are largely carried out via multi wavelength spectroscopy and (nowadays) they routinely probe the feedback in the local and the distant Universe (up to z ~ 1-2, Sect. 1.3.3) for a broad range of galaxy types. Simulations are an important tool that helps to unraveling the dynamical evolution of the gas involved in the flow and to understand the cosmological importance of feedback (Sect. 1.3.4).

1.3.1 The multiphase nature of outflows

As the outflow propagates into the ISM of the galaxy, it impacts, shocks, entrains and shreds clouds of varying temperature, densities and sizes. Thus, outflows are made up of a number of gas phases with a wide range of physical conditions, as the ISM surrounding the starburst and the AGN. These can be distinguished by different characteristics such as temperatures and densities. We can generalize these phases into six categories (Draine 2011), whose properties are summarized in Table 1.1. A quantitative estimate of the properties of all these phases in outflows (multi-wavelength approach) is important towards a comprehensive understanding of the feedback mechanism and its net effects on the host.
Different phases can be probed spectroscopically via emission and absorption lines across different wavelength ranges. Outflows are identified by the kinematic signatures they leave (e.g., blue shifted lines), in contrast to the regular rotation of the galaxy disk.
Over the past 20 years, the observational multi-wavelength data probing outflows is steadily increasing, both in quality and quantity. The main outflows component are: the hot, warm, neutral and molecular phases, and dust[4]. These are studied through X-rays, optical and radio data, via different tracers such as Fe XXV at 6.7 keV, Hα/NaD $\lambda\lambda$ 5890, 5896 and CO(1-0) at 115.3 GHz, respectively. Fig. 1.5 shows an example of how a multiwavelength data set can be combined to give a comprehensive picture of the outflow phenomenon (caught in act in the starburst NGC 253).
X-Rays outflows are mainly studied for AGNs though attempts for detecting hot gas have been done also for starbursts such as M82 (Strickland & Heckman 2009) and NGC 253 (Fig. 1.5, Pietsch et al. 2000; Bauer et al. 2007) and dwarfs (e.g., Martin 1999). AGN host galaxies have typically an X-ray spectrum rich of emission lines such as: H-like, He-like and (prominent) Fe-L features (see also Tab. 1 for the case of NGC1068, Netzer & Turner 1997). These are diagnostic for the very hot gas[5] and as they span a wide range of low to high ionization states, are particular suitable to study the structure of

[4]Note that, despite the fact that dust is often entrained in GWs (Veilleux et al. 2005), such component is not treated in great detail in this manuscript. In nearby galaxies, optical measurements (e.g., via Hα/Hβ λ 4861) allow to estimate dust masses but are rather uncertain compared to far-IR color maps (which are sensitive to both cold and warm dust). In what follow, we simply assume that dust is universally present in outflows based on the correlation between color excesses and the equivalent widths of blueshifted low-ionization lines in nearby SFGs (Veilleux et al. 2005; Heckman et al. 2000).

[5]Such gas is often called: wind fluid. It is also long thought to be the prime mover of outflows (see Sect. 1.2 and Chevalier & Clegg 1985).

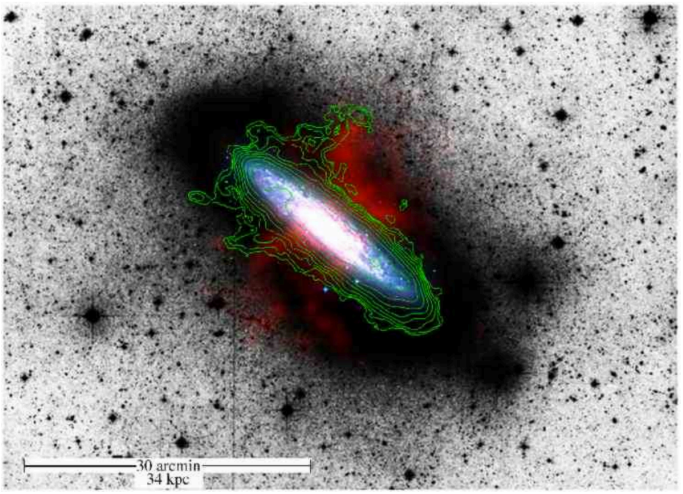

FIGURE 1.5: Multi-wavelength image of the nearby spiral NGC 253. The optical image is from Malin & Hadley (1997), overlaid in blue the DSS optical disk, in red the X-ray (0.1-0.4 KeV) emission from ROSAT (Pietsch et al. 2000), and with green contours Compact Array HI observations are marked. Figure from Boomsma et al. (2005).

TABLE 1.1: Characteristics of the ISM (and outflow) gas phases.

Phase	Temperature K	Density cm^{-3}
HIM	$> 10^{5.5}$	0.004
WIM	$\sim 10^4$	0.3-10^4
WNM	~ 5000	0.6
CNM	~ 100	30
Diffuse H_2	10-50	10^3-10^6
Dense H_2	50-10^3	1- 10^6

Notes. Acronymous stand for: HIM = Hot Ionized Medium; WIM = Warm Ionized Medium; WNM = Warm Neutral Medium and CNM = Cold Neutral Medium.

ionization of the outflows.

The large majority of observations of outflows are carried out in the optical rest frame which represent a powerful tool to investigate many fundamental properties of outflows. In fact, several emission lines such as the Hα, the [S II] $\lambda\lambda$ 6717, 6713 doublet and many oxygen lines ([O III] and [O II] λ 3727) lie at these wavelengths. These optical spectral features allow to trace warm ionized gas outflows in nearby galaxies (e.g., Heckman et al. 1990; Soto & Martin 2012, see also Sect. 1.3.2) but are also used at high-z (Sect. 1.3.3).

Historically, Hα has been widely considered the choice tracer. Indeed, studies based on Hα measurements have allowed to infer the kinematics, the morphology, the role of SF/AGN in launching ionized outflows, the variation of the kinematic properties of the outflowing material along the merger process, as well as their feedback (e.g., Arribas et al. 2014). Hα can be traced up to $z \sim 2.5$ with current near-IR ground base capabilities.

The cold gas represents the fuel of SF. Therefore, the variations of such cold gas reservoir are important for the evolution of the host and its observed properties. In the optical range, the cold neutral gas which is entraining in outflows is detected through the sodium doublet absorption features (NaD – e.g., Heckman et al. 2000; Schwartz & Martin 2004; Martin 2005; Rupke et al. 2005a a, b, c; Chen et al. 2010). Observations of the outflow's neutral phase will be described in detail in Sect. 1.3.1.1.

One of the new results achieved with the Herschel Space Observatory mission and the IRAM-PdBI[6] is

[6]IRAM stands for: Institut de Radioastronomie Millimétrique and PdBI for Plateau de Bure Interferometer.

the discovery of massive high velocity cold molecular outflows in ULIRGs (Ultra Luminous Infrared Galaxies) and AGN-host (e.g., via P-Cygni profiles of far-IR OH transitions and high-velocity wings of the CO and HCN emission lines). Sturm et al. (2011), based on Herschel data of 6 ULIRGs, suggest that the molecular outflows may be faster and more powerful in ULIRGs hosting powerful AGN. This picture has been recently confirmed, with a larger sample (19 sources) by Cicone et al. (2014), exploiting IRAM-PdBI data. All these works point to a negative feedback of these outflows (with η up to 4, Cicone et al. 2014). Evidences for molecular outflows driven by SNe are still scarce (e.g., Bolatto et al. 2013).

Multi-wavelength studies of outflows are needed to increase our understanding of the physics which occurs in outflows towards a more realistic modelling. A severe limitation of previous observational studies is that they are mainly based on long-slit spectroscopic which provides a limited knowledge of the outflow phenomenon. The physically-extended nature of outflows (occurring on kpc-scales) lends itself to spatially-resolved observations. As a result, IFS has become an important technique to detect outflows and to study their spatially resolved properties (e.g., extent, velocity structure, geometry). This is particularly relevant for describing outflows in structurally complex objects (e.g., (U)LIRGs , see Sect. 1.4). However, outflow IFS-studies for relatively large samples have only recently been carried out (e.g., Westmoquette et al. 2011; Bellocchi et al. 2013; Rupke & Veilleux 2013, and references there in).

1.3.1.1 Neutral gas outflows

A method to detect the cold neutral gas in outflows consists in tracing NaD absorption against regions with a bright stellar continuum (see Sect. 1.3.1 for other techniques).

The NaD absorption originates in the cold gas entrained by the warm snowplow (Sect. 1.2). To investigate the presence of cold gas in an warm flow, Fujita et al. (2009) modelled the effects of repeated SNe explosions driving supershells in the central region of a disk at a resolution of ~ 0.2 pc. They found that the cold gas observed in ULIRG outflows may well correspond to dense clumps in which the bubble fragments due instabilities. Observationally, current capabilities do not allow to investigate gas physics at such high resolution. Therefore, it is generally assumed that the NaD absorption arises from material entrained by the shell.

Many previous studies of outflows were performed using the Hα emission in optical data sets. However, the picture we can derive with Hα is "density-weighted". Specifically, the strength of Hα emission is weighted toward the higher density gas which likely resides in the disk (as the emission scales as the density square, Martin 2006). In these cases, to have more detailed estimate of the gas entrained in the outflows (and thus of their feedback), the most straightforward choice is to use the optical NaD feature. The strength of absorption lines does not scale with density and can occur at any location along the sight line within the source of background illumination and the observer. This allows to detect outflows (with no ambiguity in the direction of the flow) and to constrain its morphology and that of the host (see the case of LIRG IRAS F11506-3851, Fig. 4.8 in Sect. 4.5). The most severe limitations of the NaD absorption-technique consist in tracing outflows on large scales (we can see absorption only up to the projected size of the disk) and that the NaD absorption feature can be contaminated by stellar absorption. This latter issue, is addressed in Sect. 3.2.2 and also discussed in Sect. 5.1.

A number of works have investigated the cold outflow-phase NaD for a wide range of galaxy types (from dwarf – e.g, Schwartz & Martin 2004, to (U)LIRGs[7] – e.g, Rupke et al. 2005a). Villar Martín et al. (2014) found that such method is more effective for tracing SNe-driven outflows rather than AGN-induced outflows since the neutral component is more significant in starburst galaxies, as (U)LIRGs, than in quasars (Villar Martín et al. 2014). Indeed, AGN-outflows, have only been found in small samples of ULIRGs with Seyfert (Sy) nuclei (e.g., Rupke et al. 2005b; Krug et al. 2010). Nearby (U)LIRGs show the most conspicuous cases for outflows in the nearby Universe (Heckman et al. 2000; Rupke et al. 2002, 2005b,c; Krug et al. 2010) with a rate of detection of about 75%-80% (Heckman et al. 2000; Soto & Martin 2012). NaD surveys in (U)LIRGs have shown, that the typical outflow velocity is in the range of 100-600 kms^{-1} (Rupke et al. 2005c) with a few exceptional cases having velocity up to 1000 kms^{-1}. The observed broadness of the NaD lines (typically FWHM $\sim$ 300 kms^{-1}, Chen et al. 2010) is consistent with the scenario proposed by Fujita et al. (2009).

Generally, in (U)LIRGs the cold outflows traced via NaD are driven by the SF. In fact, Rupke et al. (2005c) found that mass, momentum, energy and outflows rates depend roughly linear on the SFR (and thus on the IR-luminosity and SNe-rate), based on longslit observations of 65 nearby (U)LIRGs. This dependency is also consistent with the outflow velocity - SFR relation found by Martin (2005) (Sect. 1.3.2, Eq. 1.2) indicating higher thermalization efficiency in high SFR galaxies (albeit a bright-end flattening). Outflows in starburst and (U)LIRGs may entrain considerable cold neutral material (10-10^{10} $M_{\odot}$) at a substantial high rate (10-100 $M_{\odot}\,yr^{-1}$) (Veilleux et al. 2005). However, a strong SF-quenching is not straightforward as indicate by the generaly low outflows mass loading factors – i.e., $\eta < 1$ found by Rupke et al. (2005c). Otherwise to the negative feedback, cold outflows are able to escape from less massive galaxies or to rain back to the galaxy disk due to the pull of the gravitational potential in more massive galaxies.

Overall, the above mentioned results and studies are based on longslit data which provide a limited knowledge of their geometry and kinematics.

Recent works using IFS technique have been recently expanded the census of neutral outflows mainly in (U)LIRGs. In fact, they were focused on neutral outflows in extreme sources the most luminous merger systems (Mrk 231: Rupke & Veilleux 2011) and ULIRGs (Rupke & Veilleux 2011, 2013; Bellocchi et al. 2013) and thus not very representative of the overall (U)LIRGs population. The neutral outflows in the potentially interesting LIRG range have been explored less, although at even lower luminosities it is worth mentioning the works by Jiménez-Vicente et al. (2007), Westmoquette et al. (2011), and Davis et al. (2012).

The NaD absorption is poorly studied for distant galaxies. Current ground base IR-capabilities may capture the multiphase nature of outflows via NaD and Hα lines (simultaneously) only up to z $\sim$ 2-2.5. Multiphase distant outflows can be proved, alternatively, with other absorption lines such: Lyα and Mg II $\lambda\lambda$ 2796,2803 (see Sect. 1.3.3).

[7] (U)LIRGs stands for Luminous Infrared Galaxies and Ultra Luminous Infrared Galaxies. They are described in detail in Sect. 1.4.

1.3.2 Outflows in local galaxies

In the local Universe, all the SFGs in which the star formation rate per unit area exceeds the so called "Heckman limit" (Sect. 1.2, Eq. 1.1) seem to develop GWs (Heckman 2002).
Most outflows are found to be hourglass-shaped with the cone axis being aligned with the axis of galaxy rotation (i.e., minor kinematic axis), as seen by using optical emission lines (e.g., Hα in M82, Lehnert et al. 1999 and NGC 253, Fig. 1.5). This conical morphology results from interactions with the host galaxy's disk. The opening angle or any tilt or asymmetry may reflect the distribution, thickness and the dynamical status of the disk itself. Indeed, thick and turbulent disks, the vertical growth of wind fluid is likely enhanced due to turbulence (Cooper et al. 2008 and Sect. 5.6).
Models predict that the majority of the energy in outflows exists in the hot phases, with the kinetic energy of such gas being several times the thermal energy (Strickland & Stevens 2000). However, this phase has been observationally elusive with only few cases of clear detection (see Strickland & Stevens 2000, for the case of M82).
Many observational velocity measurements of outflows are of the entrained cooler material, – e.g., cold neutral and warm ionized gas. These velocities are in the range 100-1000 kms^{-1} (Veilleux et al. 2005) and were measured using UV (Lyα and Lyβ λ 1026, – e.g., Shapley et al. 2003), optical emission ([O III] and Hα – e.g., Rupke et al. 2005b; Arribas et al. 2014) and/or absorption lines (NaD, – e.g., Rupke et al. 2005c and Sect. 1.3.1.1).
Different scaling relations, describing how the outflow properties scale with those of the host galaxy, have been found. Specifically, outflow velocity and mass outflow rate scale with the SFR of the host (Sect. 1.3.1.1). Martin (2005), on the basis of a compilation of published data for dwarf and ULIRGs and longslit spectroscopy of 18 ULIRGs at z ∼ 0.3-0.16, found that the outflow velocity scales (V) with the SFR as:

$$log(V) = (0.35 \pm 0.06)\ log(SFR) + (1.56 \pm 0.13) \tag{1.2}$$

This scaling relation was first obtain using kinematic measurement of the cold outflow phase (via NaD, Sect. 1.3.1.1) but seems to held considering also the ionized phase as found by Arribas et al. (2014). The V-SFR is expected if the mechanical energy is supplied by stellar winds and SNe explosions. The trend for which galaxies with higher SFRs launch outflows to larger velocities is in agreement with the relationship predicated by Heckman et al. (2000) for which $V_{max} \propto L^{1/4}$ (where V_{max} is the maximum outflow defined as V + FWHM/2). The mass loading of the outflows scale linearly with the SFR, as found by Arribas et al. (2014).
Many active galaxies also show signs of large-scale outflows and various techniques have been used to identify them. X-ray and UV absorption-line spectroscopy reveal that these outflows are ubiquitous, extended on kpc-scales and can achieved high-velocity up to ∼ 0.1c (see Harrison et al. 2012 and reference therein). Hα and [O III] have been also widely used to trace warm outflow signatures in AGN hosts (e.g., Davis et al. 2012; Villar Martín et al. 2014) while near-IR diagnostics have been exploited less (e.g., Müller-Sánchez et al. 2011). Contrary to what we know of SNe-driven winds, AGN outflows are not always perpendicular to the major axis of the host galaxy but randomly orientated (Veilleux et al. 2005) and represent a more extreme phenomenon (e.g., higher mass outflows rate). Based on IFS observations for a sample of 16 type 2 AGNs, Harrison et al. (2012) have shown that the [O III] traces high-velocity (510-1100 kms^{-1}) and turbulent ionized gas (FWHM ∼ 600-1500 kms^{-1})

extended over 6-16 kpc. These outflows are likely expelling gas at a considerable rate – i.e., ten times the SFR.
Molecular outflows have been observed via emission lines in stacks of nearby ULIRGs (Chung et al. 2011; Sturm et al. 2011; Cicone et al. 2014), local starbursts including (M82, Walter et al. 2002), and NGC 253, (Bolatto et al. 2013 and Fig. 1.5) and AGN-host galaxies (including MRK 231 Feruglio et al. 2010; Cicone et al. 2012). These powerful AGN-driven molecular outflows extended on kpc-scale provided strong evidence for the negative feedback scenario (SF-quenching).
These outflows where mainly detected via IR-spectroscopy (OH line) and only in few cases with spatially resolved radio observations (Cicone et al. 2014). With the advent of the Atacama Large Millimeter/Submillimiter Array (ALMA), the situation is now changing. The detailed case of the nearby Seyfert NGC 1068 (García-Burillo et al. 2014) in which the outflow and its environment were studied on scales of 20-35 parsecs with a set of molecular gas tracers is an example of the huge improvement in our understanding of the feedback that ALMA allows to make.

1.3.3 Outflows in the distant Universe

From Sect. 1.1, it is clear that starburst- and AGN- driven outflows play an important role in the formation and evolution of galaxies. In the early Universe outflows appear to be ubiquitous, being a key factor in the evolution of galaxies at these redshift. In particular, during the peak of SF ($z \sim 2$-3) outflows are expected to be very prominent and ubiquitous (Genzel et al. 2014; Förster Schreiber et al. 2014; Maiolino et al. 2012; Martin et al. 2012; Cano-Díaz et al. 2012; Newman et al. 2012). At these redshifts galaxies have SFRs of about a hundred solar masses per year (e.g., Genzel et al. 2008) as found via their (strong) Hα emission (redshifted into the near-IR). This massive SF leads to a high level of turbulence which may activate the formation of outflows.
At high redshift, the main diagnostics for outflows observed at optical wavelengths are Lyα and Mg II. These have been observed up to $z \sim 5$ (e.g., Dawson et al. 2002) with a characteristic P-Cygni profile which consist of a redshifted emission as well as blueshifted absorption. The emission is interpreted as resonant scattering off the back side of an expanding shell while the near side imprints the blueshifted resonance absorption. The Mg II line is generally observed in absorption of the background QSO continuum light and allows to infer the spatial extent (on large scale) and density of the warm outflow. For example, Martin et al. (2013) mapped the Mg II line for a $z \sim 0.9$ SFG, finding that the outflow is extended up to 18 kpc and it is traveling at an average velocity of 230 km^{-1}. The mass rate is 330-500 $M_\odot\,yr^{-1}$ and corresponds to 4-6 times the SFR of the host (80 $M_\odot\,yr^{-1}$).
However, generally, at $z > 1$, observations are limited since the galaxies at these distances are typically faint. Indeed, high-redshift samples used to study outflows contain few galaxies with masses $< 10^9$ M$\odot$ or SFR less than a few $M_\odot$ per year (Erb 2015). Therefore, since now, trends between outflow properties and galaxy properties have been more difficult to determine.
The number of large surveys of outflows in distant galaxies being carried out is increasing. For example, Erb et al. (2012) studied a sample of ~ 100 galaxies in the redshift range: 1-2 looking for outflows on the bases of Mg II and Fe II absorption and emission. Other surveys of distant outflows (based on Mg II) have been carried out by Weiner (2009) and Rubin et al. (2010) which consist of 1400 and 500 galaxies at redshifts 1.4 and 0.7-1.5, respectively. In particular, Weiner (2009), suggest that the scaling

relation within outflow velocity and galaxy mass. Indeed, they found characteristic velocities of 300-500 kms^{-1} and up to 1000 kms^{-1} in the most massive galaxies at higher SFRs. Among the various types of galaxies at high redshifts strongly star-forming Lyman Break Galaxies (LBGs) are good cases for studying outflow. LBGs samples are the largest both from a statistical point of view, and in terms of the cosmic time covered (Vanzella et al. 2009 and reference therein). Outflows in $z \sim 4$-5 LBGs seem to be analogs to those found in $z \sim 2$-3 galaxies (Vanzella et al. 2009). Furthermore, the distant outflows in LBGs are found to be able to enrich the IGM, with metals expelled up to large radii (~ 100 kpc, Steidel et al. 2010).

The large majority of the observations of outflows in distant galaxies are obtained with long-slit capabilities. Spatially resolved observations of warm outflows at redshift above 0.5 are still rare (e.g., Harrison et al. 2012; Carniani et al. 2015; Cresci et al. 2015). The hotter wind fluid, which entrains this warm gas, largely eludes direct detection at intermediate and high redshifts (Tripp et al. 2011).

In distant galaxies, outflows are found also in star forming clumps which are analogous of those found in local ULIRGs. Soto & Martin (2012) compared the outflow mass and outflow rates in a sample of ~ 40 local ULIRGs with those obtained in star forming clumps by Genzel et al. (2011). These authors found that, while the range of SFR is higher in the local ULIRGs sample with respect to high-z star forming clumps (20-180 vs. 3-40), the mass outflow rate are smaller (0.4-58 vs. 6-200). This may imply a different efficient of outflows considering their ionized phase or that other factors (e.g., filling factor) are not correctly taken into account.

What we learn from the comparison of local and distant observations of outflows is far to be exhaustive, but new capabilities will lead a deepen understanding of the outflows and their feedback. With ALMA it is now becoming possible to look for cold molecular outflows in intermediate redshift galaxies thank to its high sensitivity and resolution at millimeter (mm) and sub-millimeter (sub-mm) wavelengths (e.g., Sun et al. 2014). Additionally, upcoming James Webb Space Telescope (JWST) observations will provide a detailed view of the feedback in high redshift galaxies, producing excellent data to test current hydrodynamic simulations and semi-analytic models.

1.3.4 Outflows in a cosmological context

The growing observations of SNe- and AGN- driven outflows at any redshift and for a wide range of galaxy types, have provided a compelling evidence that outflow's feedback plays an important role in establishing the observed correlations being a key ingredient in galaxy evolution. Therefore the feedback is now included in many hydrodynamic simulations (e.g., ILLUSTRIS, Nelson et al. 2015 and reference therein) and semi-analytic models (e.g., Springel & Hernquist 2003; McNamara & Nulsen 2007; King & Pounds 2015) of galaxy formation and evolution.

Recent simulations have investigated both the SNe and AGN outflow's negative feedback in detail, especially at high redshift. For example Anglés-Alcázar et al. (2014) showed that outflows can dramatically alter the Star Formation History (SFH), kinematics, and morphology of galaxies at $z \sim 2$. Indeed, outflows with a variety of mass-loading factors and outflow velocities, are essential to producing the gas-rich, extended, and turbulent disks that are typically observed in high redshift SFGs.

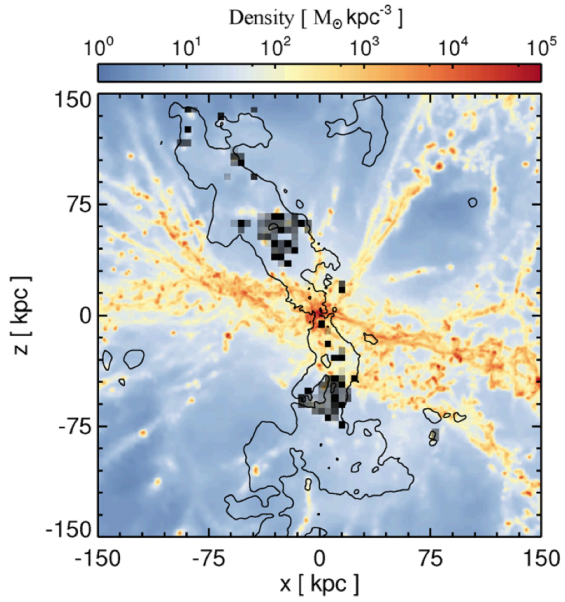

FIGURE 1.6: Map of the gas density in the zoom-in simulation with both SNe and AGN feedback at $z = 6.6$. The contours show the hot component of the AGN-driven outflow (with a velocity of 500 kms^{-1}) while dark pixels show the location of the gas in the cold phase. Figure from Costa et al. (2015).

Recently, Costa et al. (2015), performed zoom-in simulations[8] of the $z \sim 6$ six most massive haloes found in the Millennium Volume (Springel et al. 2005) to study the effect of feedback and the different outflow's phases. By focussing on the cold gas at large scale in both SNe- and AGN- driven outflows, they found that hourglass-shaped outflows (an example is shown in Fig. 1.6) occur in simulations (despite a special orientation requirement), matching IRAM-PdBI observations of outflows in bright QSOs found by Cicone et al. (2014).

Despite the success of cosmological simulations in reproducing properties of observed galaxies and even the morphology of outflows, the positive feedback is not taken into account yet. This implementation presents two challenges: empirical and qualitative. The empirical challenge is that observations of AGN-triggered SF are still scarce (see Sect. 1.1.2, Cresci et al. 2015). The quantitative challenge is that the "small scale behaviour" is not generally modelled at sufficiently high resolution (as reviewed in Bourne et al. 2015).

Galaxies can acquire new fuel for SF otherwise of cosmological inflow. An alternative gas- replenishment can occur throughout gas-recycling as a consequence of galactic fountains (i.e., the mechanism of re-accreting gas that previously has been ejected from the galaxy via outflows and it is raining back onto the disk) but, generally, cosmological simulations do not include prescriptions about that. Segers et al. 2016 attempt to assess the significance of recycled ejecta as fuel for SF in their simulation. Interestingly, their results are consistent with both the (observationally inferred) inside-out growth of galaxies (e.g., van der Burg et al. 2015) and previous studies (e.g., Kennicutt et al. 1994; Leitner & Kravtsov 2011). This emphasizes the importance of modelling the gas-recycling in simulations of galaxy formation, and the necessity of accounting for such gas in the estimation of the gas reservoir of present-day galaxies.

[8] In zoom-in simulations, a sub-volume extracted from a larger-volume simulation is re-simulated at significantly higher resolution, providing a substantial increase in resolution. Such simulations can simultaneously capture the baryon cycle on larger scales, while still achieving sufficiently high enough resolution to robustly model the internal structure and dynamics of galaxies (Anglés-Alcázar et al. 2014).

1.4 LIRGs and ULIRGs

(U)LIRGs are a class of objects exhibiting an extremely high amount of IR-Luminosity within 8-1000 μm (L_{IR}). These galaxies were discovered first by the InfraRed Astronomical Satellite (IRAS; Houck et al. 1985) as a class of starburst IR-galaxies[9] with elevated IR-luminosities: $L_{IR} = 10^{11}$-$10^{14}\,L_{\odot}$. The LIRG and ULIRGs luminosity ranges are respectively: $10^{11}\,L_{\odot} < L_{IR} < 10^{12}\,L_{\odot}$ and $L_{IR} > 10^{12}\,L_{\odot}$.

Other IR-properties can be used to further classify (U)LIRGs. Specifically, IR broad band colors, defined as the ratio of 25 μm vs. 60 μm and that of 60 μm vs. 100 μm IRAS fluxes, distinguish warm ($f_{25}/f_{60} > 0.2$ and $f_{60}/f_{100} > 0.3$, Lonsdale et al. 2006) from cold (U)LIRGs. Such classification is based on the firsts large samples of nearby IRAS-ULIRGs such as the Bright Galaxy Sample (BGS, Soifer et al. 1987) updated to Revised Bright Galaxy Sample (RBGS, Sanders et al. 2003) and the complete flux-limited IRAS 1 Jy sample (Kim et al. 1998).

This classification may be used to broadly characterize the spectral type of (U)LIRGs for which spectroscopy is not available. Accordingly only to the IR-color selection, warm (U)LIRGs (e.g., MRK 231) have IR-emission that tend to peak at rest frame mid-IR rather than far-IR. These show a compact and bright nucleus, and generally host an AGN, which could be the main energy source of the IR emission (i.e., AGN-dominated). While, cold (U)LIRGs (e.g., UGC 5101) have their IR emission peaked at far-IR and therefore, are likely powered by starbursts (i.e., SF-dominated). More insights of major IR energy-source can be gained with the analysis of the spectral energy distribution (Sanders & Mirabel 1996) or several mid-IR diagnostic lines (as 7.7μm PolyAromatic Hydrocarbons emission – i.e., PAH, [NeII] λ 12.8 μm and [OIV] λ 25.9 μm). We refer to Sect. 1.4.1 for a more detailed classification of the power source behind the IR emission.

Nearby (U)LIRGs may have in some cases simple morphologies (typically spirals), but in others can reveal to be very complex systems being often part of a merging galaxy groups. Early optical and near-IR imaging surveys (Lonsdale et al. 2006 and reference therein) revealed that signs of mergers and interactions are more common amongst ULIRGs than in lower luminosity systems. Specifically, roughly 25% of LIRGs and nearly all ULIRGs are undergoing galaxy interactions/mergers (e.g., Veilleux et al. 2002). Tidal interactions between the galaxies in the same (U)LIRG-system are believed to drive gas inflow capable of fueling the central power source.

The observational manifestation of mergers depends on the stage of the interaction in which (U)LIRGs are found. These stages can be broadly summarized as: isolated, interacting, post-coalescence. In Fig. 1.7, three different phases of the merging process are shown. Sign of ongoing and past merger activity in (U)LIRGs, can be also be identified from a kinematic point of view. This topic has been treated in great detail by Bellocchi et al. (2013) and Bellocchi et al. (2016), on the basis of the spatially resolved kinematics of Hα. Column 5 of Table 2.1 lists the morphological classification of the (U)LIRGs studied in this manuscript and in Sect. 3.4, we briefly describe their kinematic classification.

Although (U)LIRGs are relatively rare at low redshift (Sect. 1.4.3), their luminosity function is very steep (Le Floc'h et al. 2005) and they are the major contributor to the IR energy density at $z \sim 1$-2 (Caputi et al. 2007).

[9] Galaxies that emit a large fraction ($\sim 90\%$) of their total energy output in the IR are called "IR-galaxies".

FIGURE 1.7: Examples of systems at different stage of interaction. Images from the Hubble Heritage Gallery. From left to the right (numbered progressively): galaxies are in simple interaction, then became a "close pair" and finally merge.

1.4.1 Power sources and ionization mechanisms

Sub-mm and IR observations indicate that (U)LIRGs harbor large masses of molecular gas and dust (10^9-10^{10} $M_\odot$, Papadopoulos et al. 2012). Such highly opaque gas reservoir obscures the centre of the galaxies in which resides, feeding the power source (SF and/or AGN) but hampering its identification. Therefore, the origin of the strong IR emission in (U)LIRGs has been widely debated, since the presence of either an AGN or a starburst does not prove that one or the other is the principal power source for their IR-luminosity.

Several diagnostics have been proposed to discriminate the ionization mechanisms in (U)LIRGs. There is plenty of evidence showing that a large fraction of local LIRGs are mainly powered by SF. Such SF is extended on kpc-scale as traced by [NeII] 12.8μm and [NeIII] 15.6μm emission lines (Díaz-Santos et al. 2011). These lines are particularly important since their luminosity is directly proportional to the number of ionizing photons, thus, they probe young and massive stars. Additionally, the cold IR colors, typically of LIRGS, generally indicate the presence of strong starbursts (e.g., SF-dominated). In this case, LIRGs are powered by the reprocessing of UV photons that originate from populations of hot young massive stars.

Many works highlight that the occurrence of AGN in (U)LIRGs seems to increase with luminosity (Alonso-Herrero et al. 2006; Veilleux et al. 2009; Nardini et al. 2010; Alonso-Herrero et al. 2012). In fact, ULIRGs exhibit strong signatures of an AGN in their center as seen, for example, via [Ne V] lines (which is rather low in LIRGs, Veilleux et al. 2009) or a PAH-deficit (Luhman et al. 2003). Additionally, ULIRGs have typically disturbed morphologies, indicating that they represent the result of mergers of gas-rich galaxies which can in turn trigger the AGN activity. In AGN-dominated (U)LIRGs dust in an optically-thick torus surrounding the AGN absorbs large amounts of energy and re-radiates it at longer wavelengths, contributing to the large IR luminosities of (U)LIRGs. Additionally, X-rays and radio observations are powerful tools to detect AGNs in ULIRGs. Indeed, the hard X-ray band (> 10 keV), since less affected by absorption heavily obscured torus's material is widely used to infer the presence of an AGN. At radio wavelengths, indeed, the presence of an AGN can be confirmed if the brightness temperature of the central source is higher than 10^6 K (Condon 1992). An AGN may, however, remain undetected if the source is radio-quiet or the synchotron radiation is strongly self-absorbed. However, in most cases (Yuan et al. 2010 and reference therein), there is likely to be

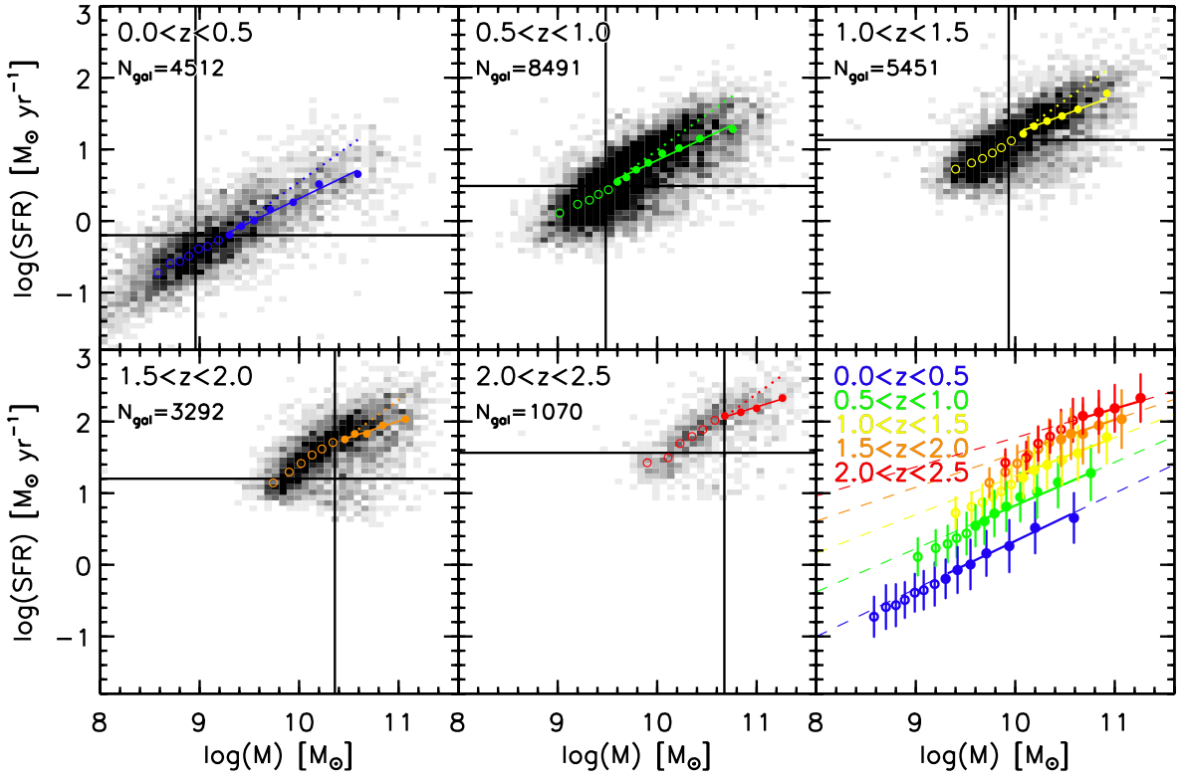

FIGURE 1.8: MS for SFGs at different redshift (five redshift bins out to z = 2.5, quoted in each panel). The gray scale represents the density of points for the selected SFGs. Vertical lines are mass and SFR completeness limits. A power-law fit (above the mass and SFR completeness limits) is displayed with a continuous line in each panel. For comparison, the linear relation is shown (dotted line). In the bottom-right panel, medians and scatter are displayed color-coded by redshift bin. Figure from Whitaker et al. (2012).

a combination of both SF and AGN contributing to the emission from (U)LIRGs. The unambiguous identification of the central energy source or the relative contributions from starburst and AGN, remains a major challenge in the study of (U)LIRGs.

The starburst-AGN coexistence in local (U)LIRGs makes these galaxies excellent laboratories for SNe and AGN feedback. Although, many studies of outflows in nearby (U)LIRGs have been made since their universal presence[10] was determined (e.g., Veilleux et al. 2005; Arribas et al. 2014) the relative importance of feedback from starburst and/or the AGN outflows is still a subject of considerable studies. In LIRGs, the intense IR luminosity is mostly powered by the SF rather than by an AGN making SNe explosions a prime candidate for driving outflows. However, in some case, the contribution of an hidden AGN may be substantial (e.g., Bedregal et al. 2009). In contrast, in ULIRGs, the AGN boost seems to be ubiquitous (e.g., Spoon et al. 2013; Arribas et al. 2014; Cicone et al. 2014; Hill & Zakamska 2014).

1.4.2 The role of (U)LIRGs in galaxy evolution

Over the last decade, deep optical and IR surveys have established that the majority of SFGs follow a simple scaling correlation (Brinchmann et al. 2004; Daddi et al. 2007; Noeske et al. 2007; Elbaz et al.

[10]Note that, generally in (U)LIRGs, the condition for launching (at least) SNe-driven outflows, so called Heckman limit (Eq. 1.1) is generally fulfilled.

2007; Wuyts et al. 2011; Whitaker et al. 2012). This tight correlation helds between stellar mass and SFR, i.e. the so-called main sequence (MS, SFR $\propto M_{\star}^{0.6}$).

The MS is observed up to z ~ 2.5-3 (Whitaker et al. 2012) with the zero-point that evolves with redshift, in the sense that high-redshift galaxies form stars at higher rate than local galaxies of similar stellar mass. Indeed, high-redshift galaxies are found to be located at higher SFR with respect to the local MS (Wuyts et al. 2011; Whitaker et al. 2012). A possible interpretation of this behavior is given in terms of a larger gas fraction in galaxies earlier in cosmic history (e.g., Combes et al. 2012 and references therein). The existence of the MS has been interpreted as evidence that the majority of galaxies throughout cosmic history form stars in a steady secular mode that requires a continuous replenishment of gas from the IGM, happening in time scales that are longer than their dynamical timescales (Sect. 1.1.2 and Wuyts et al. 2011). The existence of the MS is predicted also by simulations (Sparre et al. 2015) and semi-analytical models (Dutton & van den Bosch 2009; Davé et al. 2012).

Complementary to the MS, the Mass - Metallicity relation (MZ) provides further insights on the evolution of galaxies. The MZ connects stellar masses to both the gas phase and stellar metallicities and, as the MS, it has been observed over a range of redshifts.

These relations are indicators of how galaxies form and growth. In this picture, of major interest is the Fundamental Metallicity Relation (FMR). This has been obtained by combining MS and MZ, and thus relates the stellar mass, gas-phase metallicity and the SFR of galaxies (Mannucci et al. 2010). The FMR reflects the cycle of inflows that feed SF, the production of metals and enrichment of the ISM, and the subsequent stellar winds (see Obreja et al. 2014 and reference therein).

However, multiple short timescales processes as merger or feedback from starburst and AGN, may shape the gas reservoir and the SFH of a galaxy. Therefore, the expected position in the $M_{\star}$-SFR plane or M-Z plane is then altered (see Moustakas et al. 2013, and reference therein).

Local (U)LIRGs are exceptions to both MS and FMR. Specifically, they have a large off-set from the MS up to z ~ 1 while their off-set from the z ~ 2 MS is relatively smaller (Elbaz et al. 2011; Kilerci Eser et al. 2015). (U)LIRGs follow the FMR with high dispersions (between 0.09 dex-0.5 dex), that is similar to that of high redshift (z > 2) galaxies (Kilerci Eser et al. 2014).

These observations are consistent with the fact that (U)LIRGs are systems in interaction and their more efficient SF than MS-galaxies of the same stellar mass (larger specific SFRs larger by an order of magnitude with respect to the MS-galaxies, Rodighiero et al. 2011), is probably triggered by mergers. Therefore, local (U)LIRGs form stars in the starburst mode of SF, whereas, their high-z counterparts are forming stars in the MS domain (Elbaz et al. 2011, see also Sect. 1.4.3).

From all of these studies, the emerging general evolutionary sequence connects SFGs to quasars through galaxy mergers in which (U)LIRGs represent an important phase. More specifically, (U)LIRGs are observed as triggered by galaxy major mergers of gas- and dust- rich spiral galaxies, and caught in act in an intense phase of SF. This is then followed by a blowout phase, during which most of the material enshrouding the supermassive black hole is blown away and the system is observed as a luminous red quasar. When most of the dust is removed (e.g., via outflows), the system is eventually observed as a blue quasar (Hopkins et al. 2008). This model is consistent with the observed increase of the fraction of obscured sources with redshift up to z ~ 3 (Treister et al. 2010).

1.4.3 Distant (U)LIRG populations

Nearby (U)LIRGs are found to be rare[11] with a space density several orders of magnitude lower than that of normal galaxies (Lonsdale et al. 2006). At high redshift ($z > 1$) (U)LIRGs are more numerous. Indeed, at these earlier epochs, they have a substantial contribution to the total IR luminosity density (Le Floc'h et al. 2005; Caputi et al. 2007) compared to local ULIRGs.
However, (U)LIRGs have a starburst activity and basic structural/kinematical properties similar to that found for main-sequence high-z SFGs (Elbaz et al. 2011; Arribas et al. 2012; Bellocchi et al. 2013). Specifically, local ULIRGs tend to have intense SF concentrated into very optically thick nuclear regions, whereas galaxies of similar IR luminosity at high redshift probably have more widely distributed star forming regions of lower optical depth (Rujopakarn 2012). In particular, a compilation of physical sizes (based on radio and sub-mm observations) and IR luminosity data from the literature performed by Rujopakarn et al. (2011), show that distant ULIRGs have extended SFR regions (over 3-10 kpc), similar to local SFGs and LIRGs but with a scaled-up SFR-surface density (note that, ULIRGs are compact starburst). This indicates that distant galaxies are gas-rich and able to sustain these large SFRs in other ways rather than achieving it during mergers as seen in local ULIRGs (Elbaz et al. 2011). Observations of the spectral energy distributions (SEDs) showed that the strength of aromatic PAH emission and dust temperature of local and high-z ULIRGs are different. Overall, all these results suggest that local and high-z ULIRGs have fundamentally different characteristic and distant ULIRGs are a scaled-up version of SFGs and LIRGs.
Further studies seeking for more coherent local ULIRGs counterpart have led to the discovery of a new population of high-redshift far-IR luminous galaxies: the Sub-Millimeter Galaxies (SMGs, for a review see Blain et al. 2002 and Casey et al. 2014). These were first observe in deep extragalactic sub-mm/mm surveys using SCUBA and MAMBO (SubMillimeter CommonUser Bolometer Array and Max-Planck Millimeter Bolometer Array mounted on James Clerk Maxwell Telescope and IRAM Pico Veleta, respectively).
At high redshift SMGs are the closest analogs to local ULIRGs, with many properties remarkably similar. Both galaxy populations release the major fraction of their energy at far-IR and sub-mm wavebands. Such energy is produced by a dust- enshrouded power source (starburst or AGN) by thermal emission from dust grains. Additionally, both host large amounts of molecular gas (Neri et al. 2003; Greve et al. 2005; Tacconi et al. 2006), and have morphological evidence of recent or ongoing mergers (Veilleux et al. 2002; Conselice et al. 2003). Furthermore, studies of the sub-mm/far-IR background support that SMGs may account for most or all of it (see Lagache et al. 2005).

1.5 Thesis Outline

In this introduction, we have shown the relevance of studying complex feedback phenomena, such as outflows, since they play a major role in the evolution of galaxies and the surrounding IGM. Indeed, cosmological models of galaxy evolution require outflows to reproduce the observed properties of galaxies – e.g., without a strong stellar or AGN feedback, they lead galaxies to have much higher

[11] For example, the closest ULIRG is Arp 220 which is located 80 Mpc away from us.

SFR and larger stellar masses than observed.
The multiphase nature of outflows complicates the task of estimating the feedback. Of particular interest is to measure the mass of gas expelled by outflows in the coldest phases (i.e., the reservoir available for the SF). At optical wavelength the cold gas entrained in outflows could be studied via the NaD doublet absorption.
Outflows are ubiquitous at any redshift but local samples are crucial to understand their properties. In particular, nearby (U)LIRGs, since they host intense SF and powerful AGNs, allows to understand the relative importance of these two energy sources in powering outflows. Furthermore, (U)LIRGs share many properties with high-z populations. Therefore, they are important to understand the role of outflows in the distant Universe (at the epoch of early galaxy formation) as they offer the opportunity to study the feedback phenomena at much higher S/N and spatial resolution than with distant galaxies.
Current technology allow us to go a step further in the observations of outflows (usually carried out with long-slit spectroscopy), by using IFUs in large telescopes.

In this context, the generic goal of my thesis work is to search and characterize the neutral outflows in the most actively star-forming galaxies in the local Universe. I am particularly interested in the neutral gas phase of the outflow, which may be traced with the NaD feature in optical wavelengths. This will allow me to study the origin and fate of the outflowing gas, and its effects on the evolution of galaxies and the IGM. More specific goals include the following:
(i) to generate a purely-ISM neutral gas NaD feature by inferring the fraction of the NaD-absorption that is generated in stars;
(ii) to study high S/N spatially integrated spectra, which allow to infer the global kinematic properties of the cold gas (e.g., the line of sight velocity);
(iii) exploit the IFS data to obtain an atlas of neutral gas velocity fields and velocity dispersion maps which allow to increase the statistic, and therefore to base the general properties of the neutral outflows in (U)LIRGs on more solid grounds;
(iv) to obtain and discuss spatially resolved outflows's properties like morphology and kinematics, as well as those related to the feedback, looking for dependencies with other galaxy properties, like L_{IR} and dynamical mass;
(v) to perform a detailed study of near-IR emission lines in a QSO-ULIRG to derive observational constraint probing the positive feedback scenario.

To obtain these goals, I will analyzed a sample of local (U)LIRGs observed with VIMOS/VLT Integral Field Unit (IFU). The sample consists of 38 local (U)LIRG systems (51 individual galaxies) and it includes a large fraction (i.e., 31/38) of sources covering the less studied LIRG luminosity range (allowing to fill the gap between the extreme cases as AGN/merger ULIRGs and local SFGs). Although the sample is not complete neither in luminosity or distance, it is representative of the (U)LIRGs population. Indeed, it covers a variety of morphological types along the merging process (i.e., rotating disks, interacting systems, and mergers) and encompasses objects with different nuclear ionization types (i.e., HII, Seyfert and LINER). Furthermore, in nearly half of the objects in the sample (i.e., 22/51) show an excess of 24μm or hard-X ray emissions, or they have optical line ratios, indicating the presence of AGNs. Therefore, the size and characteristic of our sample allows to significantly expand and complement previous samples of spatially resolved neutral outflows.

This thesis is structured in the eight chapters (and two appendices), whose content is summarized as follows:

Chapter 1.

Motivation to study feedback and multiphase outflows for understanding galaxy evolution. We highlight the key role of local (U)LIRGs as ideal laboratories for a detailed study of both SNe and AGN feedback.

Chapter 2.

Presentation of the (U)LIRGs sample, the optical and near-IR IFS observations, and their data reduction. Basic principles of IFS as well as instruments used to achieve the data are described.

Chapter 3.

We describe the extraction of physical parameters relevant to the science goals. In particular we show the methods followed for the continuum modelling, and emission and absorption line fitting. This enable an accurate analysis of the gas kinematics.

Chapter 4.

The detailed study of the spatially resolved kinematic of the LIRG IRAS F11506-3851, which has implied the analysis of the neutral as well as the ionized gas and stellar component using optical and near-IR IFS techniques. We detect a neutral outflow and studied its origin and feedback (quenching of the SF).

Chapter 5.

A search for neutral gas outflows in local (U)LIRGs. We look for kinematic signature of outflows and we investigate possible trends between the observed outflows and galaxy properties. We also focus on the role of SNe and AGN in launching outflows and their feedback. Furthermore, we present the kinematics of neutral gas rotating disks and compared with whose of ionized disks.

Chapter 6.

An investigation of positive feedback in the ULIRG IRAS F05189-2524. We looked for observational evidence supporting the occurrence of SF in AGN-driven outflows. We study the kinematics and excitation mechanisms of near-IR (H and K bands) emission lines: [Fe II], Paα, $H_2$1-0 S(1) and Brγ. We have used diagnostic diagrams based on line-ratios as tools for discriminating the different kinematic components (for each line) according to their dominant source of ionization.

Chapters 7 and 8.

The future prospects and main conclusions are respectively presented in these chapters.

Appendices.

Appendix A present the integrated spectra and the atlas of 2D neutral gas kinematic. Appendix B include comments on individual sources.

Throughout this work, we assume $H_0 = 70$ kms^{-1} Mpc^{-1} and the standard $\Omega_m = 0.3$, $\Omega_\Lambda = 0.7$ cosmology.

Chapter 2

Sample and optical and near-IR integral field spectroscopic observations

This chapter introduces the sample of nearby (U)LIRGs and the background to IFS. The latter is a relatively new observing technique in Astronomy, which can provide spatial and spectral information simultaneously. IFS allows to obtain a wealth of data in one spectral setting that can be used to paint a complete 3D view of galaxies and their components including kinematics, dust distribution, ionization mechanisms, nuclear properties and ISM and IGM interactions. Veilleux et al. (2005) discerning the theoretical and observational challenges of studying outflows suggested that IFS would be well suited for probing their structure and kinematic properties.
This chapter also includes a brief description of the Very Large Telescope with the instruments used to achieve the datasets analyzed in this thesis.

2.1 Sample

The IFS (U)LIRG Survey is a large program (P.I.: S. Arribas) aimed at studying the internal ionization structure and the kinematics of a representative sample of low-z (U)LIRGs, capturing their complex two dimensional structure on kpc-scale. The complete survey is composed by ~ 70 sources, and it was carried out using IFS facilities in both the northern (INTEGRAL, Arribas et al. 1998; PMAS, Roth et al. 2005) and the southern (VIMOS, Le Fèvre et al. 2003) emisphere.
In this manuscript, we focus on 38 (U)LIRGs (51 individual galaxies) with redshifts < 0.095, which are listed in Table 2.1. For these galaxies, data were obtained with the IFS-capability of VIMOS at the Very Large Telescope, (VLT). Observations were performed during ESO (European Organisation for Astronomical Research in the Southern Hemisphere) periods P76, P78 and P81, in service mode. The technical details of the instrument (and data reduction) are described in the Sect. 2.2.1.
The sample contains a large fraction (i.e., 43/51) of sources in the less studied LIRG luminosity range $L_{IR} = 2.9 \times 10^{11}\ L_{\odot}$, on average), while a minor fraction of objects (i.e., 8/51) are classified as ULIRGs having $L_{IR} = 1.6 \times 10^{12}\ L_{\odot}$, on average. The LIRG subsample is drawn from the RBGS (Sanders et al. 2003), and has a mean redshift of 0.024 (see Table 2.1). The ULIRG subsample was mainly selected

TABLE 2.1: General properties of the (U)LIRGs VIMOS sample.

IRAS	Other	z	log ($L_{IR}/L_{\odot}$)	Class	S.C.	C^{AGN}
(1)	(2)	(3)	(4)	(5)	(6)	(7)
F01159-4443 (N)	ESO 244-G012	0.0229	11.48	1	H	AGN [a]
F01159-4443 (S)		0.0229	···	1	H/Sy	AGN [a]
F01341-3735 (N)	ESO 297-G011	0.0173	10.99 (11.18)	1	H	SB
F01341-3735 (S)	ESO 297-G012	0.0173	10.72	1	H	SB
F04315-0840	NGC 1614	0.0156	11.69	2	H	SB
F05189-2524		0.0426	12.19	2	Sy	AGN [a,b,e,g,i]
F06035-7102		0.0795	12.26	1	H	AGN [a]
F06076-2139 (N)		0.0374	11.67	1	···	···
F06076-2139 (S)		0.0374	···	1	···	···
F06206-6315		0.0924	12.27	1	Sy	AGN [a]
F06259-4780 (N)	ESO 255-IG 007	0.0388	11.91	1	H	SB
F06259-4780 (C)	ESO 255-IG 007	0.0388	···	1	···	···
F06259-4780 (S)	ESO 255-IG 007	0.0388	···	1	···	···
F06295-1735	ESO 557-G002	0.0213	11.27	0	H	SB
F06592-6313		0.0230	11.22	0	H	SB
F07027-6011 (N)	AM 0702-601	0.0313	11.04 (11.64)	0	Sy	AGN [a]
F07027-6011 (S)	AM 0702-601	0.0313	11.51	0	···	···
F07160-6215	NGC 2369	0.0108	11.16	0	···	AGN (8%) [i]
08355-4944		0.0259	11.60	2	···	···
08424-3130 (N)	ESO 432- IG006	0.0162	···	1	···	SB
08424-3130 (S)	ESO 432- IG006	0.0162	11.04	1	···	SB
F08520-6850	ESO 60-IG016	0.0463	11.83	1	···	AGN (9%) [e]
09022-3615		0.0596	12.32	2	···	AGN [9%] [h]
F09437+0317 (N)	IC 563	0.0205	10.99 (11.21)	1(0)	···	SB
F09437+0317 (S)	IC 564	0.0205	10.82	1(0)	···	SB
F10015-0614	NGC 3110	0.0169	11.31	0	H	AGN [i]
F10038-3338	IC 2545	0.0341	11.77	2	H/L	SB
F10257-4339	NGC3256	0.0094	11.69	2	H	SB
F10409-4556	ESO 264-G036	0.0210	11.26	0	H/L	SB
F10567-4310	ESO 264-G057	0.0172	11.07	0	H	SB
F11255-4120	ESO 319-G022	0.0164	11.04	0	H	SB
F11506-3851	ESO 320-G030	0.0108	11.30	0	H	AGN (<4%)[i]
F12043-3140 (N)	ESO 440-IG 058	0.0232	11.37	1	H/L	SB
F12043-3140 (S)		0.0232	···	1	H	SB
F12115-4656	ESO 267-G030	0.0185	11.11	0	H	AGN [f]
12116-5615		0.0271	11.61	2(0)	···	AGN [l]
F12596-1529	MCG-02-33-098	0.0159	11.07	1	H	AGN [a]
F13001-2339	ESO 507-G070	0.0217	11.48	2(0/1)	L	SB
F13229-2934	NGC 5135	0.0137	11.29	0	Sy	AGN (1.4%) [a,i]
F14544-4255 (E)	IC 4518	0.0157	10.80 (11.11)	1		···
F14544-4255 (W)	IC 4518	0.0157	10.80	1	Sy	AGN (6%) [i]
F17138-1017		0.0173	11.41	2(0)	H	AGN [d]
F18093-5744 (N)	IC 4687	0.0173	11.47 (11.57)	1	H	AGN (5%) [i]
F18093-5744 (C)	IC 4686	0.0173	10.87	1	H	···
F18093-5744 (S)	IC 4689	0.0173	···	1	H	···
F21130-4446		0.0926	12.09	2	H	SB [d]
F21453-3511	NGC 7130	0.0162	11.41	2	L/Sy	AGN (1.5%) [a,i]
F22132-3705	IC 5179	0.0114	11.22	0	H	AGN (<3%) [i]
F22491-1808		0.0778	12.17	1	H	AGN (<4%) [e,i]
F23128-5919 (N)	AM 2312-591	0.0446	···	1	H/L/Sy	···
F23128-5919 (S)	AM 2312-591	0.0446	12.06	1	H/L/Sy	AGN [a,c]

Notes. Column (1): Object designation in the Infrared Astronomical Satellite (IRAS) Point Source Catalogue (PSC) and in the IRAS Faint Source Catalogue (FSC, with prefix 'F'). Column (2): Other name. Column (3): Redshift from the NASA Extragalactic Database (NED). Column (4): Infrared luminosity ($L_{IR} = L_{(8-1000\,\mu m)}$) in units of solar bolometric luminosity calculated using the flux in the four IRAS bands as given in Sanders et al. (2003) when available. Otherwise, the standard prescription in Sanders & Mirabel (1996) with the values in the IRAS-FSC and IRAS-PSC catalogues was used. Note that for some targets (22 %, i.e.,11/51) new updated L_{IR} values can be found in Surace et al. (2004). However, for sake of homogeneity, we have preferred to use the values described above for the whole sample. For those systems for which it was possible to measure the L_{IR} of the individual galaxies, that of the system is indicated in parenthesis. Column (5): Morphology class defined as follows: 0 identifies isolated rotating disks, 1 interacting systems and 2 mergers. We refer to Rodríguez-Zaurín et al. (2011) and Bellocchi et al. (2013) for further details about this classification. Column (6): S.C. stands for (nuclear) spectroscopic classification of the ionization type. "H" defines HII galaxy, "L" LINER and "Sy" stands for Seyfert (see Rodríguez-Zaurín et al. 2011). Column (7): "AGN" and "SB" indicate, respectively, evidence of an AGN (from the infrared, optical and X-ray observations) and starburst galaxies. When possible we also give an estimate of the AGN contribution to the 24μm and bolometric luminosity (round and square parenthesis, respectively). *References.* [a] Arribas et al. (2014); [b] Dadina (2007); [c] Dixon & Joseph (2011); [d] Farrah et al. (2003); [e] Iwasawa et al. (2011); [f] Jiménez-Bailón et al. (2007); [g] Nardini et al. (2009); [h] Nardini et al. (2010); [i] Pereira-Santaella et al. (2010); [l] Valiante et al. (2009).

from the IRAS 1 Jy sample of ULIRGs (Kim et al. 1998) and the RBGS, and has a mean redshift of 0.069 (see Table 2.1). Additionally, some objects were chosen from the HST/WFPC2 (Wide Field and Planetary Camera 2) snapshot sample (PI: K. Borne), with an average redshift of 0.126.
Beside the luminosity criterion (that defines LIRGs and ULIRGs, Sect. 1.4), the selection technique used to build the sample take into account the morphology of the potential sources. Briefly, accordingly to the morphological/merging classification scheme given by Veilleux et al. (2002), galaxies along the merging process (i.e., rotating disks, interacting systems, and mergers, Column 5 in Table. 2.1) were selected.
The sample is not complete neither in luminosity nor in distance (Rodríguez-Zaurín et al. 2011; Bellocchi et al. 2013). However, it is representative of the [U]LIRGs population. Indeed, it covers a variety of morphological types and encompasses objects with different nuclear ionization types (i.e., HII, Seyfert and LINER). See Table 2.1, for further details.
For part of the VIMOS-sample, near-IR data were achieved recently, in two independent observing campaigns. Specifically, ten LIRGs LIRGs and seven ULIRGs in the luminosity range: $\log(L_{IR}/L_{\odot}) = 11.10\text{-}12.43$ are part of a program (P.I.: L. Colina) aimed to study the structure and excitation mechanisms of the ionized, partially-ionized and warm molecular gas, the distribution of the different stellar populations, the stellar and multi-phase gas kinematics, and the extinction properties (Piqueras López et al. 2012, 2013). As the objects in the VIMOS-sample, these 17 galaxies were selected to cover different morphological types, although this is not complete in either flux or distance. IR-observations obtained with SINFONI (Sect. 2.2.2) for IRAS F11506-3851 are part of this dataset (see Sect 4) as well other 13 (U)LIRGs.
The ULIRG F05189-2524 is part of a sample of five galaxies for which prominent quasar-driven outflows have been detected (see chapters 6 and 7). The IR-data for this small sample were achieved using the SINFONI (P.I.: R. Maiolino, P92) and the Near Infrared Camera Spectrometer (NICS) at Telescopio Nazione Galielo (P.I.: R. Maiolino, AOT 27). This observing campaign is aimed to test the positive scenario (Sect. 1.1.2) by exploiting the Paα emission line as a (nearly) extinction-free tracer of SF. NICS observations and data are not treated in this manuscript but are part of a forthcoming paper (Cazzoli et al. 2016, in prep).

2.2 Integral Field Spectroscopic observations and data reduction

Long slit and multi-object spectroscopy have been traditionally used to obtain spectra for both point and extended sources. While both techniques are efficient for single and unresolved sources, spatially resolved spectroscopy is needed for an optimal study of extended resolved sources. IFS has, indeed, the advantage of being able to provide a spectrum of a spatial element in a two-dimensional field over a potentially long wavelength coverage. An incomplete spatial coverage (or aperture bias) may be an important source of uncertainties, given that many physical properties of galaxies may vary depending on the geometry and position (e.g., kinematics, stellar populations, metallicity and extinction). Within the other main advantage of IFS, we can list: no slit effects or slit losses, no necessity to do (pre-) imaging the field and the possibility to bin the data spatially to gain S/N.
The main idea of IFS is to divide the focal plane of the telescope into a number of elements and to create a pseudo-slit to disperse the light which will be recorded on a two dimensional detector. In this way

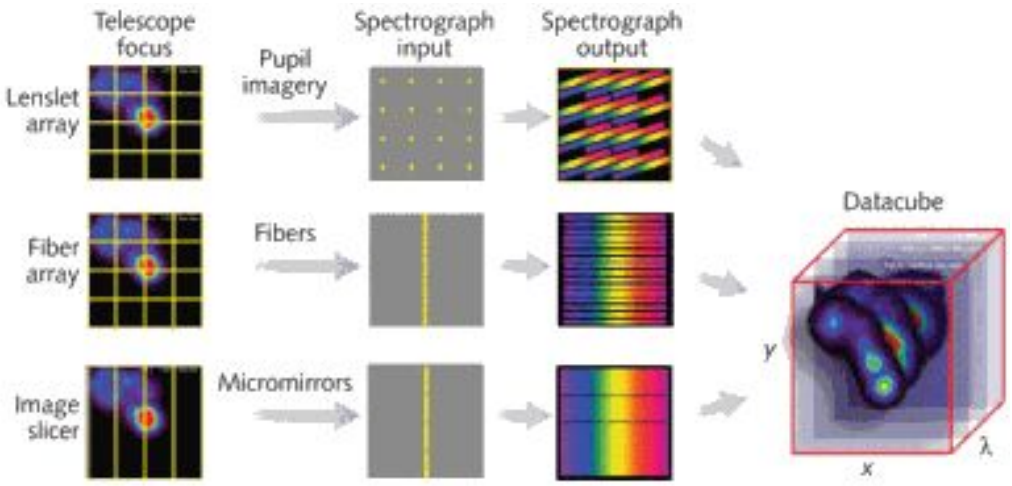

FIGURE 2.1: A schematic view of the main IFS techniques. Figure from http://star-www.dur.ac.uk/~jra/integral_field.html.

IFS is able to produce simultaneously (under the same atmospheric conditions) a spectrum of every spatial element (referred to as "spaxel") in the Field of View (FoV), with the spatial sampling and size of FoV determined by the instrument. Thus, the final output is a datacube with the two-dimensional spatial information and the spectral information as a third axis (i.e., $X \times Y \times \lambda$ datacube).
There are three major types of techniques to resample the focal plane to be arranged onto the detector for IFUs. These are lenslet arrays, fiber bundles and image slicing, which are summarized below. Figure 2.1 shows an illustration of these different techniques of integral field spectroscopy.

- LENSLET ARRAY (e.g., SAURON @ WHT).
  This technique was first proposed by Courtes (1982). The image at the telescope focus is enlarged by auxiliary optics and projected on a microlenses array. Each lenslet gives at its focus an image of the entrance pupil of the telescope. Any beam collected by the front surface of one of the lens forms an exit pupil which can be considered as the slit for a spectrograph.

- FIBER BUNDLES (e.g., VIMOS @ VLT, INTEGRAL @ WHT, GMOS @ GEMINI).
  The input image is formed at the entrance to a bundle of fibres which transfer the light to the slit of the spectrograph. The flexibility of the fibres allows a round field of view to be reformatted into one (or more) slits. Therefore, the spectra are obtained without wavelengths shifts between them.

- IMAGE SLICER (e.g., SINFONI @ VLT, NIRSPEC @ JWST, HARMONI @ E-ELT).
  The input image is formed at a mirror segmented in thin horizontal sections which are then sent in slightly different directions. A second segmented mirror is arranged to reformat the slices so that, instead of being above each other they are now laid out end to end to form the slit of the spectrograph (actually a virtual slit). The advantage of this technique is that the slicing arrangement gives contiguous coverage of the field. Because this system uses only mirrors, it is especially suitable for the IR since it is inherently achromatic and can be cooled to cryogenic temperatures.

The information content of IFS-observations can be extremely large and it can take a long time to properly build the data cube from the raw data. However, more and more software packages are becoming available for IFS data reduction and many instrument-specific pipelines are being maintained (e.g., at the ESO and Gemini observatories).

One of the main goals of this work is to analyze the spatially resolved neutral gas kinematic of the sources in the sample (see Chapt. 3). When deriving the kinematics from 2D-data cubes, the most severe aspect to take into account, is the beam smearing. This is related to the finite beam size of telescopes that causes the spectral line to be smeared on the adjacent regions. Therefore, different line-of-sight velocities are combined artificially into a single spatial pixel. The net effect is that the gradients in the velocity fields tend to become flatter (rise very slowly) in the inner regions while the line-profiles in each spaxel become broader. In other words, part of the rotation velocity is turned into line broadening that can be erroneously interpreted as gas velocity dispersion, producing a degeneracy between these two quantities (Di Teodoro & Fraternali 2015 and reference therein). This effect becomes severe and comparable to the scale of the underlying galaxy itself for observations of sources at high redshift (strongly limited in spatial resolution). The low redshift provides a good physical-scale resolution and so minimizes the effects of beam smearing.

In case of, velocity and dispersion maps typical of a rotating disk, a standard approach for estimating the effect of the beam smearing is to attempt a pure-rotating disk modelling (Davis et al. 2012 and reference therein). To evaluate the effect of the beam smearing for measurements of the kinematics of neutral winds is difficult since the large uncertainties in any kinematic model for the outflow that can be assumed. However, Bellocchi et al. (2013) with the same VIMOS dataset analyzed beam smearing effects by using the disk-like velocity fields obtained with the modelling of the Hα emission line. They find that the effects are generally negligible, i.e., of the order of few percent. In the worst case (i.e., IRAS F06259-4780 (S)) the effect is $\sim 15\,\%$ (Bellocchi et al. 2013). As for comparison, Green et al. (2014) found the beam smearing effect to be of the order of 4 kms^{-1} (although in a few cases factor of ~ 2 more significant) assuming a disk model plus an exponential light profile for modelling a sample of nearby SFGs.

2.2.1 VIMOS

The VIsible MultiObject Spectrograph (VIMOS) is a visible (3600-10000 Å) wide field imager and Multi-Object Spectrograph (MOS) (Le Fèvre et al. 2003). This is mounted on the Nasmyth B focus of Unit telescope UT3 Melipal of the ESO-VLT (whose views are displayed in Fig. 2.2). Of the three different modes of VIMOS: imaging, MOS and IFU, we use the VIMOS-IFU capability for this thesis. The VIMOS-IFU is a fiber-fed spectrograph consisting of 6400 (80×80, i.e., IFU head) fibers coupled with microlenses. Two different spatial samplings (magnifications) are available: $0\farcs67$ and $0\farcs33$ per fiber, respectively. The field of view corresponds to $54''\times54''$ or to $27''\times27''$, when the magnification is set to $0\farcs67$ and $0\farcs33$, respectively. Six grisms are accesible in IFU mode at different spectral resolution (low, medium and high). Details about these grisms are summarized in Table 2.2. The FoV is divided into four quadrants (2048×4096 detectors), each of 1600 fibers (40×40) that are bundled up and re-assembled at the other end into four parallel slits (i.e., pseudo-slits). These include 400 fibers each and provide 4 stacked, horizontal spectra along the dispersion direction. Each pseudo-slit

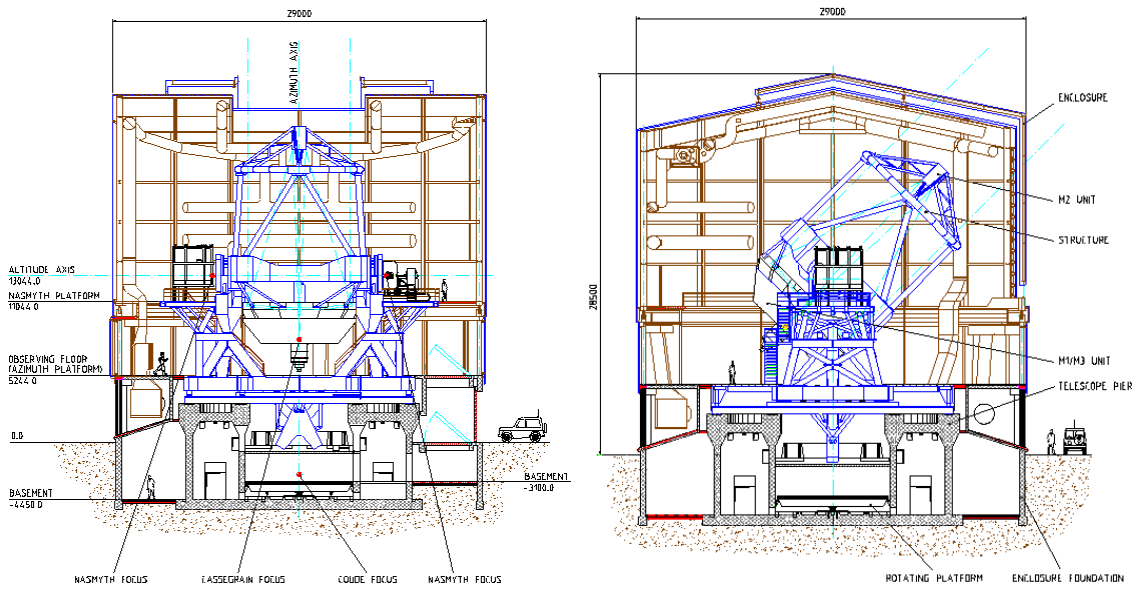

FIGURE 2.2: A frontal (left) and lateral (right) view of Unit 3 telescope of the VLT giving a definition of the main telescope components. Figure from https://www.eso.org/paranal/telescopes/ut/. The VIMOS instrument is placed in the UT3, while SINFONI is in the UT4 (which share the architecture and the main telescope components).

corresponds to a 20×20 region (fiber module) of the IFU head. Fig. 2.3 shows a schematic view of the arrangement of the components both in the mask (afterwards: quadrants) and in the IFU head.

In case of High Resolution (HR) -spectroscopy a shutter must be used to partially mask the IFU head (no multiplexing, Table 2.2) in case of high and mdium resolution spectroscopy to prevent overlapping of spectra from different pseudo-slits, leaving a 40×40 fibers square (marked in red in Fig. 2.3, right). Therefore, the FoV corresponds to $27'' \times 27''$ or to $13'' \times 13''$, and only one (central) pseudo-slit is illuminated.

The data analyzed in this thesis, were achieved by using the HR-mode, corresponding to a spectral resolution of $R \sim 2500$, which allow a spatial sampling of $0\farcs67$/fiber over a $27'' \times 27''$ FoV (1600 simultaneous spectra per pointing). For our observations, the HR Orange grism (GG435) was used for all objects covering the wavelength range: 5250-7400 Å with a mean spectral resolution of $R \sim 3470$. The data were taken under conditions with seeing estimated between 0.5 and 2.0 ($1\farcs05$ on average, Bellocchi 2014). This specific setup allows for each object to cover the wavelength range in which NaD and Hα lines lie.

A square 4 pointing dithering pattern was used. The four quadrants had a relative offset of $2\farcs7$, providing after the combination an effective FoV of $29\farcs5 \times 29\farcs5$. The exposure time per pointing ranges from 720 to 850 seconds, so that, the total integration time per galaxy is between 2880 and 3400 seconds (Bellocchi 2014).

Raw VIMOS data were reduced with a combination of the pipeline provided by ESO via ESOREX [1] (version 3.6.1 and 3.6.5). The reduction involves four main tasks: `vmbias`, `vmifucalib`, `vmifustandard` and `vmifuscience`. These include sky and bias subtraction, flat field correction, spectra tracing and extraction, correction of fiber and pixel transmission, the flux and wavelength calibration. We also used a set of customized IDL and IRAF scripts (e.g., for cleaning residual cosmic rays spikes). Once

[1] ESO Recipe Execution Tool, http://www.eso.org/sci/software/cpl/esorex.html

TABLE 2.2: Characteristics of the VIMOS grisms

Grism	Filter	λ_c Å	Wavelength Coverage Å	R	Dispersion (Å/pixel)	Multiplex
LR blue	OS blue	4800	4000 - 6700	220	5.3	yes
LR red	OS red	7500	5900 - 9150	260	7.3	yes
MR	GG475	7000	4900 - 10150	720	3.5	no
HR blue	Free	5100	3700 - 5220	1440	0.57	no
HR orange	GG435	6310	5250 - 7400	2650	0.6	no
HR red	GG475	7400	6450 - 8600	3100	0.6	no

Notes. VIMOS grisms. LR, MR and HR stands respectively for Low-, Medium- and High- Resolution. λ_c is the zero deviation (or central) wavelength, and $R = \lambda/\Delta\lambda$ is the spectral resolution for a 0.″8 IFU fiber. The last column indicate if all the pseudo-slits can be simultaneously illuminated in a single exposition (i.e., multiplexing).

the four quadrants were individually reduced (for the four dithered positions), they were combined into a single data-cube consisting of 44×44 spaxels (i.e., 1936 spectra).
The detailed description of the data reduction process is given in Monreal-Ibero et al. (2010); Rodríguez-Zaurín et al. (2011) and Bellocchi (2014). In what follows, the data reduction steps are briefly described with in parenthesis the recipes we used for each particular step. A schematic representation of the data reduction processes performed is in Fig. 2.4.

- BIAS SUBTRACTION (`vmbias`).
  This (standard) step consists of creating a master bias from a set of raw bias frames (having exposure of zero seconds, so no photons hit the detector). We used a "stacking method" which consist of calculating median of the input frames. However, other methods (e.g., average) are possible. Datasets composed by flat field lamp, arc lamp exposure and science exposure are be bias-subtracted.

- FLAT FIELDING (`vmifucalib`).
  This correction consists of dividing the frame of interest by the master flat field frame produced by `vmifucalib` from flat field exposures (frames in which the CCD receives light uniformly). The flat field is an image of the imperfections of the detector and dividing the science frame by it will cancel them with no effect on the relative counts.

- SPECTRA TRACING (`vmifucalib`).
  In this step, we obtain the position on the CCD for each fiber and then, correctly separated from each other and then extracted from the image. The presence of outliers or damaged/lost fibers is also determined.

- DISTORSION CORRECTION (`vmifucalib`). Geometric distortions of the focal plane are identified and corrected. For example, distortions could cause the spectrum to appear curved rather than rectilinear.

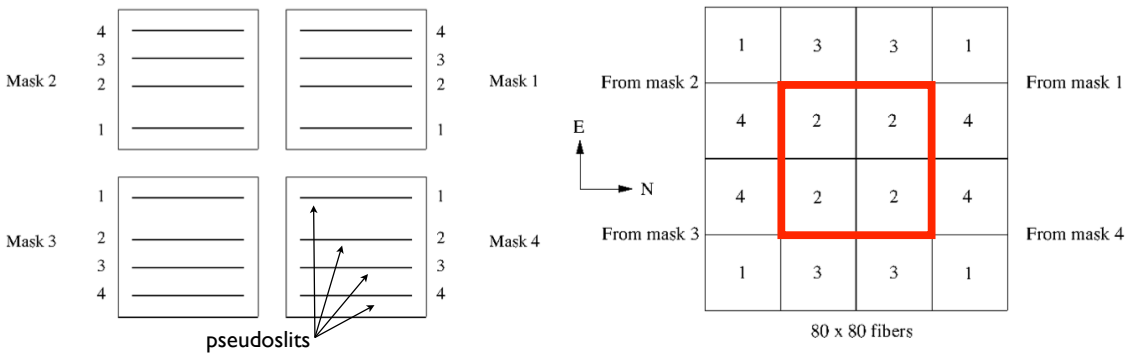

FIGURE 2.3: *Left:* View of the four VIMOS's mask. Each mask hosts four pseudoslits. *Right:* VIMOS head and its main compontents. The numbers correspond to pseudoslits (displayed on left) which are within each 20×20 fiber module IFU pseudo-slits. In red, the pseudoslits illuminated in case of our HR observations.

- WAVELENGTH AND FLUX CALIBRATION (`vmifucalib` + `vmifustandard`).
  The wavelength calibration transforms the dispersion axis from pixel into wavelength units using an arc-lamp spectrum which contains an high number of known emission lines by exciting gases (e.g., He + Ne + Ar). Afterwards, the flux calibration is achieved by applying master response curves (created from pipeline-reduced spectrophotometric standard star observations). The signal of any given galaxy can, therefore, be transformed from counts to flux density (erg s^{-1} cm^{-2} $Å^{-1}$).

- SPECTRA EXTRACTION (`vmifuscience`).
  IFU scientific spectra are extracted and resampled at a constant wavelength step after aligning the input wavelength calibration to the positions of a set of identified sky lines. The extracted spectra are eventually corrected for the relative differences in transmission from fiber to fiber.

The width of the instrumental profile, and the wavelength calibration were checked by using the [O I] λ6300.3 Å sky line. The average values for the FWHM and central wavelength for the whole sample were (6300.29 ± 0.07) Å and (1.80 ± 0.07) Å, respectively. For each spectrum, the effect of instrumental dispersion ($\sigma_{\rm INS}$) was corrected for by subtracting it in quadrature from the observed line dispersion ($\sigma_{\rm obs}$), as:

$$\sigma_{\rm line} = \sqrt{\sigma^2_{\rm obs} + \sigma^2_{\rm INS}}. \tag{2.1}$$

For the case, of IRAS F11506-3851, treated in detail in Chapter 4, instrumental profile correction and the accuracy of wavelength calibration were also checked with the 5577 Å night-sky line. In this cases, the effect of instrumental dispersion $\sigma_{\rm INS}$ are of the order of (0.75 ± 0.17) Å.

2.2.2 SINFONI

SINFONI, is the Spectrograph for INtegral Field Observations in the Near Infrared (Eisenhauer et al. 2003) situated on the 8-m UT4 (Yepun) of the ESO-VLT at the Cassegrain focus. It uses an image slicer IFU (Fig. 2.1) which contains 32 slices, each one is projected onto 64 detector pixels. There are three possible choices of slit height, leading to different pixel scales and FoV. Specifically, the choices for the scale are 250 mas, 100 mas and 25 mas, which lead to field of views on the sky of $8'' \times 8''$,

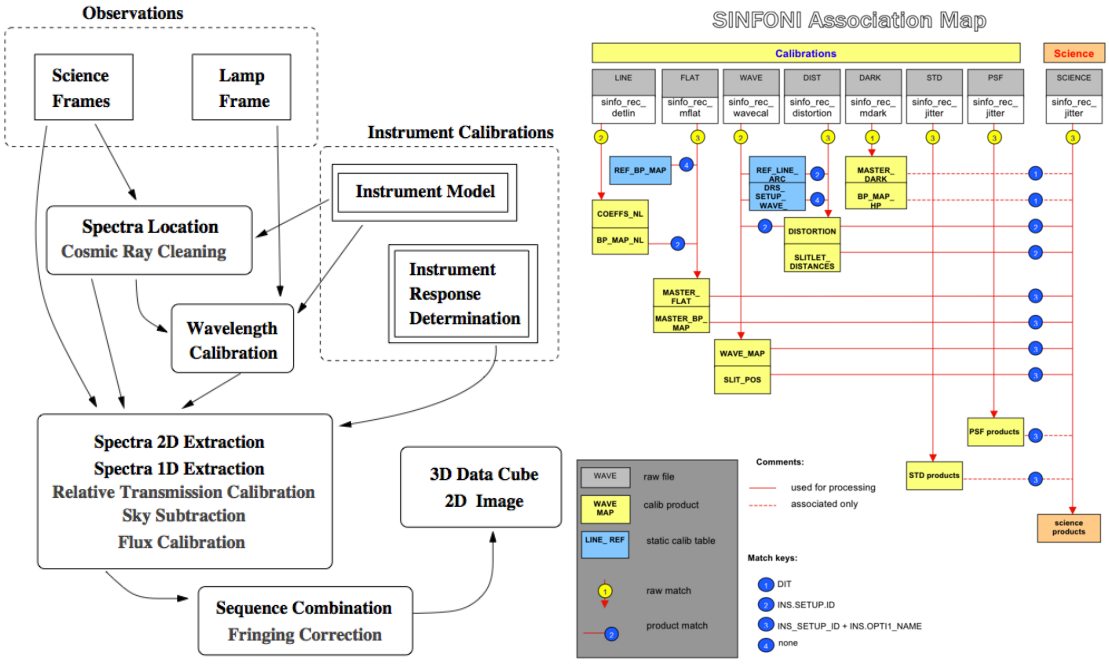

FIGURE 2.4: *Left panel.* Block diagram showing the various steps of the reduction of VIMOS IFS data. Optional steps are marked with dotted lines. Figure from Zanichelli et al. (2005). *Right panel.* SINFONI calibration cascade. Note that, in this case, the names of the different recipes are also marked. Figure from http://www.eso.org/observing/dfo/quality/SINFONI/pipeline.

$3'' \times 3''$ and $0.''8 \times 0.''8$, respectively. There are four gratings available (J, H, K, H+K) giving an overall wavelength coverage of 1.10 - 2.45 μm. A summary of the properties of the gratings is given in Table 2.3.

SINFONI is designed to be used with Adaptive Optics (AO), to provide near diffraction-limited observations (see Davies & Kasper 2012 for a review) indeed is fed by a curvature sensing AO module. This technique is able to overcome the degrading effects of atmospheric turbulence by compensating in real-time the deformation of the wavefront. The wavefront is measured from a guide star and the corrections are sent to the deformable mirror within the instrument. SINFONI's AO uses a Natural Guide Star (NGS) or a Laser Guide Star (LGS) . AO's observations are not part of this thesis, therefore, for more details we refer to other works such as Müller-Sánchez et al. (2011).

In this work we made use of two sets of SINFONI data, below we briefly comment both set of observations.

The near-IR observations for IRAS F11506-3851 were carried out in both the H and K bands (Table 2.3) with the 250 mas scale configuration, during the period 78B (February and March 2007). In Chapter 4, we focus on the study of the K band, in particular we analyzed the kinematical properties derived from the CO absorption bands, as described in Sect. 4.1.1.1.

In Chapter 6, we made use of the near IR observations for IRAS F05189-2524, carried out with the H+K grating. Observations were carried out on October and November 2013, the average seeing was 0.8. The total integration time on source was 5 hours (6.5 hours including overheads), split into 8 observations. In the case of IRAS F05189-2524, we study several emission lines, along with the stellar continuum. As mentioned in Sect. 2.1, this nearby QSO ULIRG is part of a sample of 5 ULIRGs selected on the basis of earlier molecular outflow detection. The observations, data and analysis for this sample will be presented in Cazzoli et al (2016, in prep.).

In what follow, we outline the various step for the data reduction, that applies for both set of observations. A more detailed description is given for the case for IRAS F05189-2524 (thus H+K SINFONI data) while, we refer to Piqueras López et al. (2012, 2013) for detailed description of the data reduction[2] (as well as the study of gas kinematic and extinction) for the LIRG IRAS F11506-3851.

Prior to start the actual data reduction of SINFONI data, we clean the raw frames, both science and calibrations, from the bad lines that are created by the data hardware processing. To identify and correct the detector bad lines we use a script written in IDL provided by ESO.

The basic reduction of the SINFONI observations was carried out by using the ESO's pipeline recipes through GASGANO[3]. This is an intuitive and comprehensive interface for data browsing and organisation, and for running pipeline recipes (based on the ESO Common Pipeline Library) and it is equivalent to ESOREX (used for the VIMOS data, Sect. 2.2.1).

For each observing block we follow the data-processing cascade summarized in Fig. 2.4 (right). The main idea of this cascade is for each step, to create "master files" by which is possible to reconstruct the science frames into a 3D data cube. An adequate set of input files (which is different for each recipe) is used during each step.

As a first step, we build the mask of badpixels, which is made of the dead, hot, and non-linear pixels and created dark and flat frames trough the following recipes: `sinfo_rec_detlin`, `sinfo_rec_mdark`, `sinfo_rec_mflat`. Then, to create the wavelength map (i.e., to assign a wavelength value to each pixel on your detector) we create files containing the distortion coefficients and the distance between the individual slitlets by using the `sinfo_rec_distortion` and `sinfo_rec_wavecal` recipes. For telluric standard, PSF standard and science frames, most of the files created (with previous tasks) were then used to reconstruct the cubes via the `sinfo_rec_jitter` recipe.

The sky/tellutic subtractions were then performed as follows. A standard star was observed right after each observation at the same airmass. This was typically a B star containing several stellar Hydrogen recombination lines especially of the Brackett-series in H-band (e.g., Brγ and Br (13-4) λ 1.611 μm). These were removed from the one dimensional stellar spectrum (output of the `sinfo_rec_jitter`) using the task `splot` in the IRAF environment. Then, such spectrum was divided by a blackbody of the stellar temperature (via `sinfo_utl_spectrum_divide_by_blackbody`) and normalized (`imarith` in IRAF) to get a flat spectrum with atmospheric absorption features only. The final spectrum was used to correct the science cube (`sinfo_utl_cube_arith`). Finally, all the individual reducted-datacubes, were coadded taking into account the relative shifts to obtain the final mosaic datacube (using the recipe `sinfo_utl_cube_combine`). The number of counts was converted to flux using the literature values of the star's magnitude in that band (from the Hipparcos catalogue).

[2] Shortly, the data reduction was accomplished via ESOREX - version 2.0.5. The observed object and sky frames were corrected from dark subtraction, flat fielding, detector linearity, geometrical distortion, and wavelength calibration. The background sky emission was removed using the method outlined in Davies (2007). A set of IDL routines were used to perform the flux calibration on the cube while taking the relative shifts in the jittering pattern into account, before being merged in the final datacube.

[3] https://www.eso.org/sci/software/gasgano.html

TABLE 2.3: SINFONI gratings

Grating	λ_c μm	Wavelength Coverage μm	R	Dispersion (nm/pixel)
J	1.25	1.10 - 1.40	2000	0.15
H	1.65	1.45 - 1.85	3000	0.20
K	2.20	1.95 - 2.45	4000	0.25
H+K	1.95	1.45 - 2.45	1500	0.50

2.2.3 Other capabilities and IFS-surveys

The number of IFUs is growing and many large IFS surveys are being carried out.
At the ESO-VLT, the two major IFU-instruments recently become available are KMOS (K-band Multi-Object Spectrograph), a near-infrared spectrograph with 24 small IFUs, and MUSE (Multi Unit Spectroscopic Explorer), an instrument operating in the visible wavelength range. The latter is able to sample a long wavelength range (from 4650 to 9300 Å) at relatively high spectral resolution (R ~ 3000) with an high throughput being an ideal multi-purpose instrument (Bacon et al. 2010).
One of the firsts very large IFS survey is: the Calar Alto Legacy Integral Field Area (CALIFA) survey (Sánchez et al. 2012) that is composed by ~ 600 nearby galaxies observed in the range 3500-700 Å using two overlapping setups with different spectral resolution R ~ 850 and R ~ 1650. This survey allow to study spatial variations in oxygen abundance of HII regions (Sánchez et al. 2014), stellar population age gradients (Sánchez-Blázquez et al. 2014), or kinematics (García-Lorenzo et al. 2015). Despite the fact that the NaD absorption lies in the CALIFA wavelength range for nearly all galaxies, the spectral resolution does not allow an accurate line modeling of such feature (the two lines of the doublet are found to be likely blended).
Other relevant IFS surveys are SAMI and MANGA. The first has the goal of collecting IFU observations for ~ 3500 galaxies with the the Sydney-Australian astronomical observatory Multi-object IFS (SAMI, Croom et al. 2012). SAMI is a new instrument on the 4-meter Anglo-Australian Telescope at Siding Spring Observatory which can be used in the optical spectrum (3700-9500 Å) with a range of spectral resolutions (R = 1700-13000). The second, the MaNGA (Mapping Nearby Galaxies at Apache Point Observatory, Bundy et al. 2015), will obtain spatially resolved spectroscopy for a sample of over 10000 nearby ($0.01 < z < 0.15$) galaxies optimally selected using the nuclear spectra from the Sloan Digital Sky Survey (SDSS, York et al. 2000). The observations have the characteristic to be at spectral resolution of R = 2000 across the full optical wavelength range, i.e., from 3600 to 10300 Å. The MANGA survey will provide insights on various process in the local Universe, such as initial mass function, stellar photospheres, gas properties and metallicity gradients (e.g., Belfiore et al. 2015).
The SINS survey is pushing forward the SINFONI-IFS observations to investigate in detail the dynamics and physical properties of distant ($1 < z < 4$) luminous galaxy populations (Förster Schreiber et al. 2009). In Fig. 2.2.3 some examples of the IFS-maps for galaxies of the above mentioned different surveys. The KMOS-3D (Wisnioski et al. 2015) is also a large survey of z ~ 1-2 galaxies carried out with the new multi-IFU near-IR instrument KMOS (e.g., Stott et al. 2016). As for the future, it should be mentioned that two JWST instruments (NIRSpec and MIRI) are equipped with IFUs. In the long term the instrument HARMONI for the European Extremely Large Telescope is an optical and near-IR integral field spectrograph.

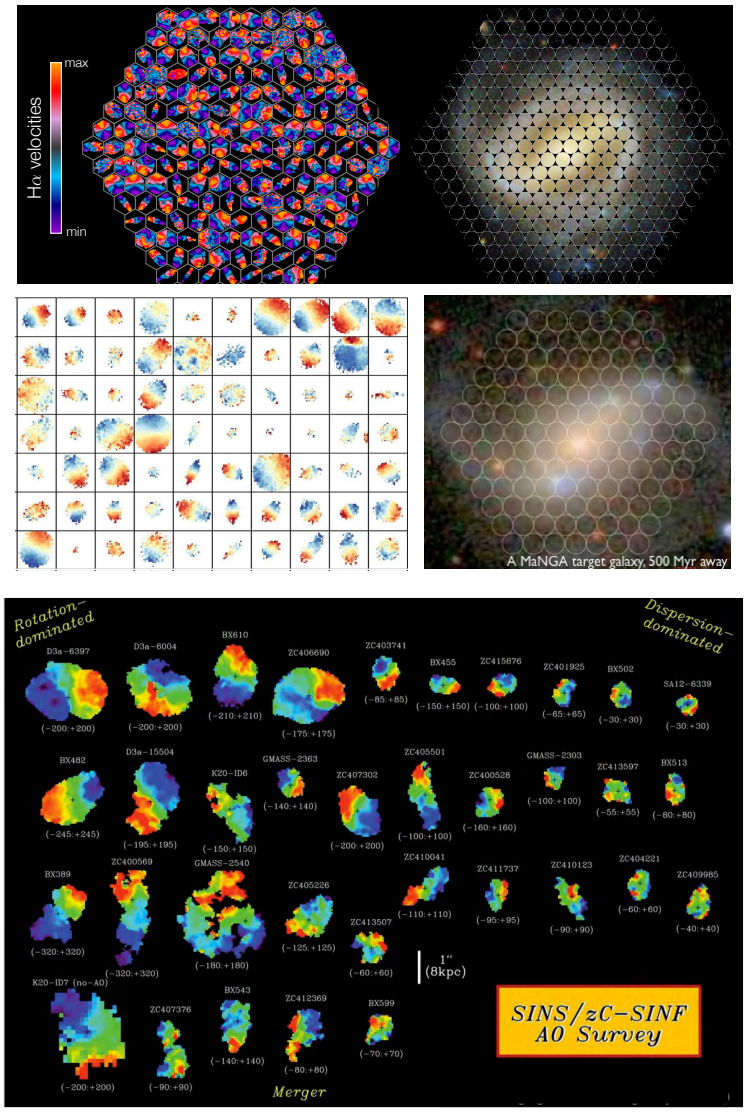

FIGURE 2.5: *Top panel.* Panels showing example from different IFS-surveys: CALIFA, SAMI and MANGA surveys, top, bottom-left, bottom-right, respectively. Figures from http://califa.caha.es/, https://www.sdss3.org/future/manga.php and http://sami-survey.org/, respectively. Maps from CALIFA and SAMI are ionized gas velocity fields (via Hα). Blue to red colours correspond to regions of the galaxies that are approaching towards us and receding from us relative to the systemic. For CALIFA and MANGA the arrangement of the fibers are shown.
Bottom panel. Panels showing example of the Hα velocity fields obtained from SINFONI observations of z ~ 1.5-2 galaxies (Förster Schreiber et al. 2009). Velocitities are color coded as in the above panel. The minimum and maximum relative velocities are labeled for each galaxy (in km/s). All sources are shown on the same angular scale; the white bars correspond to 1 arcsec, or about 8 kpc at z = 2. The galaxies are approximately sorted from left to right according to whether their kinematics are rotation-dominated or dispersion-dominated, and from top to bottom according to whether they are disk-like or merger-like (Förster Schreiber et al. 2009). Figure from http://www.mpe.mpg.de/~forster/SINS/sins_nmfs.html. See also Wisnioski et al. 2015.

Chapter 3

Data treatment

In this chapter, we present the different ISM and stellar features we considered and their analysis/modelling for both spatially resolved and spatially integrated data. We include the kinematic classification for the galaxies in the sample.

3.1 Optical and near-IR ISM-features

Our multi-wavelength approach allows us to study a large number of spectral features. In the optical range, we mainly focus on the NaD and Hα spectral features while in the near-IR, we use the following tracers: [FeII], Paα, H_2 (1-0) (S1) and Brγ. In the present section, we briefly describe the different processes that create these emission and absorption lines. The stellar component and the continuum emission are studied in both wavelength ranges, and discussed in a dedicated subsection (Sect. 3.2.1).

NaD $\lambda\lambda$ 5890, 5896 Å. The NaD absorption line doublet originates both in the cold ISM of galaxies and in the atmospheres of old stars (e.g., K-type giants, Jacoby et al. 1984). Respectively, the background source is either the starlight of the galaxy or an individual star. In this work, we focus on the study of the ISM-NaD absorption, since it provides a good probe of cold gas in outflows. Alternatively, resonant NaD emission lines can also be used to probe outflows (e.g., Rupke & Veilleux 2015) but such emission is not commonly observed in our data and therefore it is not studied in details in this work. The ionization potential of NaD is 5.1 eV, so lower than that of the hydrogen. The photons that ionized NaD are thus, in the near-UV ($\lambda \sim 2420$ Å). The transition which gives rise to the doublet is from the 3p to the 3s level (Fig. 3.1, center).

Hα λ 6563 Å. It is generally the brightest optical emission line in SFGs and probes the ionized medium (H II, Table 1.1), which in turn traces massive young stars (that ionize the gas). Therefore, it is commonly used a tracer of SF. The transition which gives to Hα is from the shell n = 3 to the shell n = 2 and it is shown in Fig. 3.1 (left) (as well as those for other hydrogen recombination lines, including

Paα and Brγ). In this work, Hα is generally taken as reference when studying the neutral-ISM kinematic. For a detailed analysis of the ionized gas spatially resolved and integrated properties we refer to Monreal-Ibero et al. (2010); Rodríguez-Zaurín et al. (2011); Bellocchi et al. (2013) and Arribas et al. (2014).

[FeII] λ 1.644 μm. This near-IR iron line arises predominantly from the partially-ionized zone behind the shock front of radiative supernova remnants. Therefore, this line is an important diagnostic to quantitatively measuring ionizing mechanisms as well as the degree of metal enrichment (as means of dating the onset of Type Ia SNe which are associated to short-living and massive stars). The transition which gives rise to the line is from the $^4D_{7/2}$-$^4F_{9/2}$ (Fig. 3.1, right). The [FeII] line has been observed in several starburst galaxies (e.g., Labrie & Pritchet 2006), including (U)LIRGs (e.g., Piqueras López et al. 2012) and AGNs (e.g., Landt et al. 2008).

Paα λ 1.876 μm. This line traces the ionizing radiation produced by very young stars ($\sim$ 10 Myr, Kennicutt & Evans 2012). The transition which gives to this emission line is from the shell n = 4 to the shell n = 3. Paα in nearby galaxies lies in the SINFONI K-band (up to z $<$ 0.3), for which the extinction is 1/10 of the optical (V) band. In heavily obscured systems such as (U)LIRGs, Paα can be considered as a (nearly) extinction-free tracer of SF (i.e., the effects of extinction are negligible with respect to that for the commonly used Hα).

H_2 (1-0) (S1) λ 2.122 μm. Molecular hydrogen is the most abundant molecule in the Universe. It plays a major role four our understanding of the processes regulating SF by initiating the chemistry of the ISM and being one of the major ISM-coolant (e.g., Habart et al. 2004). H_2 may be excited through several mechanisms. Their occurrence can be investigated in the near-IR by measurements of several H_2 lines such as the H_2 (1-0) (S1), H_2 (1-0) (S0) λ 2.224 μm emission lines. In particular, the H_2 (1-0) (S1) line is used to trace the warm molecular gas (T $\sim$ 80 K).

Brγ λ 2.166 μm. The transition which gives rise to this emission line is from the shell n = 7 to the shell n = 4. Brγ is generally used in combination with others rather than individually. Indeed, this line jointly with other hydrogen recombination line (e.g., Brδ and Paα) or stellar population synthesis models, is widely used to quantitatively study of the internal extinction or to constrain the age of the youngest stellar population in galaxies (e.g., Piqueras López et al. 2013 and Levesque & Leitherer 2013, respectively).

3.2 Spatially integrated (1D) analysis

As mentioned in Sect. 2, IFS is a powerful tool for investigating the physical properties of galaxies on spatially resolved basis. However, in some conditions, such as low S/N spectra, some spectral diagnostics, such as NaD, are difficult to detect since intrinsically weak. The IFS technique gives the

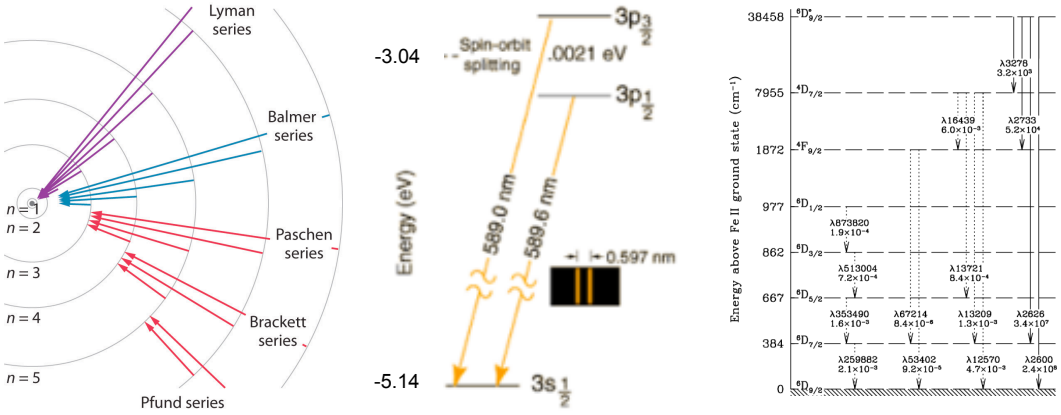

FIGURE 3.1: From left to the right, electron transitions and their resulting wavelengths for hydrogen, sodium and iron. Energy levels are not to scale. In this manuscript we analyze hydrogen lines (Hα, Paα and Brγ), the (dysplayed) sodium doublet transition and the iron $^4D_{7/2}$-$^4F_{9/2}$ one.

possibility to tackle such difficulty by selectively integrate spectra in the spaxels of interest to reach a satisfactory S/N. The resulting integrated spectrum differs from those achievable with long-slit spectroscopy since no specification about a fixed aperture[1] is required (see Fig. 4 in Rosales-Ortega 2011). Furthermore, since in the past many diagnostics were based on long-slit spectroscopy to constrain – e.g., SFR, chemical abundance and dust content in high-z galaxies, the analysis of the IFS-integrated spectra in nearby objects allow us to compare local and distant samples.

There are several ways to combine the individual spectra of an IFS dataset to obtain an integrated spectrum (see Rosales-Ortega et al. 2012 and reference therein). The preferred method depends on the specific science goal. For a proper study of the (stellar) continuum, high S/N spectra are required to model weak features.

Therefore, from the lFS data-cubes, we generated a spatially integrated spectrum per galaxy, via the S/N optimization based on the continuum method, proposed by Rosales-Ortega et al. (2012), using the pingsoft tool (Rosales-Ortega 2011). Briefly, it consist of evaluating the S/N from the continuum on spaxel by spaxel basis and then adding the S/N-sorted spectra, until the point in which the inclusion of additional spectra creates a S/N plateau (or start to decline). Before integration, the spectra were corrected from the general stellar velocity pattern. For this step, we used the narrow component of the ionized gas velocity field, which describes the systemic behavior (Bellocchi et al. 2013). This method significantly improves the modeling of weak features of the stellar continuum compared to other techniques (e.g., S/N cutoff; see Rosales-Ortega et al. 2012 for a detailed discussion).

Figure 3.2, shows the integrated spectrum for the LIRG IRAS F11506-3851 compared to other slit-like spectra extracted from the VIMOS data-cube (with different S/N). The integrated spectra for all the sources of the sample are shown in Appendix A except for IRAS F11506-3851 (see Fig. 3.2 and Fig. 4.7).

The final high S/N spectrum is suitable to various purposes. For example, by analyzing the integrated profile of Hα in the same dataset, Arribas et al. (2014) found that ionized outflows are ubiquitous in the sample.

[1]Note that, usually the term "integrated spectrum" refers to a single (long-slit) spectrum, which is often achieved by locating the aperture in the galaxy nucleus. This is not always the case for the integrated spectra from IFS data.

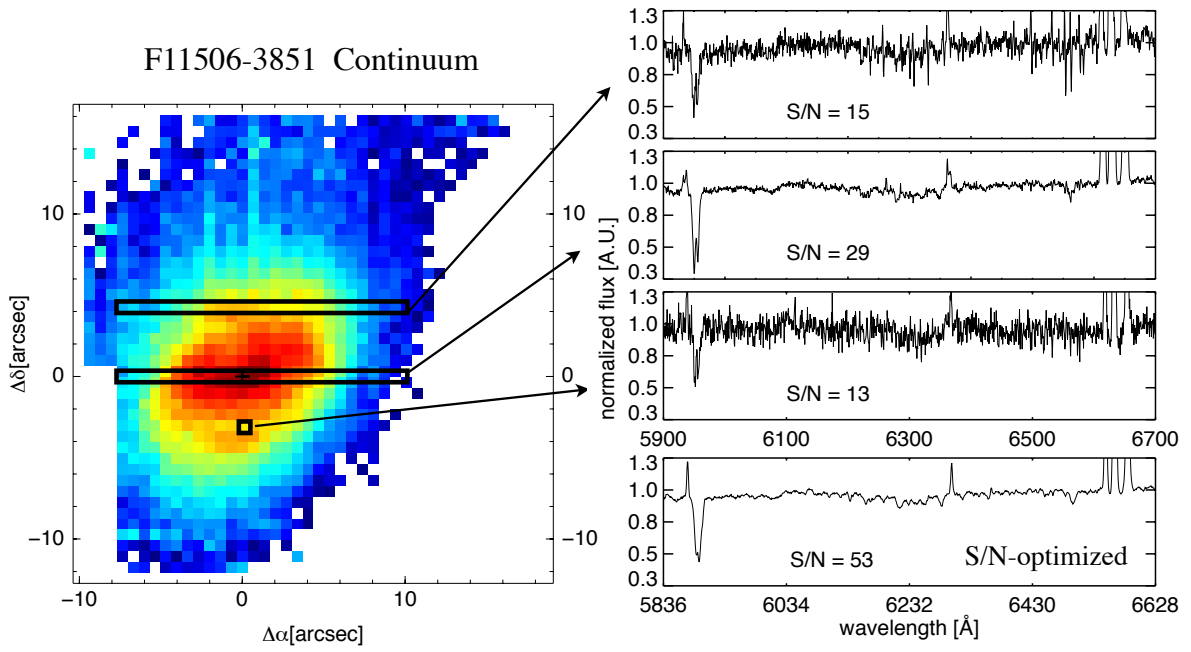

FIGURE 3.2: *Left:* Continuum map of IRAS F11506-3851 extracted form VIMOS data-cube, with overlaid the different regions used to extract the spectra (two pseudo-slit and a single spaxel). A cross marks the nucleus. *Right:* The different spectra extracted from the regions marked on the left are shown with a zoomed-view. In the lower panel, the S/N-optimized spectra used in the this work (corrected from the general stellar velocity pattern). For each panel the S/N calculated as the ratio of the average signal value to the standard deviation of the signal in a line-free wavelength-range of ~ 300 Å is quoted. In all the panel, the (normalized) flux is in arbitrary units. The S/N vary considerably within the different selected spectra, only the S/N-optimized allows a proper modelling of the continuum shape.

3.2.1 Continuum modelling

Reliable measurements of absorption and emission lines must properly account for the starlight contamination. This task is of particular importance for spectral features that have a "mixed-origin" (e.g., NaD) and weak lines such as the near-IR [Fe II] emission. It is relatively less important for bright lines such as Hα, that in (U)LIRGs, generally, overwhelms the starlight (and the Hα stellar absorption).
We applied a Penalized PiXel Fitting analysis (pPXF, Cappellari & Emsellem 2004) for the recovery of the shape of the stellar continuum in both optical and near-IR wavelength range. This package is based on a penalized likelihood approach (e.g., Merritt 1997), and works directly on the pixel space. This allow to easily exclude gas emission lines or bad pixels from the fit and allows the template to be carefully matched to the observed galaxy spectrum without any additional computational time cost. We refer to Cappellari & Emsellem 2004 for details and to de Bruyne et al. (2003) for a detailed overview on the different methods for recovery kinematic parameters.
The pPXF is able to manage large stellar libraries spanning wide ranges of physical parameters. However, mismatchs affects the outcome of cross-correlation techniques and can be considered a source of systematic error. To overcome this error pPXF constructs an optimal template with the proper linear combination of the stellar templates with a given line of sight velocity distribution (LOSVD) to match the data. Following van der Marel & Franx (1993) and Gerhard (1993), it has become standard to

expand the LOSVD as a Gauss-Hermite series:

$$LOS\,VD(v) = \frac{e^{-(1/2)y^{s2}}}{\sigma\sqrt{2\pi}}\left[1 + \sum_{m=3}^{M} h_{\rm m} H_{\rm m}(y)\right], \tag{3.1}$$

where and y = (v - V)/σ, H_m are the Hermite polynomials and M is the number of parameters of the series (V, σ, h_3, h_4, ... , h_m). Under this parametrization of the LOSVD, pPXF returns velocity, velocity dispersion and the Gauss-Hermite coefficients h_3 - h_6. These latter are the high order deviations of the LOSVD from the Gaussian shape[2]. The best-fitting parameters of the LOSVD are determined by a χ^2 minimization.

In order to model the optical stellar continuum, for each spectrum, we first defined the spectral window used during the pPXF fit. We set the wavelength range of the fit to: 5600-6600 Å, to avoid systematic effects due to low S/N pixels at the edge of the spectrum. Afterwards, we excluded spectral regions potentially affected by nebular emission (e.g., He I λ 5876) or with low S/N. Additionally we excluded the NaD absorption that is not properly matched by the stellar templates owing to the impact of interstellar absorption.

To produce the optical stellar spectra that matches the observed line-free continuum we used the Indo-U.S. stellar library (Valdes et al. 2004). This library is constituted of 1273 stars selected to provide a broad coverage of the atmospheric parameters $T_{\rm eff}$, log(g), and [Fe/H], as well as spectral types. The stellar spectra where achieved using the coudé spectrograph of the 2.1 m telescope at Kitt Peak National Observatory. Nearly all the stellar spectra (885) have a spectral coverage from 3460 to 9464 Å, at a resolution of $\sim$ 1 Å FWHM.

The integrated and model spectra are shown for each galaxy in Appendix A. The results of our approach are summarized in Table 3.1. Generally, we have obtained stellar models that in general reproduce well the optical continuum shape (the residuals are typically $< 10\%$) except few cases (see Column 4 in Table 3.1). In Columns 2, and 3 in Table 3.1 lists, for each galaxy, NaD Equivalent width as measured in the model stellar spectra and the estimated percentage contribution to the NaD by old stars, respectively. We tested the feasibility of the stellar continuum modelling on a spaxel-by-spaxel basis. Unfortunately, the spectra in individual spaxels, in general, lack of the S/N required making highly inaccurate the determination of the stellar and ISM contributions in 2D. Therefore, for the 2D analysis we used a different (and more simplistic) approach to evaluate the stellar contamination in the NaD maps, as discussed in sections 4.3 and 5.1.

The optical continuum has been studied for all the sources of the sample while only for IRAS F11506-3851 and IRAS F05189-2524 also the near-IR continuum have been analyzed (with the same software package). Figure 3.3 shows examples of the continuum modeling for the ULIRG IRAS F05189-2524 using pPXF in different sets of data (optical and near-IR). We refer to Sect. 4.1.1.1 for the application of pPXF to K-band data for IRAS F11506-3851, since a different approach to generate high S/N spectra has been used.

The near-IR H-band continuum have been modeled similarly as for the optical data. We placed

[2]Comparing Eq. 3.1 with a Gaussian function of the type: LOSVD = $Ae^{-1/2((v-v_0)/\sigma)^2}$ + B, if $h_3 = h_4 = 0$, the Gauss-Hermite becomes a Gaussian. h_3 describes asymmetric and h_4 symmetric deviations from a Gaussian. The parameter h_3 is the skewness, if positive indicates a tail towards larger velocities. While, the parameter h_4 is the kurtosis, if positive the LOSVD has smaller wings than a Gaussian, whereas for negative h_4 it has broader wings.

emission-line masks in correspondence of the [Fe II] line and a broad emission line (Fig. 3.3, center). We used the medium resolution spectral library of late type stellar templates (G, K, and M type) from Le et al. (2011). This is composed of a total of 12 stars, observed with the the InfraRed Camera and Spectrograph (IRCS) mounted on SUBARU 8.2 m telescope.
In the SINFONI K-band, as mentioned earlier, lie the stellar CO photospheric absorption bands (Fig. 3.3, bottom). Due to their intrinsic sharpness, CO bands offer an excellent feature for probing the stellar kinematics and therefore are not excluded during the stellar fit. At this wavelengths, we used the spectroscopic library of late type stars (at R = 5200-5900) which is obtained with the Near-Infrared Spectrograph (GNIRS) mounted on GEMINI South (Winge et al. 2009).

3.2.2 Stellar subtraction and ISM kinematics

We checked all the stellar continuum modeling by visual inspection of the residuals especially in the line-free continuum regions and nearby the NaD feature (e.g., we checked if any potential NaD-HeI blending may affect the continuum model). We then flagged each object with the parameter Q, indicating the quality of stellar modeling (Column 4, Table 3.1). From the total sample of 49 objects, 31 were flagged with good (Q = 2) or very good (Q = 3) modeling. For these objects, we generated a pure ISM-spectra by subtracting from the observed NaD profile the model of the stellar spectra obtained via the pPXF method. This model was also used to fix the stellar (systemic) zero velocity of the spectra. For only 3 out of 31 (i.e., F01159-4443 (N), F21453-3511, F23128-5919 (N)) was not possible to model the purely-ISM NaD line profile since the stellar subtraction resulted in an almost undetectable neutral gas NaD doublet (the stellar contamination is > 95%, Table 3.1).
We then model the purely ISM NaD line profile in the integrated spectra with one or two kinematic components (i.e., one or two Gaussian pair) following the approach described in detail in Sect. 3.3.1.1. Fig. 3.4 shows the purely-ISM NaD absorption and its modelling while the properties and the kinematics are summarized in Table 3.1 for each galaxy. In ∼61% (i.e., 17/28) of the cases a single kinematic component (a Gaussian pair) already gives a good fit, suggesting that if a second component exists in these galaxies, it is weak. Only 11 out of 28 require two kinematic components; we find that a two-Gaussian components model per line led to a remarkably good fit of the NaD absorption, significantly reducing the residuals with respect to one-Gaussian fits (Fig. 3.4).
In 21/28 of these integrated spectra show a prominent nebular emission line He I, which was included in the line fitting (i.e., modelled selectively with one or two-Gaussian components and then subtracted). This strategy has also been applied in a few cases to the spatially resolved data also (Sect. 3.3).
Since the near-IR coverage is not available for all the sources in the sample, we refer to dedicated sections for the treatment of such data sets. Specifically, the stellar kinematic is treated in detail for IRAS F11506-3851 in Sect. 4.1.1.1. While, the stellar subtraction (to emission lines) for IRAS F05189-2524 is commented in Sect. 6.2.

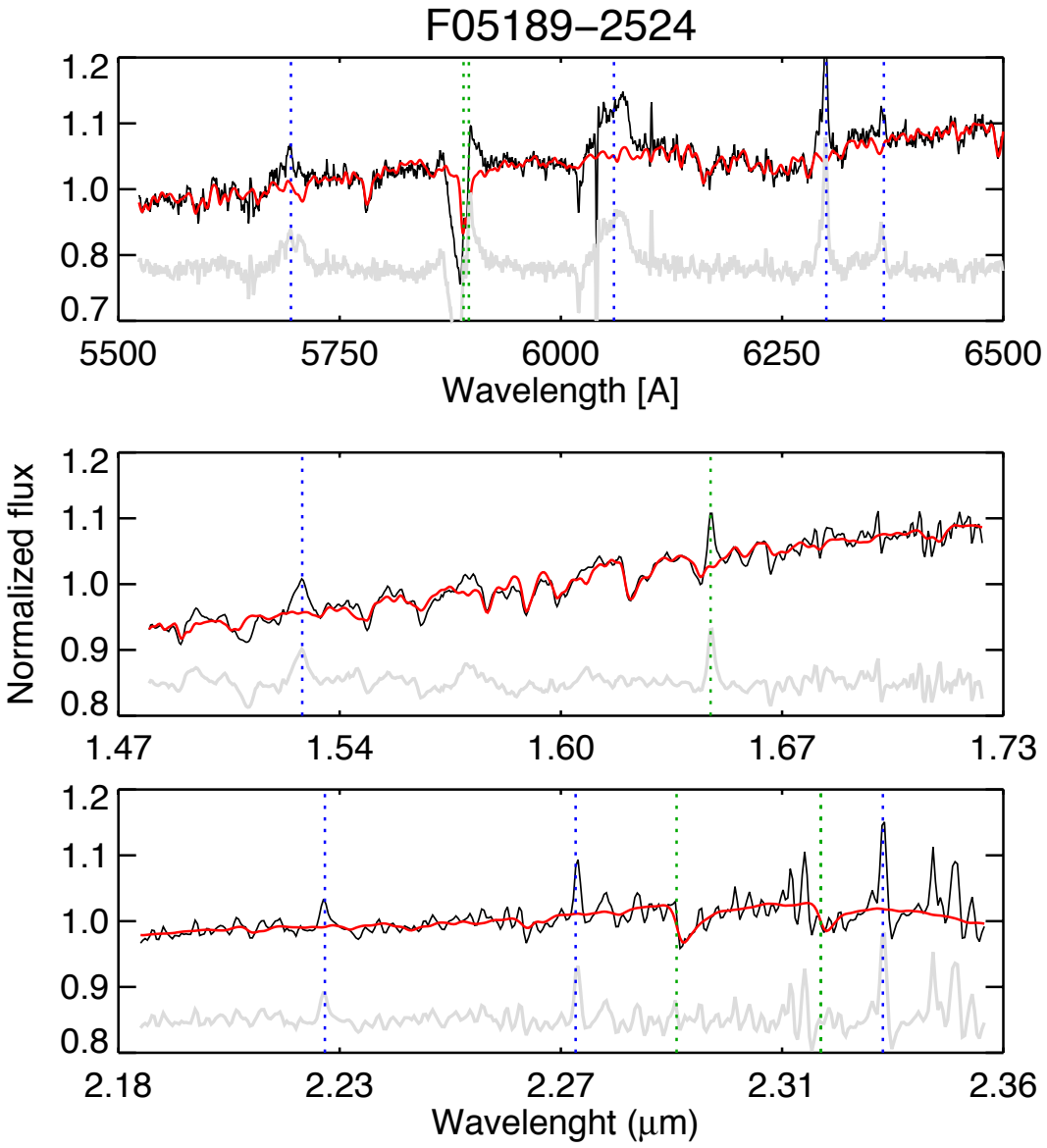

FIGURE 3.3: From top to the bottom, part of (VIMOS) optical and (SINFONI) near-IR H and K band spectra. In all the panels, in black we present the integrated spectra, and in red (overplotted) the pPXF-fit. Green and blue dotted lines mark, respectively, the central wavelength of the lines we are interested to and those which are not considered in the pPXF-fit. As mentioned in the text, CO absorption lines (bottom panel) are lines of interest but, since their purely stellar origin, are included in the stellar modeling. Note that the near-IR spectra are not corrected for the general velocity field (here are shown for illustrative purpose). The K-band spectrum of IRAS F05189-2524 does not have very high S/N and the CO stellar bands are at the edge of the grating. Fig. 4.2, show an further example of a K-band spectrum (at higher S/N) and its stellar fit.

TABLE 3.1: Results from the integrated spectra analysis

ID1	$EW_{stars}^{ppxf-fit}$	IS	Q	V^B	σ^B	V^{other}	σ^{other}	$V^{adopted}$	$\sigma^{adopted}$
IRAS	Å	%		kms^{-1}	kms^{-1}	kms^{-1}	kms^{-1}	kms^{-1}	kms^{-1}
(1)	(2)	(3)	(4)	(5)	(6)	(7)	(8)	(9)	(10)
F01159-4443 (N)	1.4 ± 0.1	30	2	-237 ± 13	127 ± 18	13 ± 3	102 ± 16	-237 ± 13	127 ± 18
F01159-4443 (S)	1.2 ± 0.1	100	2	···	···	···	···	···	···
F01341-3735 (N)	0.9 ± 0.1	72	3	-278 ± 8	71 ± 3	-105 ± 4	76 ± 6	-192 ± 6	74 ± 5
F01341-3735 (S)	1.0 ± 0.2	49	2	···	···	41 ± 4	80 ± 8	41 ± 4	80 ± 8
F04315-0840	0.6 ± 0.1	20	3	-186 ± 21	104 ± 11	-8 ± 5	109 ± 17	-186 ± 21	104 ± 11
F05189-2524	0.7 ± 0.1	38	2	-725 ± 26	150 ± 13	-451 ± 11	87 ± 7	⊘	⊘
F06035-7102	(0.6 ± 0.1)	(77)	1	···	···	···	···	···	···
F06076-2139 (N)	0.7 ± 0.1	30	3	-172 ± 29	102 ± 9	···	···	⊘	⊘
F06076-2139 (S)	0.8 ± 0.1	64	2	-176 ± 16	139 ± 14	···	···	-176 ± 16	139 ± 14
F06206-6315	(1.9 ± 2.3)	(100)	1	···	···	···	···	···	···
F06259-4780 (N)	0.9 ± 0.1	23	2	-234 ± 9	117 ± 2	-97 ± 3	91 ± 8	-166 ± 6	104 ± 6
F06259-4780 (C)	0.4 ± 0.1	39	2	-3 ± 4	92 ± 14	181 ±15	81 ± 24	93 ± 38	87 ±10
F06259-4780 (S)	(1.0 ± 0.3)	(72)	1	···	···	···	···	···	···
F06295-1735	(1.4 ± 0.7)	(100)	1	···	···	···	···	···	···
F06592-6313	0.8 ± 0.1	25	3	-193 ± 11	148 ± 13	···	···	-193 ± 11	148 ± 13
F07027-6011 (N)	0.6 ± 0.1	21	2	-328 ± 18	92 ± 10	-140 ± 4	71 ± 4	-234 ± 12	87 ± 7
F07027-6011 (S)	0.9 ± 0.1	26	2	-202 ± 18	87 ± 4	-31 ± 4	112 ± 10	-202 ± 18	87 ± 4
F07160-6215	1.2 ± 0.3	39	2	···	···	-13 ± 2	132 ± 12	-13 ± 2	132 ± 12
08424-3130 (N)	(1.0 ± 0.1)	(42)	1	···	···	···	···	···	···
08424-3130 (S)	(1.1 ± 0.1)	(34)	1	···	···	···	···	···	···
F08520-6850	(1.0 ± 0.1)	(100)	1	···	···	···	···	···	···
09022-3615	(1.2 ± 0.4)	(100)	1	···	···	···	···	···	···
F09437+0317 (N)	1.3 ± 0.2	30	2	···	···	54 ± 5	93 ± 14	54 ± 5	93 ± 14
F09437+0317 (S)	(1.7 ± 0.2)	(100)	1	···	···	···	···	···	···
F10015-0614	1.2 ± 0.1	48	2	-116 ± 5	135 ± 4	···	···	-116 ± 5	135 ± 4
F10038-3338	0.8 ± 0.1	50	2	-175 ± 5	131 ± 4	···	···	-175 ± 5	131 ± 4
F10257-4339	0.6 ± 0.1	28	2	-386 ± 11	97 ± 10	···	···	⊘	⊘
F10409-4556	1.3 ± 0.2	47	3	-180 ± 8	150 ± 6	···	···	-180 ± 8	150 ± 6
F10567-4310	1.5 ± 0.2	28	2	-146 ± 6	160 ± 4	···	···	-146 ± 6	160 ± 4
F11255-4120	0.8 ± 0.1	18	2	-405 ± 21	148 ± 26	-99 ±11	127 ± 15	-252 ± 21	138 ± 21
F11506-3851	1.2 ± 0.1	30	3	-88 ± 11	108 ± 8	173 ± 18	113 ± 14	-88 ± 11	108 ± 8
F12043-3140 (N)	(0.7 ± 0.1)	(79)	1	···	···	···	···	···	···
F12043-3140 (S)	0.9 ± 0.1	77	2	-152 ± 16	162 ± 13	···	···	-152 ± 16	162 ± 13
F12115-4656	1.5 ± 0.2	73	3	-65 ± 8	119 ± 6	···	···	-65 ± 8	119 ± 6
12116-5615	0.8 ± 0.1	22	2	-371 ± 21	98 ± 18	-156 ± 11	96 ± 16	-264 ± 16	97 ± 8
F12596-1529	(1.5 ± 0.2)	(100)	1	···	···	···	···	···	···
F13001-2339	(1.2 ± 1.1)	(63)	1	···	···	···	···	···	···
F13229-2934	0.5 ± 0.1	67	3	-140 ± 4	106 ± 3	···	···	-140 ± 4	106 ± 3
F14544-4255 (E)	(0.9 ± 0.1)	(41)	1	···	···	···	···	···	···
F14544-4255 (W)	(1.9 ± 0.4)	(100)	1	···	···	···	···	···	···
F17138-1017	(1.2 ± 0.5)	(80)	1	···	···	···	···	···	···
F18093-5744 (N)	1.0 ± 0.1	65	2	-90 ± 14	152 ± 11	···	···	-90 ± 14	152 ± 11
F18093-5744 (C)	(0.5 ± 0.1)	(56)	1	···	···	···	···	···	···
F18093-5744 (S)	0.7 ± 0.1	41	2	···	···	-41 ± 4	103 ± 13	-41 ± 4	103 ± 13
F21453-3511	1.1 ± 0.1	97	2	···	···	···	···	···	···
F22132-3705	1.1 ± 0.1	47	3	···	···	36 ± 3	109 ± 12	36 ± 3	109 ± 12
F22491-1808	(0.7 ± 0.1)	(90)	1	···	···	···	···	···	···
F23128-5919 (N)	0.8 ± 0.1	99	2	···	···	···	···	···	···
F23128-5919 (S)	(0.7 ± 0.1)	(98)	1	···	···	···	···	···	···

Notes. Column (1): IRAS name. Column (2): NaD Equivalent width as measured in the model stellar spectra (output of the pPXF routine). Column (3): The estimated percentage contribution to the NaD by old stars (Sect. 3.2.2). In brackets values obtained from poor fits (i.e., Q = 1, in column (4)). Column (4): Index of the quality of the stellar modelling of the integrated spectra (after visually inspecting the results of the pPXF analysis). It is defined as follows: 1 doubtful results, 2 and 3 medium and highly reliable results, respectively. We assign Q = 1 to both galaxies in the system 08424-3130, since only a part of the nuclear region of both galaxies is covered by our VIMOS FoV (Fig. A. 16). In particular, the area covered by the NaD absorption (and Hα, Bellocchi et al. 2013) for the Northern galaxy is very small, so that its correction for the rotation pattern (Sect. 3.2) is rather inaccurate. Columns (5-8): Velocity and velocity dispersion of the different components derived for the NaD line profiles seen in the "decontaminated" spectra (i.e., observed - stellar model). The different components are identified according to their velocities. Specifically, the superindex "B" stands for a blueshifted component (according to the criterion in Sect. 3.4), while "other" indicates a second kinematic component. Such component is typically narrower with respect to the blueshifted component, and it is found at systemic velocity (i.e., $-60 < V < 60$ kms^{-1}) or redshifted ($V > 60$ kms^{-1}) with respect to the stars. When two blueshifted components are found for the same object, that one with the lowest velocity is in the column dedicated to the "other"-component. Columns (9-10): Adopted values of velocity and velocity dispersion for the 1D-analysis (Sect. 5.2). Note that, when two blueshifted components are found, their average values is considered. The symbol ⊘ indicates the galaxies excluded for the 1D-analysis since the Gaussian modelling of the NaD absorption line profile leaves strong residual.

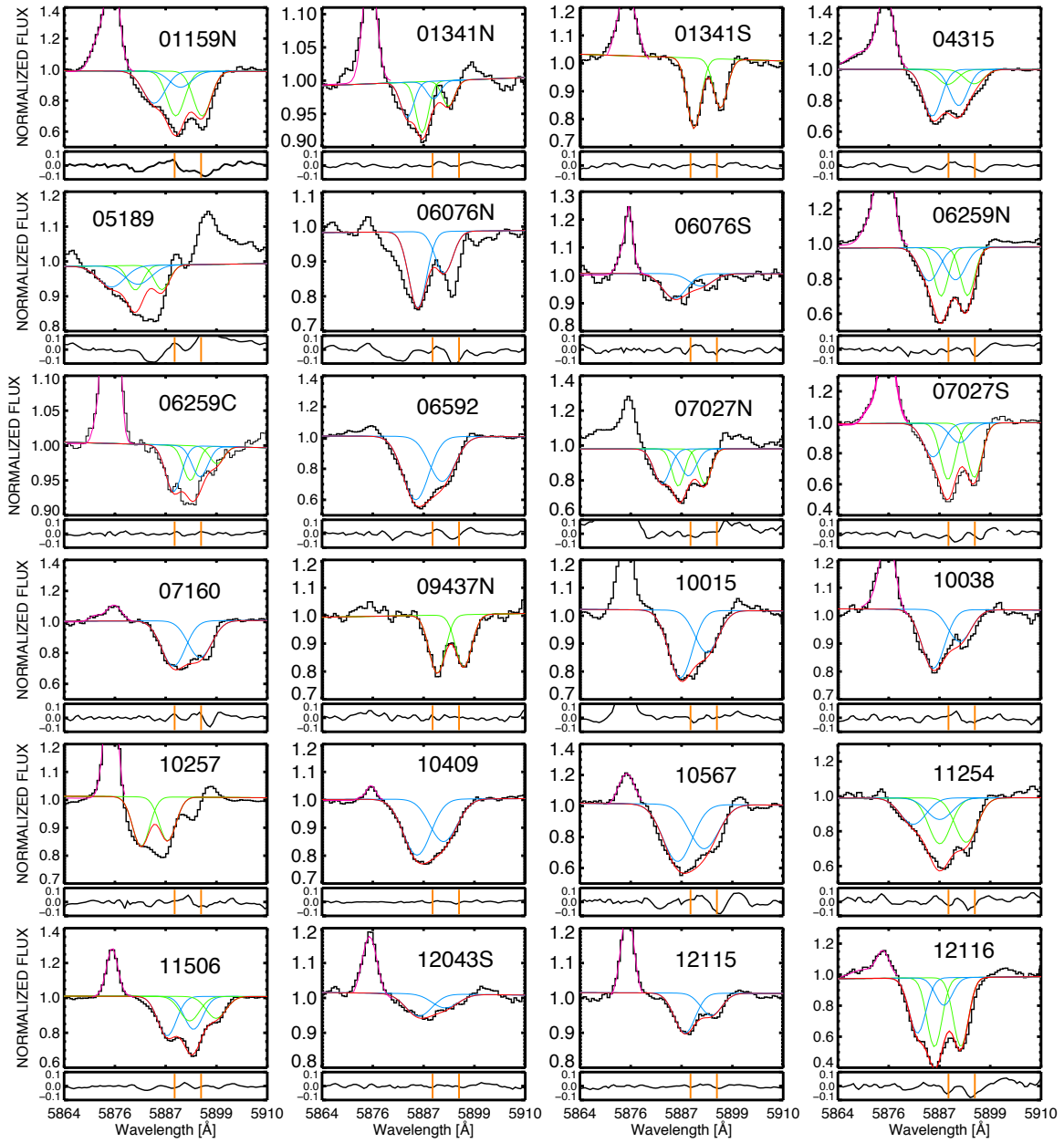

FIGURE 3.4: Normalized integrated spectra of the NaD absorption-line profile after the subtraction of the stellar contribution, in the galaxies having medium and high quality of the stellar modelling of the integrated spectra (Sect. 3.2.2). Each displayed spectrum covers a rest-frame range of ~ 46 Å (i.e, $\sim 2300\,\mathrm{kms}^{-1}$). For each source, in the upper panels, the different kinematic components, are shown in blue and green, i.e., blueshifted and systemic/redshifted component, according to our classification (Table 3.2). The red curve shows the total contribution coming from the NaD Gaussian fit. In pink, we marked the model to the HeI emission line. Such line has been successfully modelled with one (e.g., F10257-4339) or two components (e.g., F04315-0840) in 21 cases. In two cases, F07027-6011 (N) and F10015-0614, the line modelling of the (prominent) HeI emission cannot well reproduce the observed line profile. Therefore, HeI is simply excluded when fitting the NaD absorption. In the lower panels, the residuals (i.e., data - model) are presented, with the rest frame NaD wavelengths are marked in orange. The galaxy IDs follow that of Table 2.1, though here they are shortened for a better visualisation. Note the complexity of the NaD line profile in F05189-2524. The resonant line emission, which is not a common feature of GWs in nearby galaxies, is not modeled here but for a detailed discussion of this object we refer to Rupke & Veilleux (2015).

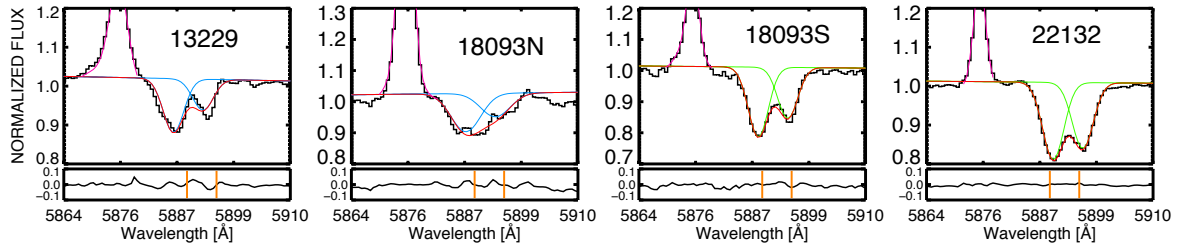

Fig. 3.4 – Continued.

3.3 Spatially resolved (2D) analysis

The optical and near-IR IFS data will be used to create emission-line and absorption-line maps. Maps are data-files stored in 2D fits-files, reflecting the original arrangement of the spaxels in the sky. In our case data-files consist of the results of the line fitting method (Sections 3.3.1.1 and 3.3.1.2) – i.e., central wavelength, velocity dispersion and peak flux, for each kinematic component.

3.3.1 Line modelling

We modelled all the features listed in the previous section (Sect. 3.1) using customized IDL scripts. These were built mainly using routines `MPFIT`, `MPFITFUN` and (largely) `MPFITEXPR` written by Craig Markwardt (Markwardt 2009). In these, we specified the initial parameters of the spectral line fit (continuum level, line flux, centroid and width) and the main script sequentially process each spectrum, fitting Gaussian profiles accordingly. The output consists of fit parameters for the continuum (slope and normalization) and for each spectral line profile (central wavelength, line width, and flux) and the value of the (summed, squared and weighted) residuals for the returned parameter values (i.e., χ^2) for the fit.

The routine quoted above underestimate the true uncertainties. For example, by using `MPFITEXPR`, the fit is unweighted (i.e., no errors were given, or the weights were uniformly set to unity). Therefore, the reported fitting error were scaled by the measured χ^2 value (normalized accordingly to the degree of freedom of the fit).

We generally found that all the feature could be optimally fitted with a single Gaussian per line (i.e., one kinematic component) except few case. In these cases, thanks to the high S/N of the spectra, we were able to fit an additional (generally broader) Gaussian profile underneath the first component. In the following sections we describe further details of the procedure for both absorption and emission features.

3.3.1.1 Absorption lines

We customized the general procedure described in the previous section to optimally fit an absorption line doublet. In this case, a kinematical component consist of a pair of Gaussians. The central wavelength is a free parameter, while the widths are constrained to be equal for the two lines, and greater than the instrumental width (Sect. 2.2.1). In addition, the ratio between the equivalent widths of the

two lines, $EW_{\lambda 5890}/EW_{\lambda 5896}$, is restricted to vary from 2 (i.e., optically thin absorbing gas) to 1 (i.e., optical thick limit) according to Spitzer (1978). The underlying continuum is taken into account by adding a linear term to the fit.

Fitting the neutral gas absorption with a Gaussian pair represents a simplification of the real case as many individual clouds (i.e., subcomponents) are likely to be present along the line of sight. However, this approach allows us to characterize the global neutral gas kinematics without introducing other model dependent variables. An alternative method that allows more complex intensity profiles is described by Rupke et al. (2005a). Our approach (followed also by also Davis et al. 2012) has the limitation of being correct only in the cases of either uniform covering factor and low optical depth or in the case of covering factor that varies with velocity as a Gaussian (independently to the optical depth). Absorption line fitting methods that consider both optical depth and covering factor are presented in Rupke et al. (2005b), and references therein. Although the observed NaD-absorption features show generally well-resolved lines and not saturated profiles (i.e., flat-bottomed), we stress that the validity of our fitting approach is limited to the cases mentioned above. As in many cases the line ratio within the two doublet lines indicates an optically thick regime, it is implicity assumed that the covering factor varies with velocity as a Gaussian in these cases.

As for the integrated spectra (Sect.3.2.2) in a few cases, we also modeled (and subtracted) the He I nebular emission line (15 Å blueward of NaD) since it was broad and strong enough to affect the final results of the NaD fitting.

We found some spectra that have strongly asymmetric profiles and their modeling requires two Gaussian pairs (i.e., a single component fitting is certainly an oversimplification). After visual inspecting all the spectra, we decided to apply a two-components line fitting for the spectra of four objects (F07027-6011 (S), F10409-4556, F11506-3851, and F12116-5615). In a few other cases, there is evidence for the presence of multiple kinematic components in individual spectra (e.g., F04315-0840, F10257-4310, F13229-2934). However, the limited S/N does not allow us a robust kinematic decomposition into two different components. Therefore, a single kinematic component fitting of the NaD absorption doublet was preferred in these cases. Figure 3.5 shows examples of the two different Gaussian fits for the galaxy IRAS F10409-4556. The existence of two kinematical components is expected as the NaD absorption feature may take part in the galaxy ordered rotation and be entrained in winds with blueshifted velocities. Therefore, we identify these components according mainly to their spatial distribution and velocities.

Within the galaxies for which we found evidence for multiple absorption components in the IFS-spectra, of particular interest is the cases of IRAS F11506-3851. In this galaxy, most of the NaD-absorption features show smooth and unblended line profiles and therefore they were modeled with a single kinematic component, i.e., a Gaussian pair (Fig. 3.5, top-left). However some spectra, mainly located in the central region, have asymmetrical and complex profiles that suggest the presence of an additional secondary component, and therefore they require two Gaussian pairs for the fit (Fig. 3.5, bottom-left).

After experimenting with these two components it was clear that the main component is due to absorption by neutral gas, while the secondary component has a stellar origin (see Sect. 4.3 for a detailed discussion of their properties and respective roles). In general, the two-component modeling of the NaD line profile is rather complicated and often leads to unphysical or non-unique solutions. Therefore, in order to preserve against spurious results, the secondary (stellar) component was constrained

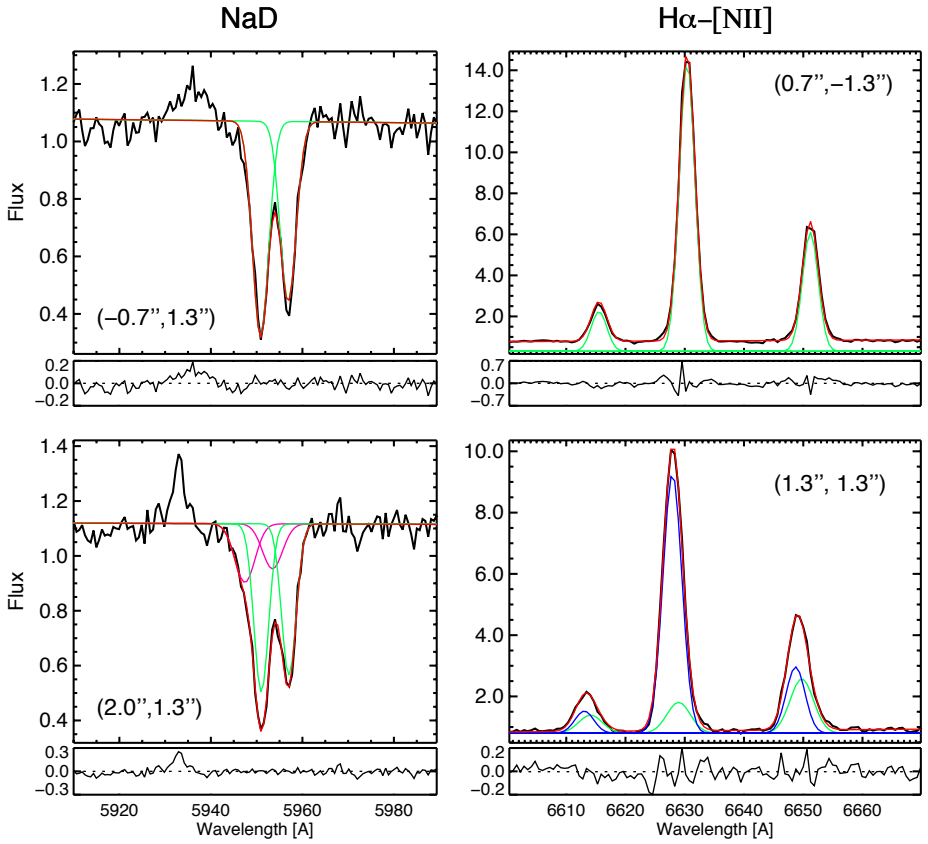

FIGURE 3.5: NaD (left) and Hα-[N II] (right) spectra for selected regions of IRAS F11506-3851. In the labels the coordinates have been indicated as the distance from the nucleus (map center, Figures 4.3 and 4.4). For each spaxel the modeled line profile (red line) and the single component (with different colors) are shown, along with the residuals (small panels). *Top:* The results of the NaD and the Hα one-component modeling. The green lines in each panel represent, respectively, the main-NaD and the narrow-Hα Gaussian functions. *Bottom:* Examples of NaD and Hα spectra with two components. The secondary-NaD and the broad-Hα curves are shown in magenta and blue, respectively, and the green and red lines represent the main component and the global fits to the observed profiles (as in the top panels).

to be within $\pm$ 100 kms^{-1} of the systemic rotating velocity as traced by the CO(2-0) λ 2.29 μm and Hα features[3]. We checked the line profile fits by visually inspecting the residuals. A fit with two-kinematic components was preferred when it produced a significant reduction of the residuals with respect to the standard one-component fit. As mentioned in Sect. 3.3.1, for each Gaussian, the output of the fitting process gives the central wavelength, the line width, and the flux along with their respective fitting errors. The intrinsic line widths were computed after removing the instrumental profile inferred from the sky lines (see Sect. 2.2.1, Eq. 2.1).

[3]As discussed in Sect. 4.2, the bulk of the ionized gas and the stars nearly co-rotate. Therefore we linked the secondary NaD component to Hα rather than to CO(2-0) since those features were obtained from the same data-cubes and therefore have homogeneous spatial sampling and calibrations.

3.3.1.2 Emission lines

Optical and near-IR emission lines, were treated similarly to the NaD absorption line. The measurements of the kinematic and fluxes of optical and near-IR emission lines were carried out using Gaussian fitting. We customized the general procedure described in Sect. 3.3.1 to optimally model emission lines. We initially fit the spectra with a single Gaussian per line analyzing the residuals and look for the possible existence of a second (broader) component.
For the whole sample, the Hα-[N II] emission line complex is analyzed (with a two components fitting) by Bellocchi et al. (2013). Only in the case of IRAS F11506-3851, the Hα-[NII] fitting was performed with great detail since the derived kinematic information allowed to constrain that of NaD (Sect. 3.3.1.1). Specifically, the observed Hα-[N II] in the spectra of IRAS F11506-3851, were accurately fitted by a single Gaussian per line although a small number of spectra, mainly in the inner region (and towards the NE), show traces of a secondary component. The IDL-fitting routine was customized to model the Hα and [N II] $\lambda\lambda$ 6548, 6583 Å emission lines, and to estimate the flux intensity, central wavelength, and widths. Specifically, the Hα-[N II] complex was fitted with one (or two) Gaussian(s) per line with the line flux ratios and wavelengths of the [N II]-lines fixed according to the atomic physics. Similarly to the NaD doublet, the widths are constrained to have a velocity dispersion greater than the instrumental resolution (see Sect. 2.2.1, Eq. 2.1) and to be equal for all the lines of the same component. Typically, the Hα-fitting errors are lower than 0.1 and 0.15 Å for the central wavelength and the width respectively, while the calibration errors are the same as those adopted for the NaD. Figure 3.5 shows examples of one- and two- Gaussian fits, respectively. The two-Gaussian fits lead to two components which in general can be distinguished according to their widths, – i.e., narrow ($\sigma = 46 \pm 10$ kms^{-1}) and broad ($\sigma = 74 \pm 5$ kms^{-1}) components. The narrow (main) component contains most of the Hα flux and it is associated with systemic rotational motions while, the broad component seems to be associated with non-rotational motions (see Sect. 4.5).
Despite the overall Gaussian-methodology could be applied for any emission line, we had particular care when dealing with near-IR emission features. Such lines are generally weak (except Paα), therefore to get an accurate (more sensitive to the mechanism responsible for the gas excitation) measurement of the emission line fluxes and equivalent widths, we need to subtract the stellar component underneath (see Sect. 3.2.1). The modelling of the Hα emission does not take into account the contribution of the stellar absorption since, generally, it is expected to be negligible in (U)LIRGs (as indicated by our stellar modelling also). Furthermore, in this case we are mainly interested to kinematic measurement rather than fluxes or equivalent width estimates. By fitting simultaneously Hα and [N II] lines the effect of possible stellar contamination in kinematics is mitigated.
Examples of the Gaussian modelling of near-IR emission lines are shown in Sect. 6.2.

3.3.2 Maps Generation

The analysis described in Chapters 4, 5 and 6 is based on the spectral maps of the different kinematic components which were generated after the line fitting procedure. These maps are: the velocity field, the velocity dispersion map and the equivalent width map. Spaxels with low S/N were masked as well as in those cases that the fit to absorption/emission lines was poor.

To produce the maps themselves, we used a set of IDL procedures – i.e., the plotting package *jmaplot* developed by Maíz-Apellániz (2004). The maps are shown, for each galaxy (for a total of 40 objects), in Appendix A. As a reference we also display the continuum image and the Hα velocity map of the systemic (narrow) component generated from the VIMOS-IFU data cube (Bellocchi et al. 2013). For each object the integrated spectrum (Sect. 3.2) is also shown.
The maps of the LIRG IRAS F11506-3851 are discussed in detail in Chapt. 4, and therefore they are not included in Appendix A, but the results are however considered in the overall statistics and figures of Chapt. 5. For this galaxy, we also obtained the maps for the stellar kinematic (see Sect. 4.1.1.1).

3.4 Neutral outflows and rotating disks: (U)LIRGs kinematical classification

One of the main diagnostics of galaxy-research is classifying galaxies, to learn about the underlying physics of the classification. In the past, various galaxy properties have already been used for classifications, for example morphology ("tuning fork" Hubble scheme) or colors (which indicate the star forming activity: blue-star-forming vs. red-and-dead galaxies). Compared to these, the kinematic classification is only an emerging technique, due to the difficulties to produce 2D velocity fields (before the development of IFS).
Previously, the galaxies in the current sample were classified according to the optical morphology (see Column (5) in Table 2.1 and Rodríguez-Zaurín et al. 2011) and the Hα kinematics (Bellocchi et al. 2013; Bellocchi 2014). The latter, is based on the 2D velocity fields and the velocity dispersion maps of the systemic (narrow) Hα-component, Bellocchi et al. (2013), and distinguishes three main groups. Briefly:

- Rotating disks.
  The expected pattern for rotation consist of: a well defined major kinematic axis of the velocity field aligned with the major photometric axis of the continuum map, and a centrally peaked velocity dispersion map.
- Perturbed disks.
  The velocity field shows a general rotation pattern but the kinematic axes show some distortions and/or the velocity dispersion map has a peak shifted off the center.
- Complex kinematics.
  The velocity field and the velocity dispersion map show significant deviations from the global rotation pattern due to, for example, strong radial motions.

This classification is similar to the one proposed by Flores et al. (2006) based on IFS-observations 35 galaxies at intermediate redshift ($0.4 < z < 0.75$).

However, from galaxy to galaxy, gaseous components may have a different kinematical behavior showing differences in their classification scheme. One of the aim of this thesis is to classify galaxies based

on their global (integrated) and spatially resolved properties of the neutral gas. Inspired by the kinematic classification described above, we construct an alternative classification scheme using the following parameters: velocity, velocity dispersion and strength of NaD. Below, we detail the two criteria, based on the integrated and the spatially resolved neutral gas properties, and in Table 3.2 we list the classification for each individual object in the sample.

1D-criterion

When identifying GWs in the integrated ISM spectra (Sect. 3.2.1) only components with central line velocities blueshifted with respect to the systemic by more than 60 kms^{-1} are considered to be outflowing (Column 9 in Table 3.1). This cutoff, which is on the order of two spectral elements of ~ 0.6 Å each, is similar to those assumed in previous studies (e.g., 50 kms^{-1} in Rupke et al. 2005b). Neutral gaseous outflows are found in 19 out of 28 [U]LIRGs (Table 3.2). We excluded from the current 1D-analysis 3 galaxies (F05189-2524, F06076-2139 (N) and F10257-4339) since the modelling of the NaD absorption line profile leaves strong residual (Table 3.1). The kinematic components which are found at systemic velocity or redshifted (Table 3.2), are not studied in detail in this work.

2D-criteria

We divide the galaxies in the present sample into two main classes: GWs hosts and rotating disks.
The search of spatially resolved GWs was done by inspecting the NaD spectral maps, looking for regions with, simultaneously:

- significant blueshifted velocities ($\gtrsim 60$ kms^{-1}) with respect to the systemic, which cannot be explained by rotation. For this identification we consider as reference the velocity field of the narrow component of Hα, for which Bellocchi et al. (2013) have shown it follows the systemic behavior (Appendix A);
- EW(NaD) > 1.3 Å, to guarantee that the NaD feature is dominated by ISM absorption;
- relatively broad kinematic component ($\sigma > 90$ kms^{-1}).

This procedure identifies 22 objects out of 40 (55%) with outflows (Table 3.2), implying a detection rate slightly lower than the one obtained from the analysis of the integrated spectra (i.e., 71%).

- Rotating disks. Velocity fields with a with well-defined approaching and receding regions (spider-like) expected in case of a rotation pattern. This criterion is similar to the one used for the classification of ionized gas kinematics (via Hα).

The velocity fields of the neutral gas observed in 11 [U]LIRGs satisfy this criterion (Figures in Appendix A and Sect. 4 for the case of the LIRG F11506-3851). In three galaxies (F07027-6011 (S), F10409-4556 and F11506-3851) the rotation is detected in one kinematic component, but an additional outflowing component is also detected (Figures A. 14, A. 24, and 4.3). However, while in case of an ideal rotating disk the velocity dispersion map should be centrally peaked, the observed neutral

gas velocity dispersion maps are generally rather irregular.
Galaxies in which the spectral maps do not follow none of the two criterions, because of the signal for the NaD doublet is rather faint or projection/observational effects, are not taken into account in this work (Table 3.2), but when possible (Sect. 3.3.1.1) the spectral maps and integrated spectra are shown in Appendix A.
The properties of the identified outflows are described for the full sample in Sect. 5.4. Neutral disks are described in Sect. 5.8.
Note that, the criteria described above are not strictly followed when treating near-IR data. Specifically for the LIRG IRAS F11506-38, we studied the stellar kinematics, which, as expected, has been found in ordinary rotation. For the ULIRG IRAS F05189-2524, we studied in detail emission lines. The above listed criteria to look for outflows are still overall valid but with some differences. Therefore, for this particular case, we refer to Sect. 6.3.

TABLE 3.2: Classification of neutral gas kinematical properties for the VIMOS sample of (U)LIRGs.

IRAS	1D	2D
(1)	(2)	(3)
F01159-4443 (N)	S+B	GW
F01159-4443 (S)	···	···
F01341-3735 (N)	B+B	GW
F01341-3735 (S)	S	···
F04315-0840	S+B	GW
F05189-2524	B+B	GW
F06035-7102	···	···
F06076-2139 (N)	B	···
F06076-2139 (S)	B	···
F06206-6315	···	GW
F06259-4780 (N)	B+B	GW
F06259-4780 (C)	S+ R	RD
F06259-4780 (S)	···	···
F06295-1735	···	···
F06592-6313	B	GW
F07027-6011 (N)	B+B	GW
F07027-6011 (S)	S+B	RD + GW
F07160-6215	S	GW
08355-4944	···	···
08424-3130 (N)	···	···
08424-3130 (S)	···	···
F08520-6850	···	···
09022-3615	···	···
F09437+0317 (N)	S	RD
F09437+0317 (S)	···	RD
F10015-0614	B	GW
F10038-3338	B	GW
F10257-4339	B	GW
F10409-4556	B	RD + GW
F10567-4310	B	GW
F11255-4120	B+B	GW
F11506-3851	R+B	GW
F12043-3140 (N)	···	···
F12043-3140 (S)	B	RD
F12115-4656	B	RD
12116-5615	B+B	GW
F12596-1529	···	···
F13001-2339	···	GW
F13229-2934	B	GW
F14544-4255 (E)	···	RD
F14544-4255 (W)	···	···
F17138-1017	···	···
F18093-5744 (N)	B	···
F18093-5744 (C)	···	···
F18093-5744 (S)	S	RD
F21130-4446	···	···
F21453-3511	···	GW
F22132-3705	S	RD
F22491-1808	···	···
F23128-5919 (N)	···	···
F23128-5919 (S)	···	GW

Notes. Column (1): Object designation in the IRAS PSC and FSC, as in Table 2.1. Columns (2) and (3): Our classification scheme, according to the integrated spectra (i.e., 1D, Column (2)) and the maps (i.e., 2D, Column (3)). Note that, if multiple classifications are quoted for the same object, each classification refers to different kinematic components. The letter "S" refers to a systemic component, while "R" and "B" indicate, respectively, the presence of redshifted (i.e., V>60 kms^{-1}) and blueshifted (i.e., V<-60 kms^{-1}) components (with respect to the stars). "GW" stands for galaxy in which footprint of a galactic winds has been found via NaD (see Sect. 5.3) and "RD" indicates the presence of a disks of neutral gas (see Sect. 5.8).

Chapter 4

Spatially resolved kinematics, galactic wind, and quenching of star formation in the LIRG IRAS F11506-3851

In this chapter, we discuss the multi-phase structure and wind properties of the nearby LIRG IRAS F11506-3851 (ESO 320-G030). Thanks to optical and near-IR IFS observation with VIMOS and SINFONI, we have obtained the 2D distribution of the NaD absorption doublet, the Hα emission line, and the CO absorption bands profiles over its inner region (within $R \leq 3$ kpc). This allowed us to trace the structural and kinematical properties of different galaxy components (gas and stars) and gaseous phases (ionized and neutral).

The work described in this chapter, has been published in a paper entitled "Spatially resolved kinematics, galactic wind, and quenching of star formation in the luminous infrared galaxy IRAS F11506-3851" by S.Cazzoli et al. in A&A, 569, A14.

4.1 The LIRG F11506-2851 as a case of study

As pointed out in the introduction (Chapt. 1), galactic winds are believed to regulate and quench both the SF and the black hole activity, being also the primary mechanism by which dust and metals are redistributed over large scales in the ISM, or even expelled outside the galaxy into the IGM (e.g., Heckman et al. 1987). (U)LIRGs are interesting populations for the study of outflows and in particular the potentially interesting LIRG range have been explored less.
We selected the LIRG IRAS F11506-3851 as a case of study for three main reasons. First, for the possibility to study near-IR properties thanks to SINFONI H and K band data. Second, for the high quality of integrated spectrum, which allow a good stellar continuum modelling (Sect. 3.2.1). Third, since the velocity field of the neutral gas (obtained with a Gaussian fit to the NaD lines, Sect. 3.3.1.1) shows feature of a galactic wind (as discussed later).

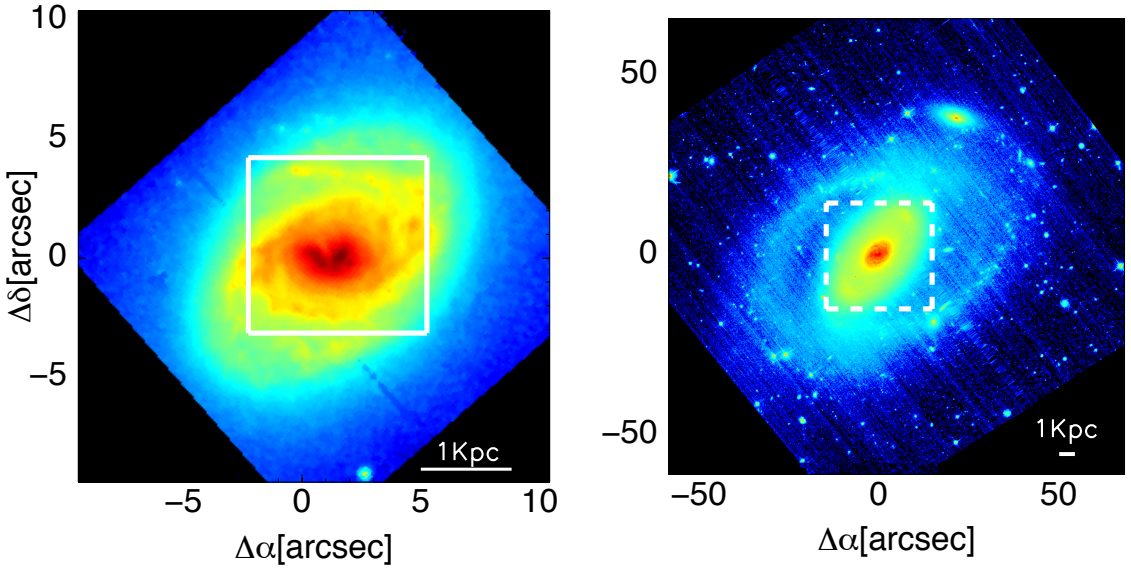

FIGURE 4.1: HST-images of IRAS F11506-3851. The left panel shows the HST-NICMOS (Near-Infrared Camera and Multi-Object Spectrometer) F160W image (Alonso-Herrero et al. 2006), whereas the right panel displays the HST-ACS F814W image (Robishaw et al. 2008). Overlaid are the SINFONI ($9'' \times 9''$, left panel) and VIMOS ($27'' \times 27''$, right panel) FoVs (the latter shown with dashed lines). We note that the FoV covered by the NaD absorption ($20'' \times 17''$) cover only the central region of the VIMOS FoV. See text for details. The white bar shows a linear scale of 1 kpc (corresponding to $4\farcs53$ at the adopted distance, Table 4.1).

This LIRG has an overall spiral structure with extended emission over ~ 30 kpc (as seen in optical and near-IR HST-images in Fig. 4.1) whose main basic properties are summarized in Table 4.1. The Hα emission shows a ring structure with well-defined bright regions, also visible in the near-IR NICMOS-Paα image and Brγ and [Fe II] (Piqueras López et al. 2012). In addition, the molecular hydrogen emission (traced via H_2 (1-0) (S1)) reveals the structure of the nuclear bar which connects both sides of the star-forming ring. No kinematical signature associated to these features are visible in the rotating disk-like velocity field or velocity dispersion maps of the ionized gas. The kinematics of the stars is also dominated by rotation, with large observed velocity amplitudes and centrally peaked velocity dispersion maps (Bellocchi et al. 2013). The mean velocity dispersion in the ionized disk of IRAS F11506-3851 (σ(Hα) $\sim 40\,\mathrm{kms}^{-1}$; Bellocchi et al. 2013) suggests a dynamical status of the ISM intermediate between that found for high-z populations (e.g., $\sigma \sim$ 60-90 kms^{-1}; Förster Schreiber et al. 2011) and that of local spirals ($\sigma \sim$ 15-30 kms^{-1}, Epinat et al. 2010). It hosts a weak AGN that has a minor contribution to the total IR-luminosity ($< 4\%$, Pereira-Santaella et al. 2010).

4.1.1 The 2D maps of the different galaxy's constituents/phases

Figure 4.3, 4.4, and 4.5 show the spatial distribution of the EWs, the velocity fields, and the velocity dispersion maps of the different kinematic components obtained from the NaD doublet, the Hα line, and the CO bands, respectively. Maps for the neutral and ionized gas are obtained following the approach outlined in Sect. 3.2.1 while for the stellar component the method is described in the following section (Sect. 4.1.1.1).

In Fig. 4.3 we also include for reference the continuum (5910-6110 Å) image derived from the VIMOS data cubes. The NaD and Hα velocity maps consider as zero-velocity inferred from Hα at the optical

TABLE 4.1: General properties of IRAS F11506-3851.

Properties	value	References
z	0.01078	de Vaucouleurs et al. (1991)
D_L [Mpc]	46.6[a]	
scale [pc/arcsec]	221[a]	
$\log(L_{IR}/L_\odot)$	11.30[b]	Moshir et al. (1992)
SFR [$M_\odot\,yr^{-1}$]	34[c]	Rodríguez-Zaurín et al. (2011)
M_{dyn} [$M_\odot$]	$(5 \pm 1) \times 10^{10}$	Bellocchi et al. (2013)
Inclination angle	$(37 \pm 3)^\circ$	Bellocchi et al. (2013)
Nuclear Spectral Class.	HII Galaxy	van den Broek et al. (1991)

Notes. [a] Luminosity distance and scale using Edward L. Wright Cosmology calculator (Wright 2006). [b] IR-luminosity (in solar bolometric luminosity and logarithmic units, as in Table 2.1) defined as $L_{IR} = L_{(8-1000\,\mu m)}$ and calculated using the fluxes in the four IRAS bands as given in Sanders et al. (2003). [c] Star formation rate computed from the IR luminosity (integrated over the range 8-1000 μm) following Kennicutt (1998).

nucleus (i.e., 3110 ± 5 kms^{-1}). We assume that the optical and the near-IR nuclei (i.e., intensity peak) are in positional agreement within the spatial resolutions of the two sets of data.

In Table 4.2, we summarize some kinematic parameters of the components traced by the different spectral features used in the present chapter (NaD, Hα, and CO bands). It is important to note that these spectral features trace the properties of different constituents, and their components do not necessarily correspond to each other. As we will discuss through the chapter, the NaD absorption has three contributors at different locations along the line of sight. Specifically, the main NaD component consists of neutral ISM clouds likely forming an irregular disk-like structure and a galactic wind emerging perpendicular to this disk (see Sect. 4.5), while the secondary NaD component is likely associated with the stars. In contrast, the main component of Hα emission probes the ionized gas systemic rotational motions, and the secondary (broad) component seems associated with radial motions. The CO(2-0) bands univocally trace the systemic rotational velocity of the stellar component.

4.1.1.1 The stellar kinematics

We also obtain the stellar kinematics traced by the near-IR CO(2-0) $\lambda\,2.29\,\mu$m and CO(3-1) $\lambda\,2.32\,\mu$m absorption bands, using a maximum likelihood approach – i.e., pPXF (Sect. 3.2.1, Cappellari & Emsellem 2004), to fit a library of stellar templates to our SINFONI data (Fig. 4.2). In particular, we use the library from Winge et al. (2009) whose spectra cover the wavelength range $2.15 - 2.43\,\mu$m with a spectral resolution and sampling of R ~ 5600 and 1 Å pixel^{-1}, respectively (see also Sect. 3.2.1). These spectra are convolved to match the SINFONI resolution before the fitting procedure is applied. We find typical errors for velocity and velocity dispersion, calculated as the 1-σ error, of less than 15 kms^{-1}. Before extracting the kinematics, we perform an adaptive spatial binning using the Voronoi method by Cappellari & Emsellem (2004). As outlined in Piqueras López et al. (2012), with this technique we maximize the S/N over the entire FoV using bins of approximately circular shape in low S/N regions, preserving the spatial resolution of those regions above a minimum S/N threshold (i.e., 25).

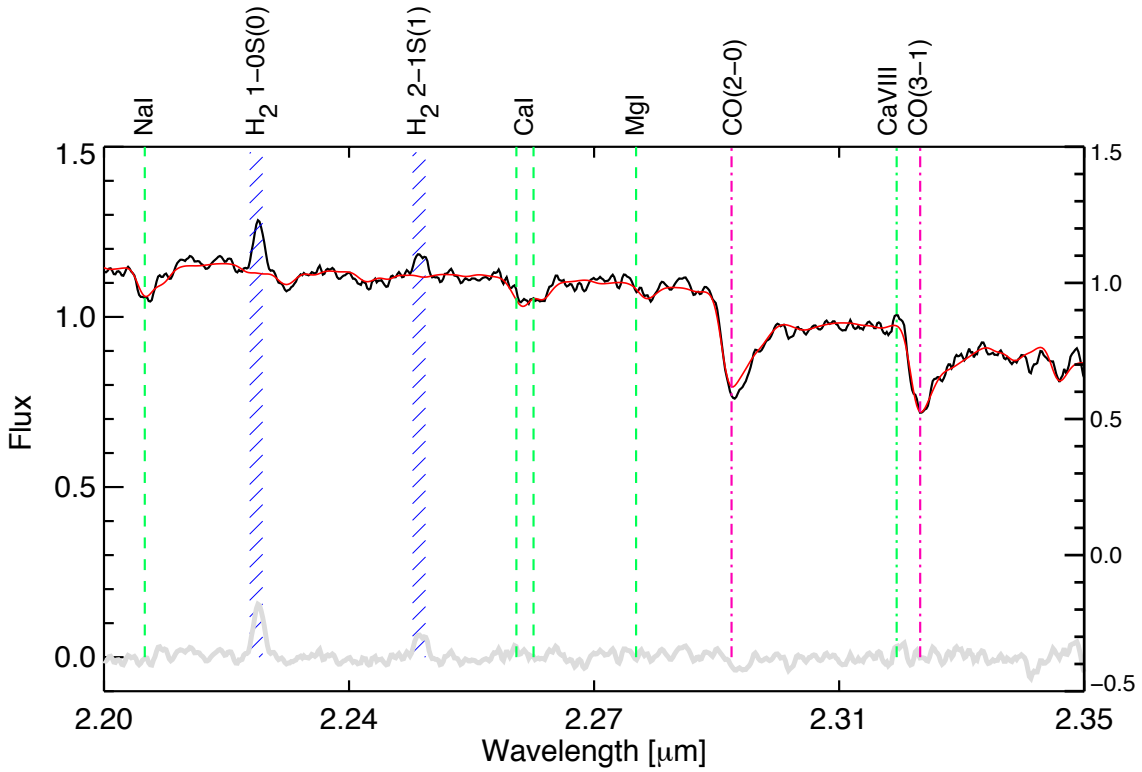

FIGURE 4.2: The near-IR normalized spectrum (black) from the central bin (with S/N ~ 27) of IRAS F11506-3851 with overlaid its best-fitting template spectrum derived with the pPXF approach (Sect. 4.1.1.1) is shown (red line; fit residuals are shown in gray). The location of the wavelength bands masked during the fitting are marked in dark blue. The most relevant spectral features are labeled at the top and marked with a dashed green line, while the CO bands are marked with a magenta dotted-point line. The residuals from this process are low, typically within -0.1 and 0.2.

TABLE 4.2: Main kinematic properties of the different constituents/phases of IRAS F11506-2851.

Constituent/ Phase	Tracer	Component (structure)	ΔV^{a} kms^{-1}	σ_c^{b} kms^{-1}	σ^{c} kms^{-1}	PA^{d} degree
Stars	CO(2-0)	main (disk)	188 ± 11	136 ± 20	78 ± 16	139
	NaD	secondary (disk)	150 ± 15	152 ± 31	82 ± 31	127
Ionized Gas	Hα	main / narrow (disk)	203 (202) ± 4	95 ± 4	45 (44) ± 10	135
		secondary /broad	145 ± 12	...	74 ± 5	60
Neutral Gas	NaD	main (disk)	83 (80)± 12	127 ± 5	84 (83) ± 10	129
		main (outflow)	-64 ± 20	...	98 ± 10	45

Notes. [a] observed velocity amplitude; [b] nuclear velocity dispersion (σ_c), [c] mean velocity dispersion (σ), and [d] position angle of the major kinematic axis. For the main-NaD and -Hα components, the values in brackets are derived over the same FoV as those for the CO (i.e., within a radius of R ≤ 1.1 kpc).

4.2 Stellar and ionized gas kinematics and dynamic structure

The velocity fields of the ionized gas and stars, as traced by the Hα (narrow component) and the CO(2-0) line (Figures 4.4 and 4.5, respectively), present point-antisymmetric velocity patterns consistent with large, kpc-scale ordered rotational motions (e.g., rotating disks). The ionized gas major kinematic axis is well aligned with that of the stars, and both are in turn coincident within uncertainties with the photometric axis as seen in the HST images (Fig. 4.1), with PA ~ 135° ± 5°. The position-velocity

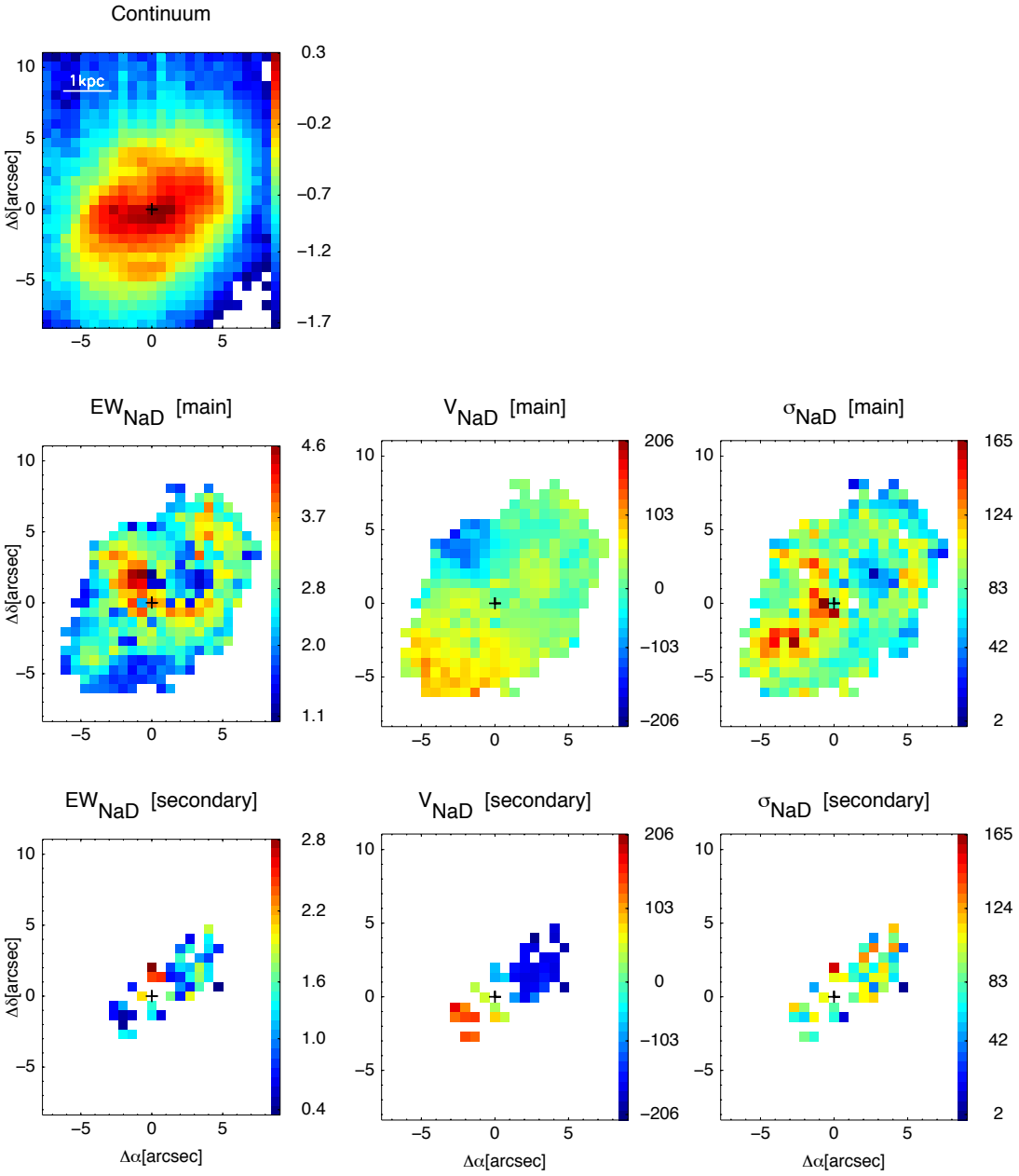

FIGURE 4.3: Neutral gas maps as derived from the NaD absorption line profiles. *First row:* optical continuum image (represented in logarithmic scale and in units of 10^{-16} erg s^{-1} cm^{-2}) obtained from the mean of the line-free continuum nearby the doublet in a 100 Å restframe-wavelength range. *Second row:* the equivalent width map for the λ5890 line, velocity field, and velocity dispersion map for the main component. *Third row:* the same as the second row but for the secondary component. EWs maps are in Å, while the kinematic maps are in kms^{-1}. The cross marks the galaxy nucleus.

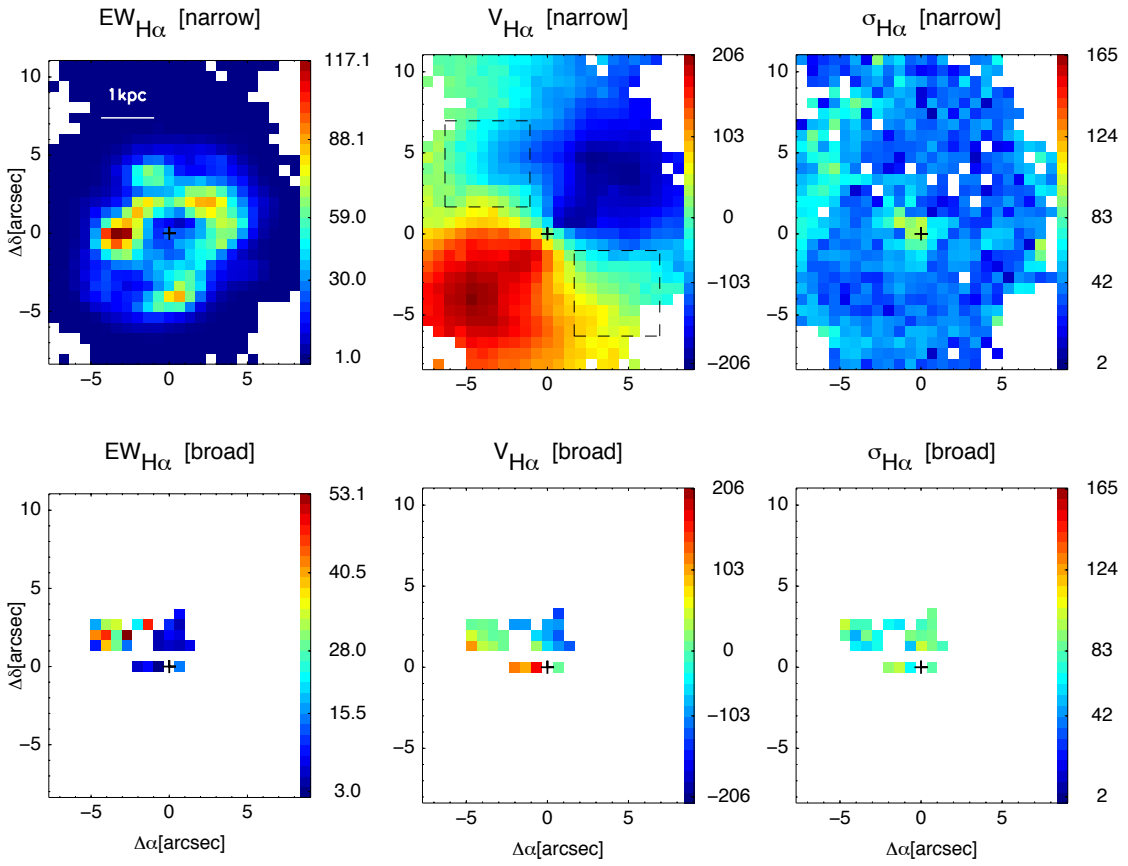

FIGURE 4.4: Ionized gas maps as derived from the Hα emission line profiles. *First row:* the equivalent width map, velocity field, and velocity dispersion map of the main (narrow) Hα omponent. *Second row:* the same as the first row but for the secondary (broad) component. EWs maps are in Å, while the kinematic maps are in kms^{-1}. We note that these maps have been zoomed-in for consistency with the NaD maps. The cross marks the galaxy nucleus, as in Fig. 4.3. The black dashed boxes in the velocity map (narrow component) mark the regions where the integrated spectra are obtained and analyzed (see Sect. 4.5).

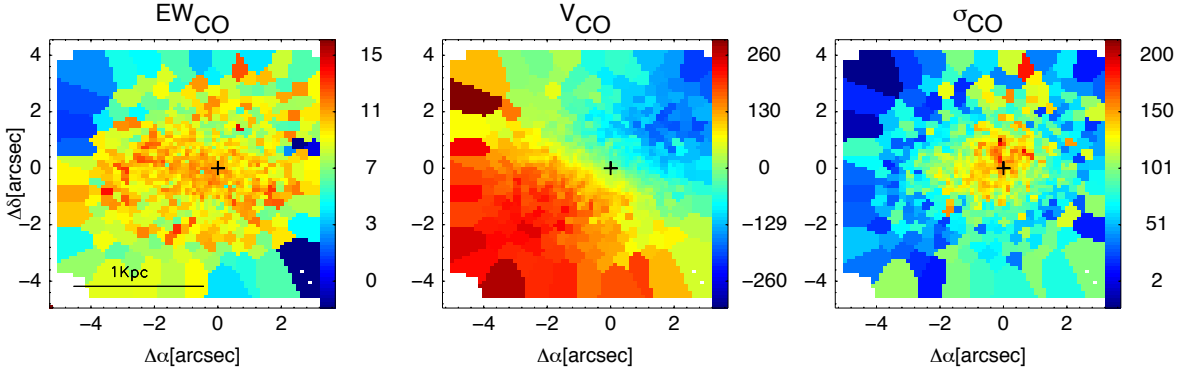

FIGURE 4.5: From left to right: equivalent width given in Å, velocity field and velocity dispersion maps, represented in units of kms^{-1}, of the stellar component in IRAS F11506-2851 as traced by the CO(2-0) IR-absorption (Piqueras López et al. in prep). The cross marks the nucleus (see Sect. 4.3). As mentioned in Sect. 4.1.1.1, data were binned using the adaptive Voronoi 2D-binning method, developed by Cappellari & Emsellem (2004). We note that the ring-like structure with height Hα-EWs (Fig. 4.4) is absent in the EW(CO) map.

diagram (PV diagram, Fig. 4.6) highlights that the stars and the ionized gas have similar rotation, although the latter has a slightly larger amplitude[1] (i.e., $\Delta V(H\alpha) = 203 \pm 4$ kms^{-1} vs. $\Delta V(CO) = 188 \pm 11$ kms^{-1}). It is interesting to mention that the observed star forming circumnuclear ring structure (R $\sim$ 0.7 kpc) identified by the large Hα-EWs (Fig. 4.4) follows the global ordered motions since no kinematic asymmetries at the ring's position are observed in the Hαvelocity map.

As expected for a rotating disk, the Hα-velocity dispersion map shows a centrally peaked pattern with its maximum value (i.e., $\sigma_c(H\alpha) = 95 \pm 4$ kms^{-1}) in positional agreement within uncertainties with the nucleus. The extra-nuclear (R $\geq$ 0.3 kpc) mean velocity dispersion (i.e., 45 ± 10 kms^{-1}) is significantly larger than that found in less active local star forming spirals (e.g., GHASP survey, $\sigma \sim 24$ kms^{-1}; Epinat et al. 2010). Although this value is not as large as those found at high-z ($\sigma \sim$ 60-90 kms^{-1}; Förster Schreiber et al. 2011), it indicates that the ionized disk is thicker than in normal spirals. Thick disks seem common in (U)LIRGs as discussed in Bellocchi et al. (2013). In addition to a relatively large mean value, the ionized gas σ-map also reveals the presence of some large-scale extranuclear regions towards the NE (R $\geq$ 1 kpc, PA from 0° to -110°) with values clearly above the average ($\sigma \sim$ 50-100 kms^{-1}). These can be explained by an increased turbulence or by the presence of an extra non-rotational component in these regions (see Sect. 4.5 for details).

Similarly to the ionized gas, the stars exhibit a centrally peaked velocity dispersion map (Fig. 4.5c), but the nuclear (R < 0.3 kpc) velocity dispersion is slightly larger than that of the ionized gas (136 ± 20 vs. 95 ± 4 kms^{-1}). On the one hand, these findings support the idea that the stellar and ionized gas central velocity dispersions are dominated by the gravitational potential of the galaxy (i.e., its mass). On the other hand, the substantially large stellar extra-nuclear, within 0.3 < R < 2 kpc, mean velocity dispersion value (i.e., 78 ± 16 kms^{-1}), indicates an extra-dynamical support for stars with respect to the already turbulent ionized gas disk. The low rotational support of the stellar disk with respect to that of the ionized gas can also be drawn from the observed (i.e., no inclination corrected) velocity-to-velocity dispersion (V/σ) ratio, calculated as the ratio between the amplitude and the mean velocity dispersion across the disk. Specifically, for stars this ratio (i.e., 2.4) indicates a larger dispersion component while that of the ionized gas (i.e., 4.5) is evidence of a rotation-dominated kinematics.

Assuming, as in Cresci et al. (2009), that the stars and the ionized gas are distributed in thin rotating disks, the scale height of the disks (h_z) can be derived as (Binney & Tremaine 2008):

$$h_z = \frac{\sigma^2 \times R}{V(R)^2}. \tag{4.1}$$

Considering the projected semi-amplitude (V(R)) and the mean velocity dispersion[2] across the galaxy disk (i.e., σ) for the stars and the ionized gas, heights of 125 and 35 parsecs are obtained. These heights were obtained at a distance $R = 2$ kpc from the nucleus, which is the radius at which the ionized gas and the stellar rotation curves flatten (as seen in Fig. 4.6).

In summary, the stars and the ionized gas nearly co-rotate. Their kinematics are consistent with the picture of a (mainly) rotationally supported ionized gas disk of about 35 pc (half thickness) embedded

[1]The velocity amplitudes are obtained as half the peak-to-peak velocity difference within a radius of ~ 1.1 kpc on either side of the galaxy.

[2]This choice implicitly assumes that the velocity dispersion is mainly due to the gravitational potential of the galaxy rather than to turbulence. Therefore, these estimates of heights represent upper limits.

in a thicker and dynamically hotter stellar disk of about 125 pc. The ionized gas shows a relatively high turbulence compared with normal spirals of lower SFR, but it is not as high as that found at high-z.

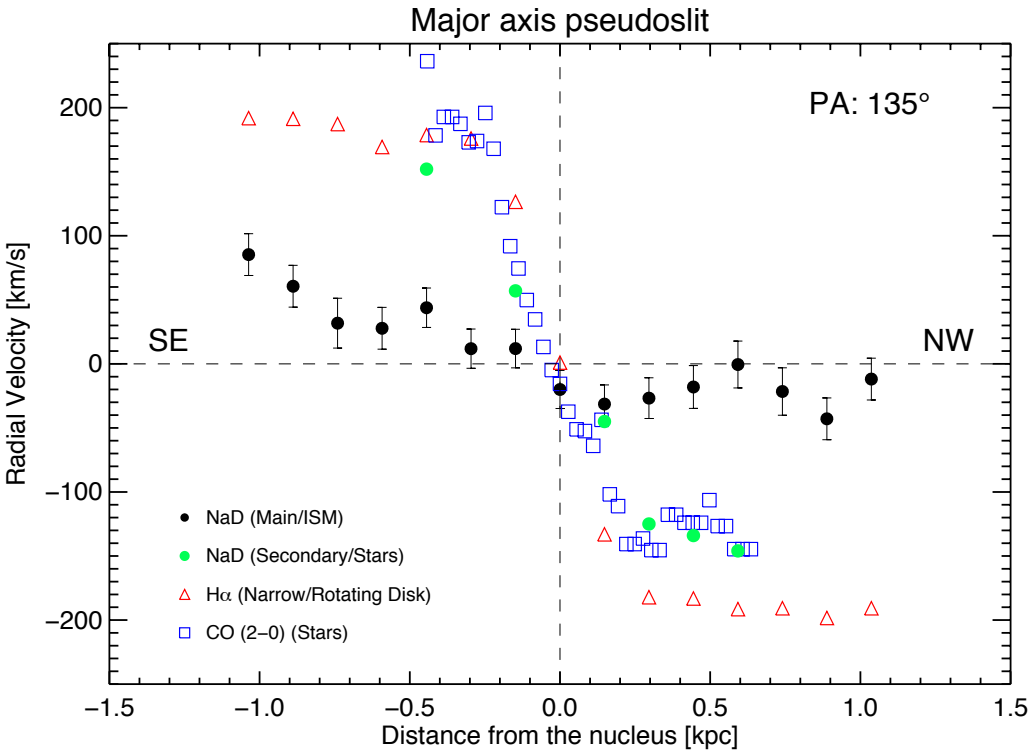

FIGURE 4.6: PV diagram along the major axis (PA ∼ 135°) for different tracers including NaD (the black and green circles indicate the main and the secondary components, respectively, see Sect. 4.1.1), narrow Hα (red triangles), and CO(2-0)(blue squares) data. Error bars are not displayed for the ionized gas, stars, and the NaD secondary component speeds since they are, typically, less than 15 kms^{-1}, therefore smaller than the corresponding symbols. We note that we did not include the PV curve for the Hα-broad component since it is not observed along the major kinematic axis and it is likely tracing non-circular motions (Sect. 4.5).

4.3 The interstellar origin of most of NaD absorption: disentangling the stellar contribution

As mentioned in Sect. 3.1, the NaD doublet originates in clouds of warm neutral gas (i.e., interstellar absorption) and in late-type stars (e.g., K-type giants, Jacoby et al. 1984). Therefore, as a first step towards interpreting this feature, we need to determine the respective roles of these two potential contributors (i.e., stars, and neutral gas). One method for evaluating the global stellar-NaD contribution consists in fitting a stellar spectra to our data. As this approach requires a relatively high S/N, we first generate spatially integrated spectra following the S/N optimization method described in Rosales-Ortega et al. (2012) (see also Sect. 3.2). We then use the pPXF method (Cappellari & Emsellem 2004) with the Indo-U.S. stellar library (Valdes et al. 2004) to produce a model spectrum that matches the observed stellar continuum (see also Sect. 3.2.1), after masking known gas emission lines and a ∼ 30 Å region centered in the NaD feature. The result of this approach is a model that in general reproduces accurately the continuum shape (as displayed in Fig. 4.7). However, the (purely stellar) modeled NaD

profile leaves a strong residual when compared with the data (insert in Fig. 4.7). Specifically, the modeled stellar-NaD spectra has $EW_{5890} = (1.1 \pm 0.2)$ Å, which correspond to only a small fraction ($\sim 1/3$) of the total observed absorption, suggesting that it is mainly ($\sim 2/3$) interstellar in origin[3].

The stellar continuum fitting method described above cannot be applied on a spaxel-by-spaxel basis, as the individual spectra lack the required S/N. However, the spectral fitting decomposition described in Sect. 3.3.1.1 suggests that the main NaD component is due to neutral gas absorption, while the secondary component is associated with the stars. On the one hand, the EW-map for the main component (Fig. 4.3) has relatively large values (typically ≥ 1.5 Å) and it exhibits a patchy and off-centered morphology that contrasts with the one for the continuum (Fig. 4.3). In addition, the slow rotating velocity field and the off-centered velocity dispersion map associated with this component significantly differ from those for the stars (see Fig. 4.5). On the other hand, the secondary component of NaD has a velocity field (Fig. 4.3) that closely follows that of the stars (Fig. 4.5), its nuclear and mean line-width are in good agreement with those for the CO(2-0) (see Table 2), and its mean EW (i.e., 1.2 ± 0.5 Å) is consistent with a stellar origin.

In summary, the application of the stellar-continuum modeling approach to the integrated spectrum indicates that most ($\sim 2/3$) of the NaD absorption in IRAS F11506-2851 is interstellar in origin, although there is a significant contribution ($\sim 1/3$) due to the stars. This is also supported by the spaxel-by-spaxel spectral fitting decomposition, according to which we have been able to disentangle the 2D structural and kinematic properties of two kinematically distinct components. While one of these components dominates the absorption and is likely tracing the neutral gas in the ISM, the secondary weak component has properties fully consistent with a stellar origin.

4.4 Morphology, kinematics and dynamical support of the neutral ISM

As discussed in the previous section, the neutral gas is traced by the main component of the NaD doublet. Its EW-map (Fig. 4.3) reveals relatively strong absorption (i.e., NaD-EWs of 2.5-4.5 Å) at projected distances of $R \sim 0.6$-1.2 kpc from the nucleus and it has an irregular and patchy morphology, which is unrelated to that of the optical continuum (Fig. 4.3).

The overall neutral gas velocity field (Fig. 4.3) lacks the typical pattern of a rotation dominated system. The deviations from an ideal rotating disk include poorly defined kinematic axes, a small velocity amplitude (i.e., 83 ± 12 kms^{-1}), and an asymmetric global structure with respect to the galaxy nucleus[4]. Moreover, contrary to what it is expected for a rotation-dominated gas disk, velocities strongly blueshifted with respect to the systemic (by up to -154 kms^{-1}) are observed along the minor axis towards the NE. While in Sect. 4.5 we give an explanation for the kinematic properties found along the semi-minor axis, in this section we will focus on the general properties of the kinematic maps of the main NaD component excluding that particular region.

Therefore, leaving aside the region with large blueshifted velocities, the velocity field of the main component of NaD (i.e., neutral gas) has a pattern consistent with a slowly rotating (irregular) disk. Its

[3]This determination is in excellent agreement with the EW(NaD) derived from the relation between the stellar MgIb λ 5174 and NaD (i.e., EW(NaD) ~ 0.75 EW(MgIb), Heckman et al. 2000), considering the median value of EW(MgIb) for the HII-selected luminous IRAS-galaxies sample by Kim et al. (1998) (i.e., 1.1 Å).

[4]Part of the irregularities observed in NaD velocity map are a consequence of its relatively small amplitude, which magnifies the effects of the errors in the overall structure of the map.

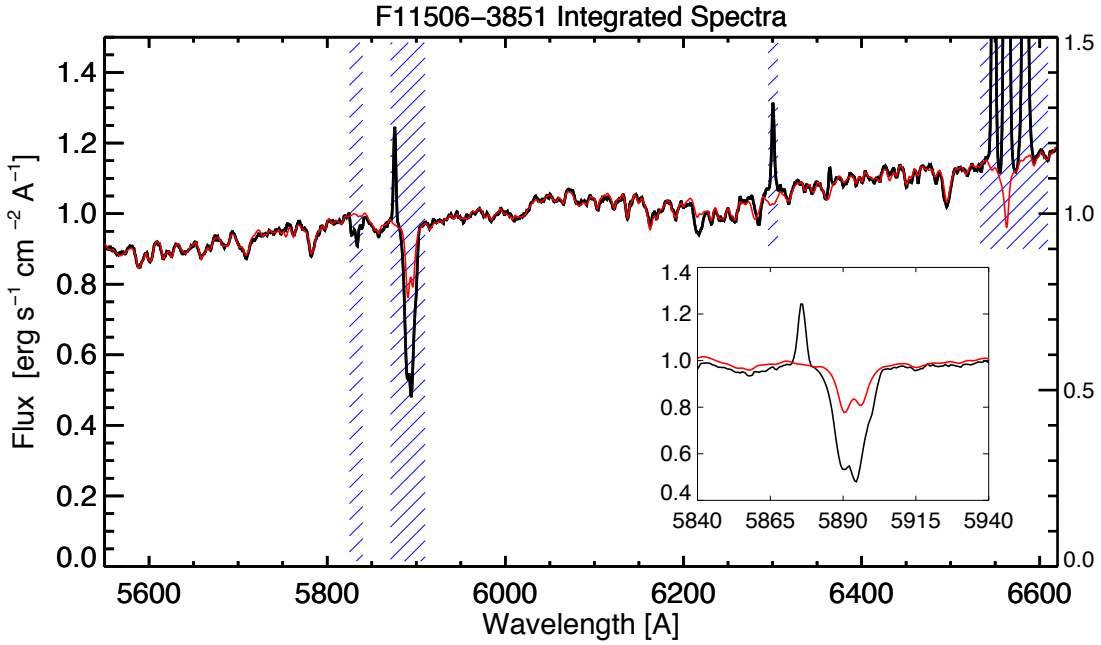

FIGURE 4.7: The integrated spectra (black) and its best-fit stellar spectra (red) obtained with the pPXF approach (Sect. 4.3) are shown. The gas emission wavelength bands masked in the fitting are marked in dark blue. The insert highlights the NaD region with a zoomed view. The lack of good agreement in the doublet feature indicates that the NaD extra-absorption is interstellar in origin.

comparison with the Hα velocity field (Fig. 4.4) indicates that the neutral disk lags in velocity compared to the ionized gas. The neutral and warm gas components have significantly different amplitudes (i.e., 83 vs. 188 kms^{-1}, respectively; Fig. 4.6), indicating that they are not kinematically coupled. Part of the above mentioned velocity-discrepancies may be due to the different location of these ISM phases. While the Hα emission is associated with dense gas regions, the neutral gas NaD clouds could be located arbitrarily between the observer and the background light (the stellar disk) along the line of sight. A different neutral gas 3D spatial distribution with respect to that of the ionized ISM and stars can be drawn from the comparison of their velocity dispersion maps. In Fig. 4.3, it is clear that the neutral gas dispersion values are larger than those measured for the ionized gas (typically by more than 50 kms^{-1} excluding the innermost region) indicating that the neutral gas is located in a thicker disk. The different pattern between the velocity dispersion maps for the stars and the neutral gas also suggests that they have different spatial distributions.

We derive the scale height (h_z) of the neutral disk adopting the thick disk model outlined in Cresci et al. (2009) (see also Genzel et al. 2008). This differs from the thin disk (Equation 4.1) as the h_z scales with the mean velocity dispersion across the disk (σ) and the rotational velocity ($\Delta V(R)$, i.e., the de projected semi-amplitude) at radius R (i.e., 2 kpc as in Sect. 4.2):

$$h_z = \frac{\sigma \times R}{V(R)}. \tag{4.2}$$

In this case, the height scale for the neutral gas is $h_z \sim 700$ pc, confirming that the neutral gas is distributed in a thick disk. However, this estimate represents a lower limit (by a factor of 2 or more) given the potential contribution of unresolved random motion that could be supporting part of the mass and thickening the disk. We note that the ISM absorption features studied here only probe the gas

clouds in front of the stars. Therefore, even if a small scale-height neutral disk is present, it would not be detected because many of the stars, contributing to the continuum light, are in front of it.
In IRAS F11506-2851, the comparison of the V/σ ratios for the different ISM phases and the stars indicates different levels of dynamical support. The neutral gas has a dispersion-dominated kinematics (V/$\sigma \sim 1$) while the stars and the ionized gas ($V/\sigma = 2.4$ and 4.5, respectively) have an increasing rotational component (e.g., disks). The low rotational support for the neutral gas is compensated by the large random motions observed, and it implies that the neutral gas is distributed in a thick disk as observed.
Summarizing, the NaD-EW map suggests a rather irregular and complex distribution of the neutral gas. Excluding a region of strong blueshifted velocities along the semi-minor axis, the overall neutral gas kinematics can be interpreted as a slow rotating disk that lags in velocity to those of the ionized gas and stars, and it is dominated by random motions as indicated by the small V/σ value. Therefore, neutral gas is distributed in a thick and dynamically hot disk, in contrast to the stars and the ionized gas, which are confined to disks with lower height scales mainly supported by rotation.

4.5 The wind kinematics and geometry

In a purely rotating disk, systemic velocities are expected along the minor axis. Contrary to this, the neutral gas velocity field (Fig. 4.3) shows strong blueshifted velocities with respect to the systemic of up to -154 ± 20 kms^{-1} along the NE semi-minor axis. This region of blueshifted velocities is triangular in shape, and its associated spectra indicate broad ($\sigma = 98 \pm 10$ kms^{-1}), and intense (EW ~ 3-4 Å) profiles[5]. Since the velocity dispersion of the individual neutral clouds is typically ~ 15 kms^{-1} (Schwartz & Martin 2004), we are likely observing the combined effect of many individual clouds which, in addition of having a relatively large cloud-to-cloud relative velocity, share a common global motion. The observed neutral gas kinematics and spatial distribution of this blueshifted region are well explained by a conical outflow that emerges perpendicular to the disk from the nuclear region suggesting a bipolar geometry – i.e., a starburst-driven GW scenario (Heckman et al. 1987; Veilleux et al. 2005). Figure 4.8 sketches the inferred geometry for the wind. In this scenario, the GW should only be detected in NaD in the approaching cone as the receding one is not illuminated by background stars. This expectation is fully confirmed by the data, as no traces for a SW cone counterpart are observed. The projection of the approaching cone covers ~ 0.9 kpc^2 (Fig. 4.3) and it subtends a narrow angle on the sky of ~ 45° (as seen from the wind's origin), suggesting a collimated structure for the wind. This opening angle agrees reasonably well with previous values found in SFGs (Veilleux et al. 2005), and in particular to those considered to be typical in LIRGs (~ 65°, Rupke et al. 2005b).
From the (deprojected) velocity distribution within the wind a mean velocity of -97 kms^{-1} is obtained. Therefore, half of the neutral gas is travelling at typical velocities of local starburst-driven GWs in LIRGs (100-200 kms^{-1}; Heckman et al. 2000; Rupke et al. 2005c) reaching a mean maximum velocity (defined as the central velocity plus one half of its FWHM; Rupke & Veilleux 2011) of -146 kms^{-1}. The fate of the neutral outflowing gas is discussed further in Sect. 4.6, with a comparison between the wind speeds and the galaxy's escape velocity.

[5]The NaD-EWs associated with the outflow region should be considered upper limits, since we are unable to fit the (weak) underlying component of the NaD likely associated with the thick neutral gas disk (Sect. 4.4).

There are some indications of the presence of an ionized counterpart of the neutral wind. The observed Hα-line profiles show the presence of a secondary kinematic component (see Sect. 4.1.1) preferentially in the NE sector. This extra component is sometimes clearly seen near the border of the projection of the outflowing neutral gas cone seen in NaD (Fig. 4.3). In addition the kinematic maps of the narrow-Hα component (Fig. 4.4) show some characteristics that may be related to the wind. First, while the minor kinematic axis is well aligned towards the SW, the NE counterpart (slightly) bends towards blue velocities, suggesting modest radial (e.g., outflowing) motions (Fig. 4.4).

To look into this feature in greater detail, we have integrated the observed Hα-spectra within two symmetrical regions of 1.2×1.2 kpc along the minor kinematic axis (black dashed boxes in Fig. 4.4). The integrated spectrum towards the NE clearly shows a blueshifted component (-99 $\pm$ 5 kms^{-1}) which is not observed in the SW counterpart (Fig. 4.9). Second, at a radius R $\geq$ 1 kpc (PA = 10°-110°) the velocity dispersion map (Fig. 4.4) shows an increment of more than 15 kms^{-1}, compared to the typical value of (45 $\pm$ 10) kms^{-1} found elsewhere in the disk (excluding the nucleus). Although the origin of these increased values is unclear, their distribution towards the NE suggests that they may be related to the wind. A consistent scenario is that the ionized gas mainly traces the outer edge of the GW rather than its inner parts, probably because the Hα emission is weighted towards the over-pressured high density gas regions.

The spatial information provided by the present IFS data also allows us to constrain the direction of the rotation of the galaxy. In general, even for well-defined disks seen in projection like IRAS F11506-2851 (Fig. 4.1), the velocity field is not sufficient to determine the direction of the rotation. In that case, if a spiral structure is observed, one has to assume if it is leading or trailing to fix the direction of rotation and, therefore, the orientation of the disk (i.e., its near side). However, because the cool neutral gas is identified in absorption against the stellar continuum, in the present case, one can determine that the NE edge is the far side of the disk. This fixes the rotation direction of the disk (clockwise) and, therefore, the spiral arms observed in the HST-NICMOS near-IR image (Fig. 4.1) are trailing, as illustrated in Fig. 4.8.

In summary, our IFS data show evidence of a neutral wind in IRAS F11506-285 and have also allowed us to constrain its geometry (extension and opening angle) and kinematic properties. These suggest the presence of a conical outflow emerging from the nuclear region perpendicular to the disk at mean velocities of $\sim$ 100 kms^{-1}. In addition, there is evidence of the presence of an ionized outflow that partially overlaps with the wind detected in NaD. Recent ALMA observations (Pereira Santaella 2016, in preparation) have confirmed the presence of the outflow in molecular gas (via CO(1-0) emission line) with an excellent consistency with that of neutral gas in this work. The particular geometry of the neutral gas wind has in turn allowed us to fix the orientation and rotation direction of the disk(s).

4.6 Outflow mass rate and the ISM / IGM metal enrichment

Of particular interest is measuring the mass of gas being expelled by the wind in its cold phases (e.g., neutral) since the evacuation of this gas may be responsible for quenching the SF. In order to estimate the mass, the mass loss rate, and the efficiency of the wind, we apply a thin-shell free wind model (FW; Heckman et al. 2000; Rupke et al. 2002, 2005a,c), considering that the mass outflow rate and the velocities are independent of radius. The wind we observe is clearly not a thin shell, but rather a filled

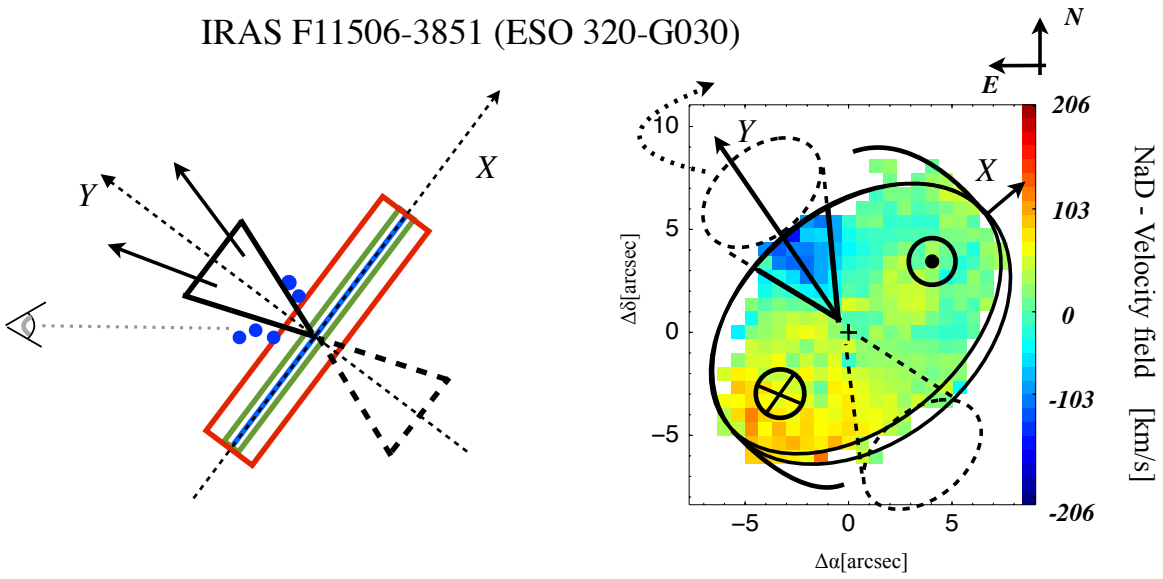

FIGURE 4.8: Geometric model of a conical wind perpendicular to the galaxy disk. In both images, the black lines represent the wind cones. The receding cone (invisible for the observer in NaD, because of the lack of background light – i.e., the stellar disk) is displayed with dashed lines. The letters *X* and *Y* mark the major and minor axes of the galaxy. *Left:* the red, green, and blue boxes represent, respectively, the neutral, stellar, and ionized disks (see Sections 4.2 and 4.4). Blue filled circles indicate the wind ionized phase (see Sect. 4.5 for details). *Right:* sketch of the bipolar GW and the spiral structure as derived using HST-ACS, VIMOS and SINFONI observations (Figures 4.1, 4.3, 4.4, and 4.5) overlaid to the NaD velocity field (Fig. 4.3. The outer tip of the trailing arms points in the direction opposite to galactic rotation (clockwise, as indicated by the dotted arrow). The symbols ⊗ and ⊙ indicate the receding and approaching sides of the disk rotation (as traced by Hα and CO(2-0)). The closest part of the disk is at SW (see Sect. 4.5 for details). The insert with letters *N* and *E* indicate: the north and the east, with respect to the detector reference frame.

cone. Nevertheless, it can be considered as a series of thin shells and since we can spatially resolve it, the thin-shell formalism is still valid. We recall that the thin-shell FW model has, however, its own drawbacks: effects due to Rayleigh-Taylor instabilities are not taken into account when calculating the wind dynamics.

Some physical models (e.g., Rupke et al. 2002, 2005a,b,c) describe in detail the outflowing material (its mass, mass rate and energy) with equations written in terms of measurable quantities, like the gas optical depth and column density. We employ a different approach to estimate the properties (e.g., column density and mass) of the cold gas entrained in the wind. The column density is calculated for all the spaxels within the wind using the linear relation between the N_{HI} and the color excess (E_{B-V}),derived by Bohlin et al. (1978) as:

$$N_{\rm H} = 4.8 \times E_{B-V} \times 10^{21} cm^{-2}. \tag{4.3}$$

The mean wind column density is $(7.7 \pm 0.4) \times 10^{21}$ cm^{-2}, which is consistent with previous estimates for winds in dwarf starbursts and low-z LIRGs (Rupke et al. 2005c). The color excess has been, in turn, derived directly from the present NaD-EW map (Fig. 4.3). We made use of the relation by Turatto et al. (2003), derived from observations of SNe in highly reddened objects:

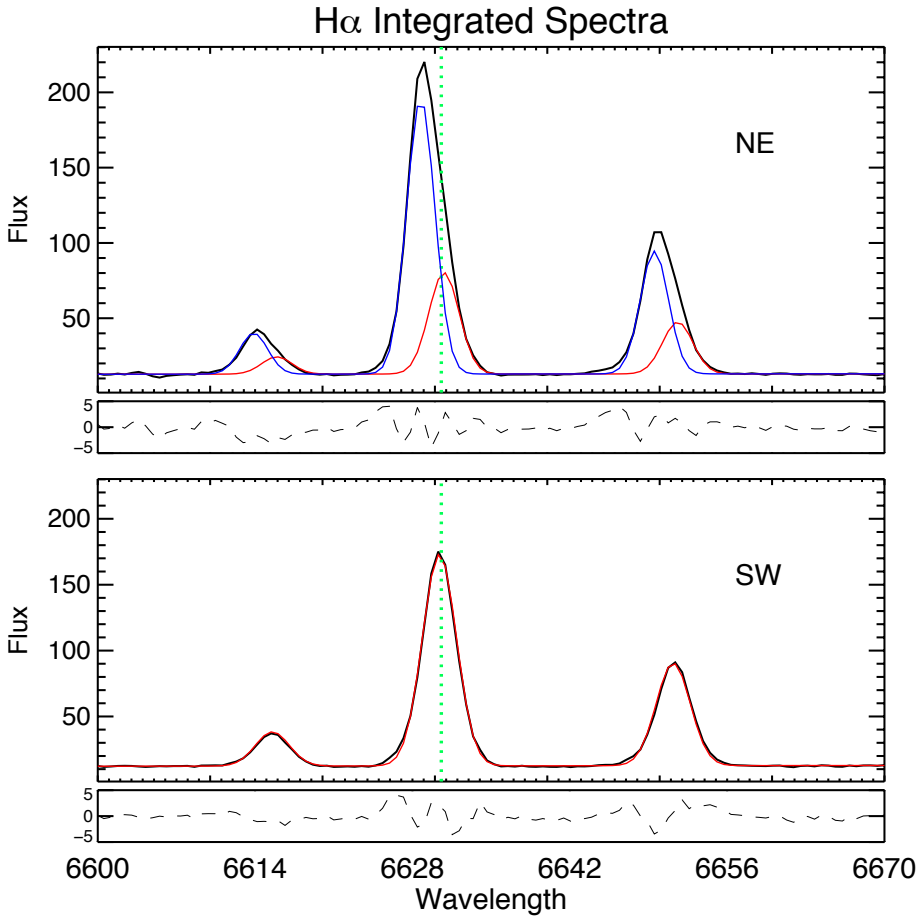

FIGURE 4.9: The Hα line-profiles integrated spectra (black) in two different regions of 1.2×1.2 kpc along the minor axis (Fig. 4.4), respectively, towards the NE (top) and the SW (bottom). Below, the residuals (i.e., data - model) are also presented. Since the asymmetry of the observed profile the NE spectrum, two components are needed to properly fit the line profile. The narrow component is shown in red in both panels, while the broad one (likely due to outflowing gas) is shown in blue only in the NE spectrum (top). The systemic velocity is shown in green with a vertical dashed line, as reference.

$$E_{B-V} = -0.04 + 0.51 \times EW(NaD) \tag{4.4}$$

Veilleux et al. (1995) showed that the correlation between the reddening and the strength of the NaD feature is stronger among HII galaxies like IRAS F11506-2851 than in LINERs and Seyfert 2 objects. In IRAS F11506-2851, the dust embedded in the wind produces an E_{B-V} in the range 0.6-2.2[6]. The above estimate of N_H is very simplistic and assumes a dust-to-gas ratio observed in our galaxy (~ 150; Wilson et al. 2008). However, in (U)LIRGs this ratio is larger (typically ~ 215; Wilson et al. 2008) and local heating (produced by high-velocity shocks) may lead to the destruction of dust grains lowering the NaD depletion level and, hence, the dust-to-gas ratio. We note that assuming solar NaD abundances (Heckman et al. 2000) and according to the systematic uncertainties in the E_{B-V}-N_H relation (grain

[6]Piqueras López et al. (2013), derived the 2D internal extinction structure (i.e., A_V map) for F11506-2851 using the near-IR Brγ/Brδ line ratio. However, the absence of the Brδ line in the inner part (within a radius of 0.″63) precludes the use of the Brγ/Brδ ratio for a reliable estimation of the reddening. The different spatial distribution of the warm and neutral gas phases (see Section 4.3) adds further uncertainty when using the ratio Brγ/Brδ for estimating the E_{B-V} in the outer parts of the outflow (i.e., neutral gas located off the disk).

depletion and ionization factor), the derived column density is uncertain to a factor of 1.5.

As in Shih & Rupke (2010); Rupke & Veilleux (2011, 2013), we used our IFS maps to infer some physical and kinematic properties associated with the wind (e.g., spatial distribution and velocities). We first estimated the total mass (M_w) of neutral gas contained in the observed cone. The neutral gas mass in each wind's element covered by a spaxel k vary accordingly with its deprojected distance from the nucleus ($R_{w,k}$) and the HI column density ($N_{H,k}$) at that location, weighted for its opening angle ($C_{\Omega,k}$). For simplicity, we have restricted ourselves to a constant covering factor (i.e., independent from the velocity) and assume the median value, i.e., $C_f = 0.37$, observed in LIRGs by Rupke et al. (2005c). Therefore the wind mass is:

$$M_w = 5.6 \times 10^8 \sum_{k=1}^{N} \left(\frac{C_{\Omega,k}}{0.4} C_f\right) \left(\frac{R_{w,k}^2}{100\,kpc^2}\right) \left(\frac{N_{H,k}}{10^{21} cm^{-2}}\right) M_\odot. \quad (4.5)$$

The amount of the neutral gas mass expelled by the wind in IRAS F11506-2851 is $M_w = (8.5 \pm 0.9)$ in log [$M/M_\odot$] units, which is within the typical values found in (U)LIRGs (Veilleux et al. 2005). We note that according to the systematic uncertainties in the calculation of the column density, M_w is uncertain to at least a factor of 1.5. As GWs are typically bi-conical in shape, and we are probing only the approaching cone. Assuming a similar ISM distribution on both sides of the galaxy a better estimate to the total mass expelled by the wind would be $M_w \sim 8.8$ log [$M/M_\odot$] (a factor two higher than our estimation). The total mass[7] of neutral gas in IRAS F11506-2851, as determined by single-dish radio observations of the H I 21cm line (Courtois et al. 2011), is $M_{HI} = 2.7 \times 10^9$ $M_\odot$. Therefore, at least $\sim 10\%$ of the neutral gas in IRAS F11506-3851 is expected to be involved in the wind (which is likely a conservative estimate, given that the NaD wind can only be traced against regions with a strong background continuum).

We then computed the time-averaged outflow rate ($\dot{M}_w$) following Rupke et al. (2005c):

$$\dot{M}_w = 11.5 \times \sum_{k=1}^{N} \left(\frac{C_{\Omega,k}}{0.4} C_f\right) \left(\frac{R_{w,k}}{10\,kpc}\right) \left(\frac{N_{H,k}}{10^{21} cm^{-2}}\right) \left(\frac{V_{w,k}}{200 kms^{-1}}\right) M_\odot/yr. \quad (4.6)$$

The notation follows that of Fig. 4.5, and $V_{w,k}$ corresponds to the deprojected velocity in each spaxel. We permitted every spaxel have its own speeds, since small velocity differences are consistent with projection effects. However, the deviations with respect to a wind with constant velocity (i.e., the median wind speed) are small ($< 15\%$). We estimate that the effects on $\dot{M}_w$ due to the average stellar contribution to the NaD profile[8] over the outflowing region are small ($< 20\%$). We infer a mass loss rate of $\dot{M}_w = 48$ $M_\odot$/yr. The relevance of the GW feedback is quantified using the mass loading parameter (η) defined as the mass outflow rate normalized to the corresponding SFR. For IRAS F11506-2851 we obtained $\eta = 1.4$, indicating that the wind contributes significantly to the exhaustion of the gas

[7] We considered the total mass associated with double-horned H I profile – i.e., the mass within the primary beam of the single-dish Green Bank Telescope observations (Courtois et al. 2011).

[8] In order to estimate this effect the spectra over the outflowing region were "decontaminated" by subtracting the stellar contribution obtained from the continuum fitting to the integrated spectrum (Sect. 4.3) at the spaxel Hα velocity. Hα was preferred to CO as a proxy of the stellar velocity, as it covers a larger FoV, and it was obtained from the same data cube as NaD. Furthermore, the Hα velocity field shows similar overall characteristics as the stellar as presented in Figures 4.4 and 4.5.

reservoir available for the SF. A more detailed analysis considering the actual spatial distribution of SF and the characteristics of the wind inferred from the present IFS data shows a more complex picture, as discussed in Sect. 4.7.

A common way to determine if winds can pollute the IGM is to compare the wind speed with the local escape velocity derived from a gravitational model for the host galaxy. Considering a truncated isothermal sphere, the escape velocity (v_{esc}) is related to the rotation speed (v_{rot}) at a radius r as:

$$v_{esc}(r) = \sqrt{2 \times v_{rot}^2 \times \left[1 + ln\left(\frac{R_{max}}{r}\right)\right]} \tag{4.7}$$

where R_{max} is the truncation radius. We adopt the deprojected stellar rotation velocity (i.e., 235 kms^{-1}) as the rotation velocity, since the stellar dynamics in galaxies represent a sensitive probe of the galactic gravitational potential and $R_{max}/r = 10$ following Rupke et al. (2002), inferring a v_{esc} of ~ 430 kms^{-1}. Since the inclination corrected speeds for the neutral gas clouds driven by the wind range within 30 - 200 kms^{-1} most (all) of the outflowing material will not be able to escape the gravitational potential of the host galaxy. Therefore, although the mass loading factor is about 1.4, the outflowing material will not contribute to the chemical enrichment of the surrounding IGM.

Given that most of the gas entrained in the wind will remain gravitationally bound to the host galaxy, but not virialized, it is expected that this material will fall back onto the galactic disk. This cycle (i.e., the expulsion and the rain-back of gas) could be responsible for the assembly of an extra-planar gas reservoir. This process could be somewhat analogous to that observed with deep observations of H I 21cm line emission in several nearby disk galaxies, where neutral hydrogen gas is deposited into the galaxy's halo environment mainly by stellar feedback (in the most extreme cases out to a few tens of kpc above the main galaxy disk; e.g., Fraternali et al. 2002; Fraternali et al. 2005; Boomsma et al. 2005; Oosterloo et al. 2007; Fraternali & Binney 2008). This extra-planar neutral gas is characterized by slower rotation compared to the galaxy disk (most pronounced at small galactic radii), it can have an asymmetric distribution, and it may contain up to $\sim 10^9$ $M_\odot$ of neutral gas (in some cases up to $\sim 30\%$ of the galaxy's total H I content; see Oosterloo et al. 2007; Boomsma et al. 2008 for examples). Because the wind in IRAS F11506-2851 originates from the nuclear region it may already have a relatively low angular momentum compared to the gas in the ionized thin disk. If NaD can survive the process of expulsion and re-accretion it may perhaps explain our intriguing result that the main NaD component in IRAS F11506-2851 traces a slowly rotating, somewhat asymmetric thick gas disk (Fig. 4.6). Geometrical effects or an over-abundance of NaD in the extra-planar gas may perhaps favor the detection of this slowly rotating thick disk above a potential neutral NaD counterpart in the thin disk (see also Sect. 4.4.)

4.7 The origin of the wind. Witnessing the quenching of the nuclear star formation process?

As already shown in previous sections, the outflow in IRAS F11506-2851 is mostly detected in the neutral gas component of the interstellar medium with a weak indication of the ionized gas counterpart. In addition to this, the apex of the cone-like morphology has been identified with the center (both kinematic and photometric center) of the galaxy. However, while most neutral and ionized gas outflows in (U)LIRGs have been associated with either an intense SF, an AGN, or both, the center of IRAS F11506-2851 does not appear to be undergoing a luminous active phase. On the one hand, the AGN appears to be weak with a low contribution ($<4\%$) to the total luminosity, as estimated from Spitzer/MIPS 24 μm measurements (Pereira-Santaella et al. 2010). On the other hand, the nuclear region is a weak source of ionized gas as traced by both the Hα (Fig. 4.4 and Rodríguez-Zaurín et al. 2011) and Brγ (Piqueras López et al. 2012) emission lines. Specifically, only less than 3 percent of the observed Brγ emission (i.e., SFR) is found in the central 400 x 400 pc region (Piqueras López et al. 2012). In addition, the Hα and the Brγ maps trace a circumnuclear ring of luminous star forming clumps, and a nucleus that appears to be depleted of current SF. This is supported by the relatively strong [Fe II emission (Brγ/[Fe II] ~ 1) indicating the presence of supernovae, and therefore of a recent nuclear starburst with an age in the range of about 6.7-7.5 Myr, according to stellar population models for instantaneous bursts (Leitherer et al. 1999).

In order to check the SNe-scenario as origin of the GW observed in IRAS F11506-2851, we compare the expected energy budget released by the SNe within the wind lifetime (~ 10 Myr [9]) and that of the wind. To predict the nuclear SNe rate we use the [Fe II]-flux measurements (within the inner 400×400 pc, Piqueras López et al. 2013) corrected for the internal extinction[10]. We infer that the nuclear SNe rate is about 2.0×10^{-3} yr^{-1} assuming the [Fe II] flux to SNe rate expression of Alonso-Herrero et al. (2003), derived from the study of M82 and NGC 253 (see Bedregal et al. 2009 for other derivations of SNe rates based on [Fe II]). Since the internal extinction could be underestimated, an upper limit to the SNe rate can be derived from the high angular resolution radio measurements (Baan & Klöckner 2006). For a nuclear luminosity of 8.34×10^{21} W Hz^{-1} at 4.8 GHz, a SNe rate of about 0.2 yr^{-1} is derived applying relations based on M82 radio supernovae (Huang et al. 1994), and evolutionary models of the radio emission in starbursts (Perez-Olea & Colina 1995). Assuming an energy budget of 10^{51} erg for each SNe-event, the total energy injected within the lifetime of the wind is 55.3 - 57.3 in log[E/erg^{-1}] units. The energy of the wind (E_w) is inferred as the sum of the kinetic energy, $v_k^2/2$, and a term, i.e., $3\sigma_k^2/2$, associated with turbulences for all spaxels k where the outflow has been detected, (see Rupke et al. 2005c):

$$E_w = \sum_{k=1}^{N} M_k \times \left(\frac{v_k^2}{2} + \frac{3\sigma_k^2}{2} \right). \quad (4.8)$$

[9] The wind lifetime has been inferred as the ratio between the maximum extent and the mean velocity of the wind (1.2 kpc and 95 kms^{-1}, respectively.

[10] We express the near-IR internal extinction ($A_{[Fe\,II]}$) in terms of the visual extinction A_v (i.e., $A_{[Fe\,II]} = 0.1961 A_v$) by using the extinction law described in Calzetti et al. (2000). In absence of a direct nuclear A_v-measurement, we consider the mean value of 7.8 magnitudes derived by Piqueras López et al. (2013), which is likely a lower limit according to the radial profile measured by these authors).

We derived a total energy of the wind of 56.4 in units of log[E/erg^{-1}], which lies within the range of the total energy injected by the supernovae as derived above. We have previously derived (see Sect. 4.6) an outflowing mass rate in neutral gas of about 48 $M_{\odot}yr^{-1}$, close to the SFR (i.e., 34 $M_{\odot}yr^{-1}$; Table 4.1) derived from the IR-luminosity. Therefore, the overall mass loading (η) factor (i.e., ratio of outflowing gas mass to total SFR) is about 1.4. However, from our VIMOS and SINFONI data it is clear that while the current SF covers an area of several kpc^2 and is distributed in several clumps, the neutral gas outflowing material is confined to a much smaller (< 1 kpc^2) and well-defined region that appears to be associated with the nucleus, where no intense SF is underway. Since the global mass loading factor of the galaxy is close to one (i.e., 1.4), the corresponding local mass loading factor for the nucleus and its associated SF would be much larger than one (i.e., $\eta >> 1$) indicating negative-feedback and therefore the possibility of seeing the quenching of the SF as a result of the combined supernovae and stellar winds. The relatively strong [Fe II] (i.e., presence of stellar populations several Myrs old where massive stars have exploited as SNe) and the weak Brγ (i.e., lack of massive young stellar populations few Myrs old) fluxes, as well as the presence of the wind, suggests that we are witnessing a quenching event in IRAS F11506-2851.

While the scenario above can be qualitatively valid and needs further exploration with higher angular resolution, the overall scenario suggested by our data is far more complex. The nucleus is the strongest warm molecular gas emitting region (Piqueras López et al. 2012) contributing 21% of the total, as traced by the H_2 (1-0) (S1) emission line. The mass of warm molecular gas in the nuclear region can be computed following Dale et al. (2005) as $M_{H2}^{warm} = 5.08 \times F(H_2) \times D_L^2$ where $F(H_2)$ is the extinction corrected H_2 (1-0) (S1) line flux in units of 10^{-16} W m^{-2} and D_L is the luminosity distance in Mpc. For an observed nuclear flux of 1.7×10^{-18} W m^{-2} (Piqueras López et al. 2012), and an extinction corrected flux of 6.8×10^{-18} W m^{-2}, the amount of warm molecular gas in the nuclear region is ~ 750 $M_{\odot}$ corresponding to a total mass in the range 0.75-75 $\times 10^8$ $M_{\odot}$ in cold molecular gas if the range of warm to cold molecular gas ratios observed in starburst galaxies is assumed (Dale et al. 2005). Thus, assuming an efficiency of 10% in the conversion of cold gas into stars, there is enough molecular gas in the nuclear region to form between about 10^7 $M_{\odot}$ and 10^8 $M_{\odot}$ of new stars in future (recurrent) episodes of SF (as seen for a small sample of nearby spirals by Gallagher et al. (2014), even if the nucleus is currently undergoing a quenching phase due to the previous starburst that took place several million years ago.

4.8 Summary and conclusions

On the basis of optical (VIMOS) and near-IR (SINFONI) IFS data we have studied the kinematic and dynamical properties of the stellar component and gas phases (ionized and neutral) in the luminous infraRed Galaxy IRAS F11506-3851 (ESO 320-G030) using as tracers the NaD absorption doublet, Hα, and the CO bands. The conclusions of the present study can be summarized as follows:

1. — *Kinematics and dynamical support for the stars and gas phases (warm and neutral).* The ionized ISM is in a rather turbulent state as indicated by its relatively high velocity dispersion ($\sigma \sim 45$ kms^{-1}), which is intermediate between low-luminosity normal spirals and high-z SFGs. Despite this, the ionized gas is largely dominated by rotation and it is distributed in a dynamically

cold disk as indicated by its large V/σ ratio ($\sim$ 4.5). The stellar velocity field is also dominated by ordered large-scale rotational motions, although it slightly lags in velocity compared to e the ionized gas. The stars have also a larger random velocity component and, therefore, the V/σ ratio (2.4) suggests that the stellar disk has lower rotational support and a larger height scale than the ionized gas (125 vs. 35 pc). In contrast to what is found for the stars and the warm ionized gas, the neutral gas shows complex kinematics. Excluding a region affected by strong radial motions (see below), the velocity field of the main NaD component indicates a modest large-scale rotation can be interpreted as due to a dynamically hot slowly rotating disk mainly supported by random motions (V/σ $\sim$1), with a height scale larger than the ionized gas and stars of about a factor of 5 and 2, respectively. These results are evidence of a complex stratification and dynamics of the different galaxy components in IRAS F11506-3851.

2. — *Stellar and ISM contributions to the NaD feature.* Applying a spaxel-by-spaxel spectral fitting decomposition to the NaD profiles we have been able to disentangle two distinct components for which their 2D structural and kinematic properties have been inferred. One of these components (main) is likely tracing the neutral gas clouds of the ISM, as its EW-map is unrelated to that for the stellar continuum and it shows strong absorptions. The secondary component has properties fully consistent with a stellar origin, as can be seen by kinematic properties similar to those obtained from the IR-CO bands, and by its low EW values. These results are also supported by the application of a stellar-continuum modeling approach to the integrated spectrum, which indicates that most of the NaD absorption ($\sim$ 2/3) is interstellar in origin, while only a small contribution is due to the stars (1/3).

3. — *Evidence of a neutral outflow.* The velocity field of the neutral gas shows strong blue-shifted velocities along one semi-minor axis (towards the NE), which indicate strong radial motions emerging from the nuclear region perpendicular to the disk, and it is, therefore, naturally interpreted in the starburst driven galactic wind scenario. The triangular morphology of this region, and its kinematic properties (e.g., velocities of up to $\sim 200\,\mathrm{km s^{-1}}$), are also consistent with a conical outflow (opening angle $\sim 45°$) extending at least 1.8 kpc. The particular geometry of the neutral gas has in turn allowed us to fix the orientation and rotation direction of the galaxy disk(s). Although the presence of an ionized outflow counterpart is less obvious, there is evidence of the presence of radial motions of ionized gas in a region that overlaps with that of the neutral wind. Recent ALMA observations (PereiraSantaella 2016, in preparation) have confirmed the presence of the outflow in molecular gas (via CO(1-0) emission line) with an excellent consistency with that of neutral gas in this work.

4. — *Wind feedback and metal enrichment.* Under a free wind model (e.g., Heckman et al. 2000), we have inferred an outflowing mass rate of about $48\,\mathrm{M_\odot\,yr^{-1}}$, which considering the total SFR of this galaxy implies a global mass loading factor ($\eta = \mathrm{M_w/SFR}$) of 1.4. However, on the basis of the measured outflowing velocities and the dynamical mass (i.e., escape velocity) of the galaxy, it is unlikely that a significant fraction of the outflowing material would escape the galaxy to chemically enrich the surrounding IGM. Therefore, the outflowing material will fall back onto the galaxy disk, which would explain the lagging and the thickening of the neutral gas disk.

5. — *Wind feedback and nuclear SF quenching.* The nuclear region has been identified as the site where the outflow originates. The large local mass loading factor ($>> 1$) associated with this region, together with its relatively modest ongoing SF (seen via Brγ and Hα emissions) and the evidence of SNe (i.e., [Fe II] emission) from a ~ 7 Myr old nuclear burst, suggest that the outflow has been generated by the effects of these SNe and it has effectively quenched SF over the past few Myr in this region. However, the large nuclear reservoir of cold molecular gas, as inferred from the H_2 (1-0) (S1) emission, suggests that recurrent episodes of SF may be occur again in the future.

Chapter 5

Neutral gas outflows in nearby (U)LIRGs via optical NaD feature

In this chapter, the kinematic properties of the neutral gas for the sample of 38 local (U)LIRGs (Sect. 2.1) is presented. We search for neutral outflows (and study their feedback-effects) on the basis of the analysis of the spatially integrated, as well as the spatially resolved IFS-spectra of the NaD feature obtained with the VLT/VIMOS-IFU.

The work described in this chapter, has been accepted for publication in A&A entitled "Neutral gas outflows in nearby (U)LIRGs via optical NaD feature " by S.Cazzoli et al. 2016.

5.1 Contamination from stellar NaD absorption

In order to measure the stellar contribution to the NaD doublet (i.e., stellar contamination, see also Sections 3.1 and 4.3) we computed the ratio between the EW(NaD) in the stellar model obtained with pPXF (Sect. 3.2), and the total EW(NaD) observed in the integrated spectra. This ratio is listed as percentages for each individual galaxy in Table 3.1 and an histogram of its distribution is presented in Fig. 5.1.

We divided the sample into three groups: i) objects for which the NaD absorption is dominated by the ISM (i.e., stellar contribution $< 35\%$), ii), medium-contaminated objects (i.e., stellar contribution between 35% and 65%), and stellar dominated objects (i.e., stellar contribution $> 65\%$). Considering only the 31 objects with good stellar continuum modeling (Fig. 5.1), the stellar contribution is dominant for 23% of the cases, while the NaD absorption is dominated by the ISM for 42% of the cases.

As mentioned above, the stellar continuum fitting method could not be applied on a spaxel-by-spaxel basis. Therefore, to evaluate the origin of the NaD absorption in the maps, we compare the values of the sodium equivalent width, EW(NaD), with that of a purely stellar NaD doublet. In fact, we consider that the NaD feature is mainly originated in the ISM when EW(NaD) > 1.3 Å. We established this (conservative) threshold considering the EW(NaD) of the stellar models obtained with pPXF, which

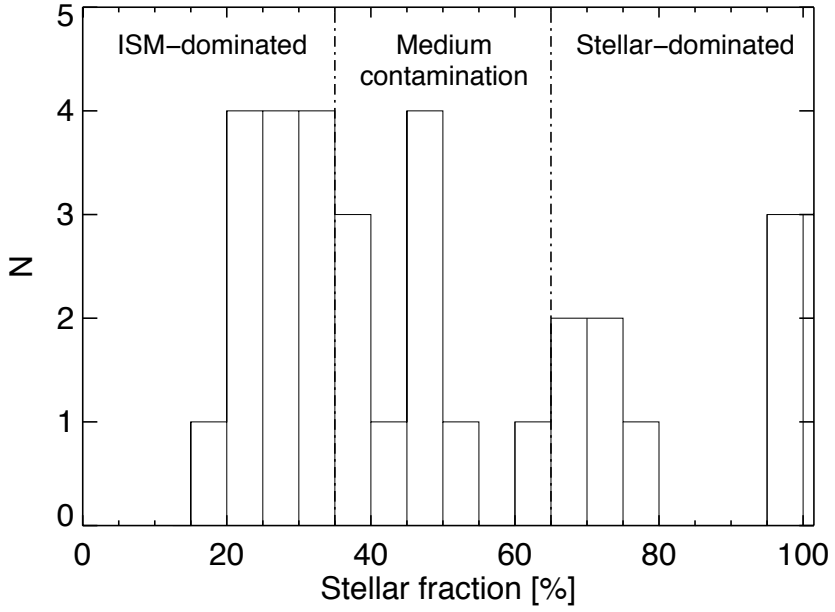

FIGURE 5.1: The distribution of the stellar contribution to the observed integrated NaD (Table 3.1) for the 31 objects with a good stellar continuum modelling (Sect. 3.2). Vertical lines follow the adopted definition for interstellar dominated, medium-contaminated and stellar dominated objects, see text for details.

are shown in Fig. 5.2 as a function of the stellar NaD fraction. In fact, independent of the fraction of NaD originated in the stars, the EW of the stellar models is on average 0.9 Å. Therefore, our choice of EW(NaD) >1.3 Å to identify a NaD feature dominated by the ISM is rather conservative as it is above the stellar contribution in 90% of the cases (or 100% within 1 σ). Therefore, the generally strong NaD absorption (with EW(NaD) >1.3 Å) seen in many regions of the (U)LIRGs (Appendix B) can be robustly associated with the cold neutral ISM. As for comparison, starburst galaxies with EW(NaD) > 0.8 Å are considered strong ISM-NaD absorbers by Chen et al. (2010).

5.2 Galactic winds in 1D (integrated spectra)

The criterion for identifying outflows in the integrated spectra, described in Sect. 3.4, identifies neutral gaseous outflows are found in 19 out of 28 (U)LIRGs. The incidence of winds in our local (U)LIRGs, i.e., 68%, is similar to that found in other samples of IR-luminous galaxies (e.g., Heckman et al. 2000; Rupke et al. 2005b). In five objects the NaD absorption is found at systemic velocity (i.e., -60 kms^{-1} < V < + 60 kms^{-1}), while in one case (IRAS F06259-4780 (C)) is redshifted.

We found that, generally, the outflows have velocities, V, in the range from 65 kms^{-1} to 260 kms^{-1} (on average ~ 165 kms^{-1}).

In Fig. 5.3 (left) we show the neutral gas outflow velocities obtained from the spatially integrated analysis as a function of the SFR. A regression of the type $V \propto SFR^n$ to this mainly LIRGs sample excluding objects with evidence of strong AGNs yields $n = 0.15 \pm 0.06$. This dependency is in rather good agreement with the results of Rupke et al. (2005c) ($n = 0.21 \pm 0.04$) for their sample of (mostly) ULIRGs. These results are also fairly consistent with those of Martin (2005) ($n = 0.35$), who considered a sample of ULIRGs and three dwarf galaxies of low SFRs. As shown in Fig. 5.3, the different LIRG

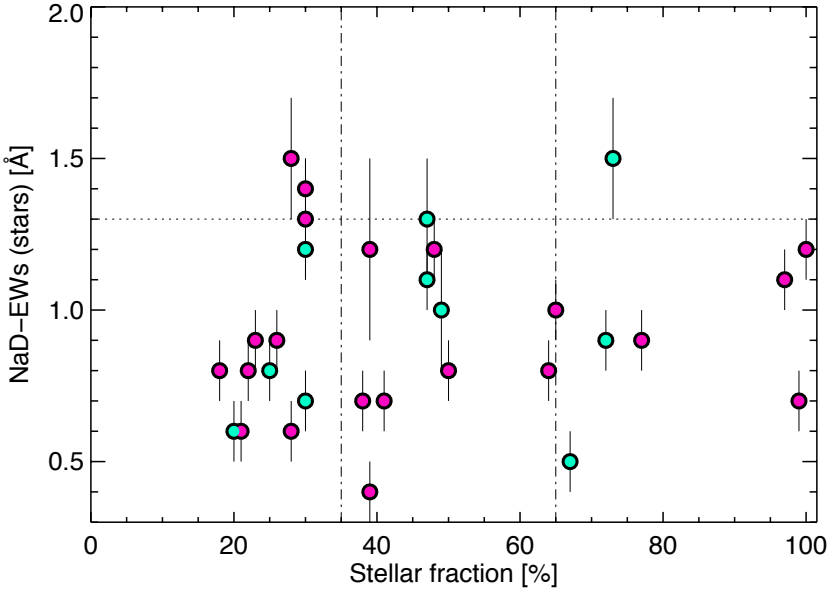

FIGURE 5.2: NaD equivalent widths estimated in the best-fit stellar spectrum, obtained via pPXF (Sect. 3.2), versus the integrated stellar contribution (Table 3.1). Horizontal line indicates our conservative choice of EW(NaD) (i.e., 1.3 Å) for identifying the NaD originated in the ISM in the maps (Sect. 5.1). Vertical lines follows the adopted definition for interstellar dominated, medium contaminated and stellar dominated objects (Sect. 5.1). Symbols are colour-coded accordingly to the quality of the stellar modelling on the integrated spectrum (e.g., Q, Table 3.1). Specifically, light blue and pink symbols indicate, "good" and "very good" quality of stellar modelling, Q = 2 and Q = 3, respectively.

and ULIRG samples complement each other well, sampling the SFR rather homogeneously over nearly 2 orders of magnitude. The general trend defined with these 1D (i.e., integrated and long-slit) data is consistent with an index n in the range 0.1-0.2. The effects of inclination and the presence of AGNs make it difficult to constrain this value further with those samples.

The comparison of the kinematic properties of the neutral outflows with their ionized counterparts (Arribas et al. 2014) for the same objects, is shown in Fig. 5.4.

On the one hand, we find that the outflow velocities (measured at the center of the line) are significantly higher for neutral than for ionized outflows in all cases. On the other hand, the neutral gas velocities seem on average slightly smaller than the commonly used ionized gas maximum outflow velocities, which are defined as $V_{max} = |\text{-}\Delta V| + FWHM/2$ (Westmoquette et al. 2011; Genzel et al. 2011).

Our measurements seem to contradict previous single aperture studies for which ionized and neutral winds are correlated in Seyferts but not in starburst (Rupke et al. 2005b). On a spatially resolved basis, only weak evidence of a correlation between the velocities of the neutral and ionized gas outflow phases (within a given galaxy) are found by Rupke & Veilleux (2013) for a sample of six nearby merger (U)LIRGs (including three obscured QSOs). However, all these findings are not fully comparable as they differ in terms of type of object and ionized gas tracers.

For the velocity dispersions, both neutral and ionized outflows show similar median values of 115 and 138 kms^{-1}, respectively, if the strongest AGNs are excluded.

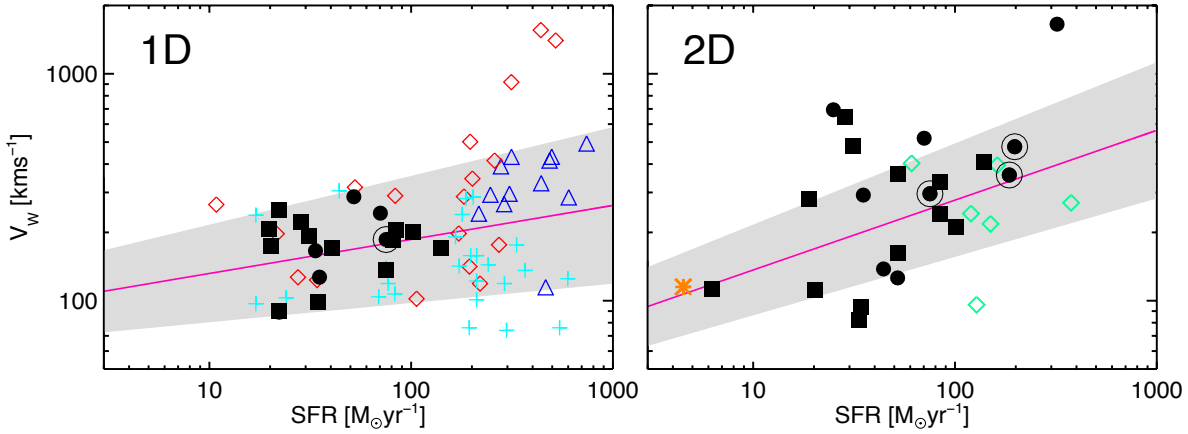

FIGURE 5.3: Velocity relative to systemic of the outflowing component vs. SFR of the host galaxy, for samples analyzed on the basis of 1D (i.e., integrated and long-slit, left) and 2D (IFS, right) data. The present sample is represented with black filled symbols in both panels. We identify pure starbursts and AGN-hosts with squares and circles, respectively, while very strong-AGN are marked with an additional circle. In the left panel, other (U)LIRGs samples from Rupke et al. (2002), Rupke et al. (2005b) and Martin (2005), are marked with red diamonds, light blue crosses and blue triangles, respectively. In the right panel, green diamonds indicate the IFS-based major merger-ULIRGs results by Rupke & Veilleux (2013) and the orange asterisk marks the result for the wind in M100 obtained by Jiménez-Vicente et al. (2007) . The pink lines, in both panels, represent the trends of the type $V \propto SFR^n$ found for our samples (excluding the strongest AGNs). See text for details. The shaded grey bands indicate uncertainties.

5.3 Galactic winds in 2D: detection rate

The procedure for identifying outflows in the spectral maps, described in Sect. 3.4, identifies 22 objects out of 40 (55%) with outflows (see Table 3.2). This implies a detection rate slightly lower than the one obtained from the analysis of the integrated spectra (i.e., 71%). This is likely a consequence of adopting a stricter criterion for the identification of outflows in the spectral maps. However, the agreement in the identification of a GW and/or rotation between these two procedures is high. From the 25 objects for which it was possible to make a kinematical classification via both, spatially resolved and spatially integrated spectra, 18 have outflow signatures and four rotation or systemic signatures, according to the two methods. Therefore, we find inconsistency only in three cases. In two cases (F12115-4656 and F12043-3140 (S), Figures A. 27 and A. 28), this is because the putative outflows only cover a small faint region of the maps and, as a result, are undetected in the integrated spectra. In the other case (F07160- 6215, Fig. A. 15),the neutral gas velocity field has a complex structure and the wind partially overlaps the approaching side of the rotation pattern, making the 2D identification difficult.

Previous works have shown that the ability of detecting neutral GWs with absorption tracers depends on the galaxy inclination angle. Specifically, Heckman et al. (2000) found a probability of $\sim 70\,\%$ of detecting outflowing gas in absorption in starburst galaxies with an inclination less than 60°. Similar trends are seen also in more recent studies of the relation between EWs(NaD) and the galaxy inclination angle (e.g., Chen et al. 2010). As seen in Fig. 5.5, in our sample GWs are detected in galaxies observed in a wide range of inclination angles (i.e., 10°-80°). Although, we also find a large percentage of GWs ($\sim 78\,\%$) detected in galaxies at low inclination angles (<60°), this percentage is similar to the total number of galaxies with low inclination whether a GW is detected or not.

In addition to the 22 objects with neutral gas GW detection, 10 targets show spider-like NaD velocity

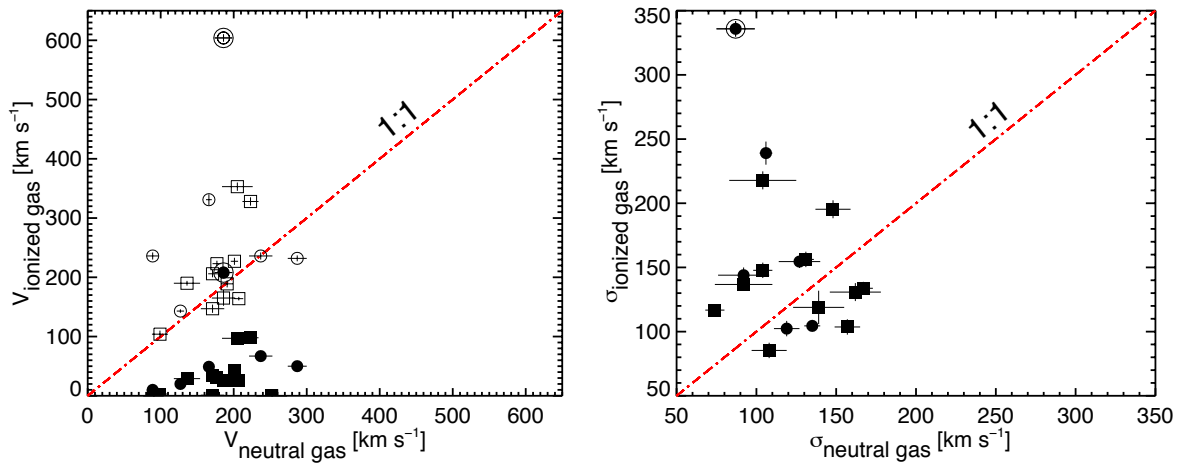

FIGURE 5.4: Comparison of neutral and ionized outflows velocities (left) and velocity dispersions (right), as derived from the (1D) integrated spectra. Results for the ionized outflows come from Arribas et al. (2014). The symbols used are the same as in Fig. 5.3. Specifically, filled squares and circle are for starbursts and for AGN-hosts, respectively, while very strong-AGN are marked with an additional second circle. In the left panel, solid symbols indicate velocities measured at the center of the line, while for empty symbols the ionized gas velocities are V_{max} from Arribas et al. (2014). The dot-dashed line indicates the 1:1 relation in both panels.

field in at least one kinematic component. This indicates disk rotation and this subsample is discussed in Sect. 5.8. Nine sources (eight LIRGs and one ULIRG) lack any clear outflows or rotation signatures either because of a lack of blueshifted velocities or because the putative disk kinematic is very irregular; these sources are excluded for the following discussion. The maps and integrated spectra of these nine sources, however, are shown in Appendix A. Table 3.2 (Column 2) summarizes the different kinematic patterns found in the maps.

5.4 Spatially resolved neutral GWs properties: 2D-kinematic and geometry

From the spectral maps we derived the (typical) wind velocity (V_w) as the deprojected median value[1] over the region identified as GW. The inclination corrected outflow velocities of the neutral gas entrained in GWs are in the range $\sim$ 80-700 kms^{-1}, similar to the velocities found previously for starburst driven winds in local star forming galaxies and (U)LIRGs (Heckman et al. 2000; Martin 2005; Rupke et al. 2005c; Chen et al. 2010). An exception to the general behaviour is the outflow in the ULIRG IRAS F06206-6315 with velocities that exceed 1000 kms^{-1} which host an AGN (Table 5.1).
The outflow velocity inferred from the maps has also a clear correlation with the global star formation rate (Fig 5, right). In particular, on the one hand, $V \propto SFR^n$ with $n = 0.40 \pm 0.07$ for all cases, and $n = 0.30 \pm 0.05$ excluding the objects with an AGN. This is in rather good agreement with previous results, including those obtained from the integrated spectra (see Fig. 5.3, left). On the other hand, the wind velocity does not seem to correlate with the dynamical mass of its host (Fig. 5.6).

[1]In this work, we consider that the GWs are perpendicular to the disk. Therefore, we deproject using the inclination of the galaxy (as listed in Bellocchi et al. 2013).

Results from a previous IFS-survey of local major-merger (U)LIRGs (Rupke & Veilleux 2013) indicate that in such systems the typical neutral gas outflow velocity dispersion is large, up to 1000 kms^{-1} (FWHM) in the case of MRK231. In our sample of (mainly) LIRGs, the typical velocity dispersions of the observed winds are lower ($\sigma \sim$ 95-190 kms^{-1}; FWHM $\sim$ 230-460 kms^{-1}). However, these values are significantly higher than the thermal velocity dispersion of the warm neutral gas (i.e., 8 km^{-1}, Caldú-Primo et al. 2013). This indicates that a wide range in neutral gas velocity is integrated along the line of sight or that the winds are turbulent and associated with shocks (as seen in the ULIRG F10565+2448 by Shih & Rupke 2010). In the standard GW scenario, (e.g., Heckman et al. 2000) broadening effects are consistent with outflowing gas in interaction (e.g., via shocks) with the surrounding material and with the presence of turbulent mixing layer on cloud surface.

In our sample, outflows are in many cases consistent with being along the minor axis of the ionized gas rotation (Appendix A). Thanks to the present IFS data, we are also able to infer the morphology outflow in about half of the sample (see figures in Appendix A). These outflows appear to be extra-planar, conical (the projected area is triangular in shape), and extended on kpc scales, which is consistent with the expectations from the standard GW model (Heckman et al. 2000). With the present data set, it is unpractical to develop a customized and more detailed model invoking superbubbles or different geometries (which is beyond the scope of this paper). We, therefore, assume a simple outflow model where the GWs are emerging perpendicular to the disk in all cases.

The measured outflow extension values (Table 5.1) are in good agreement with those reported previously for neutral gas GWs in (U)LIRGs (e.g., Veilleux et al. 2005). However, because of the lack of a bright continuum at large radii, the outer regions of the outflows may not have been detected with absorption line techniques (e.g., via NaD), and thus the quoted extensions should be considered lower limits.

In those outflows with a cone-like morphology, we identify the cone apex (near the galaxy nucleus) and boundaries in the spectral maps, and then we measure the wind 3D opening angles (i.e., C_Ω; see Table 5.1). We find C_Ω values are in the range between 0.1 and 0.6, in agreement with those (indirectly) estimated from the wind detection rate by Rupke et al. (2005c) and Veilleux et al. (2005) in local starburst and LIRGs (i.e., $C_\Omega \sim 0.4$). These are, however, lower than those inferred by these authors in local ULIRGs ($C_\Omega \sim 0.8$). Our results do not support a correlation between C_Ω and SFR (or the V_w/L_{IR}, Fig. 5.8), though we note that the uncertainties associated with the determination of C_Ω are large.

While in half of the cases it is not possible to infer the morphology of the outflows, it is relatively straightforward to estimate the wind projected area for all 22 GWs detected (Table 5.1). On average, the projected area of the neutral winds is 5 kpc^2. A spatially resolved broad Hα emission is seen in many objects of our sample (Bellocchi et al. 2013), but its presence shows no obvious correlation with the observed neutral GWs. Specifically, the neutral outflows are more extended with respect to the Hα broad component in 15 of the cases. Considering these cases, the areas covered by the outflow and the broad Hα component generally only overlap partially (12 cases).

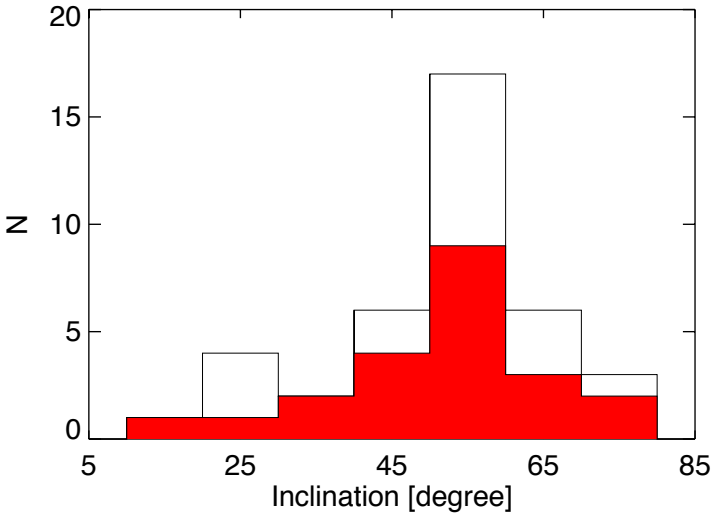

FIGURE 5.5: Distribution of the galaxy inclination angles for the 40 (U)LIRGs with reliable NaD-IFS detection (Sect. 3.3.2). Objects for which a GW has been detected are marked with a filled-red histogram (Sect. 3.4).

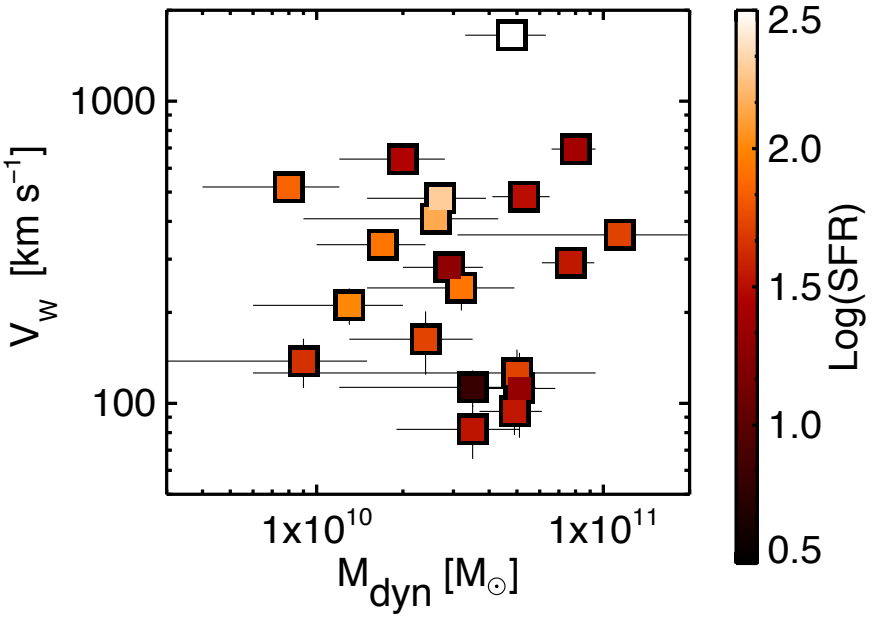

FIGURE 5.6: Wind velocity versus galaxy's dynamical mass. Symbols are color coded by the logarithm of the SFR. Vertical error bars are 1-σ standard deviations inferred from the wind velocity fields. Points for IRAS F05189-2524 and IRAS F07027-6011 (N) are not shown, since there is no reliable estimation of their dynamical mass (Bellocchi et al. 2013).

TABLE 5.1: Kinematics, geometry, and feedback properties of detected neutral GWs in the sample of (U)LIRGs.

ID1	R	Area	V_w	σ_w	C_Ω	N_H	M_w	$\dot{M}_w$	η	E_w	P_w
IRAS	kpc	kpc^2	kms^{-1}	kms^{-1}		10^{21} cm^{-2}	10^8 $M_\odot$	$M_\odot yr^{-1}$		10^{56} erg^{-1}	10^{41} erg^{-1} s^{-1}
(1)	(2)	(3)	(4)	(5)	(6)	(7)	(8)	(9)	(10)	(11)	(12)
F01159-4443 (N)	2.3	1.6	126 ± 50	197 ± 50	0.3	9.5 ± 1.1	7.4 ± 0.7	21.2 ± 4.2	0.4 ± 0.2	11.1 ± 2.7	9.8 ± 1.0
F01341-3735 (N)	3.0	1.8	113 ± 31	159 ± 19	0.2	2.8 ± 0.3	2.7 ± 0.3	7.3 ± 1.9	1.2 ± 0.2	2.4 ± 0.5	2.1 ± 0.4
F04315-0840	2.3	2.5	335 ± 64	150 ± 44	0.4	4.3 ± 0.8	1.0 ± 0.3	22.1 ± 5.8	0.3 ± 0.1	2.1 ± 0.8	15.4 ± 3.8
F05189-2524	···	13.3	358 ± 115	192 ± 97	···	3.2 ± 0.3	(0.6 ± 0.1)	(7.9 ± 0.8)	(0.05 ± 0.01)	(1.5 ± 0.2)	(6.4 ± 1.4)
F06206-6315	10.1	19.9	1654 ± 168	203 ± 79	0.1	3.8 ± 0.7	4.5 ± 1.0	113.5 ± 27.7	0.4 ± 0.1	147.2 ± 43.3	1260 ± 120
F06259-4780 (N)	3.1	9.8	408 ± 45	121 ± 32	0.6	4.5 ± 0.4	2.8 ± 0.5	47.8 ± 8.8	0.3 ± 0.1	6.8 ± 1.8	35.8 ± 6.3
F06592-6313	2.2	4.4	643 ± 103	157 ± 53	0.6	5.6 ± 0.6	2.1 ± 0.6	70.7 ± 17.9	2.5 ± 0.5	11.9 ± 4.2	131.2 ± 33.8
F07027-6011 (N)	···	7.2	296 ± 59	166 ± 33	···	5.1 ± 0.6	(1.0 ± 0.1)	(9.4 ± 1.3)	(0.1 ± 0.01)	(1.5 ± 0.1)	(4.7 ± 1.6)
F07027-6011 (S) ‡	···	4.0	163 ± 77	140 ± 46	···	4.6 ± 1.1	(0.9 ± 0.2)	(5.4 ± 1.2)	(0.1 ± 0.01)	(0.8 ± 0.1)	(1.5 ± 1.0)
F07160-6215	3.0	1.1	694 ± 55	114 ± 50	0.2	3.6 ± 0.8	0.6 ± 0.2	23.0 ± 6.2	0.9 ± 0.2	3.6 ± 1.0	45.5 ± 12.1
F10015-0614	···	3.2	292 ± 29	106 ± 33	···	6.1 ± 1.1	(1.1 ± 0.1)	(11.1 ± 1.6)	(0.3 ± 0.06)	(1.3 ± 0.1)	(3.9 ± 0.8)
F10038-3338	4.0	5.8	211 ± 58	145 ± 27	0.3	4.2 ± 0.8	2.4 ± 0.6	17.1 ± 5.5	0.2 ± 0.04	3.0 ± 1.3	7.2 ± 1.8
F10257-4339	2.3	3.1	241 ± 76	163 ± 52	0.4	2.4 ± 0.5	1.3 ± 0.6	26.2 ± 8.9	0.3 ± 0.06	2.0 ± 0.9	18.6 ± 6.1
F10409-4556 ‡	···	10.9	483 ± 70	174 ± 63	···	3.9 ± 0.5	(0.7 ± 0.1)	(12.6 ± 1.0)	(0.4 ± 0.1)	(2.5 ± 0.1)	(13.3 ± 1.4)
F10567-4310	···	2.1	112 ± 70	119 ± 40	···	7.2 ± 1.1	(1.3 ± 0.2)	(5.8 ± 1.8)	(0.3 ± 0.06)	(0.8 ± 0.1)	(1.0 ± 0.3)
F11255-4120	···	1.8	282 ± 70	203 ± 68	···	5.6 ± 0.9	(1.1 ± 0.2)	(9.6 ± 1.4)	(0.5 ± 0.1)	(1.7 ± 0.1)	(4.9 ± 2.1)
F11506-3851 ‡	1.8	0.9	98 ± 31	98 ± 20	0.2	5.0 ± 0.4	2.5 ± 0.3	23.6 ± 5.1	0.9 ± 0.1	0.4 ± 0.1	1.4 ± 0.1
12116-5615 ‡	···	3.6	520 ± 114	115 ± 58	···	4.0 ± 1.3	(0.7 ± 0.2)	(11.6 ± 1.0)	(0.2 ± 0.03)	(1.8 ± 0.1)	(8.7 ± 0.6)
F13001-2339	···	4.8	361 ± 46	120 ± 65	···	3.5 ± 0.6	(0.6 ± 0.1)	(7.8 ± 0.9)	(0.2 ± 0.03)	(1.1 ± 0.2)	(4.0 ± 0.6)
F13229-2934	1.4	1.1	82 ± 33	139 ± 25	0.5	2.7 ± 0.2	0.4 ± 0.1	2.6 ± 0.7	0.1 ± 0.01	0.3 ± 0.1	0.6 ± 0.3
F21453-3511	···	5.6	138 ± 51	146 ± 70	···	2.6 ± 0.6	(0.5 ± 0.1)	2.6 ± 0.7	(0.05 ± 0.01)	(0.4 ± 0.1)	(0.7 ±0.3)
F23128-5919	3.4	7.3	477 ± 88	142 ± 57	0.4	1.7 ± 0.8	0.6 ± 0.1	12.9 ± 7.4	0.1 ± 0.01	1.8 ± 0.4	13.5 ± 6.8

Notes. Column (1): IRAS name. Column (2): Observed extent of the neutral winds corrected for the inclination using the inclination values of Bellocchi et al. (2013). Column (3): Area covered by the GW. Column (4): Inclination corrected median velocities. Column (5): Median velocity dispersion over the GW area. Column (6): Wind opening angle. Column (7): Average wind column density. Column (8): Wind mass in the neutral phase. Column (9): Mass outflow rate. Column (10): Outflow loading factor defined as the mass outflow rate normalized to the corresponding SFR. Column (11): Wind energy. Column (12): Wind power. The symbol: ‡, marks the galaxies for which a two-components NaD modelling have been done (Sect. 3.3.1.1). In brackets values obtained for those GWs for which the morphology is not well constrained (Sect. 5.4).

5.5 Galactic winds feedback in 2D

While it is relatively straightforward to demonstrate that a GW is present, it is more difficult to robustly calculate the rates at which mass and energy are being transported out by the wind (i.e., its feedback effects). In order to quantify the neutral wind feedback, in the form of outflowing mass, outflow mass-rate and loading factor, we have adopted a "Free Wind" (FW) model (as in Sect. 4.6). Details of the model are given in Heckman et al. (2000), Rupke et al. (2002) and Rupke et al. (2005c).

Briefly, this model consists of a starburst surrounded by thin shells of a free-flowing wind, a shocked wind (i.e., GW ionized phase), and entraining clouds of neutral ISM. One drawback of this model is that a thin shell could be broken leading to the formation of filaments. Indeed, a starburst-driven wind, in its expansion through the ISM, entrains clouds that are denser than the ambient ISM. A dense cloud embedded in a subsonic flow experiences pressure differences along the surface. This may lead to Rayleigh-Taylor instabilities and the fragmentation of clouds with the consequent formation of filaments that are not accounted for by the FW model (Heckman et al. 2000). Although this scenario is possible, the spatial resolution of the VIMOS data does not allow us to probe possible filaments and, therefore, the shell is a natural and simple interpretation of our observations of GWs. Other approaches are, however, possible (e.g., single radius FWs or superbubbles; Rupke & Veilleux 2013). To estimate how much of the neutral gas is brought out into the outflow, the knowledge of the column density of the wind ($N_{\rm H}$) is required. To obtain spatially resolved column densities, we used a method which relates $N_{\rm H}$ to the strength of the NaD absorption (i.e., its equivalent width) via the reddening ($E_{\rm B-V}$). Specifically, first, Turatto et al. (2003) via a light-curve fitting of low resolution spectroscopy of SNe found that the equivalent width of the NaD correlates well with the redding (see also Veilleux et al. 1995). Second, Bohlin et al. (1978) found that the $E_{\rm B-V}$ follows a well defined linear relation with $N_{\rm H}$ (Eq. 4.3 in Sect. 4.6,), analyzing a large sample of galactic stars. Combining these relations[2] we found the following dependence of $N_{\rm H}$, with EW(NaD):

$$N_{\rm H} = \frac{-0.025 + 0.335 \times EW(NaD)}{0.2 \times 10^{-21}} \, cm^{-2}. \tag{5.1}$$

The median column density in our sample is 4.2×10^{21} cm^{-2} (see Table 5.1). This approach, which has also been followed in Davis et al. (2012) and Cazzoli et al. (2014), is applied here on a spaxel-by-spaxel basis. However, this ignores issues such as the spatial variation of the ionization state of NaD (Murray et al. 2007), metal depletion on dust grains, line saturation effects (e.g., the square-root part of the curve of growth), and variations in gas-to-dust ratio (Wilson et al. 2008).

Alternatively, column densities may be computed following Hamann et al. (1997). By using spatially resolved and spatially integrated data, we found values in rather good agreement with the current estimate and previous works (e.g., 1.6×10^{21} cm^{-2} by Rupke et al. 2005c). Specifically, we found average values of 4.6×10^{21} cm^{-2} and 2.0×10^{21} cm^{-2} for 2D and 1D cases, respectively.

Additionally, we also estimated $N_{\rm H}$ with the EW-ratios ($R_{\rm NaD}$) of the (1D) integrated spectra (after removing the stellar contribution) via the sodium curve of growth (Draine 2011). For this, we only

[2]For the present work we have considered the average relation within the two extreme relationships, found by Turatto et al. (2003). Note that, the relation for heavily reddened objects, used in Sect. 4.6 (Cazzoli et al. 2014), encompasses only one data point for EW(NaD) > 1.2 Å.

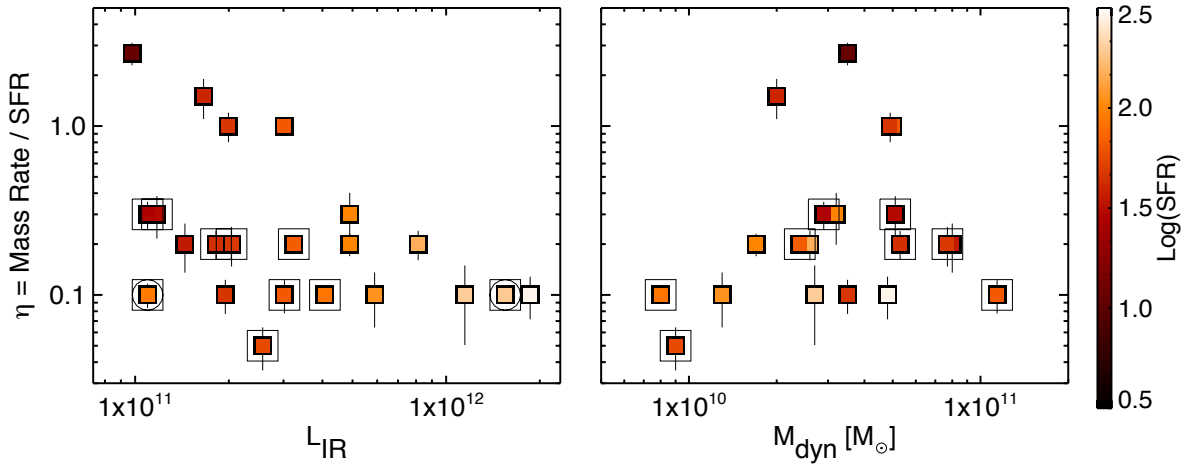

FIGURE 5.7: The wind loading factor plotted against the infrared luminosity (left, Table 1) and dynamical mass (right) color-coded by the logarithm of the SFR. In both panels those galaxies for which we were unable to infer in detail the wind morphology are marked with an additional square. In the left panel, the galaxies which lack of a reliable estimation of the dynamical mass (F05189-2524 and F07027-6011 (N), Bellocchi et al. 2013) are marked with circles.

considered optically thin ($R_{NaD} \geq 1.5$, Rupke et al. 2005a) outflowing components (14/24 cases), obtaining a median value of 1.1×10^{21} cm^{-2}. This is smaller than the results obtained from Eq. 4.3 quoted above and the typical value found by Rupke et al. (2005c).

For the present paper, we will consider the values obtained from Eq. 4.3 which are in good agreement with those from the method described in Hamann et al. (1997). A more detailed estimation of N_H (e.g., from more complex line-profile modeling as in Rupke et al. 2005a), is beyond the aim of this work.

Our IFS observations do probe the wind shape in half of the cases (as discussed in Sect. 5.4) allowing us to constrain the radial extent and variation of the velocity of the outflow with position. We customized the FW model, allowing each spatial element of the wind to have its own velocity and distance from the wind's origin. We used the column density and velocity measured in each spatial resolution element (k) to derive the wind mass (M_w) and outflow rate ($\dot{M}_w$), following Rupke et al. (2005c), as

$$M_w = 5.6 \times 10^8 \sum_{k=1}^{N} \left(\frac{C_{\Omega,k}}{0.4} C_f\right) \left(\frac{R^2_{w,k}}{100\, kpc^2}\right) \left(\frac{N_{H,k}}{10^{21} cm^{-2}}\right) M_\odot. \quad (5.2)$$

$$\dot{M}_w = 11.5 \times \sum_{k=1}^{N} \left(\frac{C_{\Omega,k}}{0.4} C_f\right) \left(\frac{R_{w,k}}{10\, kpc}\right) \times \left(\frac{N_{H,k}}{10^{21} cm^{-2}}\right) \left(\frac{V_{w,k}}{200\, kms^{-1}}\right) M_\odot yr^{-1}. \quad (5.3)$$

These equations describe the mass and mass outflow rate for a GW flowing into a solid angle $C_{\Omega,k}$ with a cloud covering factor C_f. We consider the observed GWs as a series of thin shells, each one located at radius $R_{w,k}$ with the corresponding inclination-corrected velocity $V_{w,k}$ and column density ($N_{H,k}$) inferred, as previously discussed. The extent R, median velocity V and average column density N_H, as well as the mass and mass outflow rate, which are derived from our observations assuming the FW model, are listed in Table 5.1. C_f is assumed to be 0.37 as in Sect. 4.6 and Rupke et al. (2005c).

As mentioned in the previous section, in 10 cases we cannot infer the wind morphology mainly because of projection effects (Table 5.1). In these cases, to calculate the wind mass and mass rate, we assumed

a fiducial radius of 3 kpc and a wind opening angle of 0.4, which are the characteristic values seen for the subsample for which we can derive the actual wind morphology. We also considered the median values of V, and N_H distributions measured over each GW region.

The wind mass estimates range between 4×10^7 $M_\odot$ to 7.5×10^8 $M_\odot$ with a mean value of 1.6×10^8 $M_\odot$. These values are roughly in agreement (lower by a factor of 3 when comparing averages) with those reported by Rupke et al. (2005c) obtained for neutral outflows in their local LIRGs sample (i.e., 6.3×10^8 $M_\odot$ on average).

Previous long-slit studies of Rupke et al. (2005b,c) and Martin (2006), on the basis of the FW wind model, found that the mass of neutral outflows in (U)LIRGs can be up to 10% of the dynamical mass (estimated via CO measurement). For our sample, the wind mass is typically $\sim 3\%$ of the dynamical mass of the galaxy. These results indicate that neutral outflows in (U)LIRGs may carry away a significant amount of gas mass that would otherwise be available for further star formation (Sato et al. 2009). However, in general, we found that the mass outflow rate (i.e., $\dot{M}_w$) is not larger than the global SFR (Table 5.1). Specifically, the outflow loading factor (i.e., $\eta = \dot{M}_w/\mathrm{SFR}$) is $\eta < 1$ in nearly all objects (Table 5.1), indicating that the mass-loss rates (in the neutral phase) are relatively unimportant for quenching the SFR. However, an estimation of the mass-loss rates which take into account other wind's phases (e.g., molecular) may lead to an increase of the significance of the feedback.

These results are in rough agreement with previous measurements of η in nearby (U)LIRGs (Rupke et al. 2005c) and empirical models (e.g., Zahid et al. 2012), for which $\eta \leq 1$. Values of η above the unity, which indicates a strong mass loading of the outflow by the galaxy ISM, have been found in active galaxies (Veilleux et al. 2005).

In the left panel of Fig. 5.7, we show the loading factor as a function of the infrared luminosity which are in negative correlation. Excluding those galaxies for which we were unable to estimate in detail the wind morphology, the Paerson coefficient, r_{PC} hereafter, is $\sim$ -0.6. A similar trend has been found by Rupke et al. (2005c) though using the K-band magnitude (as a tracer of the IR-luminosity). Nevertheless, considering the same subsample, our analysis also supports the absence of any dependence of η on dynamical masses of the host for the neutral phase ($r_{PC} < 0.1$) as seen in the right panel of Fig. 5.7 (where the dynamical mass versus the mass loading factors have been presented). This is in contrast to the inverse dependency on η and the dynamical mass found for the ionized phase of GWs in 32 LIRGs without AGNs (Arribas et al. 2014). We note however that the present sample (12 objects) is relatively small and it includes 6 galaxies hosting weak AGNs.

In summary, the present results indicate that the neutral gas loading factors are small (<1) and, therefore, the feedback effects are not expected to be large if we only take the neutral gas phase of the outflows into consideration. For the objects with a well-defined morphology, the loading factors show a trend with the infrared luminosity, but they seem uncorrelated with the host mass. The relative small number statistics (i.e., 12 objects, including 6 weak AGNs) prevent us from considering the latter trend as a firm conclusion.

5.6 The gas cycle: IGM and ISM pollution via outflows

The GWs that originated in the disk of spiral galaxies, in principle, could have the ability to eject large percentage of the cold gas reservoir available for star formation into the IGM (Veilleux et al. 2005). We

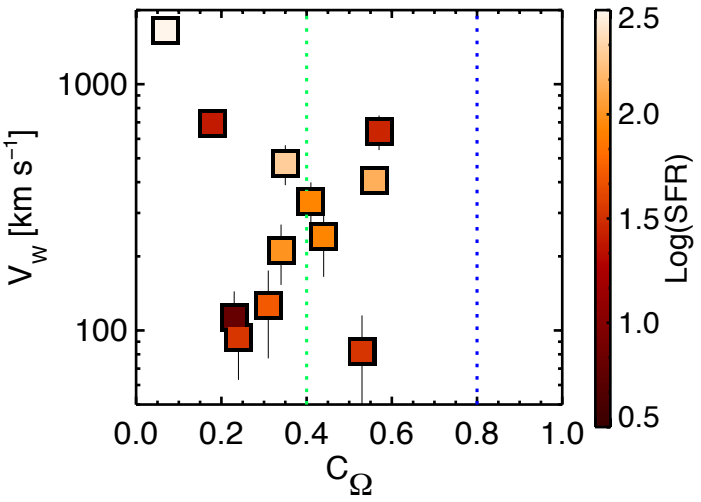

FIGURE 5.8: The wind velocity plotted against the wind opening angle (C_Ω) colour coded by the logarithm of the SFR. Vertical green and blue dotted lines, represent the typical values of C_Ω found in LIRGs and ULIRGS, respectively (Rupke et al. 2005c). Uncertainties for velocities are the 1-σ standard deviations (inferred from the wind velocity fields) while, for C_Ω, assuming a 20%-error, they are typically ~ 0.1.

compare the wind velocity to the escape velocity of each galaxy to investigate the fate of the outflowing material.

Following a simple recipe (Arribas et al. 2014 and reference therein) for a galaxy with dynamical mass (M_{dyn}), we estimate the escape velocity (v_{esc}) at r = 3 kpc (considering an isothermal sphere truncated at R_{max} as the gravitational model for the host galaxy) as

$$v_{\rm esc} = \sqrt{\frac{2GM_{\rm dyn} \times \left[1 + ln\left(\frac{R_{\rm max}}{r}\right)\right]}{3r}}\ kms^{-1}, \tag{5.4}$$

where G is the gravitational constant (i.e., 4.3×10^{-3} pc $M_\odot$ (kms^{-1})^2) and $R_{max}/r = 10$. This approach allows us to take into account both the dependence of the dynamical mass estimation to rotation and dispersion motions and assumes that the halo drag is negligible. We refer to Bellocchi et al. (2013) for a detailed description of the dynamical mass estimation.

For the two galaxies (F05189-2524 and F07027-6011 (N)) for which the dynamical mass estimation was not possible (due to AGN contamination, Bellocchi et al. 2013), we calculate v_{esc}, as in Sect. 4.6 (Eq. 4.7), as follows:

$$v_{\rm esc} = \sqrt{2 \times v_{\rm rot}^2 \times \left[1 + ln\left(\frac{R_{\rm max}}{R}\right)\right]}\ kms^{-1}. \tag{5.5}$$

Similar to the previous case, this simpler approach assumes a truncated isothermal gravitational potential and no halo drag. We consider that the Hα velocity amplitude, which is defined as the half of the observed peak-to-peak velocity corrected for the inclination of the galaxy, (Bellocchi et al. 2013) is a good proxy for v_{rot} and $R_{max}/r = 10$ (as in the previous case).

Table 5.2 lists the escape velocities and outflow velocity in units of the escape velocity i.e., V_w/v_{esc}. This ratio ranges from 0.2 to 4.2 (Fig. 5.9) with a median (average) value of 0.9 (1.1).

There are ten objects for which $V_w/v_{esc} > 1$ and, therefore, a significant amount of their outflowing gas could pollute the IGM (Fig. 5.9, right). The most extreme case is IRAS F06206-6315, where an AGN is likely playing a role in boosting the velocity of the outflowing gas to exceed the escape velocity (see also Sect.5.7). Excluding this object, the sample indicates a (weak) correlation in the sense that V_w/v_{esc} is higher for the less massive galaxies as found for the ionized outflows (Arribas et al. 2014). This result is consistent with the prediction that the less massive galaxies have the most severe impact on the IGM pollution.

In the majority of the cases, we find that the median wind velocities do not exceed the escape velocities (i.e., $V_w/v_{esc} < 1$, Table 5.2), indicating that most of the cold outflowing material that we probe with our NaD measurement is likely falling back to the disk. This circulation of the gas could in principle favor the redistribution of metals, modifying the abundance gradients in the galaxy disk (Spitoni et al. 2010). This fountain scenario is consistent with the presence of clouds of neutral gas, either above the main disk in disk-like layers (in slow rotation) or sparsely distributed (i.e., raining back showing, in projection, an irregular velocity field). In the latter case, the neutral gas is still raining back in the form of high velocity clouds (HVCs; Spitoni et al. 2013), which are gravitationally bound to the host galaxy, but not virialized.

However, V_w refers here to the median velocity in the outflow and, therefore, even for values of $V_w/v_{esc} < 1$, part of the gas entrained in the wind could in principle escape.

The efficiency of the observed winds of polluting the IGM, is in any case, a lower limit. Specifically, by using absorption lines as tracers of the outflowing gas we are limited to observing gas at a distance smaller than the projected size of the stellar disk. Tenuous and hot material (in absence of radiative cooling) or molecular gas, may be found at larger radii (up to 10 Kpc in M82, Lehnert et al. 1999) and is more likely to escape.

In Fig. 5.9 we consider the ratio V_w/v_{esc} as a function of dynamical mass and dynamical ratio of the ionized disk (i.e., V/σ, from Bellocchi et al. 2013) in order to study the factors controlling the recycling of gas and metals. As expected, gas and metals are more likely to escape to the IGM (higher V_w/v_{esc}) in galaxies with small potential wells.

In addition, we note that there is a tendency for V_w/v_{esc} to increase in turbulent and thicker ionized gas disk (i.e., higher disk height and lower dynamical ratio, Fig. 5.9, right). In such disks, the gas turbulence may help the wind to escape, thereby enhancing its vertical growth. This is in agreement with a scenario in which the wind fluid follows the path of least resistance (Cooper et al. 2008).

5.7 Wind engine and energetics

The outflow kinematic properties are more extreme in galaxies that host a powerful AGN (Veilleux et al. 2005). Therefore, the outflow velocity can be used as a discriminant of starburst-driven versus AGN-driven winds as suggested by Rupke et al. (2005a) and Rupke & Veilleux (2013). The influence of AGNs on the velocity (and power) of outflows has also been seen in ionized (Arribas et al. 2014) and molecular (Cicone et al. 2014; Sturm et al. 2011) wind phases.

As mentioned in Sec. 5.4, the ULIRG IRAS F06206-6315 likely hosts an AGN-driven GW, according to the observed outflow kinematics (Table 2.1). In addition to this extreme case, there are ten other objects where evidence for the presence of an AGN has been found according to X-ray and infrared

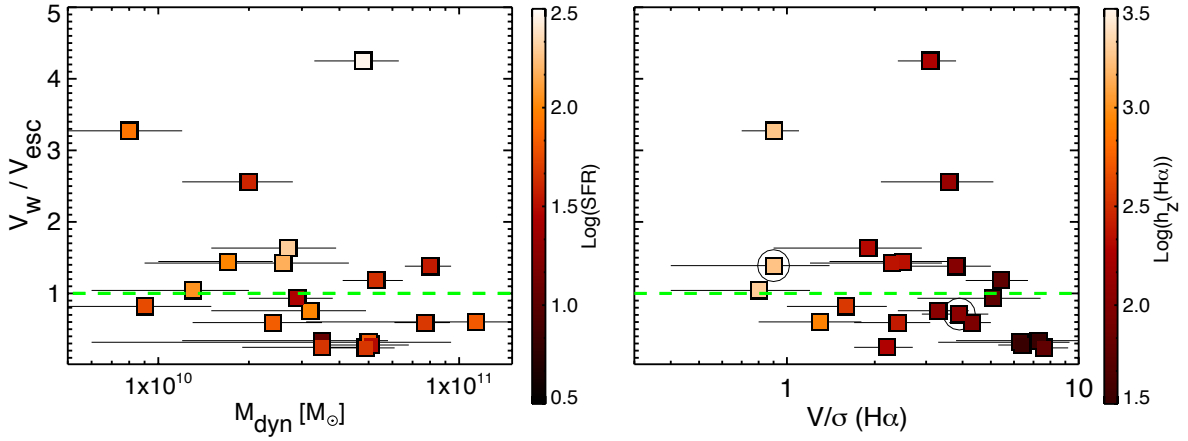

FIGURE 5.9: The ratio of wind velocity (Table 5.1) and the galaxy escape velocity plotted against the dynamical mass (left), and the Hα dynamical ratio from Bellocchi et al. (2013) (right). These plots are color-coded by the logarithm of the SFR and the disk thickness of the ionized gas disks (Table 5.2), respectively, right and left. The green horizontal line indicates where V_w/v_{esc} is 1. In the right panel, the galaxies with no dynamical mass estimation (F05189-2524 and F07027-6011 (N), Bellocchi et al. 2013) are marked with circles (as Fig. 5.7).

observations or optical emission line ratios and kinematics (Tables 2.1 and 5.1). Despite of that, from the observed neutral wind kinematics in these objects (Table 5.1) it is not obvious that the AGN is significantly boosting the outflows, probably because it is not powerful enough.

To further address the issue about the wind driver, the energy (E_w) of the winds as in Sect. 4.7 (Eq. 4.8) and their power (P_w) using the shell formalism and using the FW-model outlined in Sect. 5.5, as follows:

$$P_{\rm w} = 1.4\times10^{41}\sum_{\rm k=1}^{N}\left(\frac{C_{\Omega,\rm k}}{0.4}C_{\rm f}\right)\left(\frac{R_{\rm w,k}}{10\,kpc}\right)\left(\frac{N_{\rm H,k}}{10^{21}cm^{-2}}\right)\times\left(\frac{V_{\rm w,k}}{200kms^{-1}}\right)^{3}+1.5\times\left(\frac{b_{\rm w,k}}{200kms^{-1}}\right)^{2}ergss^{-1}. \quad (5.6)$$

Where σ is the velocity dispersion and b, the Doppler width (defined as: b = FWHM/2 $\sqrt{\ln 2}$, Rupke et al. 2005c) for each spaxel. Similarly as in Sect. 5.5, for the 10 cases for which we cannot estimate the wind morphology, we measured on spaxel-by-spaxel basis V, N_H and b, and used their median values (calculated over the area where the wind is observed). In addition, we assumed a wind radius and opening angle of 3 kpc and 0.4, respectively.

Excluding the case of IRAS F06206-6315, the estimated wind energies are in the range from 3×10^{55} ergs to 1.2×10^{57} ergs, while the powers are in the range between 6×10^{40} ergs s^{-1} and 1.4×10^{43} ergs s^{-1}. The median energy and power are $4\,(2)\times10^{56}$ and $14\,(6)\times10^{41}$ ergs s^{-1}, respectively, excluding (including) the winds because it was not possible to determine their morphology.

For comparison, Rupke et al. (2005c) found that the typical wind energy and power in local LIRGs are 5×10^{56} ergs and 4×10^{41} ergs s^{-1}, respectively. The average wind energy in the present work is generally consistent within errors with that of the above mentioned work, although our estimation of the wind power is generally larger (by a factor of about three).

To investigate the wind origin, in Fig. 5.10, we compared the wind power of the neutral outflows and the kinetic power of the starburst associated to SNe (i.e., KP). The latter has been calculated with the

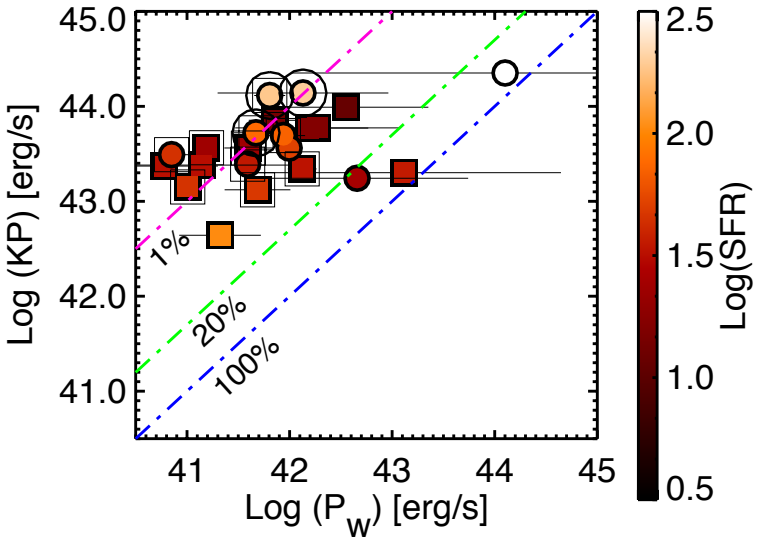

FIGURE 5.10: Logarithm of kinetic power of the starburst associated to SNe (KP) as a function of the wind power (P_w), color coded by their SFR. Symbols are as in Fig. 5.3. Specifically, filled squares and circle are for starburst and for AGN-hosts, respectively, while very strong-AGN are marked with an additional second circle (as in Fig. 5.7). In addition, those galaxies for which we were unable to estimate in detail the wind morphology are marked with an additional second square. The pink, green and blue lines represent respectively the positions for which the power of the wind is equal to the 1%, 20% and 100% of the kinetic power supplied by the starburst.

receipt of Veilleux et al. (2005):

$$KP \sim 7 \times 10^{41}\, SFR/M_{\odot} yr^{-1}. \tag{5.7}$$

In nearly all of the cases, the wind power is within 1% and 20% of the kinetic power supplied by the starburst (about ∼5% on average). This is in agreement with a scenario in which these winds are originated in dense core of powerful nuclear starbursts (Veilleux et al. 2005). However, our result is in partial contrast with hydrodynamical simulations, which often assume wind thermalization efficiencies in the range 10-100% (e.g., Strickland & Stevens 2000) and direct measurements of the thermalization efficiency. For example, for the nearby starburst M82, Strickland & Heckman (2009) found that medium-to-high thermalization efficiencies (> 30%) are required in hydrodynamical models to match the set of observational constraints derived from hard X-ray observations.

We see only two cases, for which an unlikely thermalization efficiency of ∼ 90-100% could be required. For the ULIRG IRAS F06206-6315, the presence of an AGN suggests that its outflow is rather driven by the energy liberated by the accretion of gas into the black hole. For the LIRG IRAS F06592-6313, an AGN-driven outflow could be a reasonable possibility, although there is not evidence for this outflow at optical wavelengths. However, we note that the large uncertainties associated with P_w also make these cases consistent with lower thermalization efficiencies. For the other galaxies, the AGN contribution is in principle not required to explain the observed energetic

TABLE 5.2: Galaxy properties: escape velocities and disks thickness.

ID1 IRAS (1)	v_{esc} kms^{-1} (2)	V_w/v_{esc} (3)	$h_z(H\alpha)$ pc (4)	h_z(NaD) pc (5)
F01159-4443 (N)	397	0.3	35 ± 7	···
F01341-3735 (N)	332	0.3	30 ± 5	···
F04315-0840	232	1.4	218 ± 44	···
F05189-2524	258	1.4	1757 ± 352	···
F06206-6315	389	4.2	187 ± 37	···
F06259-4780 (N)	286	1.4	227 ± 45	···
F06259-4780 (C)	···	···	246± 49	2759 ± 552
F06592-6313	251	2.6	135 ± 27	···
F07027-6011 (N)	416	0.7	110 ± 22	···
F07027-6011 (S) ‡	275	0.6	248 ± 50	2431 ± 486
F07160-6215	502	1.4	100 ± 20	···
F09437+0317 (N)	···	···	111 ±22	713 ± 143
F09437+0317 (S)	···	···	46 ± 7	1879 ± 376
F10015-0614	492	0.6	87 ± 17	···
F10038-3338	203	1.0	1969 ± 394	···
F10257-4339	318	0.8	109 ± 22	···
F10409-4556 ‡	409	1.2	57 ± 11	1390 ± 278
F10567-4310	401	0.3	32 ± 6	···
F11255-4120	303	0.9	56 ± 11	···
F11506-3851 ‡	393	0.2	35 ± 6	1541 ± 308
F12043-3140 (S)	···	···	347 ± 69	1315 ± 263
F12115-4656	···	···	40 ± 8	1845 ± 369
12116-5615 ‡	159	3.2	1779 ± 355	···
F13001-2339	600	0.6	828 ± 166	···
F13229-2934	332	0.2	191 ± 38	···
F14544-4255 (E)	···	···	142 ± 28	1287 ± 257
F18093-5744 (S)	···	···	122 ± 24	1261 ± 252
F21453-3511	169	0.8	350 ± 70	···
F22132-3705	···	···	43 ± 9	922 ± 184
F23128-5919	292	1.6	200 ± 40	···

Notes. Column (1): ID. Column (2): Escape velocity for those galaxies hosting a GW (Table 1) as derived in Sect. 5.6. Column (3): The ratio between the inclination corrected wind median velocities (Table 5.1) and the escape velocity. Columns (4) and (5): Vertical ionized and neutral gas disk heights traced via Hα (narrow component, Bellocchi et al. 2013) and NaD, respectively (Sect. 5.8). As in Table 5.1, the symbol: ‡, marks the galaxies for which a two-components NaD modelling have been done (Sect. 3.3.1). We assumed a conservative 20% systematic error for all the h_z values.

5.8 Thick disks in slow rotation

As mentioned in Sect. 3.4, the velocity fields of the neutral gas observed in 11 (U)LIRGs have the spider diagram pattern characteristic of a rotating disk (Figures in Appendix A and Sect. 4 for the case of the LIRG IRAS F11506-3851). In three galaxies (F07027-6011 (S), F10409-4556 and F11506-3851) the rotation is detected in one kinematic component, but an additional outflowing component is also detected (Figures A. 13, A. 24, and 4.3). However, while in case of an ideal rotating disk the velocity dispersion map should be centrally peaked, the observed neutral gas velocity dispersion maps are generally rather irregular.

The observed NaD feature in these 11 galaxies shows a wide range of stellar contribution (Table 3.1), though in most of the objects (8/11) the stellar absorption is not dominant (i.e., $<50\%$). For the three galaxies where the NaD absorption is dominated by the stellar contribution (F09437+0317 (S), F12043-3140 (S) and F12115-4656), the rotation curves may be difficult to interpret in terms of neutral gas motions. However, it is important to consider that the stellar contribution is computed in the integrated light. Therefore, in some cases even if the stellar absorption in the integrated spectrum is substantial, the 2D distribution may help to identify regions where the NaD absorption is dominated by neutral gas or the stellar component, as in IRAS F11056-3851 (Chapt. 4). Without the knowledge of the stellar properties and kinematic in these galaxies we can not investigate this further.

From our spectral maps, we extracted the velocity and velocity dispersion values for both the neutral and ionized (i.e., Hα narrow disk-like component) ISM phases in a $\sim 1\farcs0$ pseudo-slit along the NaD major kinematic axis. The corresponding position-velocity diagrams (PV diagrams) are plotted in the upper panels of Fig. 5.11, and show a variety of shapes for the rotation curves of both ionized and neutral gas components in the inner regions (typically within 3 to 8 kpc). Similarly, in the lower panels of that figure, the velocity dispersion radial profiles are shown.

We found that for 9 out of 11 galaxies, the rotation axes of the neutral and ionized gas disks are fairly aligned, with offsets smaller than 15° (Table 5.3), although in two cases (F10409-4556 and F09437+0317 (S)) the kinematic axes of the neutral gas disks are poorly constrained. The neutral gas is found in slower rotation than the ionized gas in the majority of the cases (i.e., 8/11), while the neutral gas seems to corotate with the ionized gas in only two cases. In addition, in IRAS F06259-4780 (C) the neutral gas disk is observed in counter-rotation with respect to the ionized gas disk. In this context, it is interesting to note that a counter-rotating neutral gas component was also found in the inner few kpc of M82 (Westmoquette et al. 2012).

The radial profiles of the velocity dispersion are either flat (e.g., IRAS F18093-5744 (S)) or with considerably large deviations from what is expected for a thin rotating disk at large radii. These deviations are particularly evident in the case of IRAS F22132-3705 (with values in the range of 110-200 kms^{-1}). In Fig. 5.12, we show the comparison of the ionized and neutral V/σ ratios of the ISM-disks. We found that the neutral disks are dynamically hotter (i.e., low V/σ values, Table 5.3) than the ionized ones and, therefore, likely thicker (i.e., larger h_z). This confirms that the ionized gas resides in regions of high density close to the innermost regions of the disk, while the neutral gas is located further out.

Therefore, to estimate the h_z of the disks we follow two different approaches (as in Sect. 4.4), which are outlined in Cresci et al. (2009) and Binney & Tremaine (2008). Specifically, for the ionized disks we

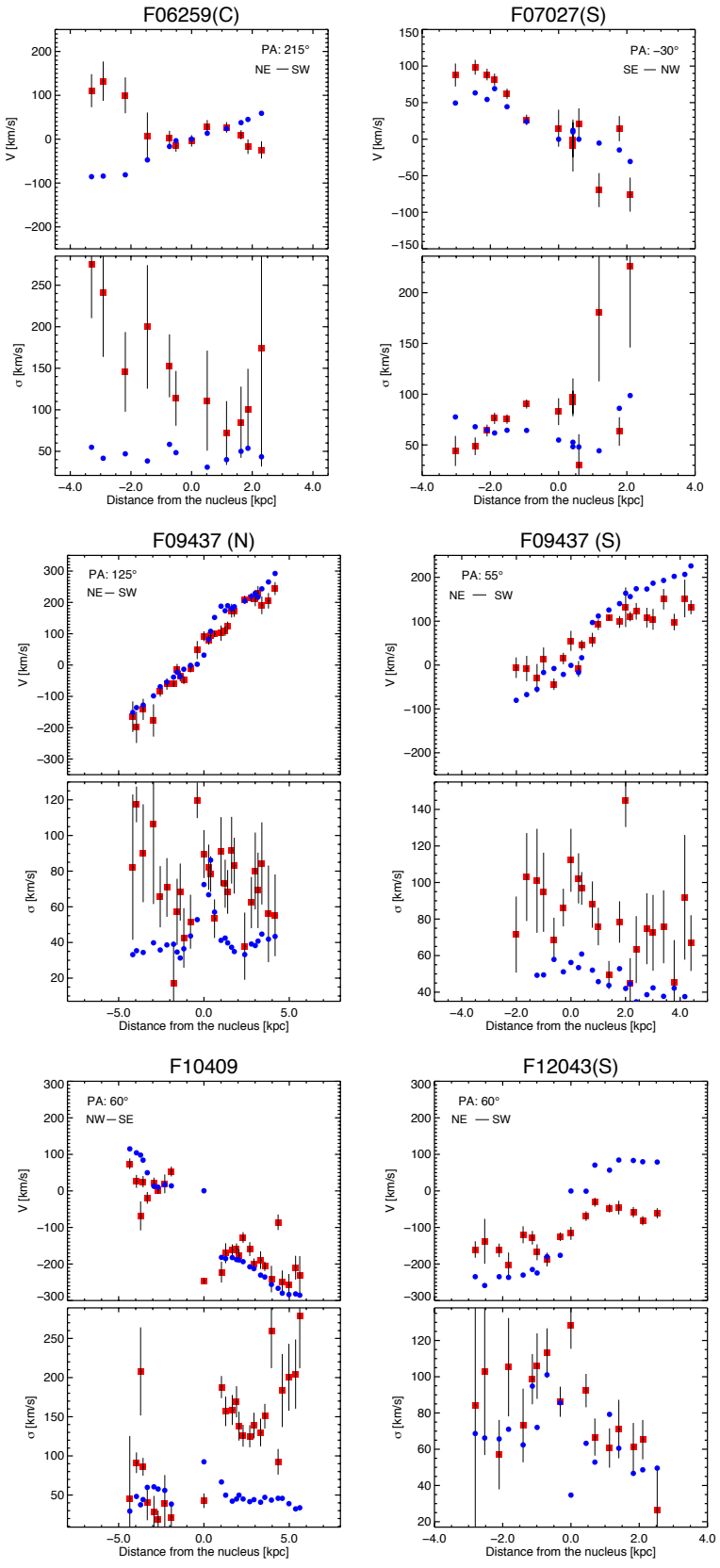
F06259(C)
PA: 215°
NE — SW
F07027(S)
PA: −30°
SE — NW
F09437 (N)
PA: 125°
NE — SW
F09437 (S)
PA: 55°
NE — SW
F10409
PA: 60°
NW — SE
F12043(S)
PA: 60°
NE — SW
V [km/s]
σ [km/s]
Distance from the nucleus [kpc]

Fig. 5.11.

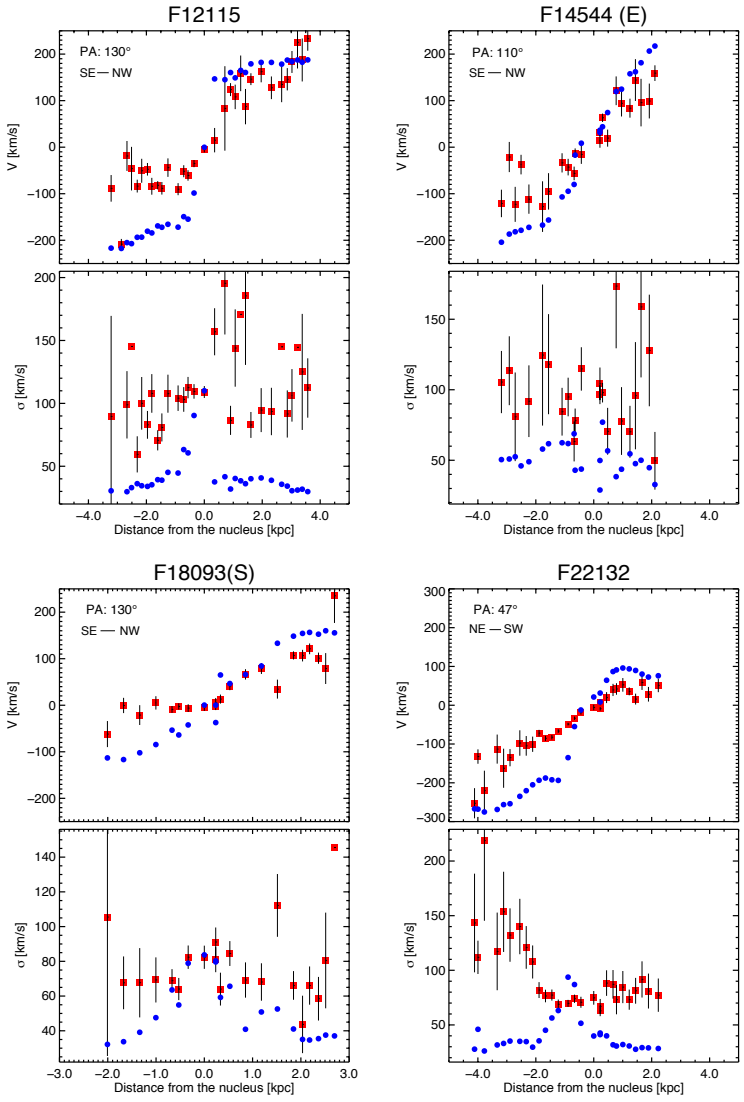

FIGURE 5.11: For those galaxies classified as disks (Table 5.3), two panels aligned vertically show the PV-curves (top) and the velocity dispersion radial profiles (bottom) along a pseudoslit aligned accordingly to the major axis of the neutral gas rotation (traced via NaD). In all the panels, the red squares and the blue circles mark, respectively, the points for the neutral and ionized gas, traced via the NaD absorption and the Hα emission (narrow component). The galaxy IDs follow that of Table 2.1, though here they are shortened for a better visualisation. Note that, the velocity fields of Hα, have been taken as reference for an ordinary rotation, and typically extend up to a radius larger than the NaD velocity field. For the detailed analysis of the ionized gas kinematics we refer to Bellocchi et al. (2013). The LIRG IRAS 11506-3851 is discussed in detail in Sect. 4.4 thus the correspondent panel is not included here.

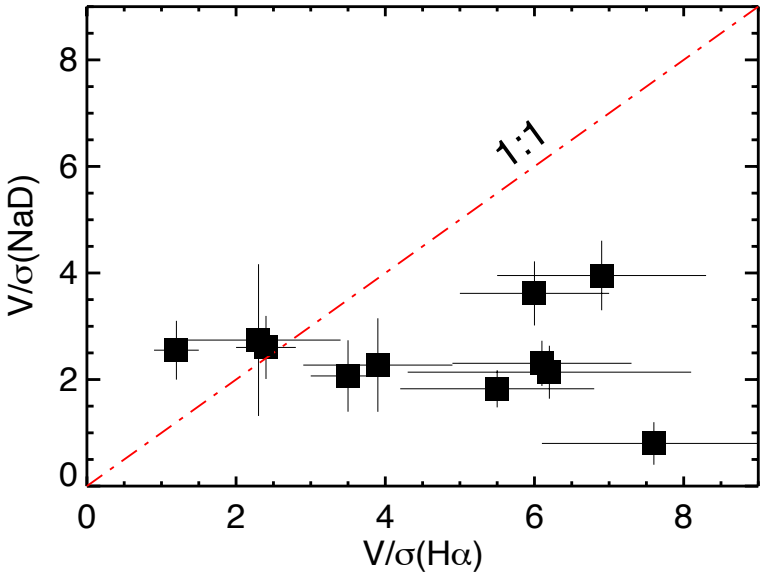

FIGURE 5.12: Comparison within the V/σ ratios of ionized and neutral ISM-disks (Table 5.3). We refer to Bellocchi et al. (2013) for the V/σ values for the ionized gas. The red dashed-dot line represents the 1:1 correlation. The neutral disks are typically thicker and more dispersion dominated with respect to the ionized ones.

used the approximation proper for thin disks (Eq. 4.1), while, for the neutral disks, we used an approximation more suitable for thick disks (Eq. 4.2). In both cases, we considered as ΔV the (inclination-corrected) semi-amplitude of the velocity field, as σ the mean velocity dispersion across the galaxy disk (excluding the nuclear regions) and a nominal radius (R) of 2 kpc. We chose this radius since it is the typical distance at which the rotation curve starts to flatten (Fig. 5.11). The results are summarized in Table 5.2. We find that the neutral gas disks are thicker by a factor up to 46 ($\sim$ 15 on average) than the ionized gas disks.
When the same approach (formula) is used for the neutral and ionized disks, the results indicate that the neutral disks are still significantly thicker (i.e., by a factor 8 on average) than the ionized disks.

5.9 Summary and conclusions

We have studied the properties of neutral gas outflows in a sample of 51 local (U)LIRGs ($z \leq 0.09$) on the basis of VLT/VIMOS IFS of the NaD feature. For the analysis, we followed two approaches. First, for each galaxy we combined the spectra in the data cube to obtain a high S/N spatially integrated spectrum. Second, for a subsample of (U)LIRGs, we analyzed the NaD spectra on a spaxel-by-spaxel basis to trace the spatially resolved 2D structure of the neutral gas. The main conclusions can be summarized as follows:

1. *Stellar and ISM contributions to the NaD feature.* We evaluated the contribution of old stars to the NaD absorption via a stellar continuum modeling (pPXF analysis) of the spatially integrated spectra. The fraction of stellar contribution ranges from about 20% to 100%, but in nearly half of the cases for which high quality modeling was possible, the NaD is mainly originated in the ISM (i.e., stellar fraction $< 35\%$). This analysis also allows us to derive a threshold of

TABLE 5.3: Kinematics and dynamical support of thick neutral gas disks.

ID1 IRAS (1)	Δ V kms^{-1} (2)	V_{shear} kms^{-1} (3)	σ kms^{-1} (4)	ΔPA degree (5)	V/σ (6)
06259-4780 (C)	78 ± 32	203 ± 105	95 ± 6	205	2.7 ± 1.4
F07027-6011 (S) ‡	87 ± 14	108 ± 51	81 ± 2	10	3.7 ± 1.1
F09437+0317 (N)	221 ± 35	227 ± 34	73 ± 2	5	3.6 ± 0.6
F09437+0317 (S)	98 ± 28	150 ± 29	82 ± 1	0	2.9 ± 0.5
F10409-4556 ‡	166 ± 22	168 ± 33	107 ± 1	0	1.8 ± 0.3
F11506-3851 ‡	83 ± 12	61 ± 22	83 ± 12	6	0.8 ± 0.4
F12043-3140 (S)	166 ± 22	130 ± 36	86 ± 2	20	2.6 ± 0.6
F12115-4656	162 ± 26	177 ± 41	100 ± 1	10	4.0 ± 0.7
F14544-4255 (E)	143 ± 36	178 ± 55	90 ± 2	10	2.1 ± 0.6
F18093-5744(S)	149 ± 43	122 ± 31	75 ± 1	5	2.6 ± 0.6
F22132-3705	212 ± 36	119 ± 28	81 ± 3	5	2.1 ± 0.5

Notes. Column (1): IRAS name. Column (2): NaD velocity amplitude defined as the half of the observed "peak-to-peak" velocity (i.e., half the difference between the maximum and minimum values is considered without applying the inclination correction) measured in the PV-diagrams. Column (3): NaD velocity shear defined as the half of the difference between the median of the 5 percentile at each end of the velocity distribution, as in Bellocchi et al. (2013) (not corrected for the inclination). Column (4): Neutral gas mean velocity dispersion. Column (5): Kinematic misalignment between the position angles (i.e., PAs) of the neutral gas rotational major axis and that of ionized gas. The kinematic PAs are derived by inspecting the ionized and neutral velocity maps. Col (6): Neutral gas dynamical ratio between the velocity shear (corrected for the inclination) and the mean velocity dispersion values. The symbol: ‡, marks the galaxies for which a two-components NaD modelling have been done (Sect. 3.3.1.1).

EW(NaD) = 1.3 Å, above which the NaD absorption in (U)LIRGs is likely dominated by the ISM. Since the results from the stellar continuum modelling on a spaxel-by-spaxel basis could be uncertain, we consider that threshold to identify regions dominated by ISM absorption in the maps.

2. *Outflow kinematics from the integrated spectra.* For the objects with a reliable stellar modeling, we generate a purely ISM NaD absorption spectrum after subtracting the stellar model. In 22 objects we measure blueshifted NaD profiles, which indicate typical neutral gas outflow velocities in the range 65-260 kms^{-1}. Excluding the galaxies with powerful AGNs, the neutral outflow velocity shows a dependency with the SFR of the type $V \propto SFR^{0.15}$, which is in fair agreement with previous results. The neutral outflow (central) velocities are significantly higher than those for the ionized gas, but they are in rather good agreement with the ionized gas maximum outflow velocities that we considered. This suggests that the wind entrains and accelerates the cold ambient gas, which is likely located at relatively large distances from the regions where the ionized gas resides. The velocity dispersions for both neutral and ionized outflows show similar median values (if the strongest AGNs are excluded).

3. *2D Neutral outflows: Detection, morphology, and kinematics.* In the neutral gas velocity fields of 22 out of 40 targets, we found clear signatures of GWs. These neutral winds are conical in shape in 12 out of 22 objects. For the remaining objects, we were not able to constrain the morphology mainly owing to projection effects. We generally observe collimated outflows with

$C_\Omega \sim 0.4$ .The inclination-corrected outflow velocities of the neutral gas entrained in GWs is in the range $\sim$ 80-700 kms^{-1}, except for the ULIRG IRAS F06206-6315 for which the typical wind velocity exceeds 1000 kms^{-1}. The typical velocity dispersions are in the range $\sim$ 95-190 kms^{-1} (i.e., 230-460 kms^{-1} in FWHM), indicating either that a wide range of velocities are integrated along the line of sight or that these winds are turbulent. The V-SFR relation inferred for the 2D analysis is similar to that obtained from the integrated spectra. No clear correlation is seem between the outflow velocity and the dynamical mass.

4. *GWs Feedback: Slowed star formation and gas recycling.* Based on a simple FW model, we found that the wind mass estimates range from 0.4×10^8 $M_\odot$ to 7.5×10^8 $M_\odot$ (1.6×10^8 $M_\odot$, on average), reaching up to $\sim 3\%$ of the dynamical mass of the host. The mass rates are only $\sim$ 0.2-0.4 times the corresponding SFR in most cases indicating that, generally, mass losses are small for slowing down significantly the star formation. The derived mass loading factors ($\eta = \dot{M}_\mathrm{w}/\mathrm{SFR}$) correlate better with the starburst infrared luminosity ($r_\mathrm{PC} \sim$ -0.6) than with the host galaxy mass ($r_\mathrm{PC} < 0.1$). The comparison of the median wind velocity and host escape velocity indicates that, in the majority of the cases, most of the outflowing neutral gas rains back into the galaxy disk. We found that on average $V_\mathrm{w}/v_\mathrm{esc}$ is higher in less massive galaxies, confirming that the galaxy mass has a primary role in shaping the recycling of gas and metals. We also found a tendency in the sense that $V_\mathrm{w}/v_\mathrm{esc}$ is higher in more turbulent and thicker ionized gas disks.

5. *GWs power source.* The comparison between the wind power and kinetic power of the starburst associated with SNe indicates that the starburst could be the only main driver of the outflows in nearly all the (U)LIRGs galaxies, as wind power is generally lower than 20% of the kinetic power supplied by the starburst. In the case of IRAS F06206-6315, the outflow is likely AGN driven, as also indicated by its kinematics.

6. *Kinematics of disks.* A significant number of (U)LIRGs (11/40) show spider diagrams, such as neutral gas velocity fields, plus rather irregular velocity dispersion maps in one kinematic component. The comparison between the rotation curves of the ionized and neutral disks indicates that the neutral disk lags compared to ionized disk in the majority of the cases (i.e., 8/11). While in two cases the neutral gas seem to nearly corotate with the ionized gas, we also find a case (IRAS F06259-4780 (C)) in which the neutral gas disk counter-rotates with respect to the ionized disk. Our kinematics measurements indicate that nearly all the neutral gas disks are dynamically hotter and thicker (by a factor up to 46, 15 on average) with respect to the ionized disks.

Chapter 6

Investigating positive feedback in the ULIRG IRAS F05189-2524

In this section the near-IR IFS-analysis of the kinematics and ionization mechanism of the outflow caught in act in the ULIRG IRAS F05189-2524 are presented.

6.1 The ULIRG IRAS F05189-2524 as a candidate for testing the positive feedback

IRAS 05189-2524 is well known nearby ULIRG whose main basic properties are summarized in Table 6.1. This warm ULIRG ($f_{25}/f_{60} \sim 0.25$, Papadopoulos et al. 2012) is classified as a late stage merger from optical imaging (Veilleux et al. 1999). It has as a very compact nucleus as seen in radio to X-ray imaging, with a prominent tidal structure extended up to 10-15 kpc. It consists of east-west and north-south tidal loops which are visible only in UV and optical images. A compilation of some of archival images at different wavelength is shown in Fig. 6.1.
The ground based UV/optical long-slit spectroscopy by Farrah et al. (2003), showed the presence of two compact and optically luminous knots. One of them contains a prominent AGN plus a young (3-4 Myr) starburst with a large population of Wolf-Rayet stars as indicated by the detection of N IV] λ 1488 UV line by Farrah et al. (2003). Spectroscopic observations of broad emission lines at optical, IR (e.g., SED fitting Farrah et al. 2003) and X-ray wavelength (Risaliti et al. 2000; Imanishi & Terashima 2004), also suggest the presence of an AGN (optically classified as Sy 2). At mid-IR wavelength, the compact nucleus is marginally resolved and no host emission was detected in Spitzer IRAC 5.8 and 8.0 μm and MIPS 24 μm images (Asmus et al. 2014, Fig. 6.1, top-right). The AGN in this ULIRG is X-ray luminous with $L_{x\,(2-10\,keV)} \sim 1.3 \times 10^{43}$ ergs s^{-1} (Dadina 2007). However, the X-ray nuclear emission detected in Chandra observations is not resolved (Ptak et al. 2003, Fig. 6.1, bottom-right). An extended hard X-ray emission is also detected beyond the nuclear region on scales of $\sim$ 10 kpc, but its contribution to the total hard X-ray flux is low ($\sim$ 10 %, Ptak et al. 2003). In summary, all these observations suggest that in this ULIRG starburst and AGN coexist with the latter able to provide a significant fraction ($\sim$ 70 %; Veilleux et al. 2009) of the total IR luminosity.

TABLE 6.1: General properties of IRAS F05189-2524

Properties	value	References
z	0.0425	Huchra et al. (1983)
D_L [Mpc]	188.2 [a]	
scale [pc/arcsec]	839 [a]	
$\log(L_{IR}/L_\odot)$	12.19 [b]	Rodríguez-Zaurín et al. (2011)
SFR [$M_\odot\,yr^{-1}$]	190 [c]	
Inclination angle	$(18 \pm 9)^\circ$	Bellocchi et al. (2013)
Nuclear Spectral Class.	Sy 2	Surace & Sanders (2000); Veilleux et al. (1999)

Notes. [a] Luminosity distance and scale using Edward L. Wright Cosmology calculator (Wright 2006). [b] IR-luminosity in solar bolometric luminosity and logarithmic units. As in Table 2.1, the IR-luminosity is defined as $L_{IR} = L_{(8-1000\,\mu m)}$ and calculated using the fluxes in the four IRAS bands as given in Sanders et al. (2003). [c] Star formation rate computed from the IR-luminosity. Arribas et al. (2014), calculated a SFR of 50.2, considering the reddening corrected Hα Luminosity (from Rodríguez-Zaurín et al. 2011) transformed for a Chabrier (2003) initial mass function.

No evidence of rotation is seen via either Hα line or NaD absorption. In particular, the velocity field and velocity dispersion map of the narrow component of Hα line show evidence of radial motions and disturbed velocity dispersion distribution. A broad ($\sigma \sim 270\,kms^{-1}$, on average) H$\alpha$ kinematic component is found outflowing at velocities $\sim 380\,kms^{-1}$ (on average, Fig. A.5) in the inner ~ 3 arcsec, overlapping the region where a neutral outflow has also been found at similar velocity ($\sim 360\,kms^{-1}$, on average, Table 5.1). Blue shifted broad lines are also seen via high ionization lines of [O III], [Ar III] $\lambda\lambda$ 7127, 7752 and [S III] $\lambda\lambda$ 9069, 9531 (Westmoquette et al. 2012 and reference therein). The fact that the outflow is found via the recombination and forbidden emission lines and absorption lines rules out an AGN broad-line-region origin (Westmoquette et al. 2012), supporting the presence of a galactic outflows, likely driven by the AGN. Additionally, the outflow carries a large amount of dust as found by Rupke & Veilleux (2015) via optical-IFS. The multiphase nature of the outflow caught in act in the present VIMOS-IFS observations is supported by the molecular outflow found by Veilleux et al. (2013) via OH 119 μm line (Herschel data). The outflow has been found with peak and maximum velocities up to ~ 350 and ~ 850 kms^{-1}.

Accordingly to the feedback-models of Ishibashi & Fabian (2012) and Zubovas et al. (2013), the molecular gas in the AGN driven molecular outflow of IRAS F05189-2525 may undergo vigorous star formation as a consequence of gas compression. This ULIRG, is therefore, one of the nearest and best laboratory for studying such potential positive feedback in the outflow.

6.2 Line measurements and kinematics

Once we reduced near-IR SINFONI IFS-data (Sect. 2.2.2), we have removed the stellar continuum emission from H-band spectra in the cube following the procedure described in Sect. 3.2.1, to properly model the [Fe II] emission line profiles. An example of the stellar modelled spectra (and its subtraction) is shown in Fig. 3.3 (middle panel). Then, we have identified in the IFS-spectra the four emission lines under study: Paα, Brγ, H_2[1] and [Fe II] and visually inspect their line profiles. These are typically broad and asymmetric, as commonly observed among AGN spectra, and a single gaussian (i.e., one per emission line) fits cannot account for such complex line profiles. We therefore decide to model all

[1] In this Chapter, we only study the Hydrogen line (1-0)S(1) at 2.121 μm, as mentioned in Sect. 3.1 but other H_2 lines are however present in our data. If not otherwise specified, the [Fe II] is the $^4D_{7/2}$-$^4F_{9/2}$ transition at 1.644 μm (see Sect. 3.1).

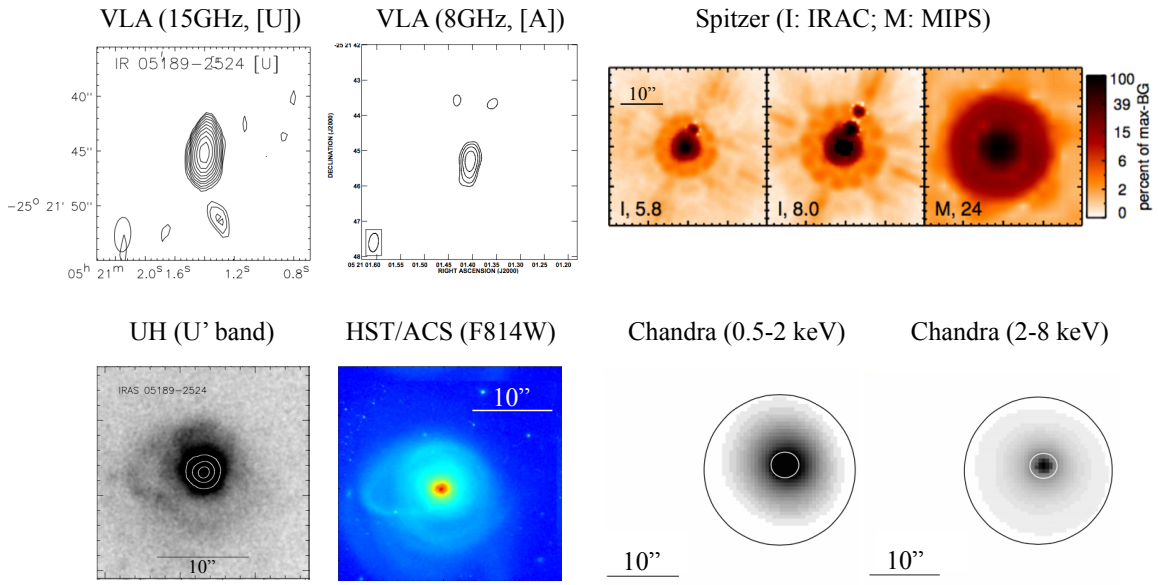

FIGURE 6.1: Compilation of images of the ULIRG IRAS F05189-2524. North is up, and east is to the left in all images. *Top-left:* Contour maps for archival Very Large Array in band U (left) and A (right). Images from Thean et al. (2000) and Clemens et al. (2008), respectively. *Top-right:* From left to the right, Spitzer mid-IR images at 5.8, 8.0 and 24 μm from Asmus et al. (2014). The apparent off-nuclear compact sources in the first two images are instrumental artefacts. *Bottom-left:* UV (left) and optical (right) images from Surace & Sanders (2000) and Bellocchi et al. (2013), respectively. The UV image is achieved with the Orbit camera of the University of Hawaii 2.2-m telescope on Mauna Kea with the U' filter ($\lambda_{\rm central} = 3410$ Å). The logarithmic contours illustrate the flux-structure where regions are saturated (due to the gray-scale). The optical image is acquired with HST-ACS with the filter F814W. *Bottom-right:* The 0.5-2.0 and 2.0-8.0 keV Chandra X-ray images (scaled logarithmically) from Ptak et al. (2003), left and right respectively. The outer and inner ellipses show global and nuclear regions analyzed in Ptak et al. (2003).

the line profiles with two kinematic components (a couple of Gaussian) as described in Sect. 3.3.1.2. The two components can be distinguished according to their velocity and widths as narrow-systemic and broad-blue shifted components.

We have made several attempts to fit the four emission lines on spatially resolved basis, but the broad component was in some cases difficult to detect (especially for the weaker lines). To accurately measure emission line kinematics and fluxes, the IFS-spectra have been smoothed with a three-spaxels boxcar average and then integrated. For this step, we consider four regions (R), selected in order to avoid AGN contamination (so the central 2×2 central spaxels are excluded) and to cover the area where a broad asymmetric Paα emission line was detected[2] contiguously. Figure 6.2 shows the K-band continuum with highlighted the four selected regions, the corresponding lines profiles are shown in Fig.6.3.

Given the complexity of the line profiles, and after experimenting with a two-components Gaussian fit, we decided to fit simultaneously the kinematics of the four emission lines. As a reference for the velocity dispersion, we first consider the average velocity and velocity dispersion of Hα derived by our optical-IFS but the modelling leads to unphysical or non-unique solutions. In order to preserve against spurious results, the kinematic of the broad component of Paα has been allowed to vary within 3-σ of that of Hα (i.e., within 90 and 55 kms^{-1}, for velocity and velocity dispersion, respectively).

[2]The modelling of Paα with two components in IFS-spectra was not always satisfactory and in some cases discrepancies with the broad component seen in other lines were evident. However, since it the strongest line among those selected for the study, we consider the asymmetries in Paα line-profile to flag the spaxels where a broad component is present. The area covered by this component is $3\farcs0\times2\farcs5$.

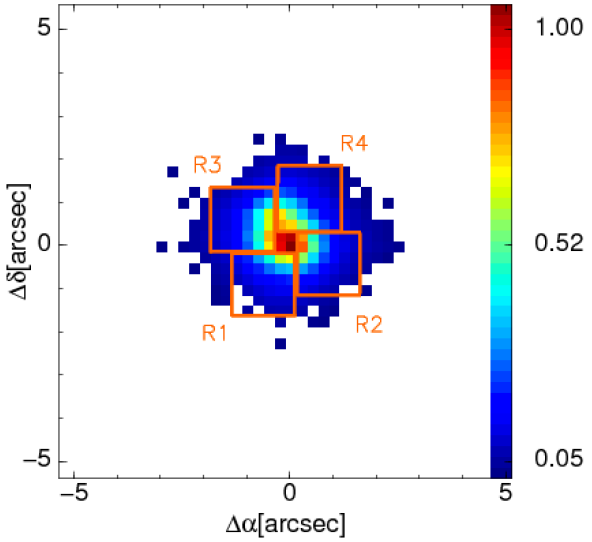

FIGURE 6.2: Continuum image scaled to the intensity of brightest spaxels in the K-band (i.e., the nucleus). Red boxes mark the regions (R) selected for the analysis.

This is justified by the fact that, as a consequence of differential dust extinction, optical and near-IR lines may have different profiles. On the one hand, a broad component seems to exist at Hα velocity (although with substantially lower velocity dispersion). On the other hand the modelling leaves for al the emission lines strong residuals in the red part of the line profiles. We then consider the results obtained modelling the Paα line in region 3 as reference, since this modelling, already, gives low residuals without any kinematical constraints. We obtained integrated measurements of the velocity, velocity dispersion and fluxes of the emission lines observed in the four different regions. We found that the narrow component is generally within -55 and 65 kms^{-1} with respect to the systemic and with velocity dispersion lower than 135 kms^{-1} except two cases – i.e., the iron line in region 3 and 4. The broad component is found, in all the four regions, at generally lower outflowing velocity (in the range 60-120 kms^{-1}, except in R1) with respect to what found in the present and previous works using other tracers (Sect. 6.1) but at similar velocity dispersion ($\sim$ 325 kms^{-1}, on average) within uncertainties. The kinematics of the narrow and broad components is summarized in Table 6.2. The fluxes measurement are treated in the next section when addressing the gas ionization/excitation mechanisms.

6.3 Testing the occurrence of star formation in outflows with near-IR emission line-ratios

The outflowing ISM can be ionized by many different mechanisms, which can be discriminated via optical and IR line-ratios (selected to be essentially unaffected by reddening). These are often used as diagnostics for the hardness of the ionizing radiation or other physical properties such as metallicity, electron density and electron temperature. The Baldwin, Phillips and Terlevich diagram (hereafter, BPT-diagram, Baldwin et al. 1981) is the empirically derived diagnostic diagram based on optical emission line ratios as [O III]/Hβ vs. [N II]/Hα (alternatively, [S II]/Hα or [O I]/Hα), which have been studied ever since to identify emission line regions/galaxies. On the basis of the principal excitation

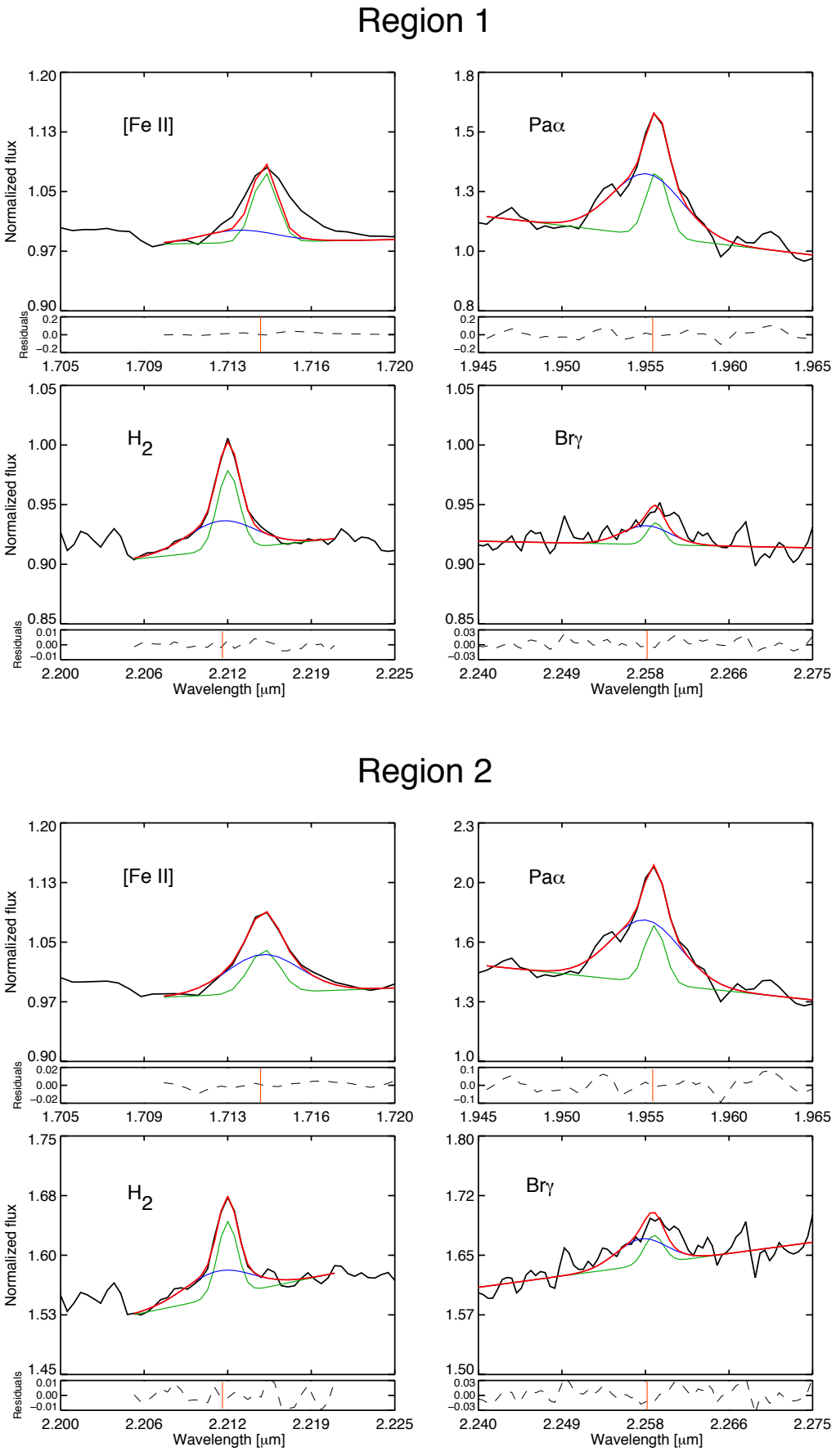

FIGURE 6.3: Line fitting of emission lines observed in the four selected region of the ULIRG IRAS F05189-2524. The narrow component is shown in green, while the broad one is shown in blue. The red curve shows the total contribution coming from the Gaussian fit. Below, the residuals (i.e., data - model) are presented.

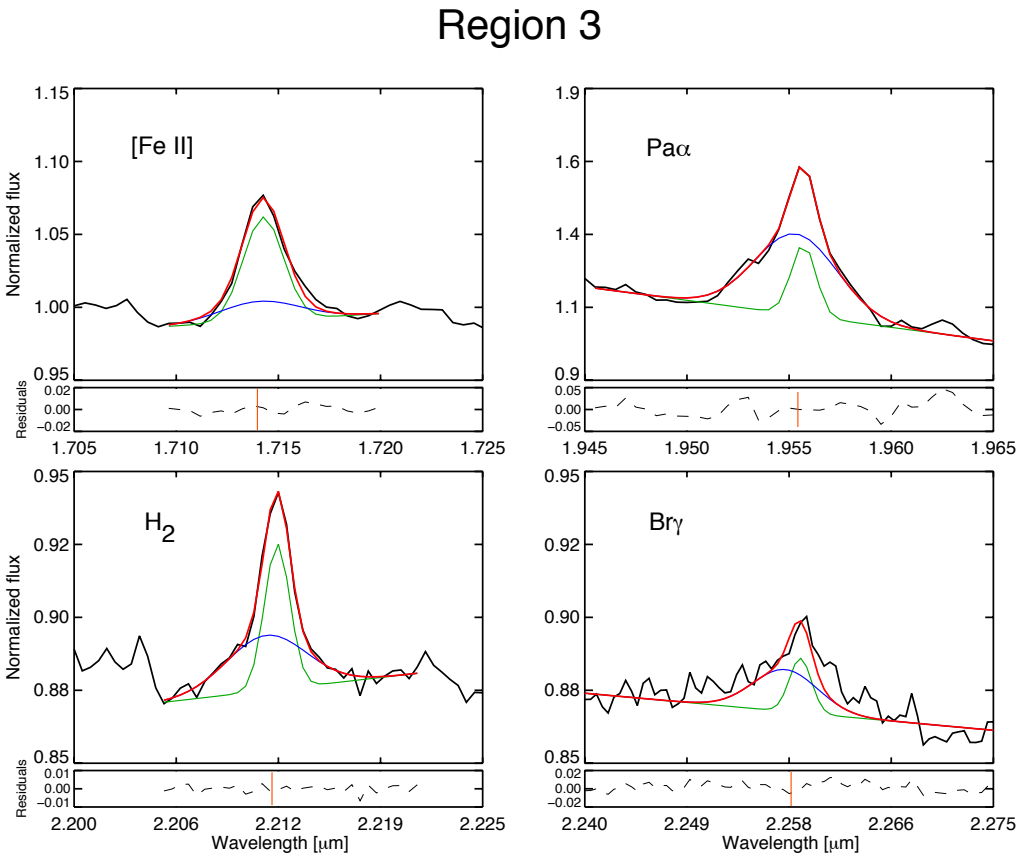

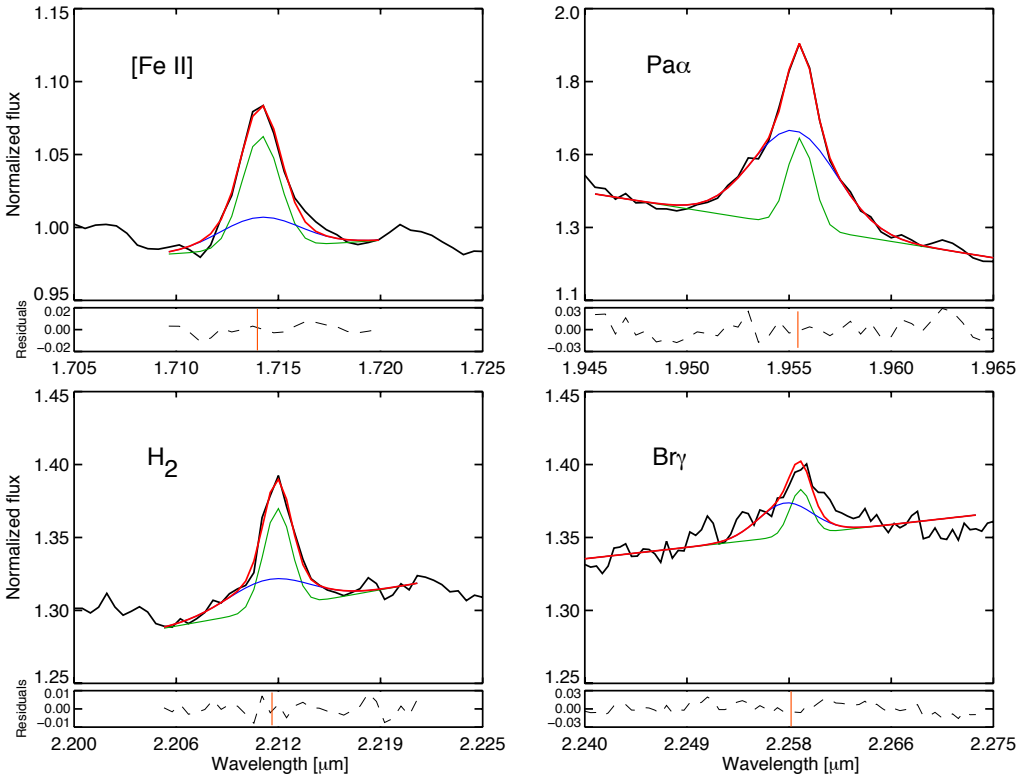

Fig. 6.3 – Continued.

TABLE 6.2: Kinematic measurements in IRAS F05189-2524

	Region 1			
	Narrow		Broad	
	V	σ	V	σ
[Fe II]	-49 ± 15	96 ± 22	-263 ± 32	288 ± 39
Paα	-7 ± 13	99 ± 18	-102 ± 31	322 ± 36
H_2	14 ± 4	111 ± 6	-63 ± 13	341 ± 68
Brγ	76 ± 81	115 ± 68	-62 ± 13	336 ± 66
	Region 2			
	Narrow		Broad	
	V	σ	V	σ
[Fe II]	-55 ± 11	120 ± 27	-63 ± 30	285 ± 18
Paα	-28 ± 12	95 ± 16	-118 ± 25	322 ± 30
H_2	5 ± 7	100 ± 9	-92 ± 18	340 ± 68
Brγ	48 ± 10	134 ± 27	-131 ± 26	345 ± 69
	Region 3			
	Narrow		Broad	
	V	σ	V	σ
[Fe II]	-36 ± 10	171 ± 12	-62 ± 12	341 ± 68
Paα	-4 ± 5	93 ± 10	-63 ± 10	309 ± 18
H_2	-3 ± 5	106 ± 8	-97 ± 19	331 ± 56
Brγ	62 ± 12	125 ± 25	-117 ± 23	369 ± 73
	Region 4			
	Narrow		Broad	
	V	σ	V	σ
[Fe II]	-54 ± 11	161 ± 22	-62 ± 12	341 ± 68
Paα	-27 ± 5	98 ± 8	-76 ± 9	316 ± 14
H_2	-2 ± 7	114 ± 9	-77 ± 15	341 ± 68
Brγ	63 ± 13	120 ± 24	-117 ± 23	310 ± 62

Notes. Derived velocity (V) and velocity dispersion (σ) in kms^{-1} for the narrow and broad components for each of the emission lines profile extracted from the four regions displayed in Fig. 6.3.

mechanism, the BPT-diagram separates emission line regions/galaxies into 4 different categories: star-forming HII regions/galaxies, Sy 2 galaxies, LINERs and intermediate or composite regions/galaxies (Kewley et al. 2006 and reference therein).

As mentioned, most of the study of the excitation and ionization of ISM in galaxies are widely based on optical BPT-diagrams, and works based on near-IR emission lines ratio have been more limited. At near-IR wavelengths, the diagnostic diagram based on the ratios [Fe II] λ 1.257μm/Paβ λ 1.282μm[3] vs. H_2/Brγ is an efficient tool for separating emission-line objects according to their dominant type of activity, the starburst or the AGN (Riffel et al. 2013 and reference therein). Iron lines probe SNe-shocked gas and environments irradiated by X-rays, while hydrogen lines directly trace the gas ionized by young massive stars (Dale et al. 2004). Thus the [Fe II]-to-hydrogen line ratio can be interpreted as indicator to the age of SF. The horizontal axis (H_2/Brγ) discriminate between SNe-shocks or hard X-ray heating from power-law sources (Larkin et al. 1998; Dale et al. 2004). By studying this diagram, Dale et al. (2004) found that there is an approximate trend proceeding from the upper right to the lower left of increasing SF activity and decreasing AGN activity.

In Fig.6.4 (top) we present the diagnostic diagram for the selected four regions in IRAS F05189-2524 based on the line measurements described in Sect. 6.2. The observed [Fe II]/Paα ratio was converted into [Fe II] λ 1.257μm/Paβ by assuming the case B recombination (coefficients from Draine 2011). Therefore, [Fe II] λ 1.257μm/Paβ = 2.77 × [Fe II] λ 1.644μm/Paα.

[3] At the redshift of IRAS F05189-2524, [Fe II] λ 1.257μm and Paβ are shifted into the J-band (Table 2.3).

Inspection of Fig. 6.4 indicates that the ratios for the narrow component of all the four regions are indicative of AGN dominance, though the [Si VI] λ 1.964μm (known to exist in AGN, e.g., Maiolino et al. 1998) is undetected. Similarly, for the broad component the ratios lie in the area which identify AGNs but a substantially lower [Fe II] λ 1.257μm/Paβ, where no data from the literature are present. We studied this intriguing result with an alternative diagram which has been, recently, proposed by Colina et al. (2015) to investigate the excitation structure of the ISM. These authors study the distribution of line ratios for different galaxies dominated by SF, AGN or composite and select corresponding prototype regions in near-IR SINFONI IFS-maps of local (U)LIRGs in the [Fe II]/Brγ-H_2/Brγ plane. They found that also spatially resolved regions with different extinction mechanism have different ratios (which are slightly different with respect to previous works, e.g., Riffel et al. 2013). We plot our measurements in their diagnostic diagram in Fig. 6.4 (bottom). As in the Riffel et al. (2013) diagram, the ratios for both broad and narrow components lie in the AGN area excluding the dominance of ionizing radiation from young ionizing stars. However, also in this case, no regions in Colina et al. (2015) have ratios similar to those observed in the ULIRG IRAS F05189-2524. Compared with the results of Riffel et al. (2013) and Colina et al. (2015), our measurements seem to present either an [Fe II] emission deficit or H_2 excess.

6.4 Conclusions

We presented near-IR H+K spectroscopy of the ULIRG IRAS F05189-2524 to test the positive feedback scenario proposed by Ishibashi & Fabian (2012) and Zubovas et al. (2013). To this purpose, we have studied the kinematic and dominant ionization/excitation of the multiphase outflow in this ULIRG using Paα, Brγ, H_2 and [Fe II] emission lines. The conclusions of the present study can be sumarized as follows:

1. — *Outflow kinematics.* The multi-components decomposition near-IR emission lines has shown that an extended broad and outflowing component is present at velocities in the range 60-120 kms^{-1} (except in R1) and with a large velocity dispersion ($\sim$ 325 kms^{-1}, on average) in partial agreement with previous works.

2. — *Ionization mechanism of the gas in the outflow.* We found that the mechanism of excitation of both narrow and broad components the AGN-photonization and not SF. However, by using two different diagnostic near-IR diagrams we found that our measurements indicate either an [Fe II] emission deficit or H_2 excess, which will be investigate in the future (e.g., studying the [Fe II]/Brγ vs. [O I] λ6300 /Hα plane as in Dannerbauer et al. 2005).

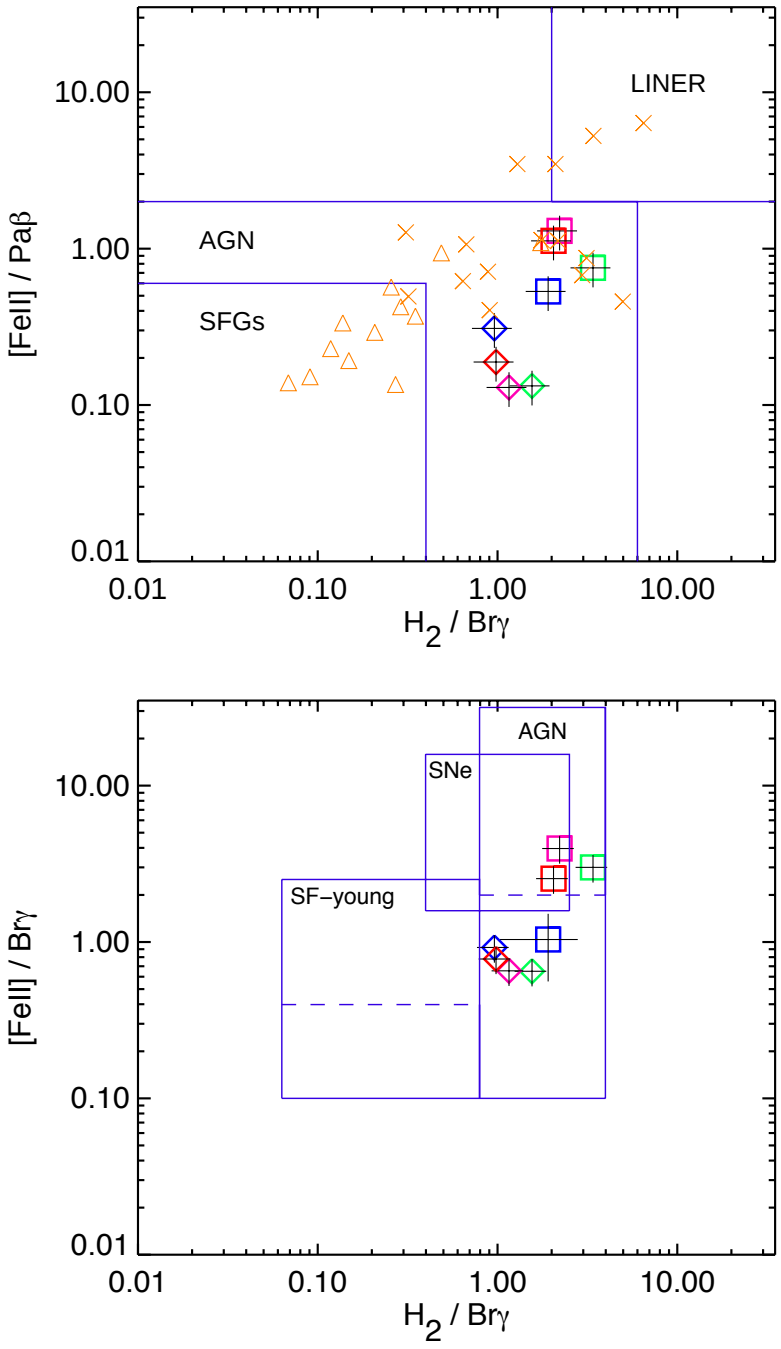

FIGURE 6.4: Near-IR diagnostic diagrams based on near-IR line ratios as in Riffel et al. (2013) and Dale et al. (2004) (top), and Colina et al. (2015) (bottom). For both panels, purple boxes identify the areas defined by the authors to identify regions dominated by AGN, LINERs, young ionizing stars or starbursts (SF-young and SB, respectively), and SNe explosions (which are named accordingly, in the plot). Squares and diamonds, indicate respectively, points for the broad and narrow components in IRAS F05189-2524. The ratios for four regions are indicate with different colours: green (R1), blue (R2), magenta (R3) and red (R4). In the top panel, orange symbols indicate the data point in Riffel et al. (2013), specifically triangles are SFGs and crosses AGNs. In the lower panel, dashed lines limit where the ratios of the observed data-points lie.

Chapter 7

Future work

We have presented the analysis of spatially integrated and spatially resolved kinematics of the outflowing ISM-gas in a sample of nearby (U)LIRGs. This study shows that these galaxies are capable of powering kp-scale outflows that can impact the evolution of their host galaxies (by regulating SF and AGN activities) and of the surrounding-IGM. However, a number of key questions about outflows and feedback remain still to answer. The main outstanding issues that are going to be addressed in on-going and future projects are:

Investigating the occurrence of SF in outflows in a larger sample of local ULIRGs.
As mentioned in Sect. 2, IRAS F05189-2524 is part of a sample of 5 galaxies selected for being in a significant outflowing molecular phase. Four galaxies were observed either SINFONI or NICS, while only one (i.e., IRAS F13120-5453) have both set of observations.
For the galaxies observed with SINFONI (IRAS F10565+2448 and F13120-5453), we will apply a similar data-treatment as for IRAS F05189-2524. Results from a preliminary analysis indicate that the narrow component of [Fe II], Paα, $H_2$1-0 S(1) and Brγ emission lines in these ULIRGs is dominated by rotation (as shown in the velocity and velocity dispersion maps in Figures 7.1 and 7.2). The second broad component is detected in a large number of spaxels but is difficult to constraint without increasing the S/N of single spectra – e.g., via Voronoi binning or boxcar average, as in the cases of IRAS F11506-3851 (Sect. 4.1.1.1) and IRAS F05189-2524 (Sect. 6.2), respectively.
Of the three galaxies observed with NICS (whose spectra are shown in Figures 7.3 and 7.4) only for IRAS F13120-5453 and MRK 231 we have both H and K near-IR data. For these galaxies, we will able to obtain the two diagnostic diagrams based on line ratios, described in Riffel et al. (2013) and Colina et al. (2015) as in the case of IRAS F05189-2524 (Sect. 6.3). Of particular relevance is the case of MRK 231. On the one hand, in the NICS K-band spectrum (Fig. 7.3, bottom) Paα shows a prominent blue wing which can be used to constrain the kinematics of the broad component of the other (weaker) lines. On the other hand, the results obtained studying the dominant source of ionization of the outflowing gas (as in Sect. 6.3) can be compared to the large amount of ancillary data available for this galaxy. We will dedicate a slightly different analysis to IRAS F08572+3915. This galaxy is observed only in the K-band with lower S/N with respect to the other galaxies (Fig. 7.4, top).

Quantifying outflow feedback on large scale in four local LIRGs.

As mentioned in Sect. 2.1, sufficiently strong outflows may enrich the IGM and explain, for example, the missing baryon problem (Silk 2003). We are going to study the IGM in the ∼100 kpc around four local LIRGs (GCT-OSIRIS data not yet delivered, PI: M. Pereira Santaella) by studying the NaD absorption in background galaxies, looking for a kinematic signature of LIRG's outflows. If detected, we will be able to quantify the feedback – i.e., IGM-enrichment, in relation with the properties of the host (e.g., SFR or AGN luminosity). The possibility to observe tens of background objects simultaneously with the OSIRIS MOS mode (as shown in Fig. 7.5), makes this study relevant since, previous works are generally limited to one line of sight.

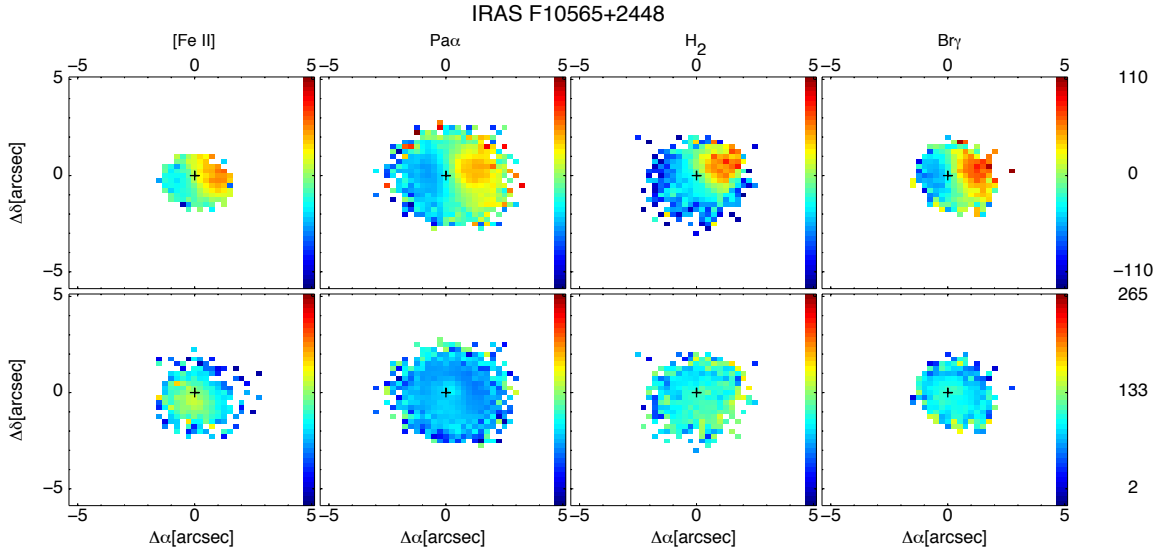

FIGURE 7.1: Velocity and velocity dispersion maps of the four near-IR emission lines observed in IRAS F10565-2448, top and bottom panels respectively. Maps are in kms^{-1} units. A cross marks the brightest spaxel in the K-band.

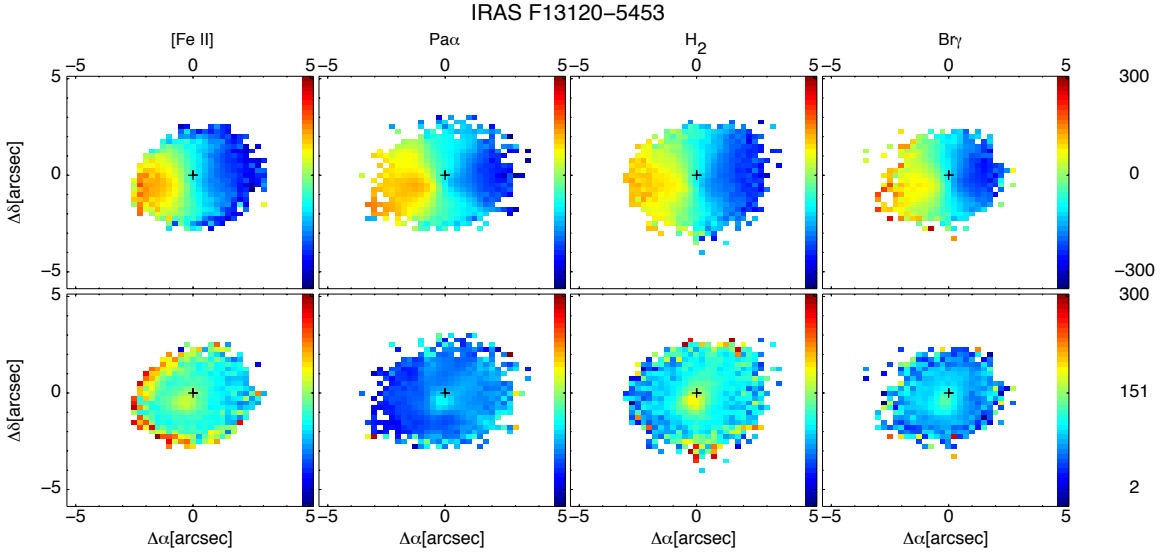

FIGURE 7.2: The same as in Fig. 7.1 but for IRAS F13120-5453.

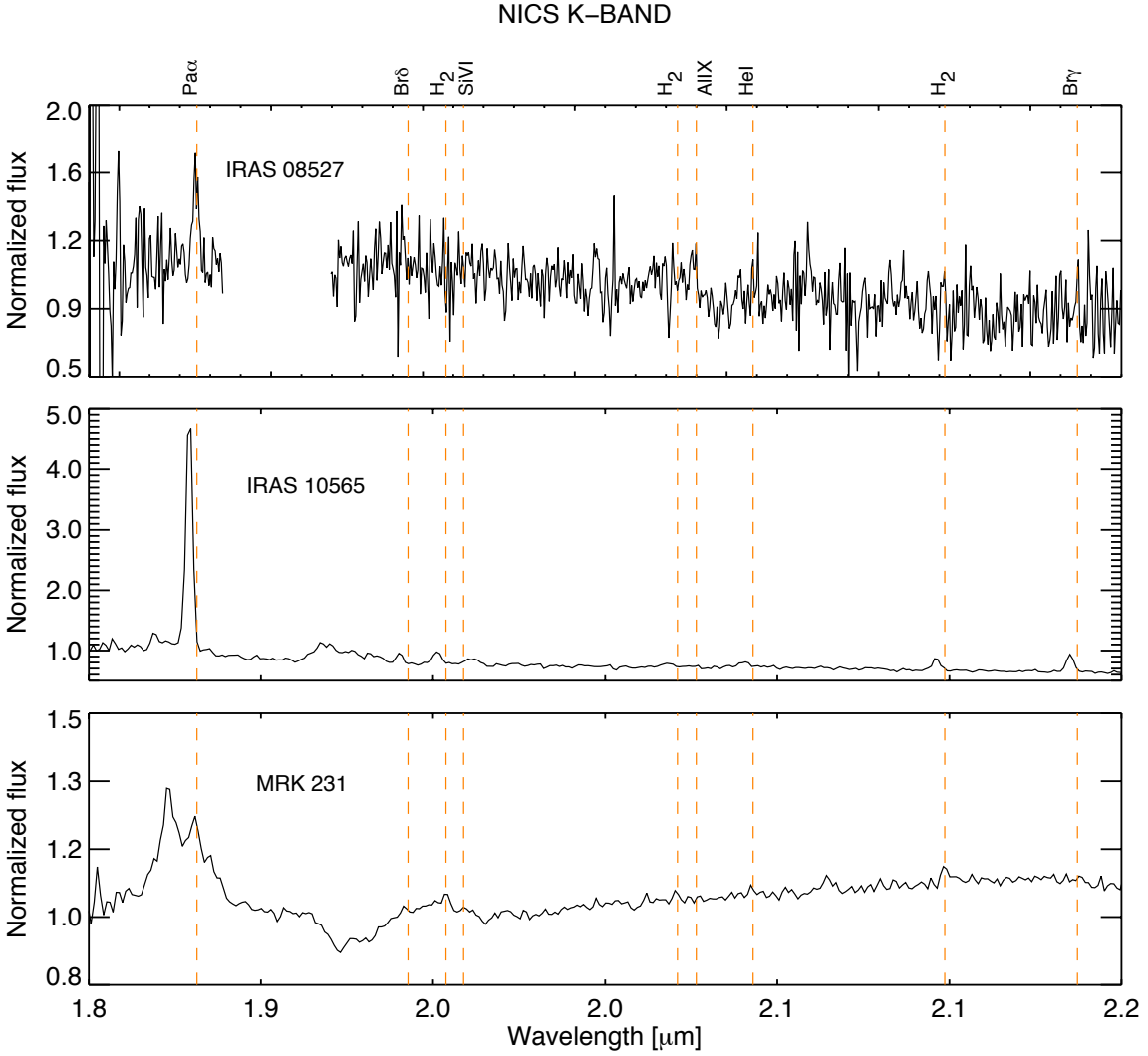

FIGURE 7.3: NICS K-band long slit (rest frame) spectra for three ULIRGs. From top to the bottom: IRAS F08572+3915, IRAS F10565-2448 and MRK 231 (the name in the panel is shortened for a better visualization). The most relevant spectral features are labeled at the top and marked with a dashed orange line. In the top panel, we excluded the spectral region within 1.88-1.95 μm, the (noisy) spectral region within 1.88-1.95 μm, have been excluded to aid in clarity of display.

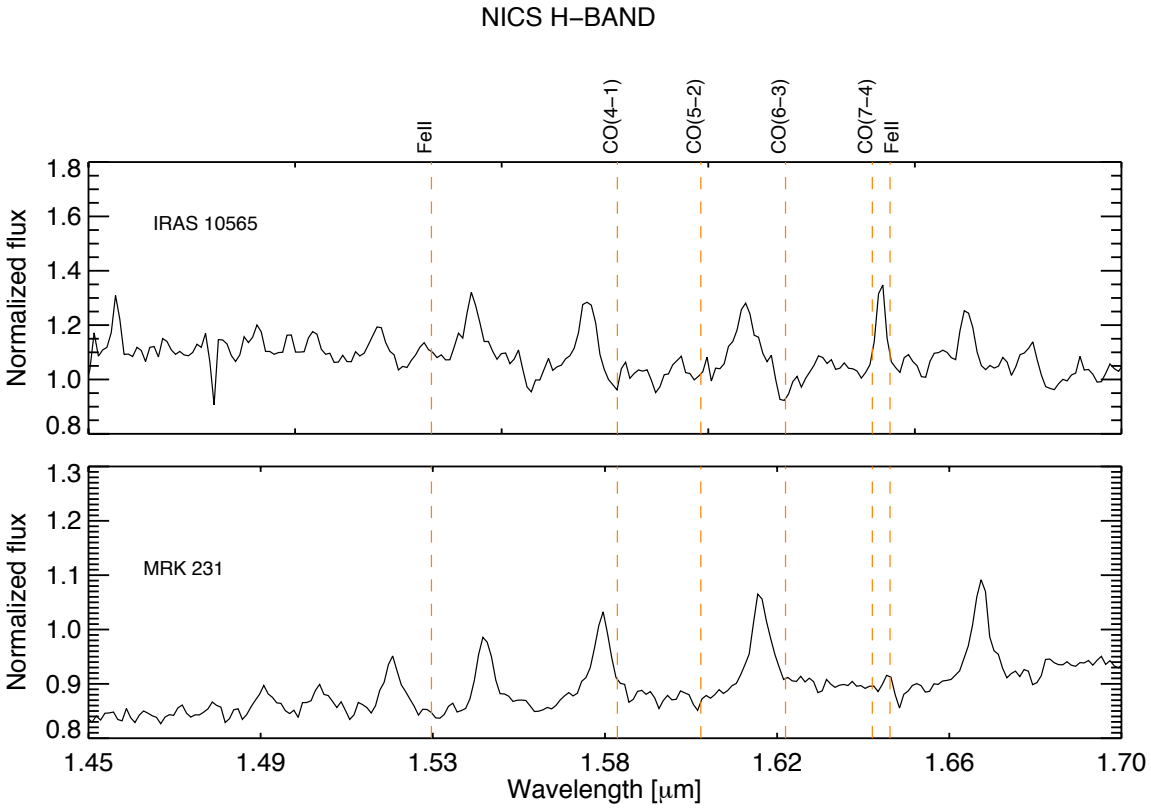

FIGURE 7.4: The same as in Fig. 7.3 but for the NICS H-band long slit (rest frame) spectra for the ULIRGs IRAS F10565-2448 (top) and MRK 231(bottom). The noticeable emission lines are of the Bracket series, but are not studied in detail in this thesis.

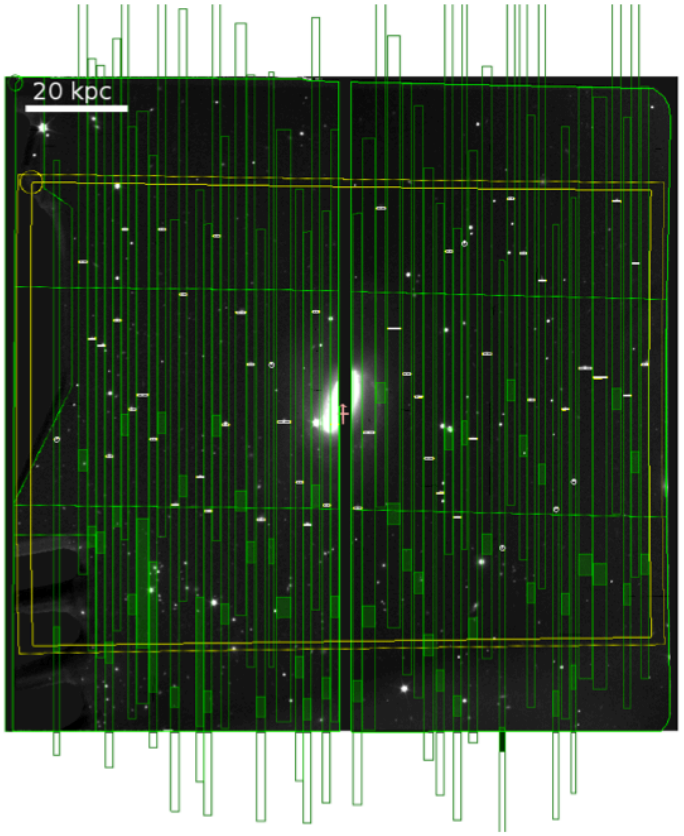

FIGURE 7.5: Design of the OSIRIS MOS mask for the LIRG NGC 23. The background objects are 37 (plus six fiducial stars which are used for the mask alignment). The background objects are selected based on their R-band magnitude (< 22 mag) and their location (to cover uniformly the FoV). Rectangular slits are $1\farcs2 \times 5\farcs0$.

Chapter 8

Conclusions

One expectation of the standard hierarchical galaxy formation scenario is that the history of the baryonic matter in galaxies should parallel that of their parent dark matter haloes. Nevertheless, the observed galaxy stellar mass function shows a break at both low and high mass ends with respect to predictions indicating the need of a feedback/regulation mechanism. Outflows have been proposed as an effective way to quench (and enhance) star formation (SF) and active galactic nuclei (AGN) activities providing a direct way of connecting the small spatial scales of sources to the surrounding environment (on kpc scale). Outflows are ubiquitous at any redshift but local samples are crucial to understand their properties. In this thesis, I investigated the importance of feedback phenomena in the evolution of local extremely star forming galaxies such as luminous and ultraluminous infrared galaxies ((U)LIRGs). These are important galaxy populations for studying outflows since represent a transitional phase from star-forming to quiescent galaxies offering a unique insight for the understanding of how feedback mechanisms regulate the gas reservoir.

The aim of this thesis is to study how negative and positive feedback phenomena and gas recycling, as consequence of starburst and AGN activities, are able to shape the gas life-cycle and observed properties via multiphase outflows. To this purpose, this thesis has presented an optical and near infrared (IR) analysis for a sample 38 local (U)LIRGs (51 individual galaxies at $z \leq 0.09$) which mainly covers the less explored LIRG luminosity range. The sample is not complete neither in luminosity nor in distance but it is representative of the (U)LIRGs population.

The study of outflows in representative samples of low-z galaxies is of particular relevance, since they will set the ground for future high-z Universe studies. In particular, local (U)LIRGs offer the opportunity to study the outflow phenomena at environments similar to those observed at high-z in star forming galaxies, but with a much higher signal-to-noise (S/N) and spatial resolution.

The results are based on optical integral field spectroscopic (IFS) observations for all the galaxies sample, while the analysis of near-IR IFS data was performed only for two of these galaxies. Spatially resolved spectroscopy is well suited for study complex phenomena as outflows. In fact, the advantage of performing spatially resolved spectroscopy, with respect to long-slit or imaging, is the simultaneous access to a third dimension, which allow to relate changes in spectral properties to spatial locations. Therefore, I can combine morphological information and accurate kinematic measurements towards a better understanding of the outflow phenomenon.

In Chapter 4, I have performed the analysis of the VIMOS and SINFONI IFS data of the nearby LIRG IRAS F11506-3851, and I have carried out a study of its gaseous (neutral and ionized) and stellar components. In Chapter 5, I have performed a statistical study of the neutral gas properties for all the sample of nearby (U)LIRGs observed with VIMOS. In Chapter 6 I have studied the kinematics and the ionization mechanism for the outflow in a more extreme object: the nearby AGN-ULIRG IRAS 05189-2524. What follows is a concise conclusion of the work presented in these chapters.

Spatially resolved kinematics, galactic wind, and quenching of star formation in the LIRG IRAS F11506-3851. I have studied the galaxy gaseous (neutral and ionized) and stellar components using the NaD absorption doublet, the Hα emission line, and the near-IR CO absorption bands.

- I have found that the spatially resolved kinematics of the ionized gas and the starts are dominated by rotation, with large observed velocity amplitudes (202 and 188 kms^{-1}, respectively) and centrally peaked dispersion maps (95 and 136 kms^{-1}, respectively).
- I have mapped the ISM-NaD absorption which reveals a complex kinematic structure dominated by two main components. On the one hand, the (irregular) thick slowly disk which lags significantly compared to the ionized gas and stars (with a velocity amplitude of 80 kms^{-1}). On the other hand a kpc-scale outflow is observed with a conical morphology along the semi-minor axis (likely perpendicular to the disk) with observed blue shifted velocities up to ~ 150 kms^{-1}.
- I have found that the outflow is ejecting a significant amount of gas (3×10^8 M$_\odot$) from the central regions at a rate of 1.4 times larger than the ongoing SF. These results strongly suggest that we are witnessing (nuclear) quenching due to SF feedback in IRAS F11506-3851.
- I have compared the expected energy budget released by the SNe within the wind lifetime finding that the outflow is likely powered by the recent starburst (~ 7 Myr ago, as traced by the [Fe II] emission) rather than the AGN which appears to be weak with a low contribution ($< 4\%$) to the total IR-luminosity.
- On the basis of the measured outflowing velocities and the dynamical mass (i.e., escape velocity) of the galaxy, it is unlikely that a significant fraction of the outflowing material would escape the galaxy to chemically enrich the surrounding inter galactic medium (IGM). Therefore, the outflowing material will fall back onto the disk, which would explain the lagging and the thickening of the neutral gas disk.

Neutral gas outflows in nearby (U)LIRGs via optical NaD feature. I have studied the properties of the neutral gas in all the IFS-VIMOS sample via high S/N spatially integrated spectra and 2D spectral maps.

1D: I have estimated the fraction of stellar contribution (ranging from 20% to 100%), modelling the stellar continuum. In nearly half of the cases for which a high quality modelling was possible, the NaD is mainly originated in the ISM (i.e., stellar fraction $< 35\%$).

- I have measured blueshifted NaD profiles in 22 objects, which indicate typical neutral gas outflow velocities in the range: 65-260 kms^{-1}. Excluding the galaxies with powerful AGNs, the neutral outflow velocity shows a dependency with the star formation rate (SFR) of the type $V \propto SFR^{0.15}$, in fair agreement with previous results.

- I have compared the kinematics of neutral and ionized multiphase outflows. I found that the neutral outflow (central) velocities are significantly higher than those for the ionized gas, but they are in rather good agreement with the ionized gas maximum outflow velocities considered. This suggests that the wind entrains and accelerates the cold ambient gas, which is likely located at relatively large distances from the regions where the ionized gas resides. The velocity dispersions, for both neutral and ionized outflows show similar median values (if the strongest AGNs are excluded).

2D: In 22 out of 40 galaxies, the spatially resolved neutral gas kinematic shows clear signatures of outflows, which are generally collimated and conical in morphology.

- The inclination-corrected outflow velocities of the neutral gas entrained in outflows are generally in the range $\sim$ 80-700 kms^{-1}. These 2D velocities correlate with the SFR similarly as the scaling relation found in the integrated spectra analysis, but no clear correlation is seen between the 2D outflow velocities and the dynamical mass.

- I have found that the wind mass ranges from 0.4 to $7.5 \times 10^8\,\mathrm{M}_\odot$, reaching up to $\sim 3\%$ of the dynamical mass of the host. The mass rates are typically only $\sim$ 0.2-0.4 times the corresponding global SFR indicating that, in general, the mass-loss is small for slowing down the SF significantly.

- In the majority of the cases, the velocity of the outflowing gas is not enough to escape the host potential well and, therefore, most of it will rain-back into the galaxy disk. On average V/v_{esc} is higher in less massive galaxies, confirming that the galaxy mass has a primary role in shaping the recycling of gas and metals.

- The comparison between the wind power and the kinetic power of the starburst associated to SNe indicates that only the starburst could drive the outflow in nearly all the (U)LIRGs galaxies, as the wind power is generally lower than the 20% of the kinetic power supplied by the starburst.

- For a significant number of (U)LIRGs (11/40), the neutral gas kinematics has been found in ordinary rotation with neutral gas velocity fields showing a spider-pattern (plus rather irregular velocity dispersion maps). The comparison between the rotation curves of the ionized and neutral disks indicates that the neutral disk lags compared to ionized disk in the majority of the cases (i.e., 8/11). Our kinematics measurements indicate that nearly all the neutral gas disks are dynamically hotter and thicker (by a factor up to 46, 15 on average) with respect to the ionized disks.

Investigating positive feedback in the ULIRG IRAS F05189-2524. I have investigated the kinematics and ionization mechanism of the multiphase AGN-driven outflow in this ULIRG. I have studied a set of near-IR emission lines: [Fe II], Paα, $H_2$1-0 S(1) and Brγ with integral-field and integrated spectroscopy of H and K bands of VLT/SINFONI.

- The multi-components decomposition near-IR emission lines has shown that an extended broad and outflowing component is present at velocities in the range 60-120 kms^{-1} (except in one region) and with a large velocity dispersion (~ 325 kms^{-1}, on average) in partial agreement with previous works.
- To investigate if the outflow is able to undergo vigorous SF, I have used near-IR diagnostic diagrams to discriminate the dominant source of ionization of the two kinematic components used to model emission lines. We found that the mechanism of excitation of both narrow and broad components is the AGN-photonization. This exclude the ionization from young ionizing stars expected in case of positive feedback. However, by using the diagnostic near-IR diagrams I have found that our measurements present either an [Fe II] emission deficit or H_2 excess which will be investigated in the future (e.g., combining near-IR and optical line ratios).

In Chapter 7, I present H+K band SINFONI data for two additionally ULIRGs and the first stages of mapping the observed near-IR emission lines. For both ULIRGs, I have modelled emission lines profiles with one component whose kinematic can be interpreted as in ordinary rotation (though some irregularities). The mapping of the different components seen in the IFS-SINFONI spectra of these objects will be presented in a future work, and complemented by a set of long slit near-IR spectroscopic observations of two other ULIRGs. In this Chapter, I also include a short description of a further study dedicated to probe the IGM enrichment caused by 100 kpc-scale outflows on the basis of the detection and kinematic of the NaD absorption in background galaxies.

Finally, these type of studies will set the ground for future studies. More insights on the outflows feedback will come in the next decade thanks to upcoming ground based telescopes or space missions, as the European Extremely Large Telescope and James Webb Space Telescope, respectively.

Chapter 9

Conclusiones

Una previsión del modelo estándar de formación de galaxias (modelo jerárquico) es que la historia de la materia bariónica en las galaxias debería evolucionar paralelamente a la de sus halos de materia oscura. Sin embargo, la función de masas estelar observada en galaxias muestra diferencias respecto a lo que predicen los modelos para galaxias de baja y alta masa. Esta discrepancia indica la necesidad de mecanismos de regulación. Por ejemplo, los *outflows* (en inglés, a veces traducido como "super-vientos") han sido propuestos como un fenómeno eficaz para controlar la tasa de formación estelar y la actividad de los núcleos galácticos (SFR y AGN, respectivamente por sus siglas en inglés). En particular, los *outflows* son fenómenos capaces de enlazar la pequeña escala espacial de su fuente al entorno circundante sobre escalas de kpc. Los *outflows* se han observado en diferentes fases del medio interestelar, y en cualquier época cósmica. En esta tesis he investigado la importancia de *outflows* y fenómenos de regulación en la evolución de galaxias locales con formación estelar intensa como las Galaxias Luminosas y Ultraluminosas en el infrarrojo ((U)LIRGs, por sus siglas en inglés). En particular, estas poblaciones son especialmente adecuadas para estudiar los *outflows* ya que representan una fase de transición en la evolución de las galaxias ofreciendo una perspectiva única para la comprensión de los mecanismos de regulación.

El objetivo es estudiar cómo estos fenómenos afectan el ciclo del gas/metales y las propiedades observadas en las galaxias. Para ello esta tesis presenta un análisis de datos en el óptico y en el infrarrojo cercano para una muestra 38 (U)LIRGs locales (51 galaxias individuales a $z \leq 0.09$) cubriendo el rango de baja luminosidad (LIRG), que es el menos estudiado. La muestra no es completa ni en luminosidad ni en distancia, pero es representativa de las (U)LIRGs. Estas poblaciones de galaxias locales permiten estudiar los mecanismos de regulación en entornos similares a aquellos observados en galaxias lejanas, con la ventaja de poder alcanzar una relación señal-ruido y una resolución espacial mucho más altas.

Los resultados de este trabajo, están basados sobre el ánalisis de datos de espectroscopía de campo integral en los rangos óptico (para la muestra de (U)LIRG locales) y infrarrojo cercano (para dos galaxias). La espectroscopía de campo integral, está optimizada para los estudios espectroscopicos de regiones espacialmente extensas. Por lo tanto, esos datos permiten de combinar medidas cinemáticas y morfológicas para una mejor comprensión del fenómeno de los *outflows*.

En el Capítulo 4 se ha estudiado en detalle el *outflow* en la galaxia LIRG prototípica IRAS F11506-3851. En el Capítulo 5, se ha extendido el análisis de los *outflows* de gas neutro a toda la muestra de

objetos observada con VLT/VIMOS. En el Capítulo 6, se he estudiado la cinemática, el mecanismo de ionización e investigado la posible presencia de formación estelar en el *outflow* en la ULIRG IRAS 05189-252 mediante observaciones realizadas con VLT/SINFONI en el rango del infrarrojo cercano. Lo que sigue es un resumen de los resultados presentados en estos capítulos.

Cinemática espacialmente resuelta, *outflow* y supresión de la formación estelar en la LIRG IRAS F11506-385. En este objecto, he estudiado las fases neutra e ionizada del medio intestelar y la componente estelar con datos de espectroscopía de campo integral obtenidos con VIMOS/VLT y SINFONI/VLT. Se han utilizando como trazadores el doblete de absorpción del NaD y la línea de emisión Hα, y las bandas de absorpción del CO en el óptico y en el infrarrojo cercano, respectivamente.

- Los campos de velocidad del gas ionizado y de las estrellas están dominados por rotación, con una amplitud de velocidad elevada (202 y 188 kms^{-1}, respectivamente) y mapas de dispersión de velocidades cuyo máximo (95 y 136 kms^{-1}, respectivamente) se encuentra en el núcleo.
- La fase neutra del gas interestelar, trazada con el NaD, presenta una estructura cinemática compleja, con dos componentes principales. Por un lado, se encuentra un disco grueso y irregular que rota considerablemente más despacio comparado con el disco de gas ionizado y de las estrellas (con una amplitud de la velocidad de 80 kms^{-1}). Por otro lado, hay evidencias de un *outflow* con morfología cónica originado en el núcleo y perpendicular al disco de la galaxia con velocidades observadas al azul de hasta ~ 150 kms^{-1}.
- El *outflow* expulsa una cantidad significativa de gas (3×10^8 M$_\odot$) desde las regiones centrales a una tasa de 1.4 veces más alta que la formación estelar en curso. Estos resultados sugieren que la supresión de la formación estelar (nuclear) en IRAS F11506-3851 es debida a la regulación del *outflow*.
- La emisión debida a supernovas es relativamente fuerte en las regiones centrales, tal como se deduce de la linea [Fe II], e indica un reciente (~ 7 Myr) episodio de formación estelar que pudo originar el *outflow*. No es necesaria la aportación de energía por el AGN (que contribuye $< 4\%$ a la luminosidad infrarroja de la galaxia) para generar el *outflow*.
- En base a la comparación entre las velocidades de los *outflows* y la velocidad de escape correspondiente a la masa dinámica de la galaxia, la mayor parte del gas del *outflow* no puede escapar del potencial gravitatorio de la galaxia y enriquecer el medio intergaláctico. Por lo tanto, este gas retornará al disco de la galaxia. Este resultado puede explicar el ensanchamiento y la baja velocidad de rotación del disco de gas neutro.

Supervientos de gas neutros en (U)LIRGs locales trazados con NaD. He estudiado las propiedades del gas neutro en toda la muestra de galaxias observada con espectroscopía de campo integral através espectros espacialmente integrados de alta relación signal-ruido (1D) y de los mapas (2D).

1D: La contribución estelar al NaD ha sido estimada modelando el continuo estelar y varía entre el 20% y el 100%. En casi la mitad de los casos para los cuales el modelo del continuo es

satisfactorio, el doblete de NaD se origina principalmente en el medio interestelar (contribución estelar $< 35\%$).

- Se encuentran evidencias de *outflows* en 22 objectos. Los *outflows* tienen velocidades al azul, V, que están en el rango: 65-260 kms^{-1}. Excluyendo las galaxias con alta contribucción del AGN, la velocidad de los *outflows* muestra una dependencia con la SFR del tipo: $\mathrm{V} \propto \mathrm{SFR}^{0.15}$, en acuerdo bastante bueno con resultados anteriores.

- La comparación de la cinemática del gas neutro e ionizada, sugiere que el *outflow* arrastra y acelera el gas frío (neutro) del entorno. Este ultimo está localizado a una distancia más grande de las donde reside el gas ionizado. Las dispersiones de velocidad de *outflows* de gas neutro y ionizados muestran valores medianos similares (excluyendo las galaxias con alta contribución del AGN).

2D: En 22 de 40 galaxias, la cinemática espacialmente resuelta del gas neutro muestra evidencias de *outflows* con morfología cónica y colimados (en general).

- Las velocidades de los *outflows* de gas neutro (corregidas por inclinación) son generalmente en el rango $\sim$ 80-700 kms^{-1}. Estas velocidades 2D tienen una correlación con el SFR similar a aquella encontrada en el análisis de los espectros integrados. Sin embargo, las velocidades de los *outflows* y las masas dinámica de las galaxias no muestran correlación.

- Se encuentra que las masas de los vientos están en el rango desde 0.4 a 7.5×10^8 $\mathrm{M}_{\odot}$, y en unos casos hasta alcanzan el $\sim 3\%$ de la masa dinamica de la galaxia anfitriona. Las tasas de pérdida de masa de los *outflows* es $\sim$ 0.2-0.4 veces la SFR de la galaxia, indicando que, en general, los *outflows* no pueden disminuir considerablemente la SFR.

- En la mayoría de los casos, se encuentra que la velocidad del gas de los *outflows* no es suficiente para que el gas pueda escapar del potencial gravitatorio de la galaxia, retornando al disco de la galaxia. En promedio $\mathrm{V}/\mathrm{v}_{\mathrm{esc}}$ es más alto en galaxias menos masivas, confirmando que la masa de la galaxia tiene un papel primario en el ciclo de gas y metales.

- La comparación entre la energía de los *outflows* y la energía cinética del brote de formación estelar asociado a SNe indica que sólo el "starburst" podría originar los *outflows* en casi todas las (U)LIRGs, siendo la energía del *outflows* generalmente inferior que el 20% de la energía cinética del brote de formación estelar.

- Para un número significativo de (U)LIRGs (11/40), la cinemática del gas neutro es compatible con un disco en rotación, con campos de velocidad con el típico "patrón de araña", y mapas de dispersión de velocidad irregulares. Los discos neutros son más lentos que aquellos de gas ionizado en la mayoría de los casos (8/11). Las medidas de cinemática indican que casi todos los discos de gas neutro están suportados por movimentos aleatorios y que son más gruesos respecto a los discos ionizados (hasta un factor 46, 15 en promedio).

Investigación de la regulación positiva en la ULIRG IRAS F05189-2524. En este objecto, he investigado la cinemática y el mecanismo de ionización del *outflow* multifase originado por el AGN.

He estudiado líneas de emisión en el infrarrojo cercano: [Fe II], Paα, $H_2$1-0 S(1) y Brγ con datos de espectroscopia a campo integral en la banda H y K, obtenidos con el instrumento VLT/SINFONI.

- La descomposición en múltiples componentes de las líneas de emisión infrarrojas ha revelado la presencia de una componente ancha y extensa, asociada a *outflows*, con velocidades en el rango 60-120 kms^{-1} (excepto en ciertas regiones) y con elevada dispersión de velocidades ($\sim$ 325 kms^{-1}, en promedio). Estos resultados están en acuerdo parcial con otros trabajos previos.
- Mediante diagramas de diagnóstico en el infrarrojo cercano, ha sido posible discriminar la fuente dominante de ionización de cada una de las componentes cinemáticas empleadas para modelar las líneas de emisión. Se encuentra que el mecanismo de excitación en ambas componentes, ancha y estrecha, se corresponde con fotoionización debido al AGN. Esto excluye procesos de ionización debidos a estrellas jóvenes, que son los esperados en caso de regulación positiva debido a formación estelar. Utilizando dos diagramas de diagnóstico diferentes en el infrarrojo, nuestras medidas indican que, o bien esta galaxia presenta un déficit de emisión de [Fe II], o bien un exceso de emisión en la línea de H_2. Este resultado será estudiado con mayor profundidad en el futuro (por ejemplo combinando la relación entre lineas en el infrarrojo cercano y en el óptico).

En el Capítulo 7, se presentan datos preliminares del análisis de datos obtenidos con SINFONI en las banda H y K (infrarrojo cercano) para dos ULIRGs. Para ambas, he modelado los perfiles de las líneas de emisión: [Fe II], Paα, $H_2$1-0 S(1) y Brγ, con una componente cuya cinemática puede ser interpretada como rotación (aunque con algunas irregularidades). Los mapas de la diferentes componentes observadas en los espectros de estos objetos será presentada en un trabajo futuro, junto con datos de rendija en el infrarrojo cercano de dos otras ULIRGs. En este Capítulo, está también incluida la descripción de un trabajo dedicado a estudiar el entorno de LIRGs locales (sobre escalas de 100 kpc) para analizar el enriquecimiento del medio intergaláctico causado por *outflows* sobre la base de la detección y el estudio de la cinemática de la absorpción NaD en galaxias de fondo.

Concluyendo, este tipo de estudios de *outflows* espacialmente resueltos pondrán la base para estudios futuros. Más detalles sobre la regulación por *outflows* vendrán en los próximos años gracias a observaciones con futuros telescopios terrestres y misiones espaciales, como el Telescopio Europeo Extremadamente Grande ($\sim$ 40m) y el Telescopio Espacial James Webb, respectivamente.

Publications

From the present thesis project:

- Spatially resolved kinematics, galactic wind, and quenching of star formation in the luminous infrared galaxy IRAS F11506-3851.
  Authors: **S. Cazzoli**, S. Arribas, L. Colina, J. Piqueras López, E. Bellocchi, B. Emonts, R. Maiolino, A&A 2014, 569, A14.

- Neutral gas outflows in nearby (U)LIRGs via optical NaD feature.
  Authors: **S. Cazzoli**, S. Arribas, R. Maiolino and L. Colina,
  A&A 2016 (accepted).

- Investigating the positive feedback in local ULIRGs.
  Authors: **S. Cazzoli**, R. Maiolino, S. Arribas et al. (2016, in preparation).

From related collaborative projects:

- Sub-kpc star-formation law in the local luminous infrared galaxy IC 4687 as seen by ALMA.
  Authors: M. Pereira-Santaella, L. Colina, S. García-Burillo., P. Planesas, A. Usero, A. Alonso-Herrero, S. Arribas, **S. Cazzoli**, B. Emonts, J. Piqueras Lṕez, and M. Villar-Martín.
  A&A 2016, 587, A44.

- Star-formation histories of local luminous infrared galaxies.
  Authors: M. Pereira-Santaella, A. Alonso-Herrero, L. Colina, D. Miralles-Caballero, P. G. Pérez González, S. Arribas, E. Bellocchi, **S. Cazzoli**, T. Díaz-Santos, J. Piqueras López.
  A&A 2015, 577, 78-53

Appendix A

VIMOS maps and integrated spectra of individual sources

In this Appendix, we present the neutral gas equivalent width (EW), velocity field (V), and the velocity dispersion (σ) maps for those objects for which we were able to obtain the spectral maps (Sect. 3.3.2). The VIMOS data for the LIRG IRAS 11506-3851 are discussed in detail by (Chapt. 4) thus the comments and the correspondent maps are omitted here.

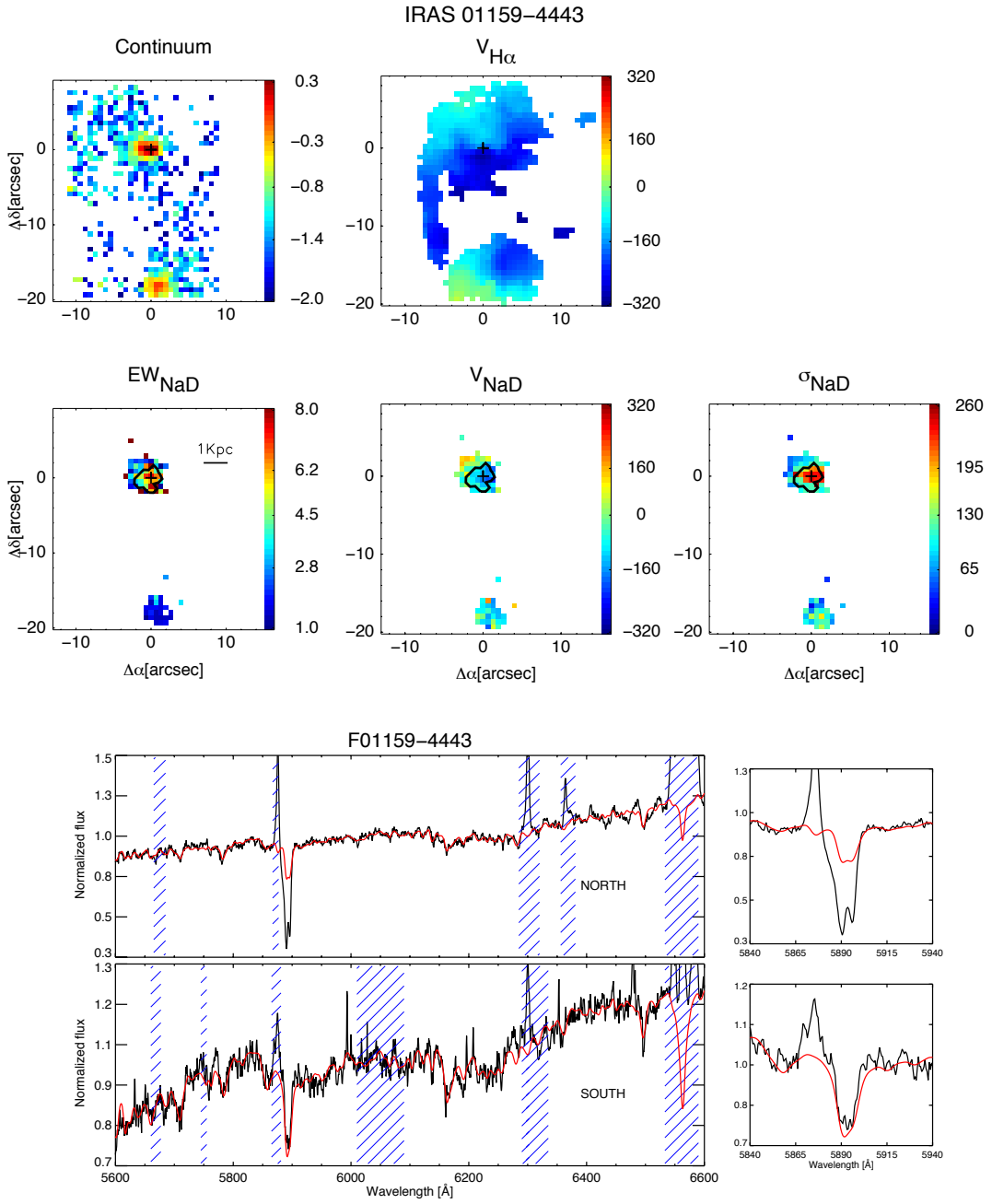

FIGURE A.1: IRAS F01159-4443. *Top:* The continuum image obtained from the mean of the line-free continuum nearby the doublet in a 100 Å rest frame-wavelength range, in units of erg s^{-1} cm^{-2} Å^{-1} after applying a factor of 10^{-16} and the ionized gas velocity field (in kms^{-1} units) traced via the Hα-narrow component (both included as reference). *Center:* VIMOS observed maps obtained modelling the NaD line profile ($\lambda\lambda$ 5890,5896 Å). From left to right: equivalent width (in Å units), velocity and velocity dispersion (both in kms^{-1} units). In all the maps, the brightest spaxel of the VIMOS continuum is marked with a cross and the galaxies orientation is north up, east to the left. The maps are color-coded according to their own scale (i.e., range of the velocity, velocity dispersion and EWs sampled) to facilitate the contrast and to highlight weak features. Black contours (if present) indicate the spaxels in which the neutral gas is identified as entrained in a GW. *Bottom:* the rest-frame spectra extracted from the original cube via a S/N optimization algorithm (Sect. 3.2) for the northern and southern galaxies. The red line marks the modelled stellar spectrum that matches the observed continuum, obtained applying the pPXF method (Sect. 3.2.1). The most relevant spectral features blocked for modelling a line-free continuum are shown in blue.

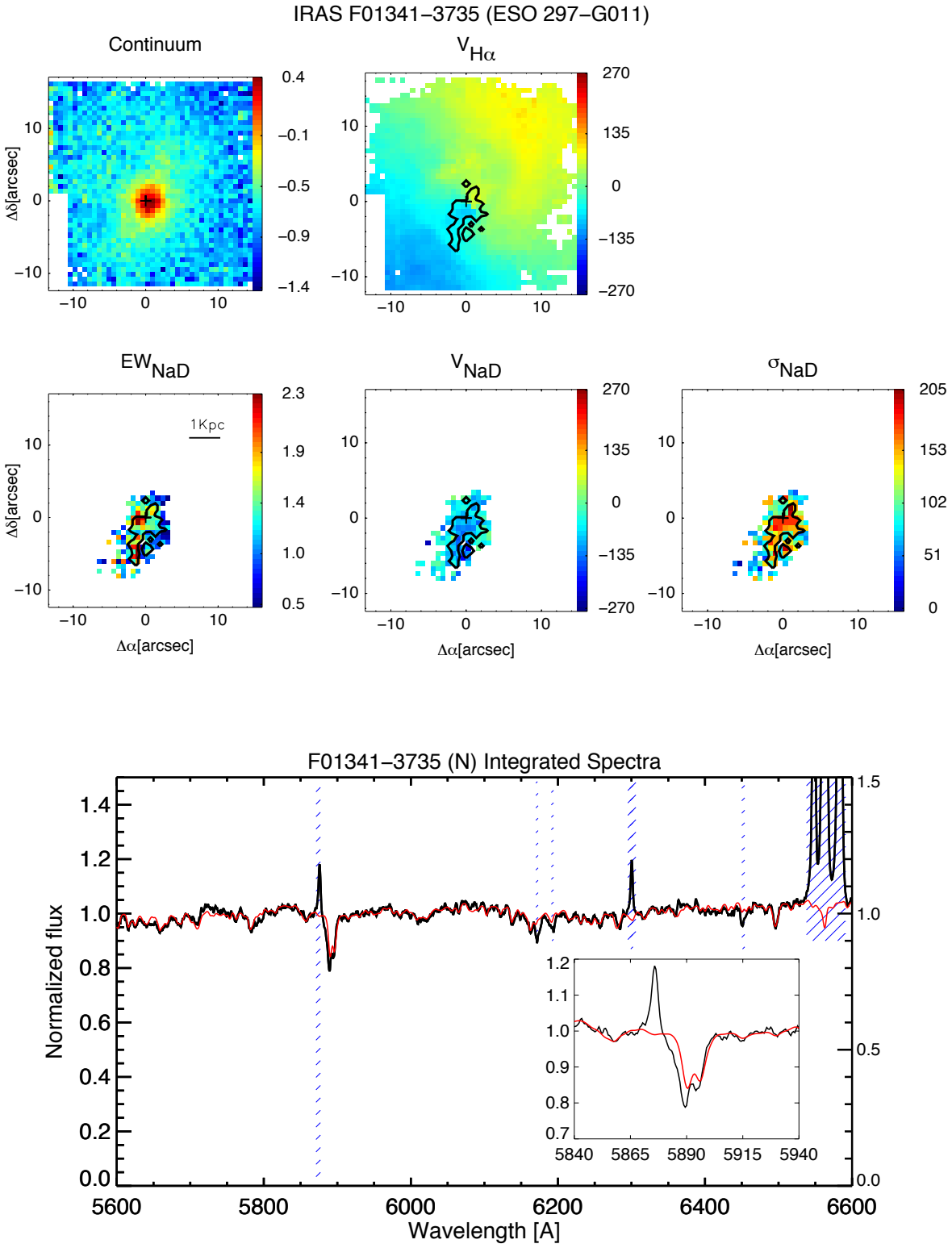

FIGURE A.2: As Fig. A.1 but for IRAS F01341-3735 (ESO 297-G011).

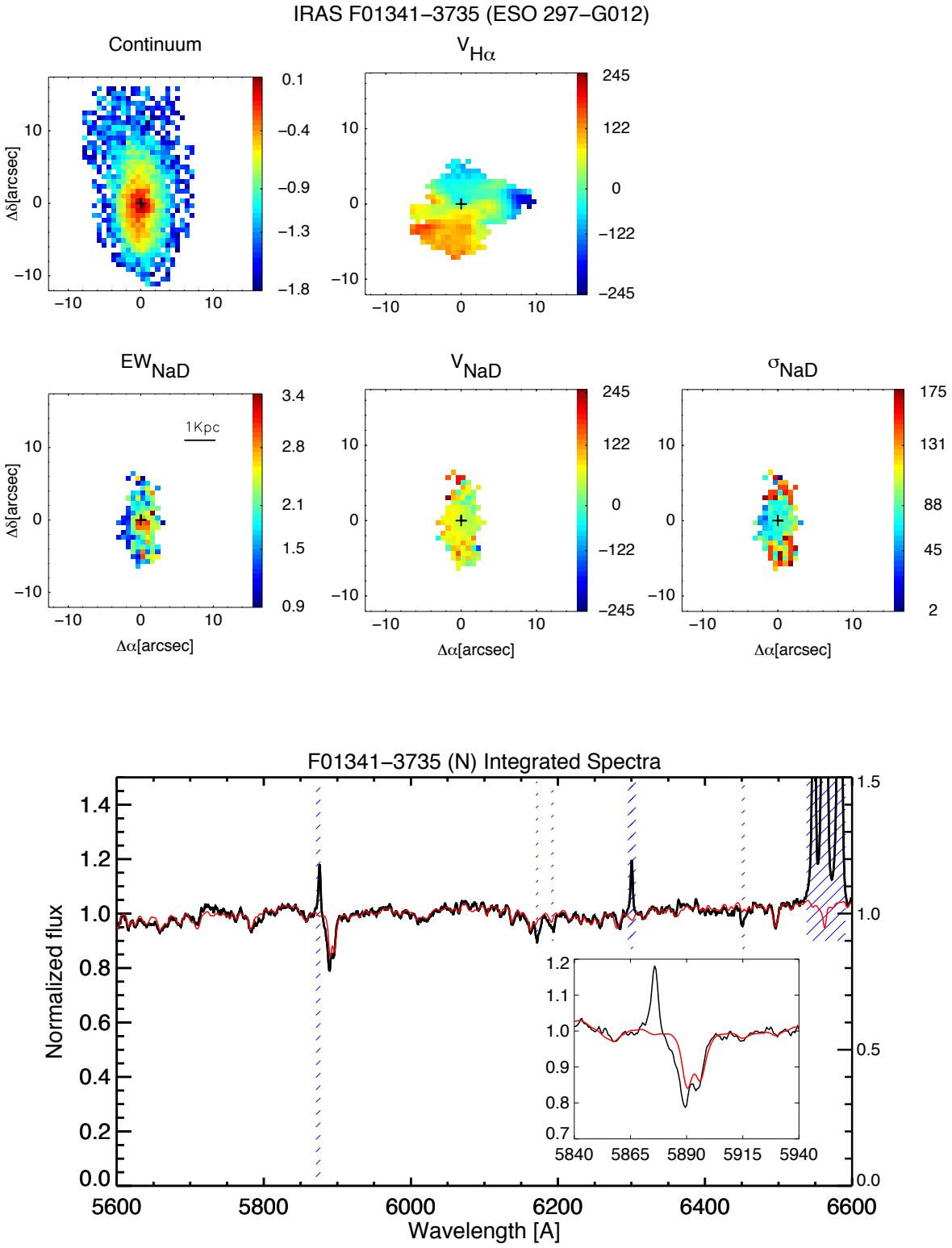

FIGURE A.3: As Fig. A.1 but for IRAS F01341-3735 (ESO 297-G012).

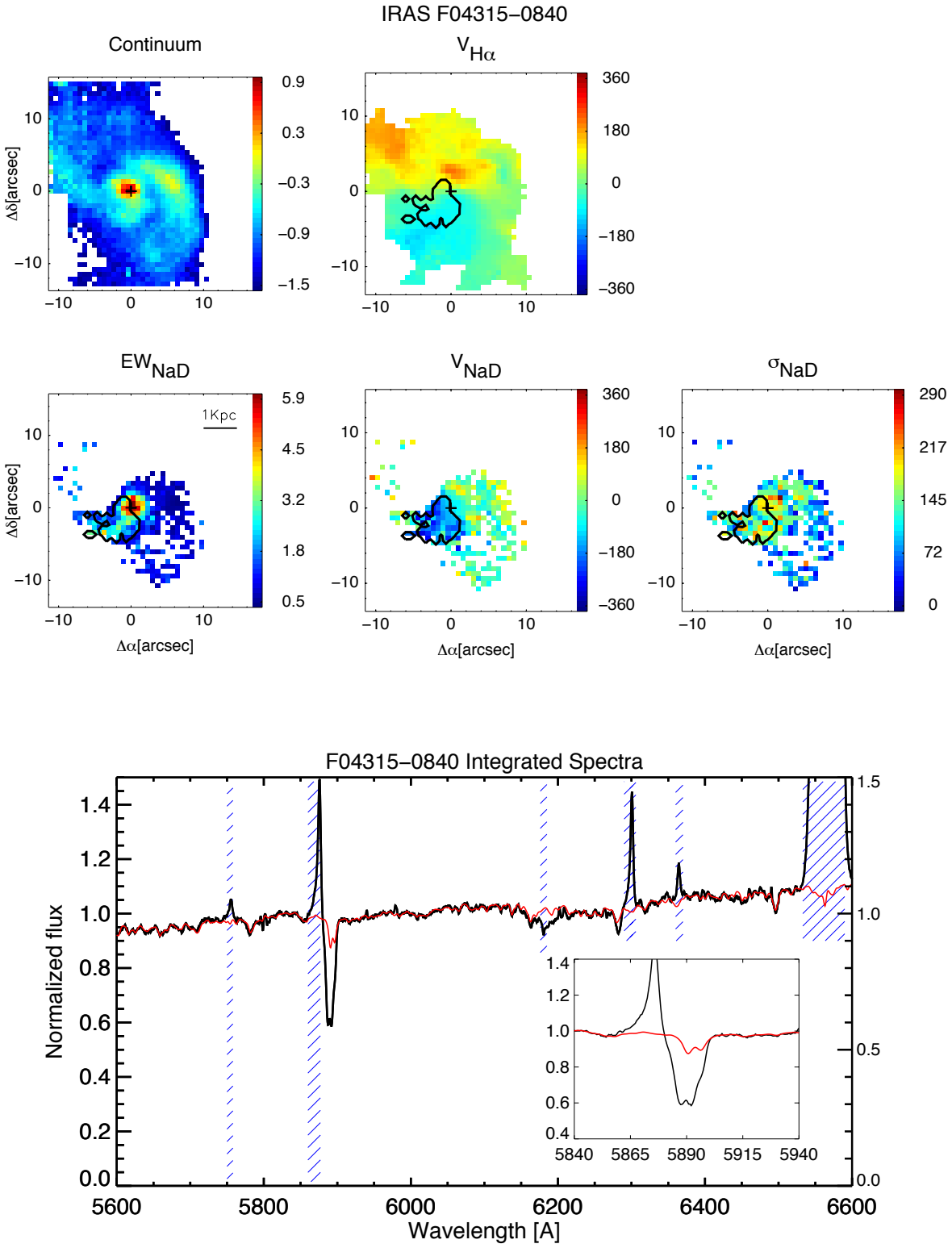

FIGURE A.4: As Fig. A.1 but for IRAS F04315-0840.

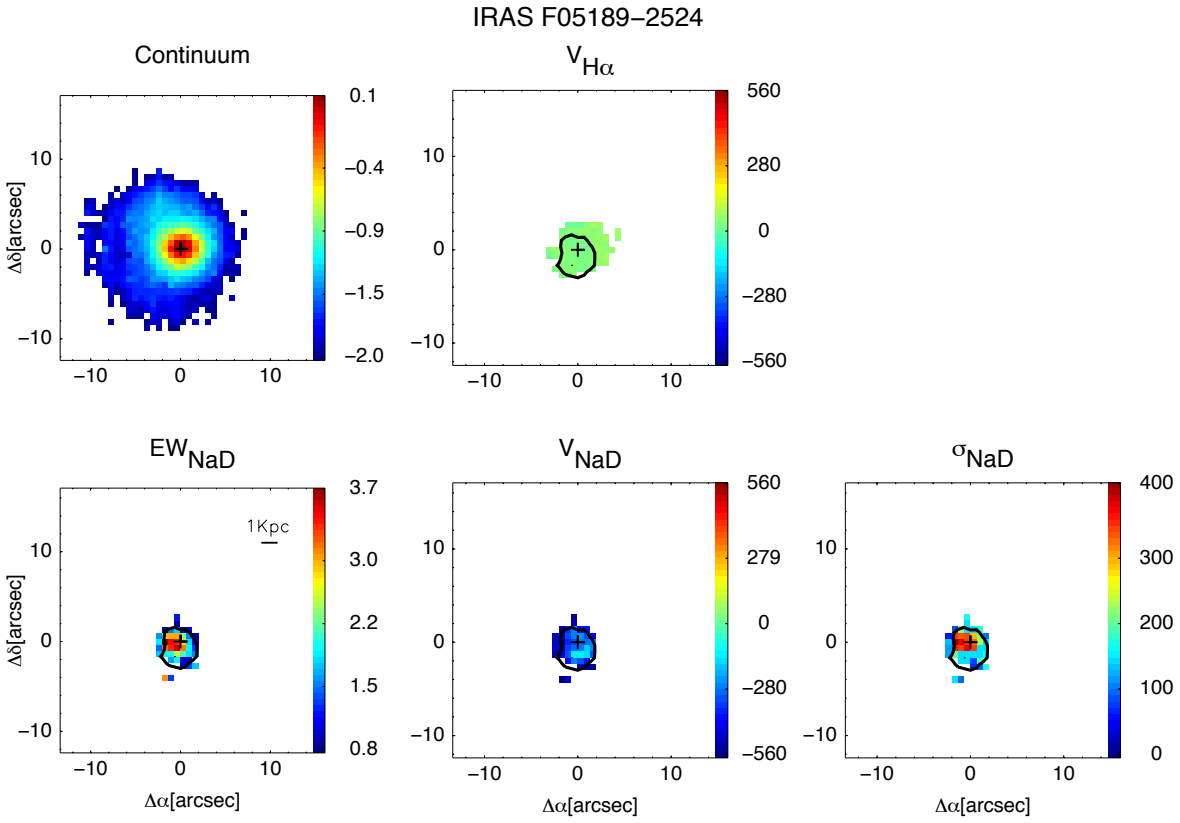

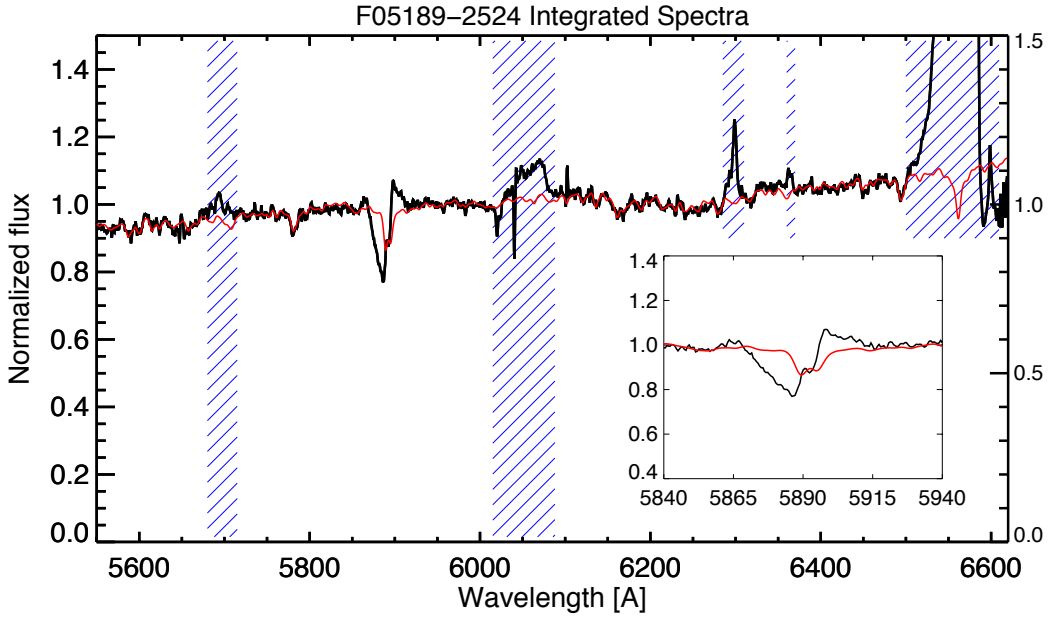

FIGURE A.5: As Fig. A.1 but for IRAS F05189-2524.

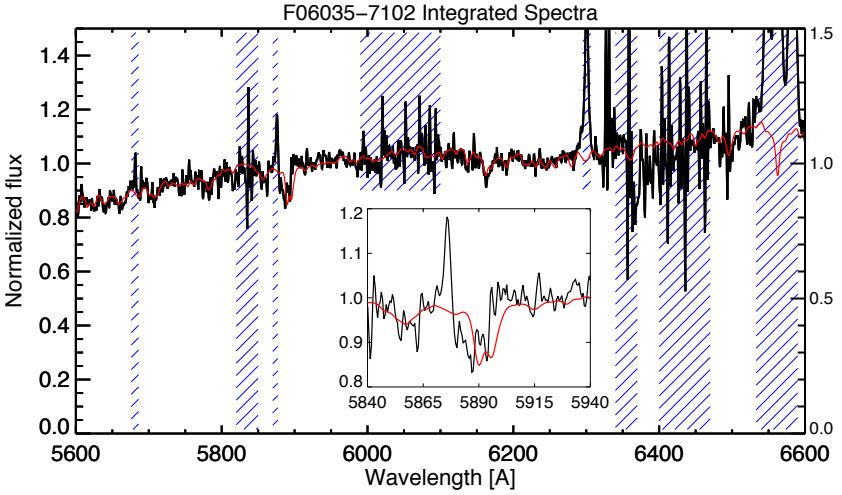

FIGURE A.6: As in the lower panel of Fig. A.1 but for IRAS 06035-7102.

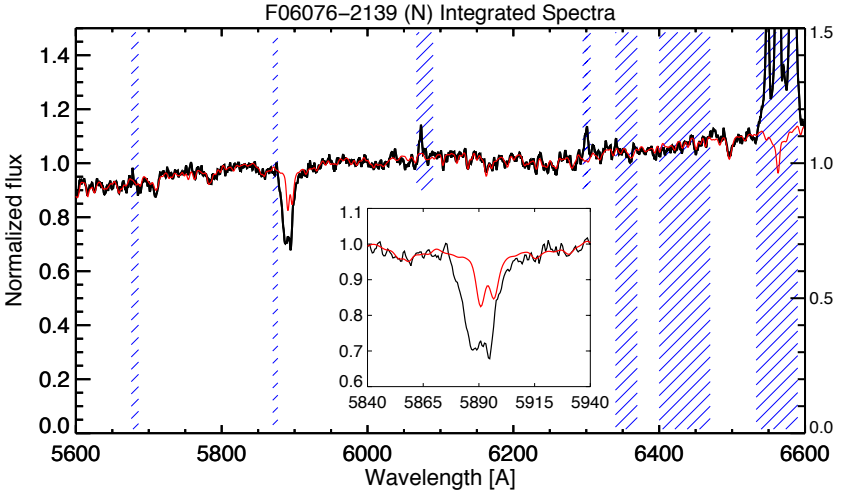

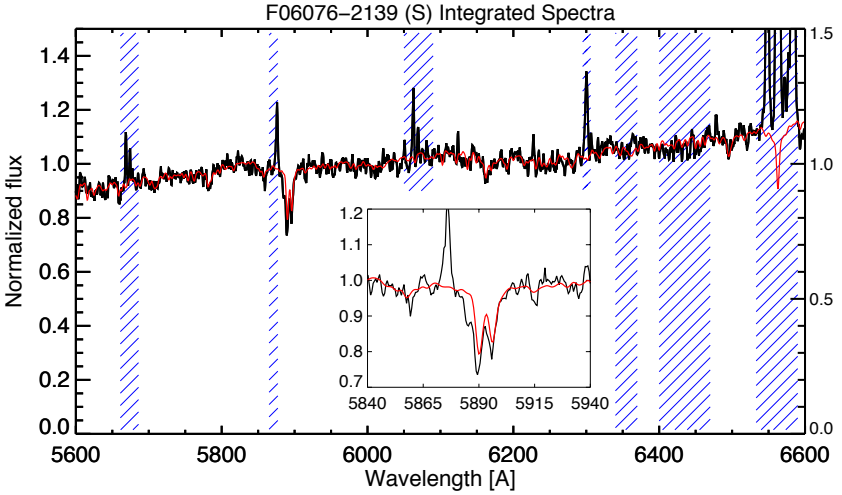

FIGURE A.7: As in the lower panel of Fig. A.1 but for IRAS F06076-2139 north and south (from top to bottom).

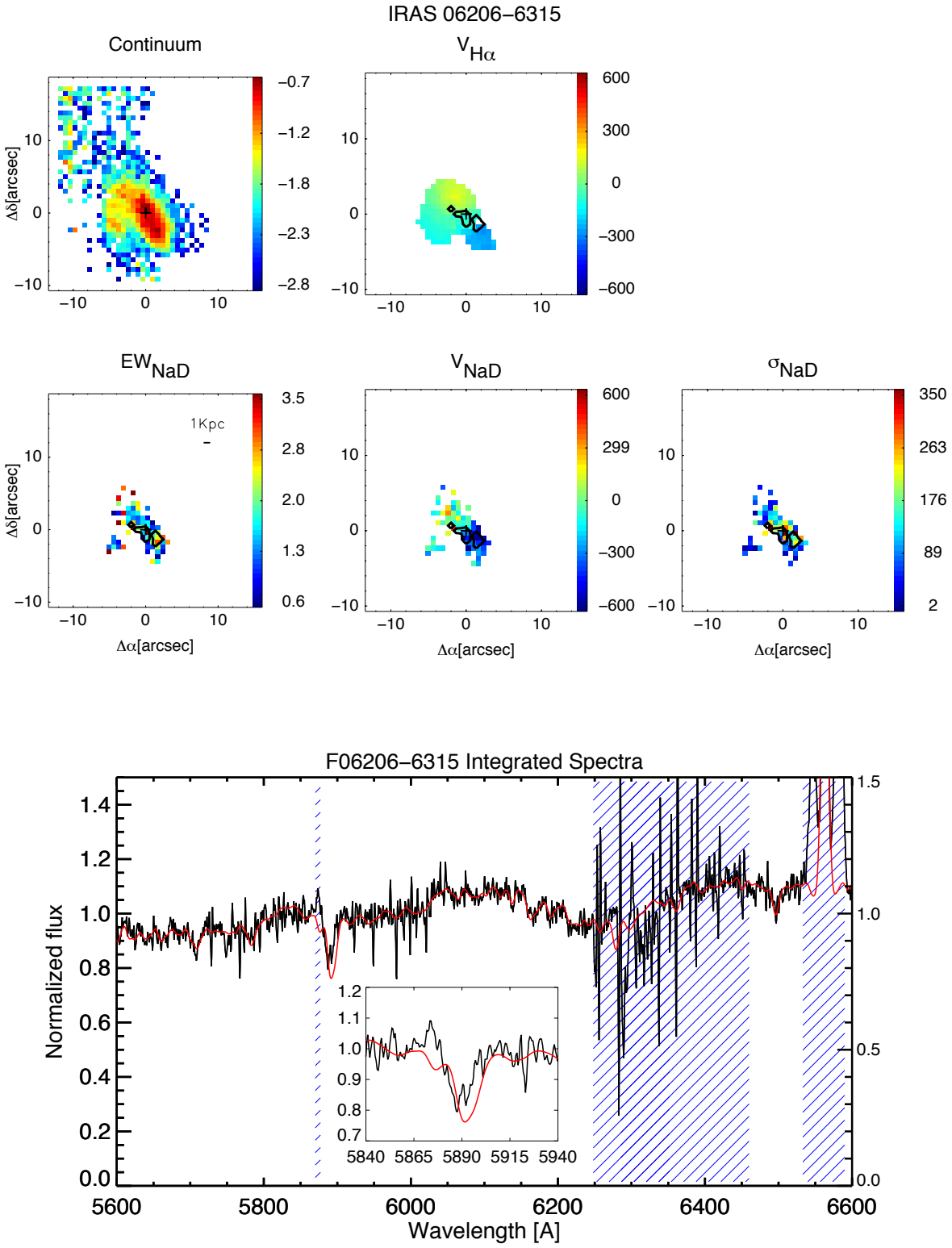

FIGURE A.8: As Fig. A.1 but for IRAS F06206-6315.

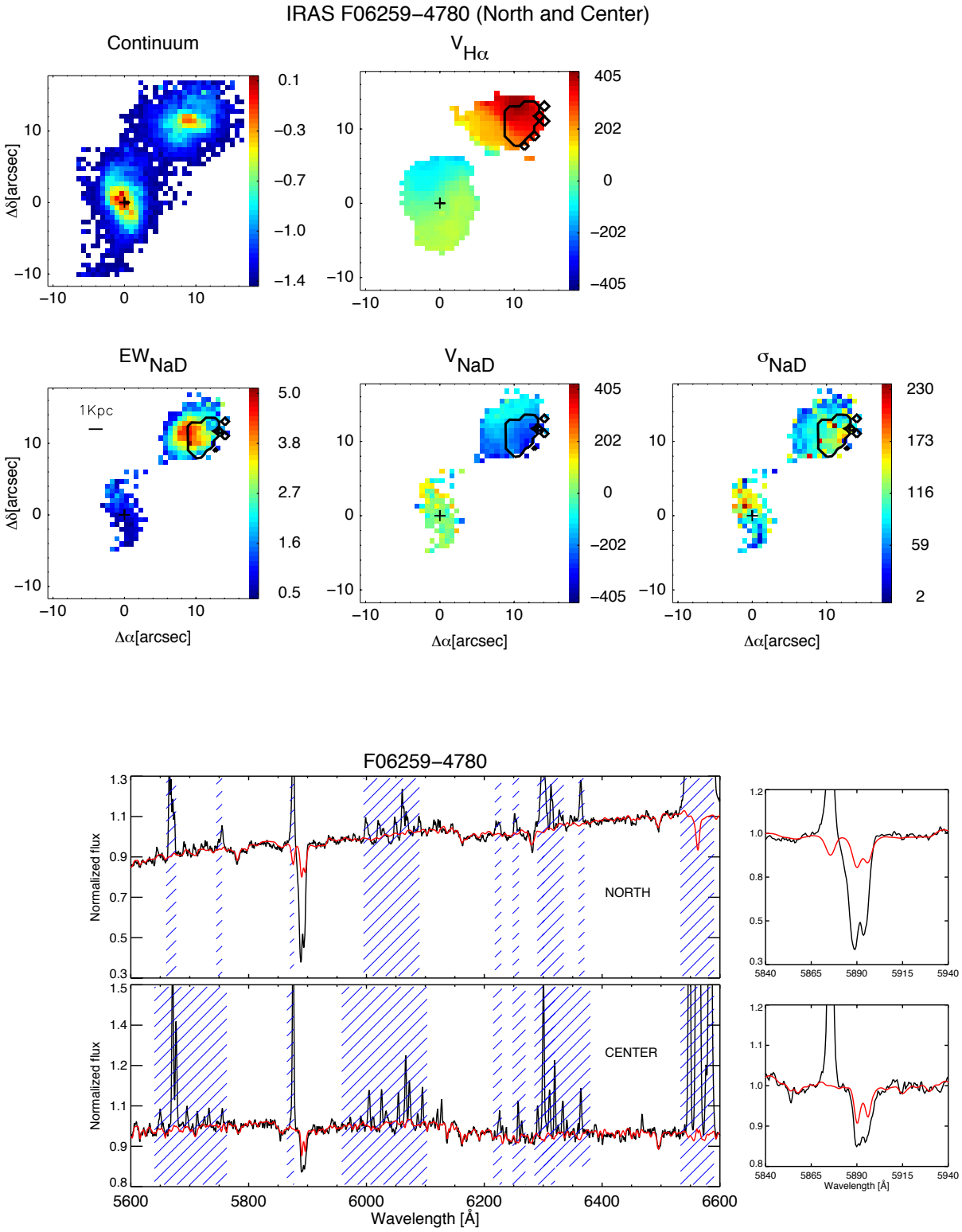

FIGURE A.9: As Fig. A.1 but for IRAS F06259-4780 north and Center.

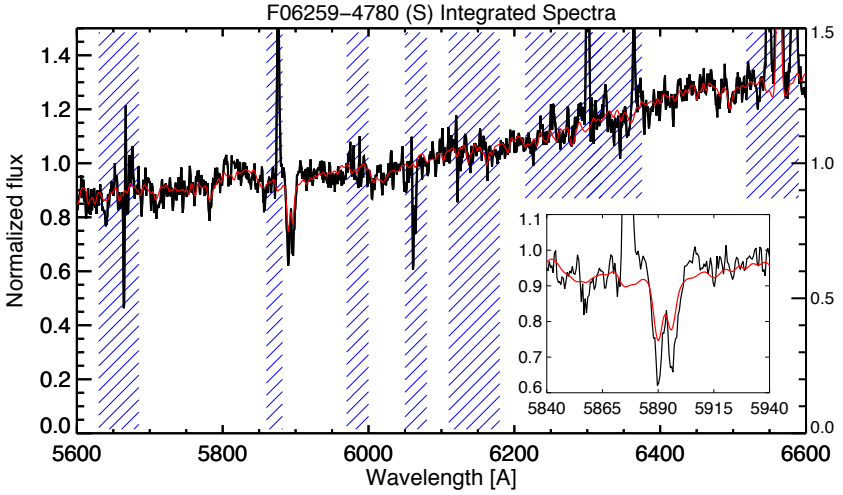

FIGURE A.10: As in the lower panel of Fig. A.1 but for IRAS F06259-4780 (S).

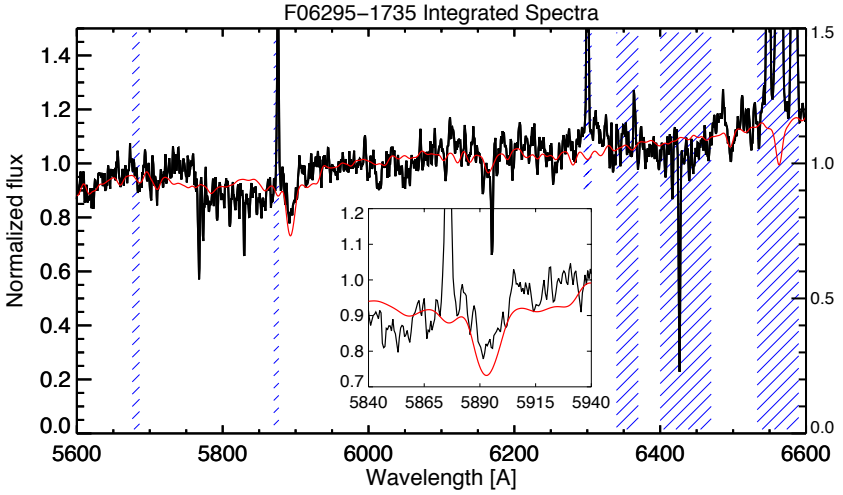

FIGURE A.11: As in the lower panel of Fig. A.1 but for IRAS 06295-1736.

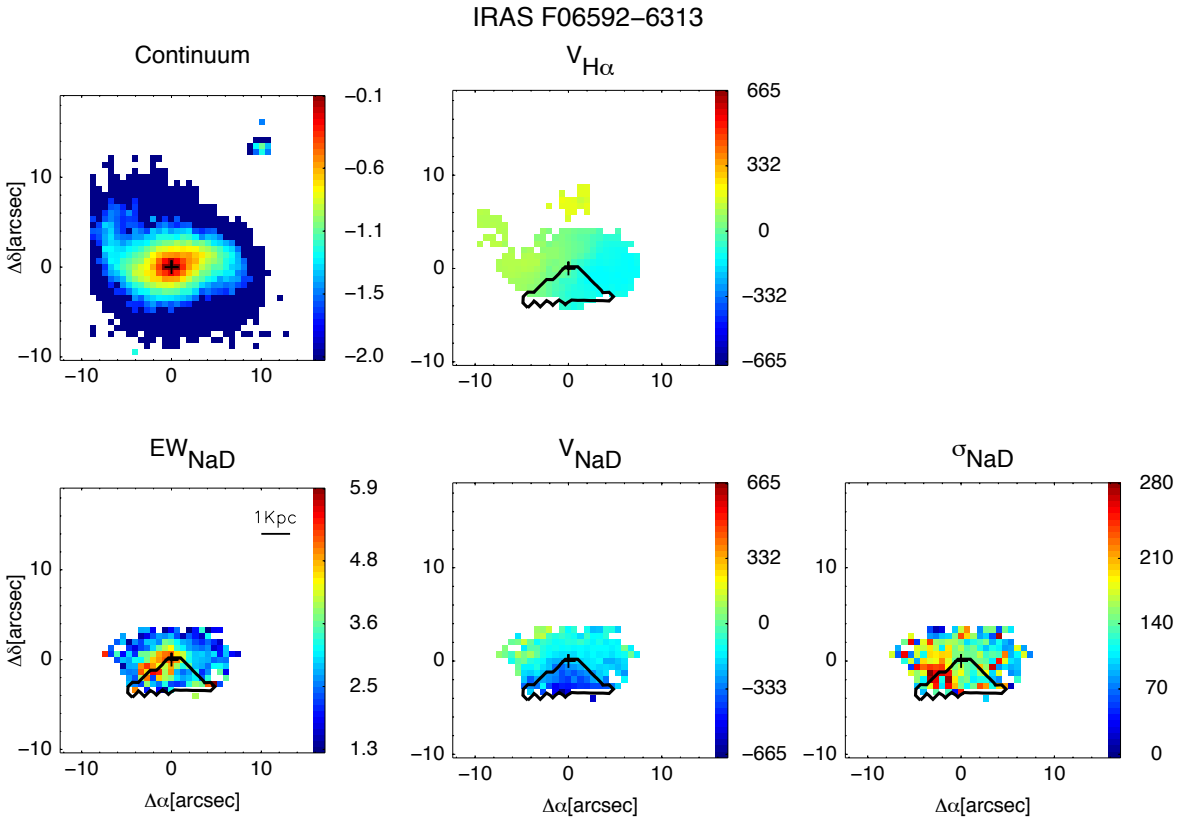

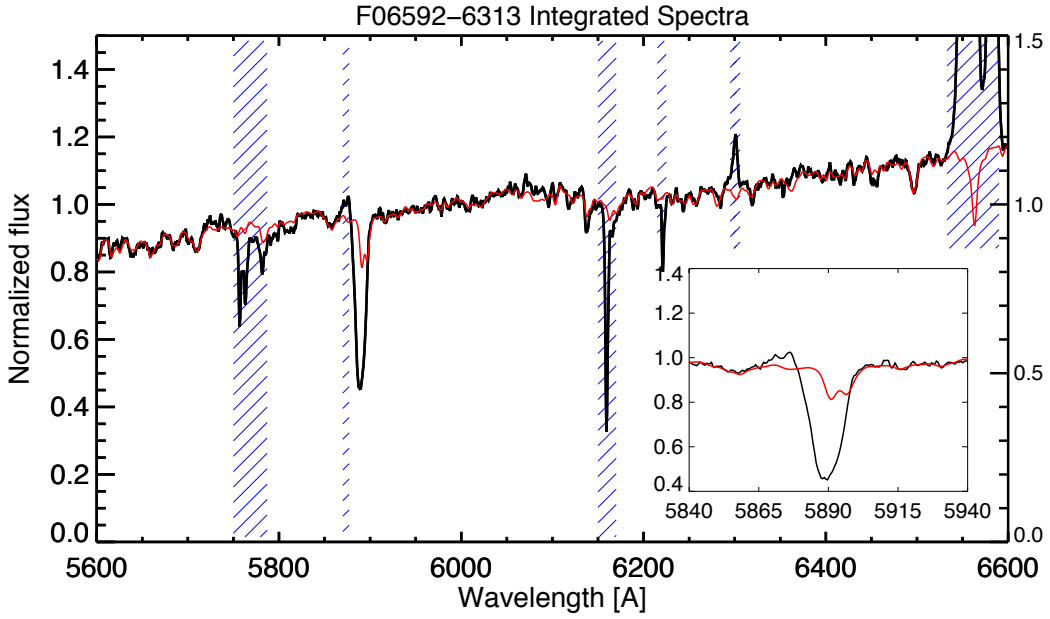

FIGURE A.12: As Fig. A.1 but for IRAS F06592-6313.

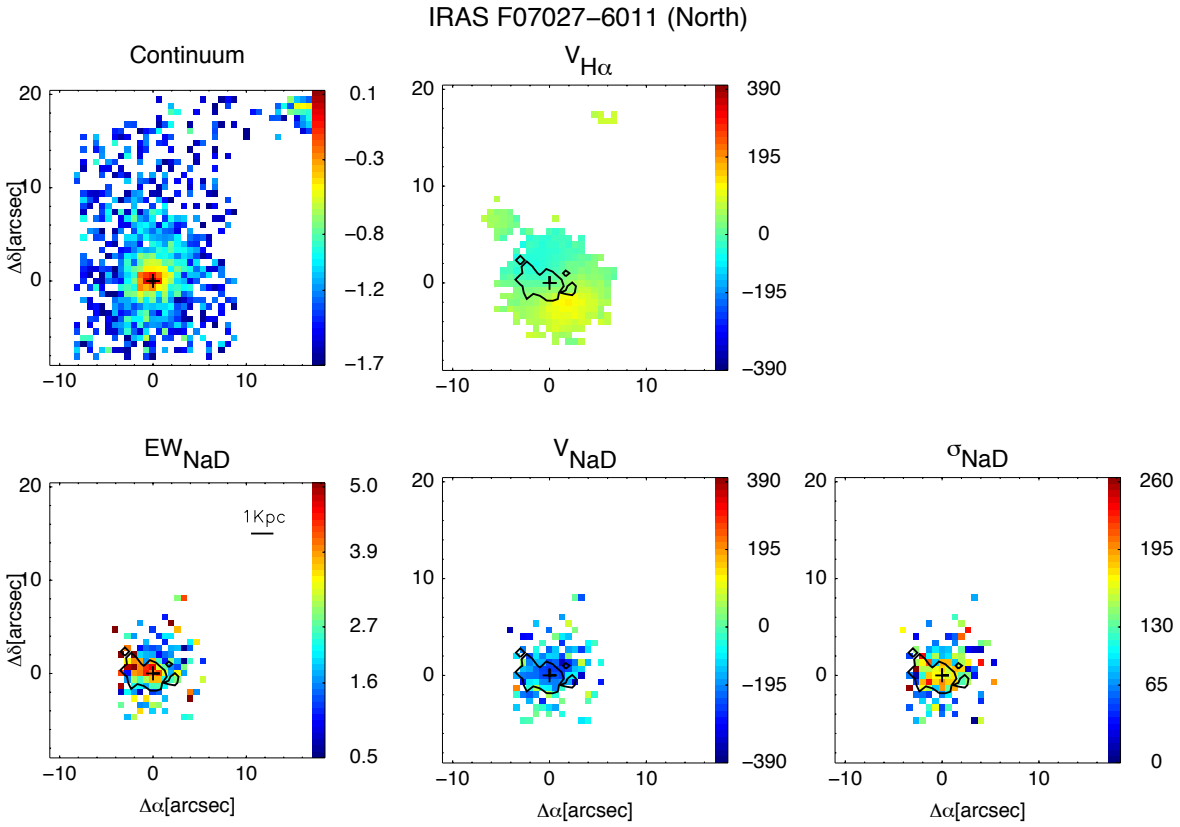

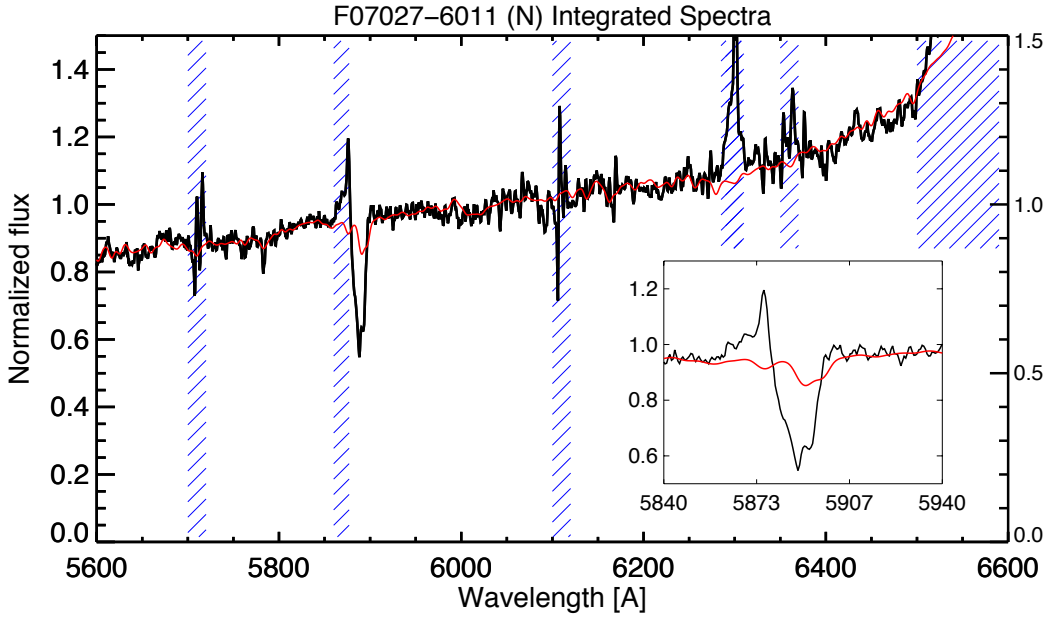

FIGURE A.13: As Fig. A.1 but for IRAS F07027-6011 (N).

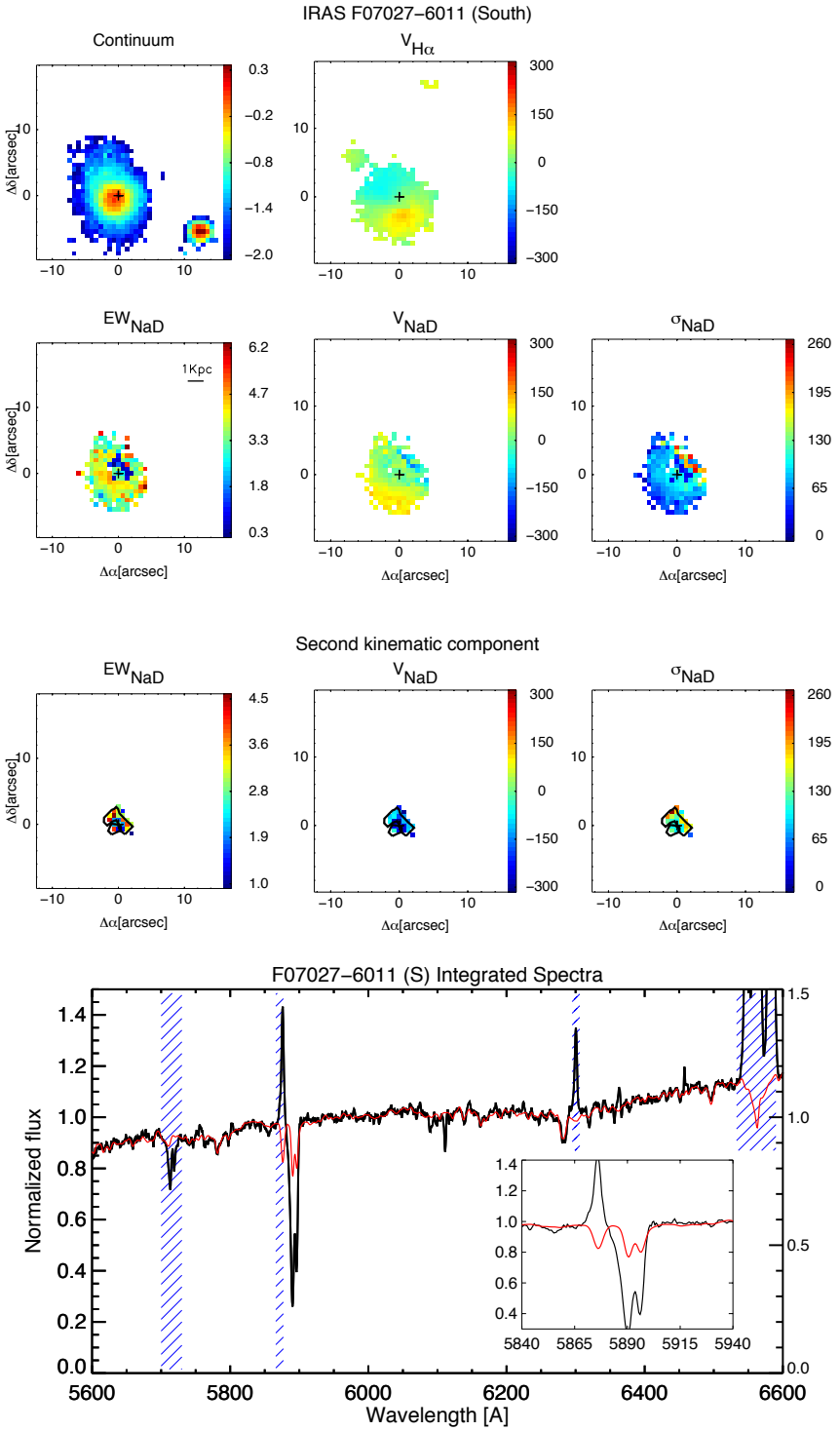

FIGURE A.14: As Fig. A.1 but for IRAS F07027-6011 (S). Maps of the second kinematic component of NaD are also included (third row.)

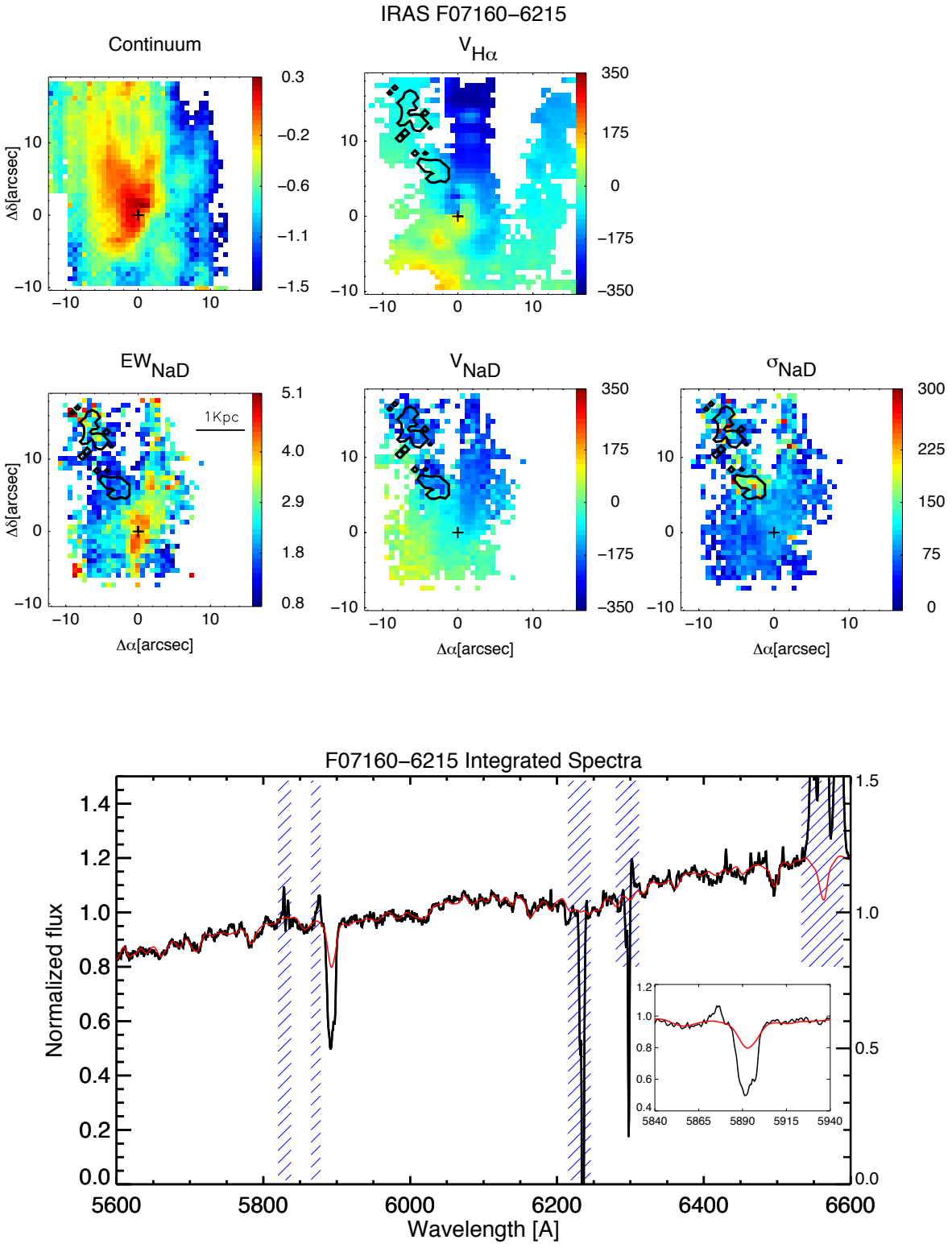

FIGURE A.15: As Fig. A.1 but for IRAS F7160-6215.

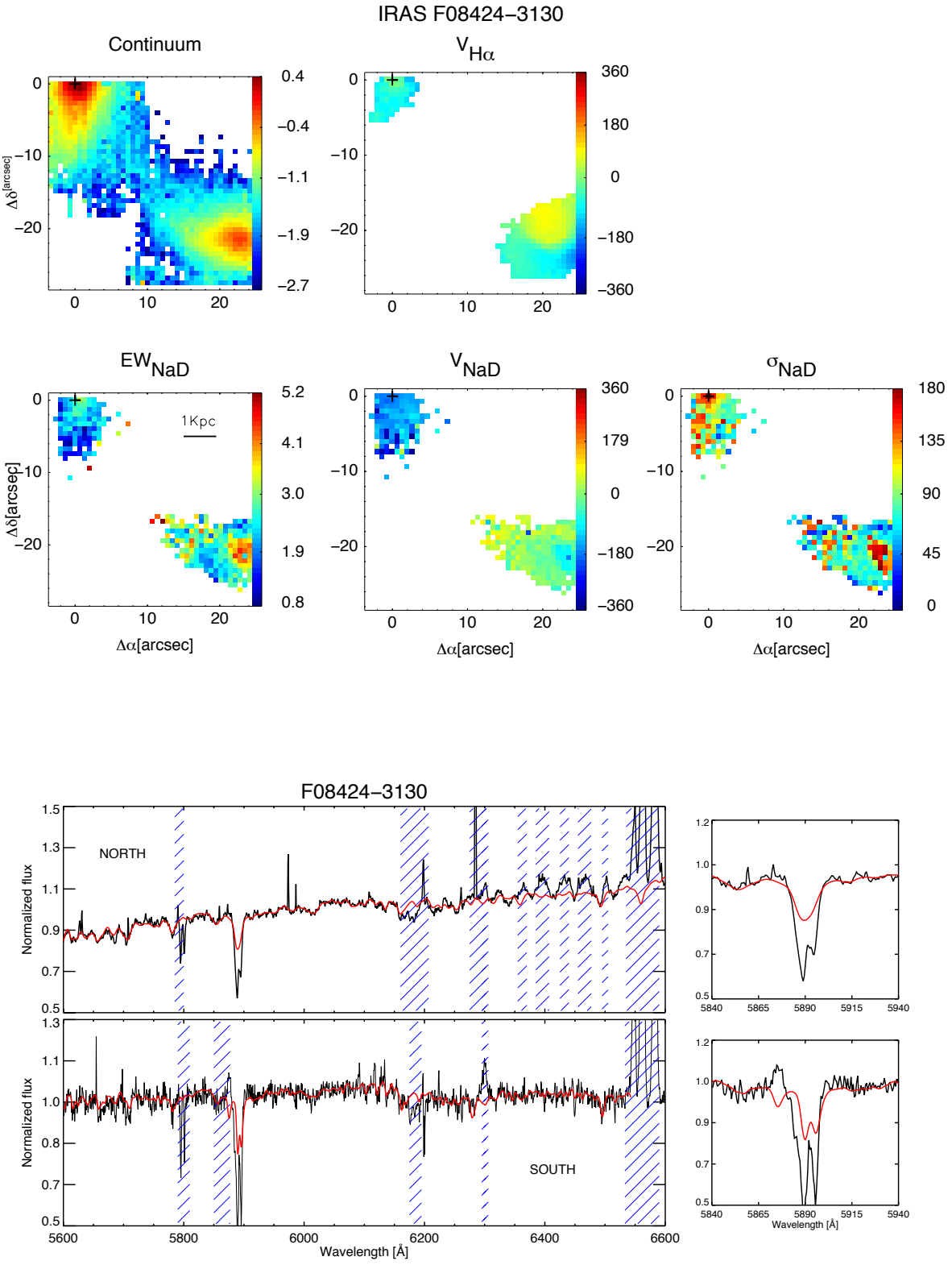

FIGURE A.16: As Fig. A.1 but for IRAS F08424-3130.

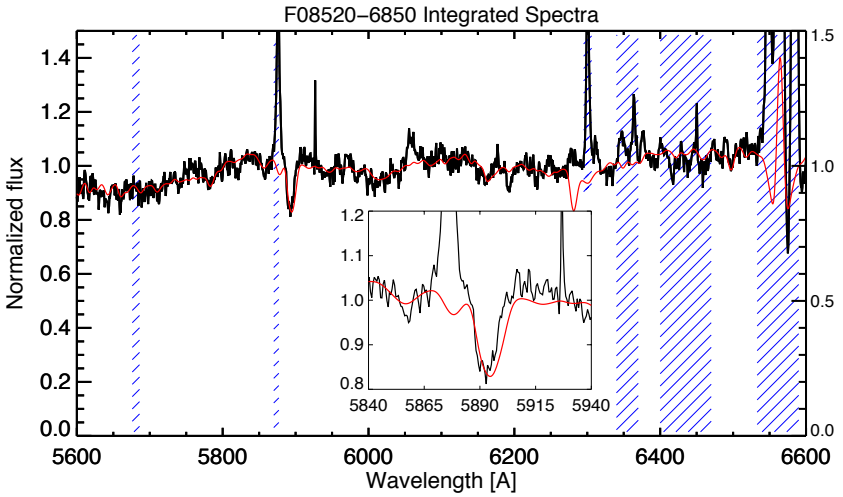

FIGURE A.17: As in the lower panel of Fig. A.1 but for IRAS 08520-6850.

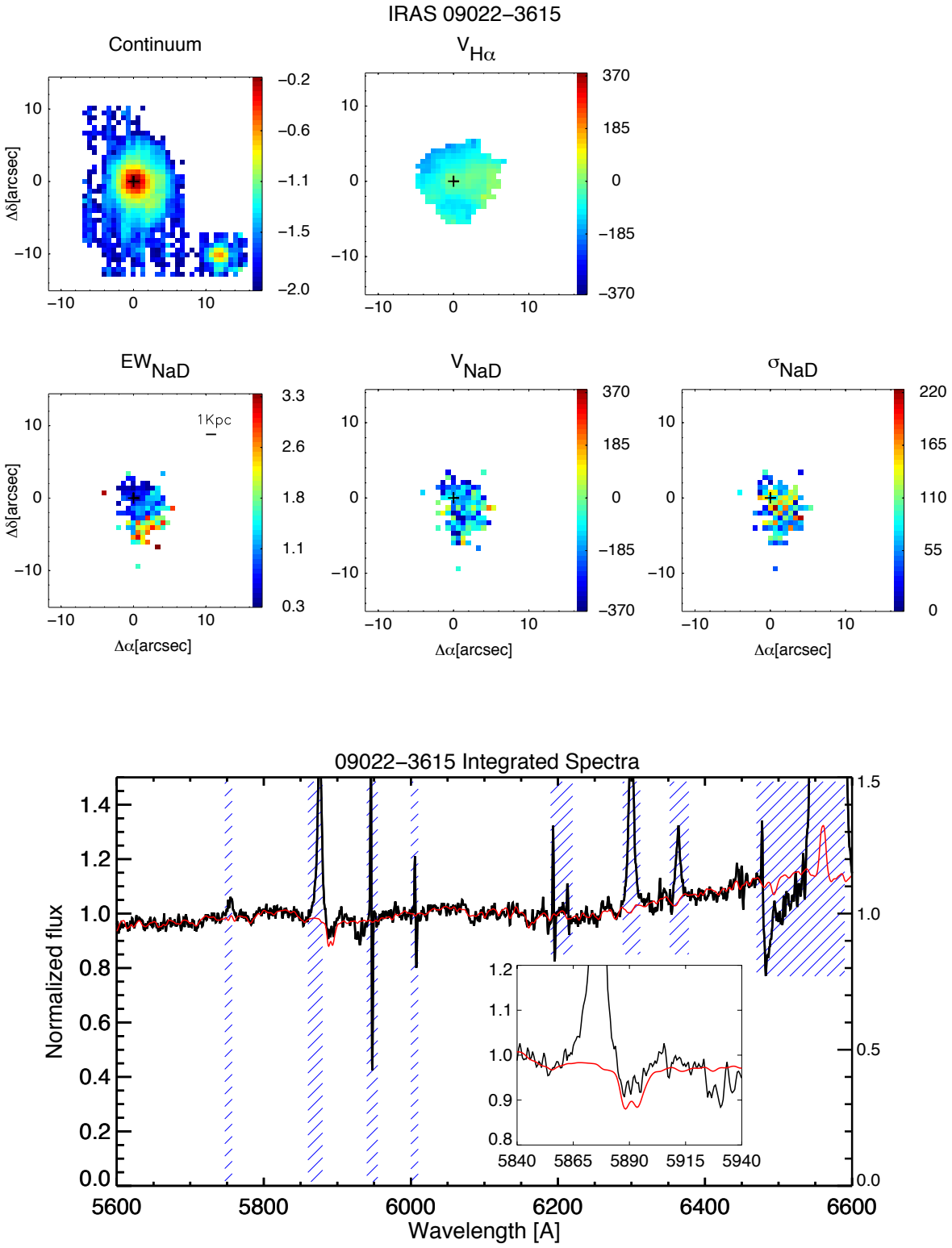

FIGURE A.18: As Fig. A.1 but for IRAS 09022-3615.

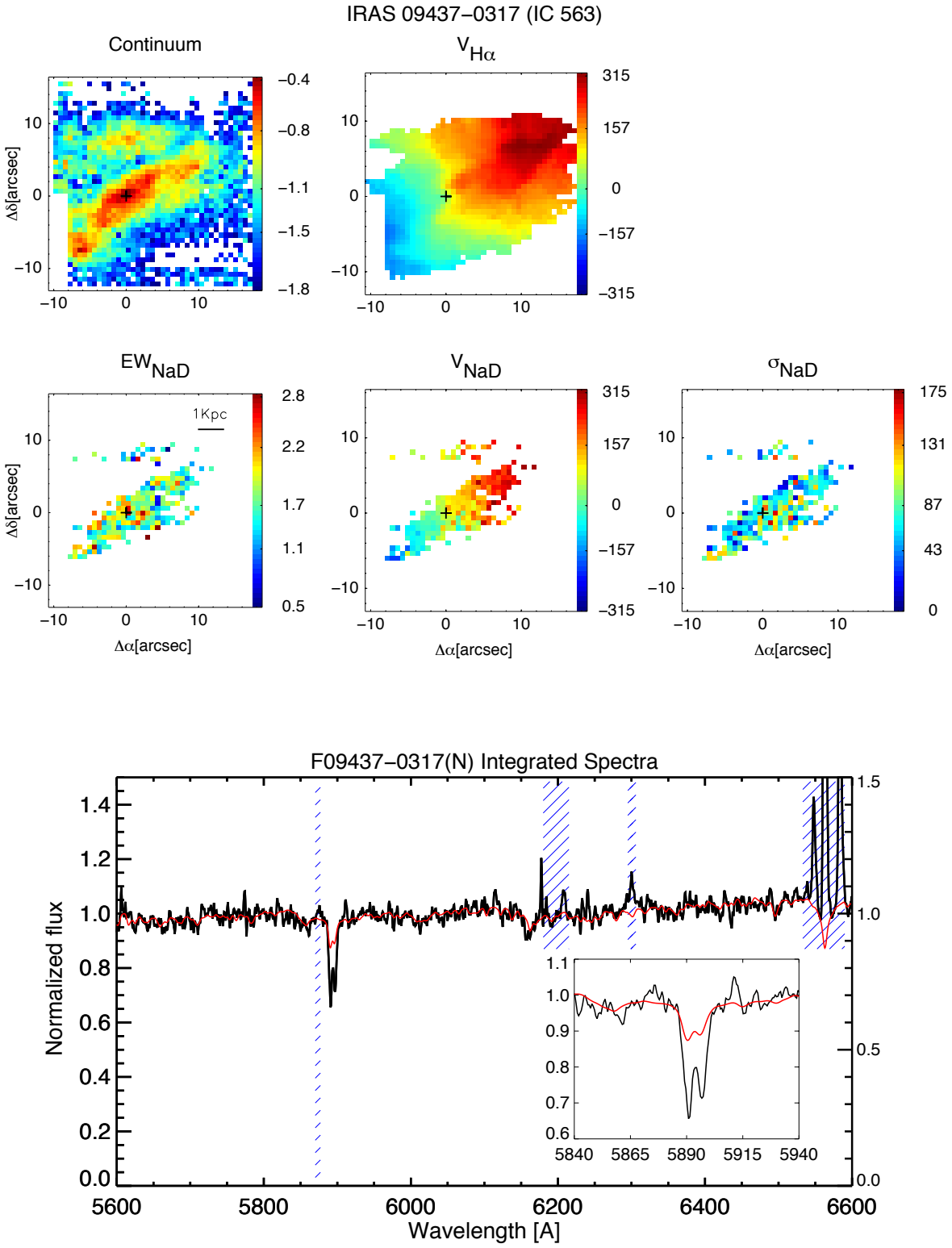

FIGURE A.19: As Fig. A.1 but for IRAS F09437-0317 (N).

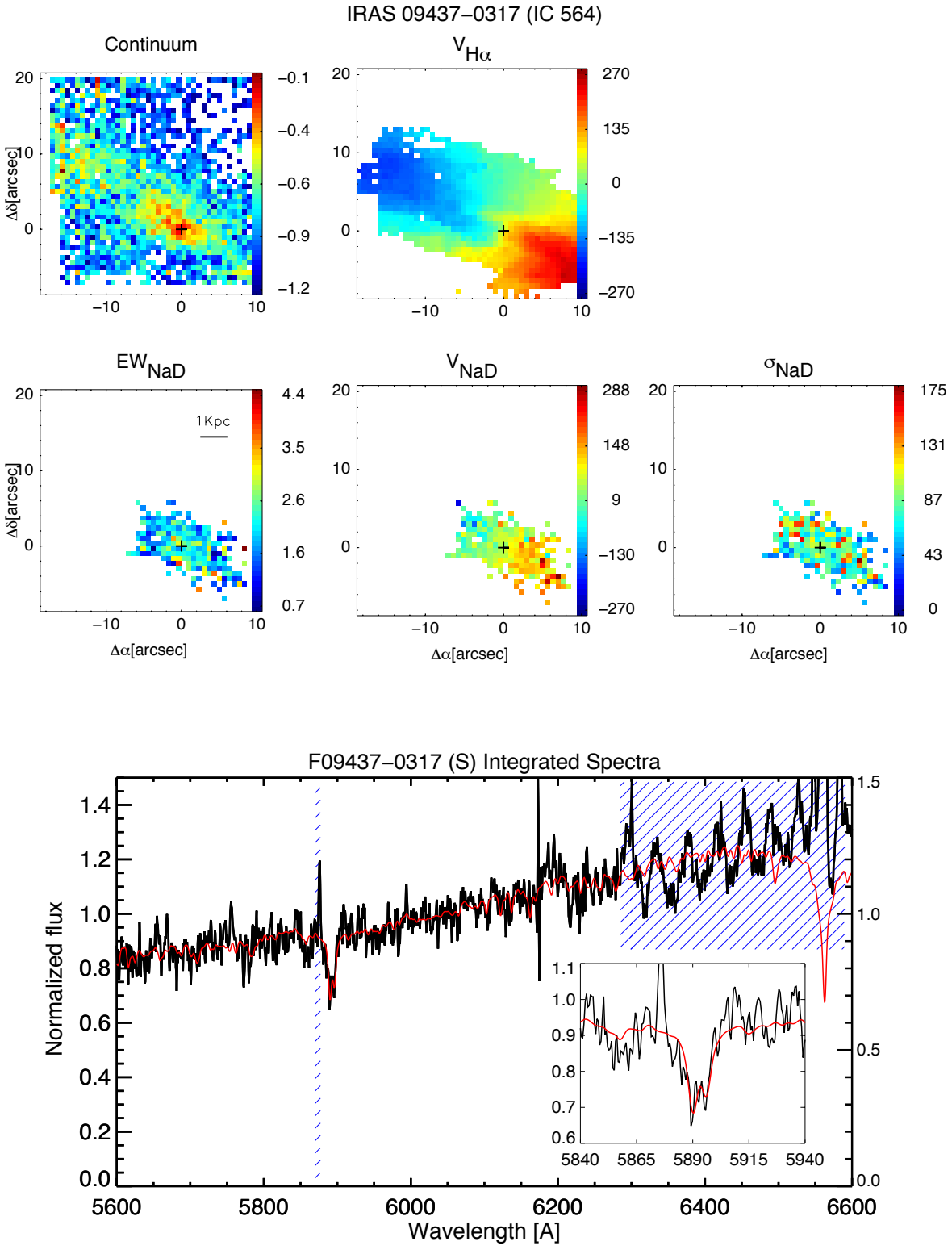

FIGURE A.20: As Fig. A.1 but for IRAS F09437-0317.

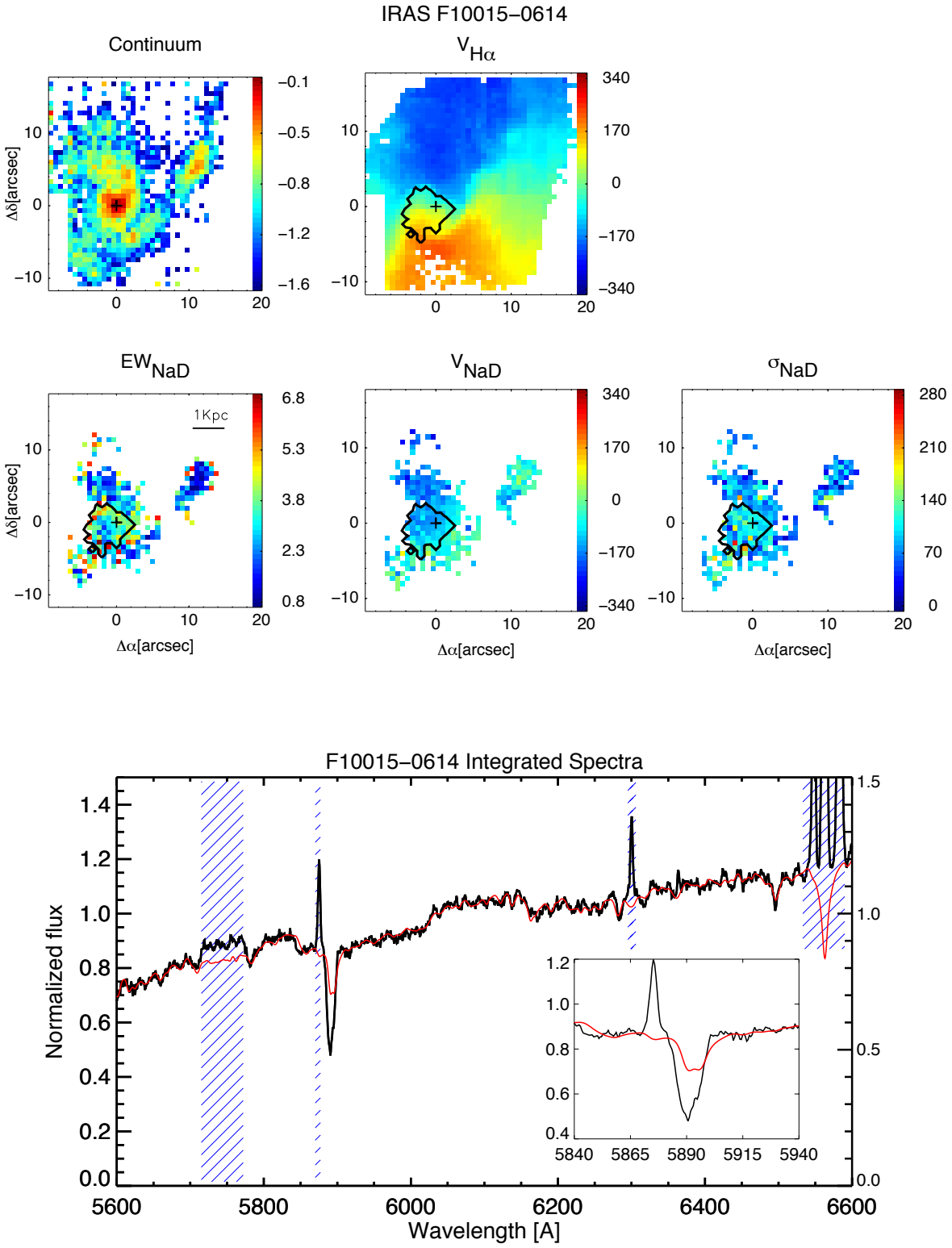

FIGURE A.21: As Fig. A.1 but for IRAS F10015-0614.

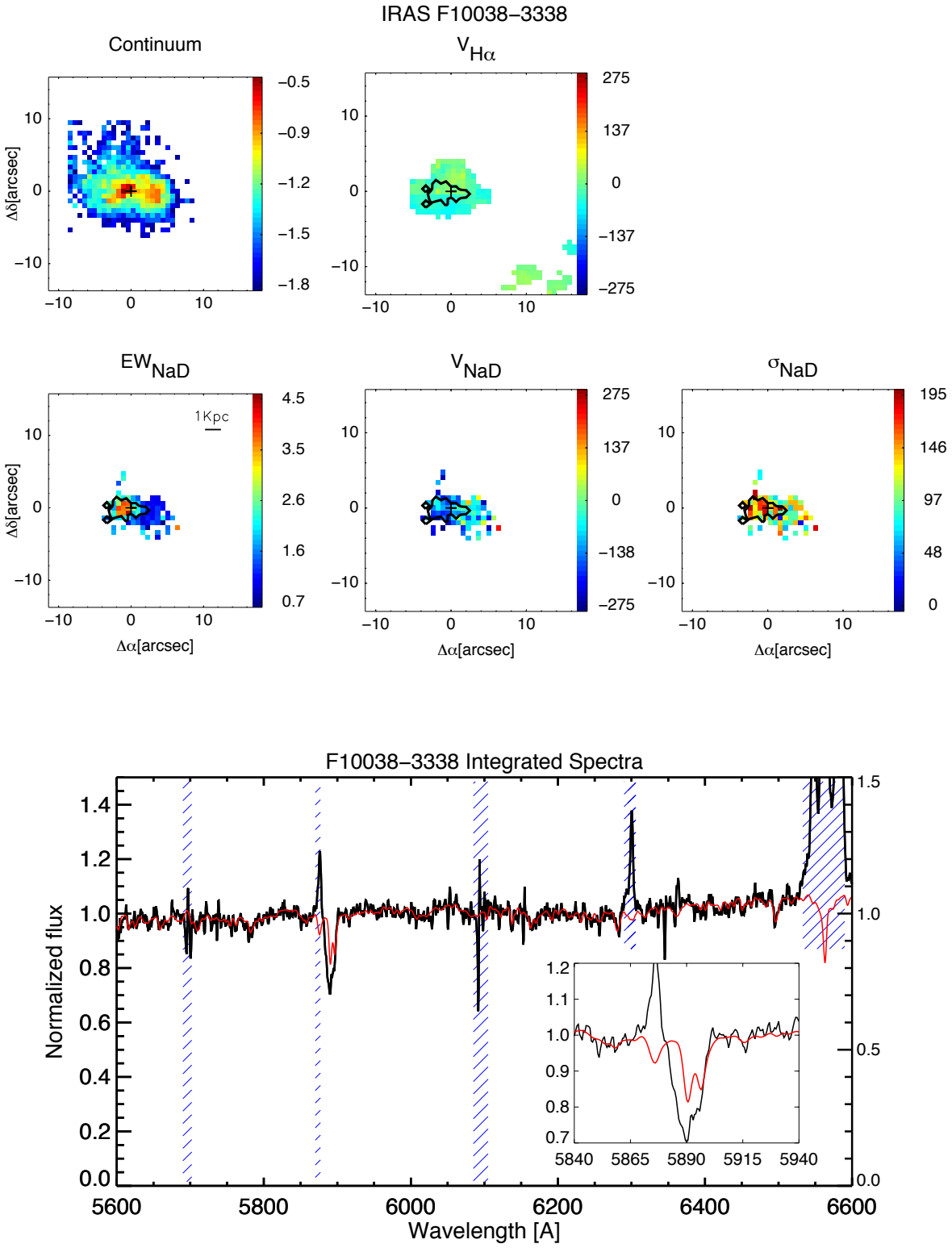

FIGURE A.22: As Fig. A.1 but for IRAS F10038-3338.

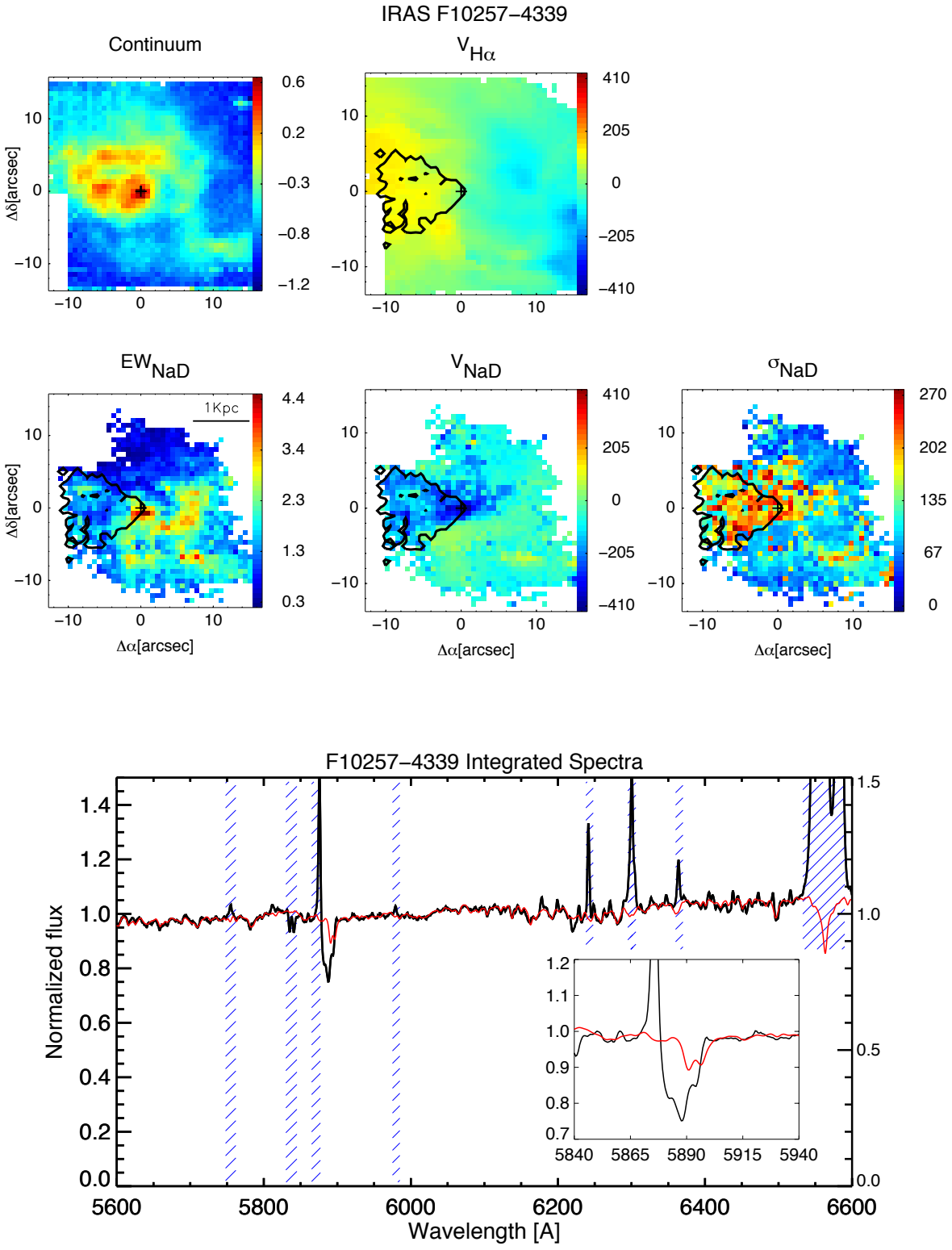

FIGURE A.23: As Fig. A.1 but for IRAS F10257-4339.

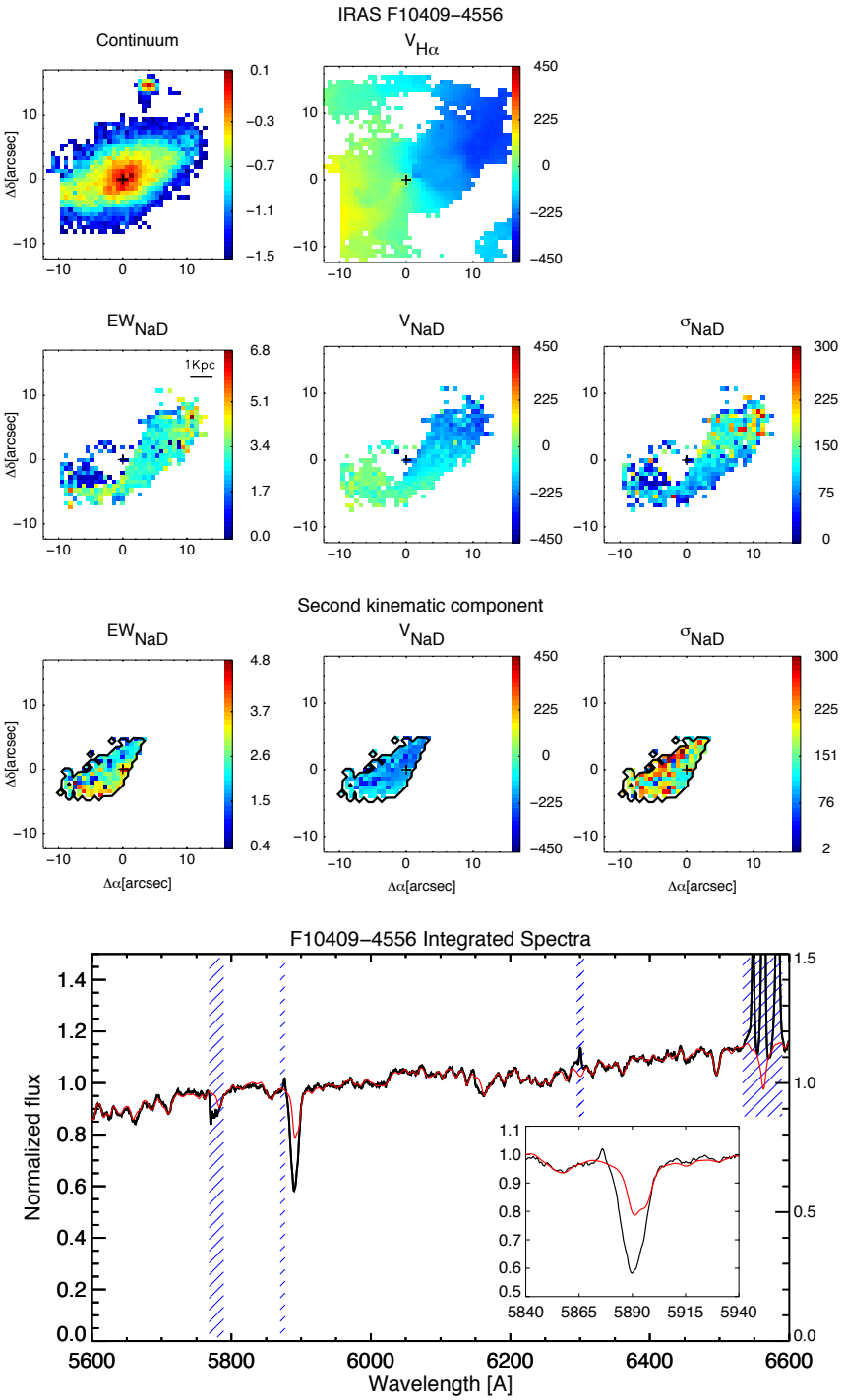

FIGURE A.24: As Fig. A.14 but for IRAS F10409-4556.

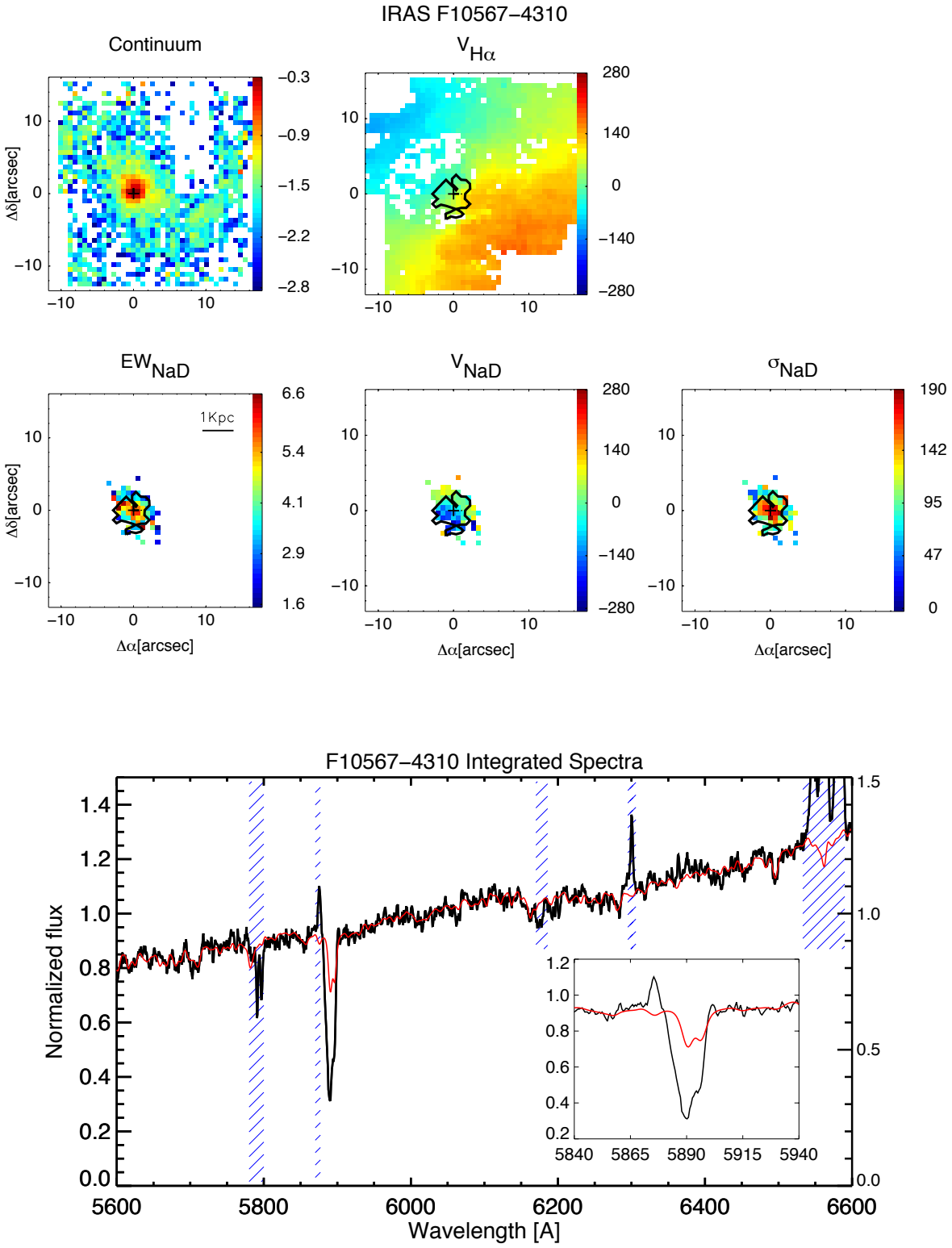

FIGURE A.25: As Fig. A.1 but for IRAS 10567-4310.

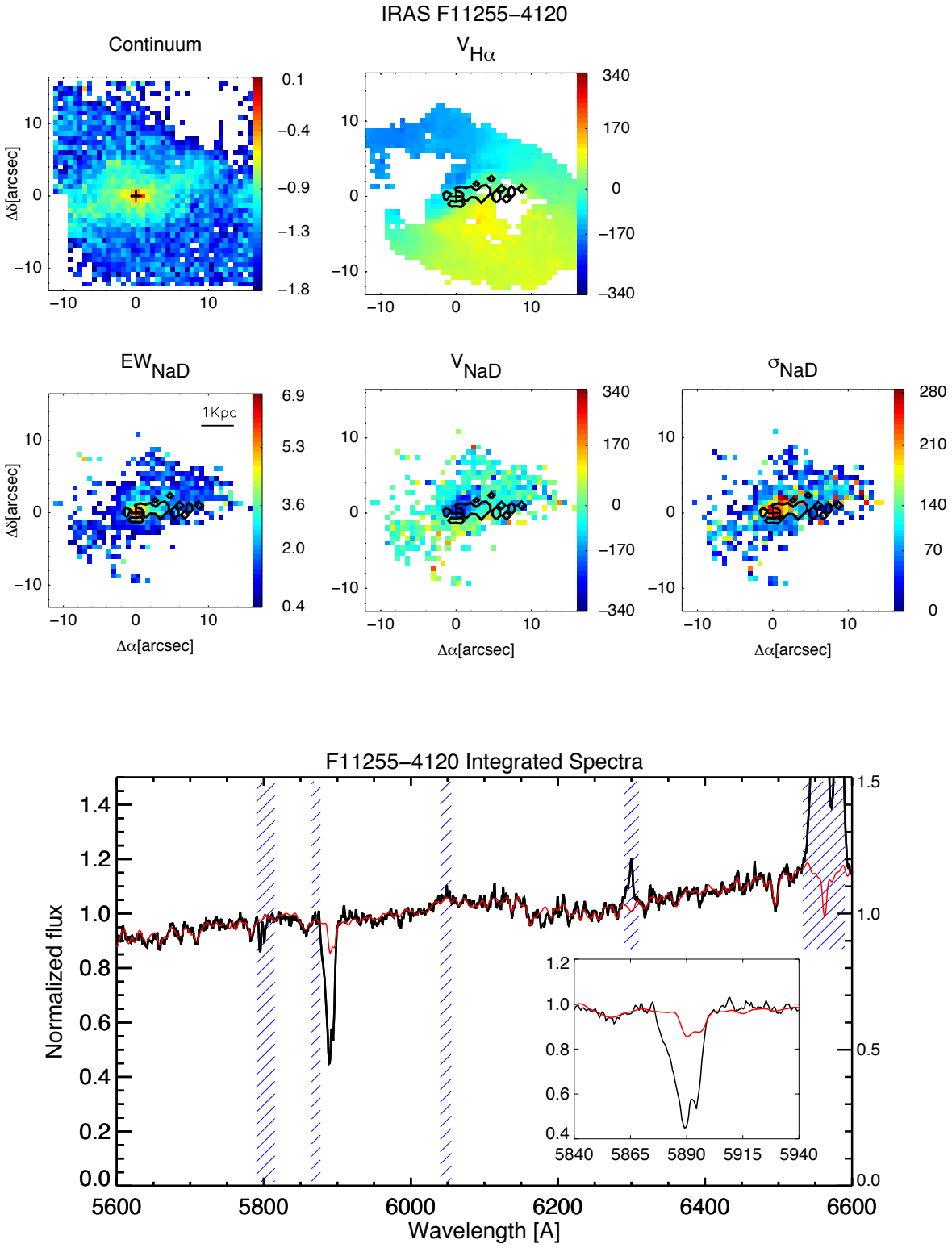

FIGURE A.26: As Fig. A.1 but for IRAS F11254-4120.

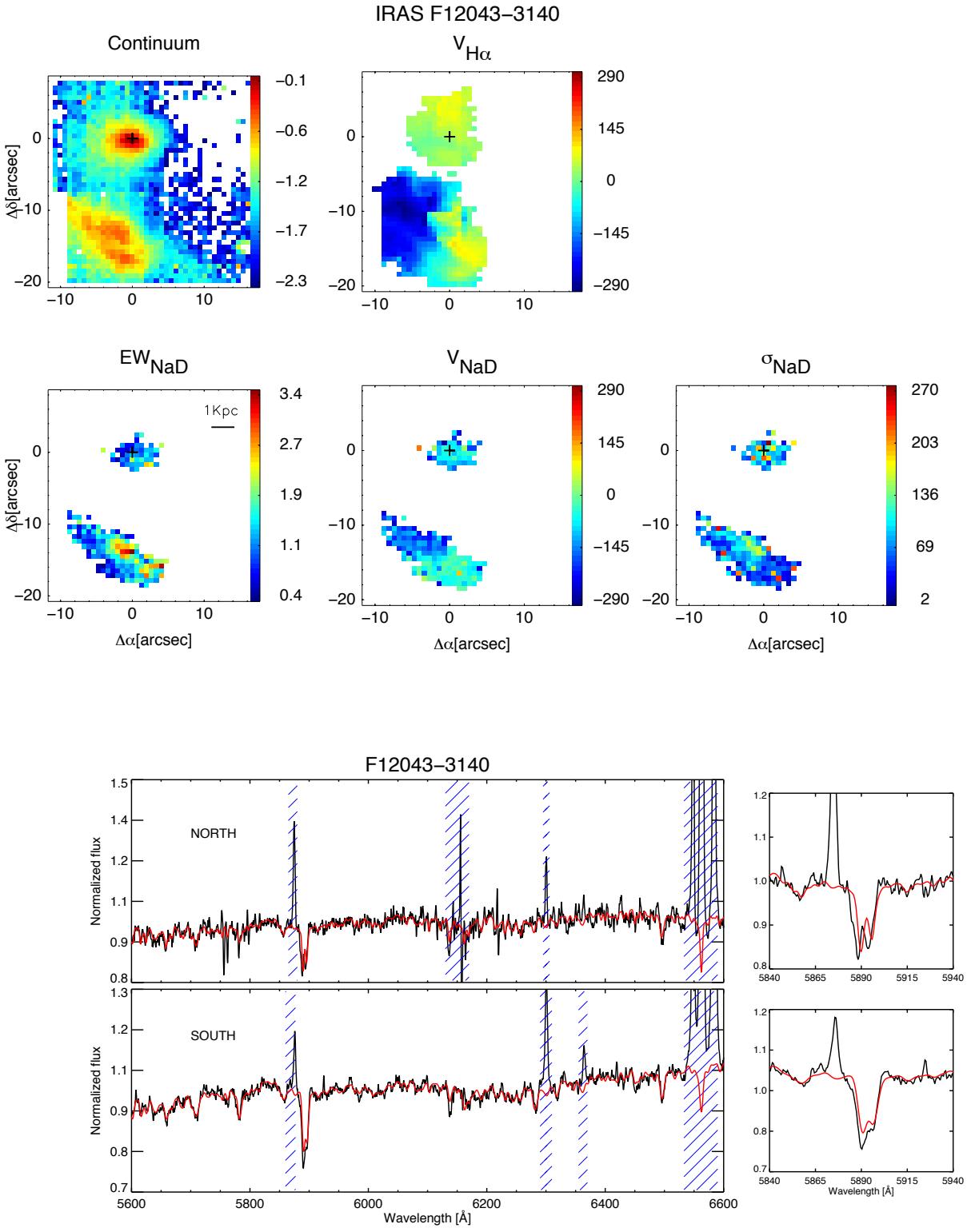

FIGURE A.27: As Fig. A.1 but for IRAS F12043-3140.

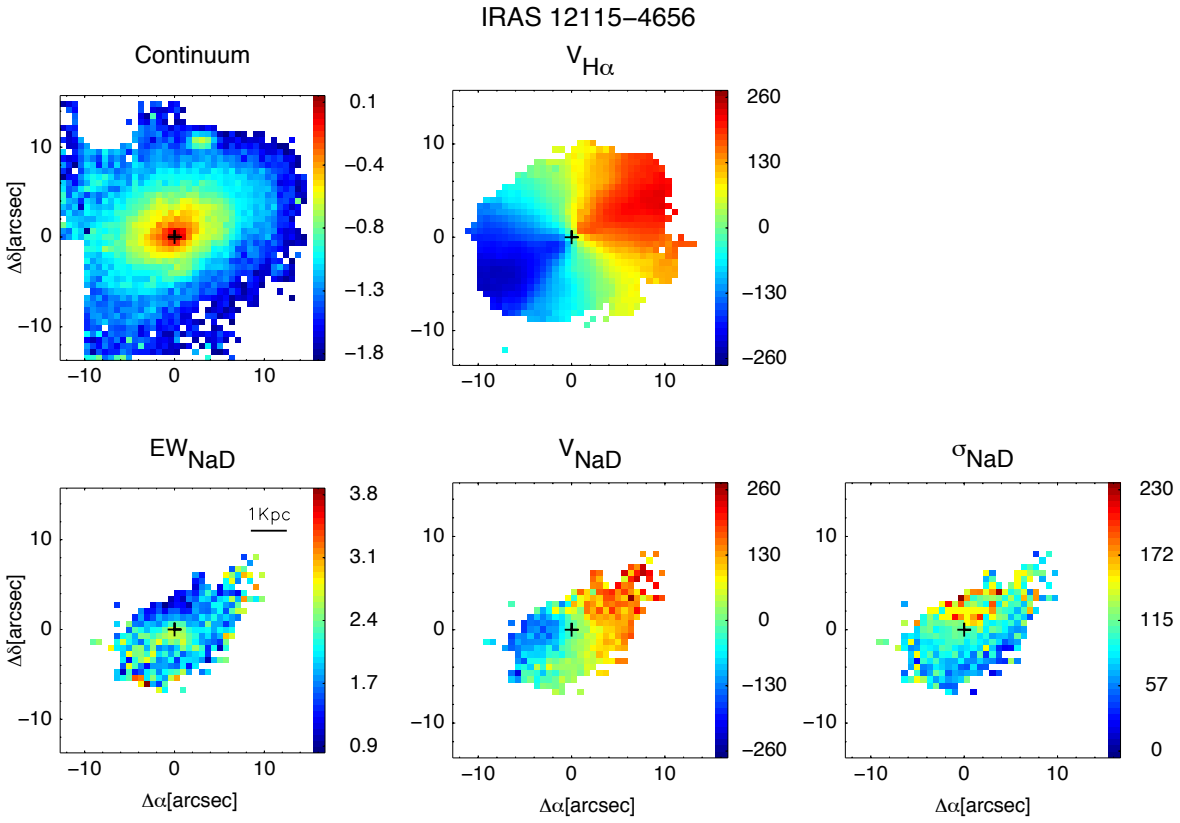

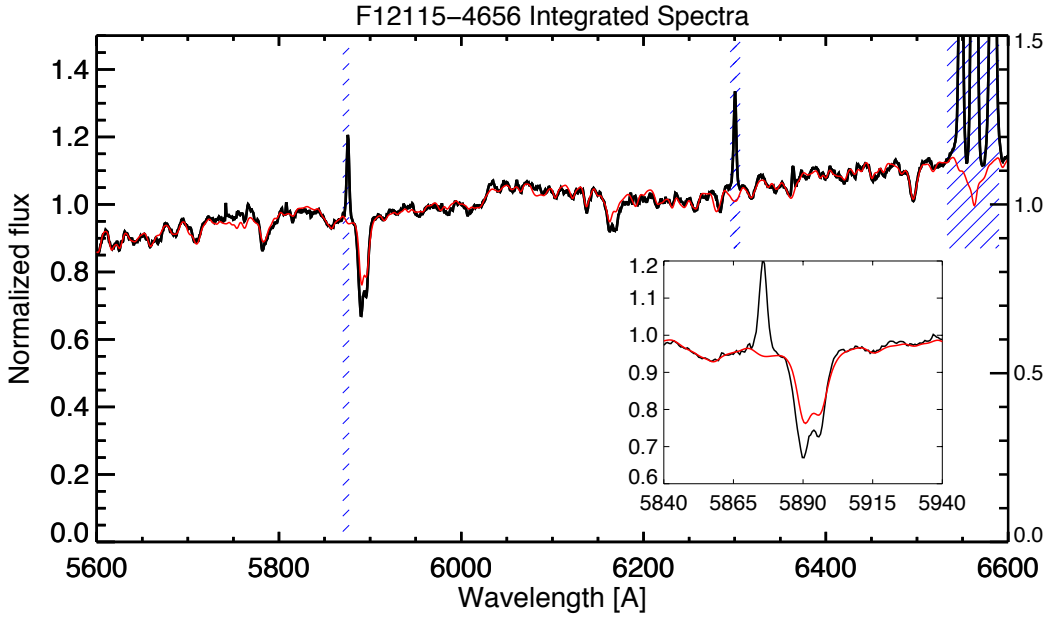

FIGURE A.28: As Fig. A.1 but for IRAS F12115-4656.

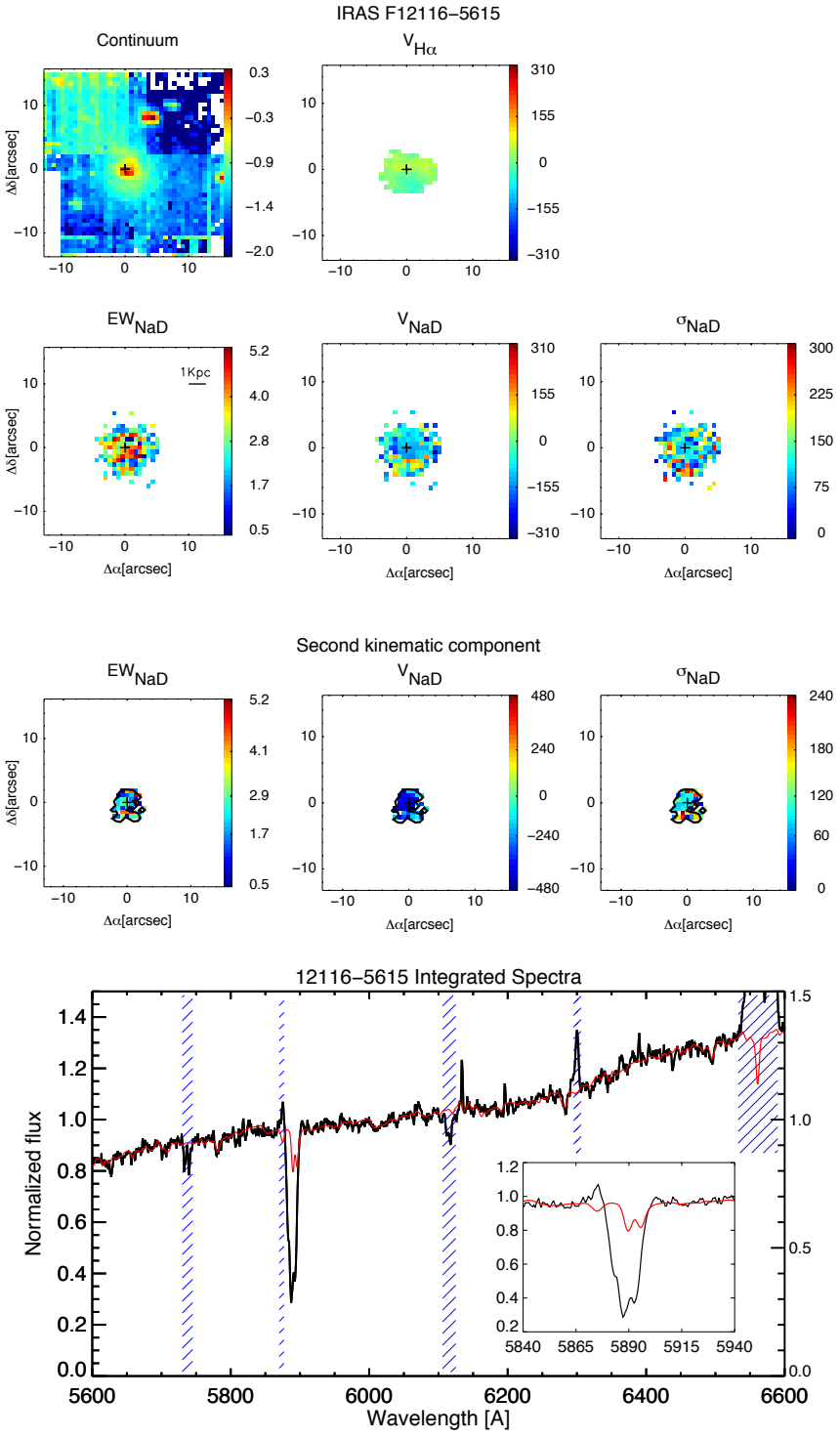

FIGURE A.29: As Fig. A.14 but for IRAS F12116-2339.

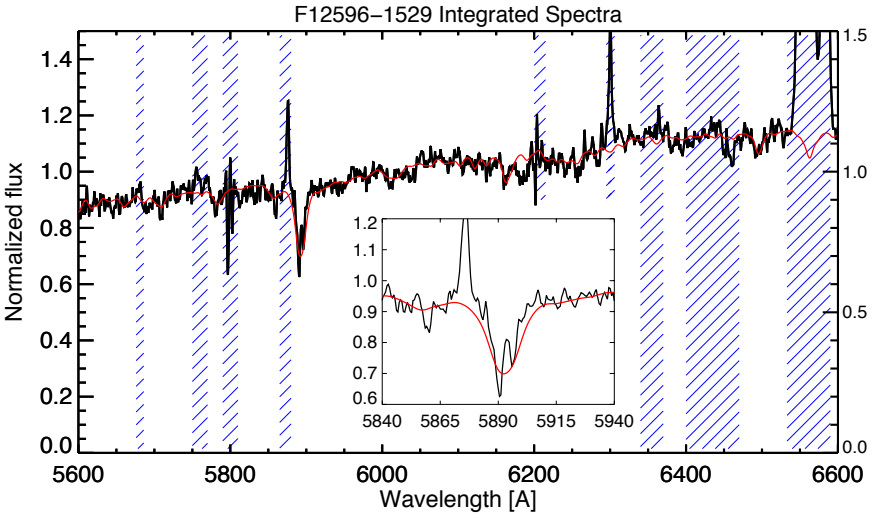

FIGURE A.30: As in the lower panel of Fig. A.1 but for 12596-1529 north and south (top to the bottom, respectively)

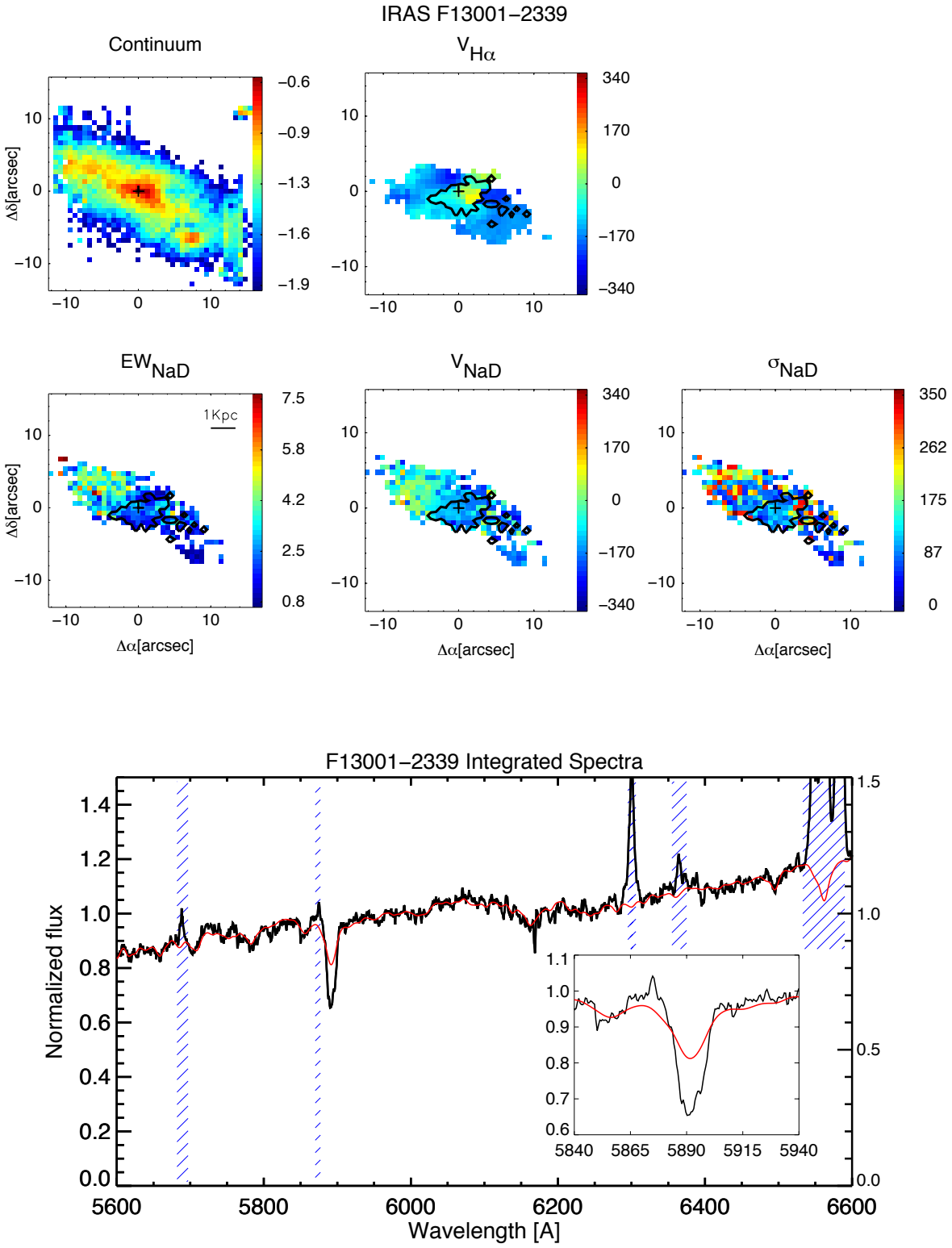

FIGURE A.31: As Fig. A.1 but for IRAS F13001-2339.

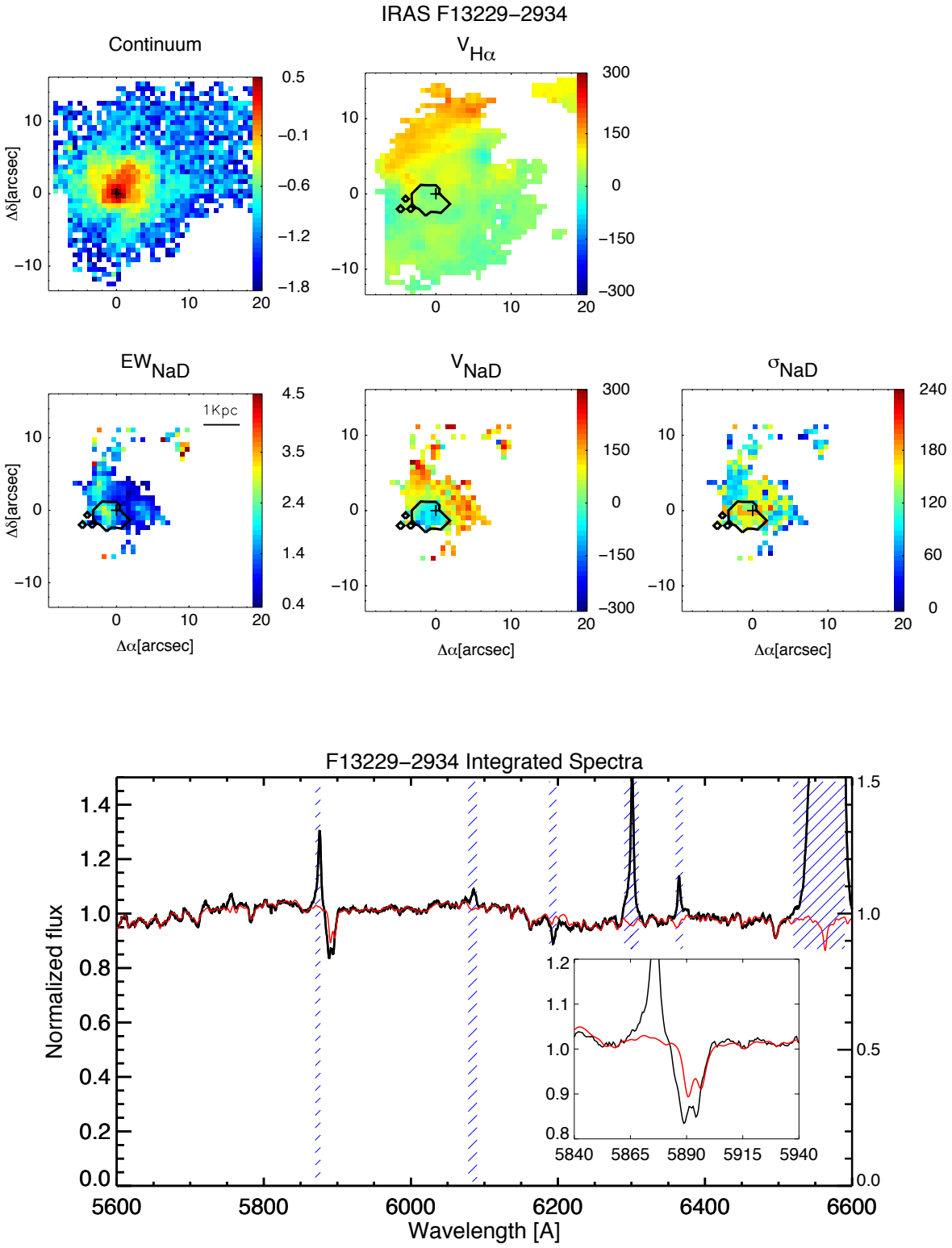

FIGURE A.32: As Fig. A.1 but for IRAS F13229-2934.

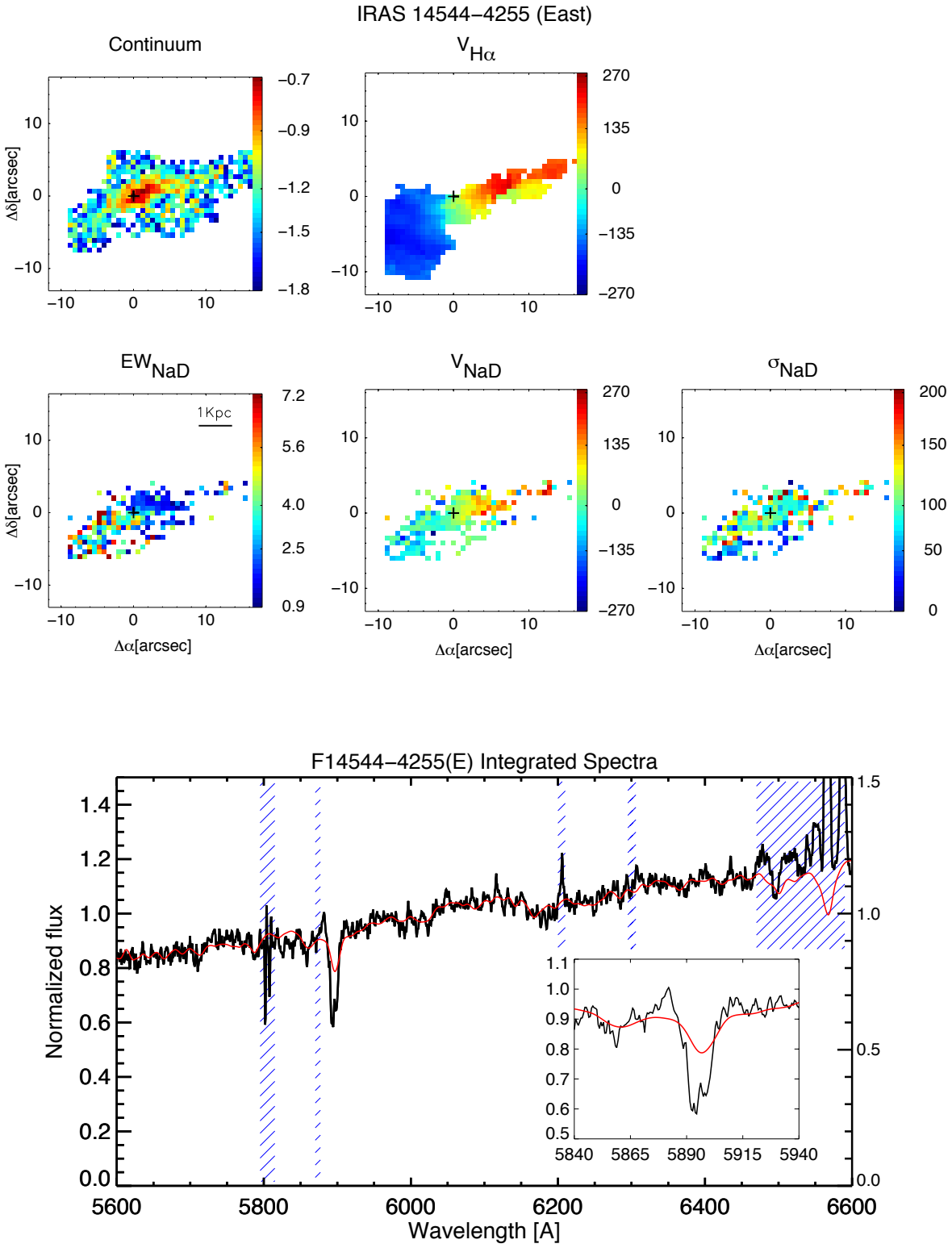

FIGURE A.33: As Fig. A.1 but for IRAS 14544-4255 (E).

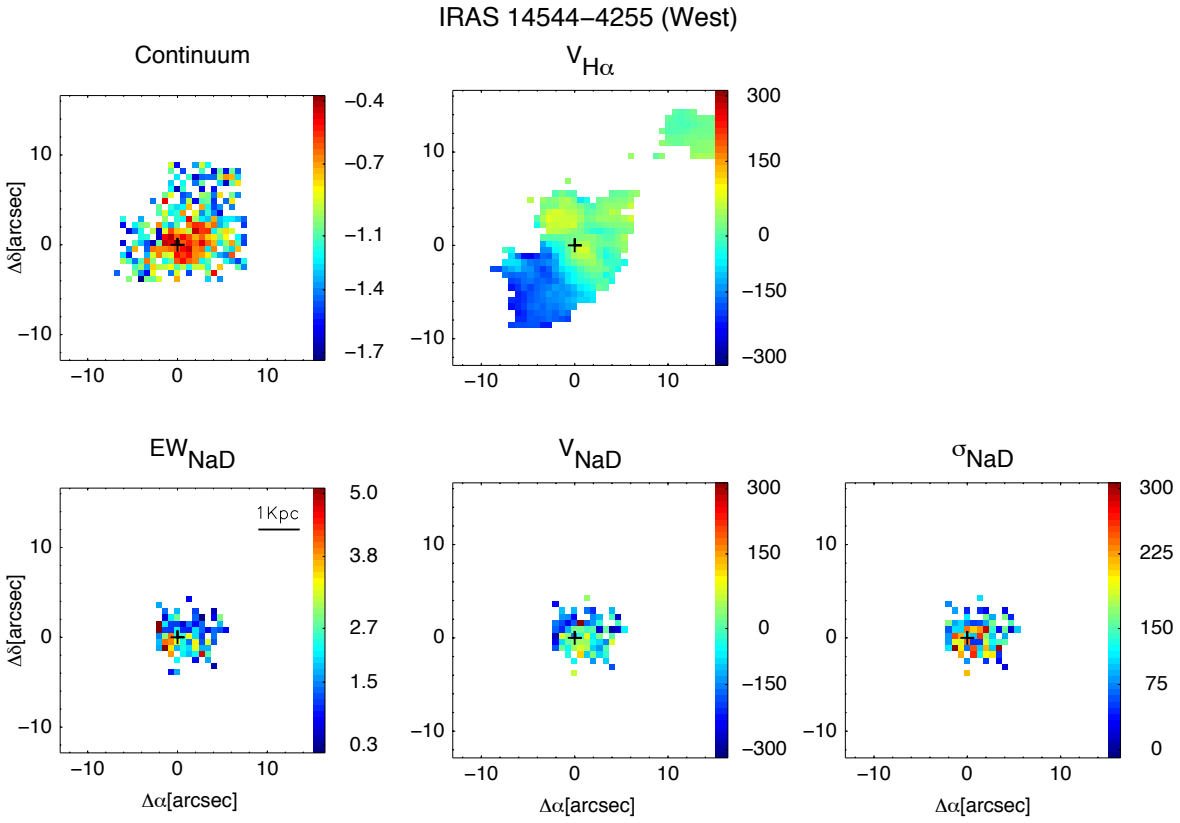

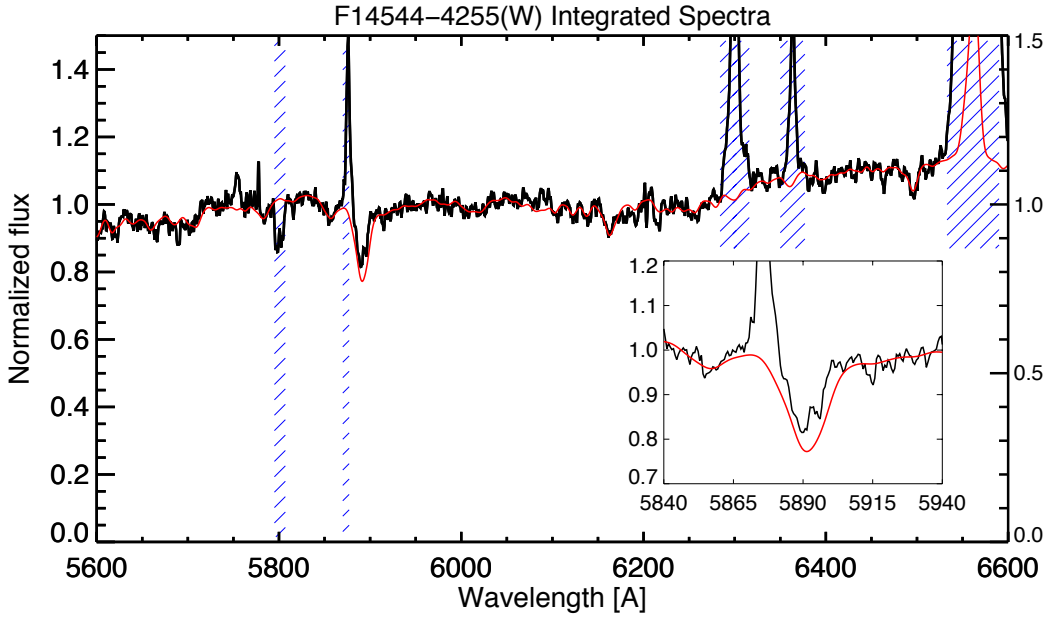

FIGURE A.34: As Fig. A.1 but for IRAS 14544-4255 (W).

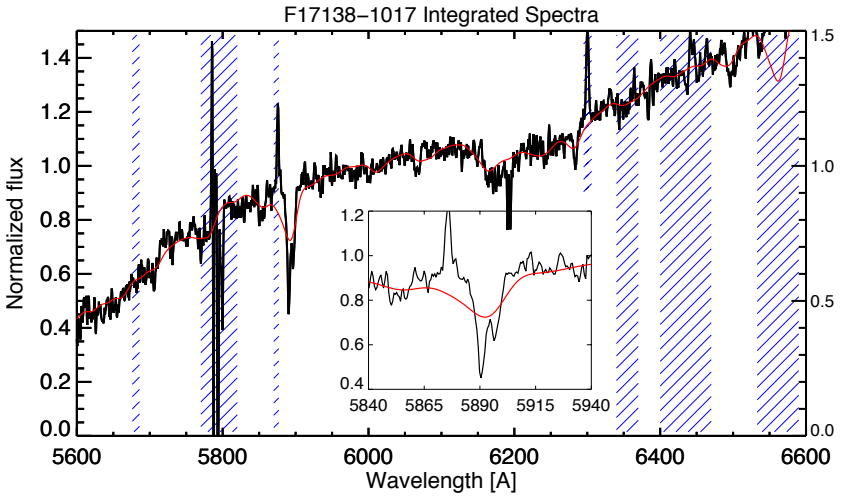

FIGURE A.35: As in the lower panel of Fig. A.1 but for IRAS 17138-1017

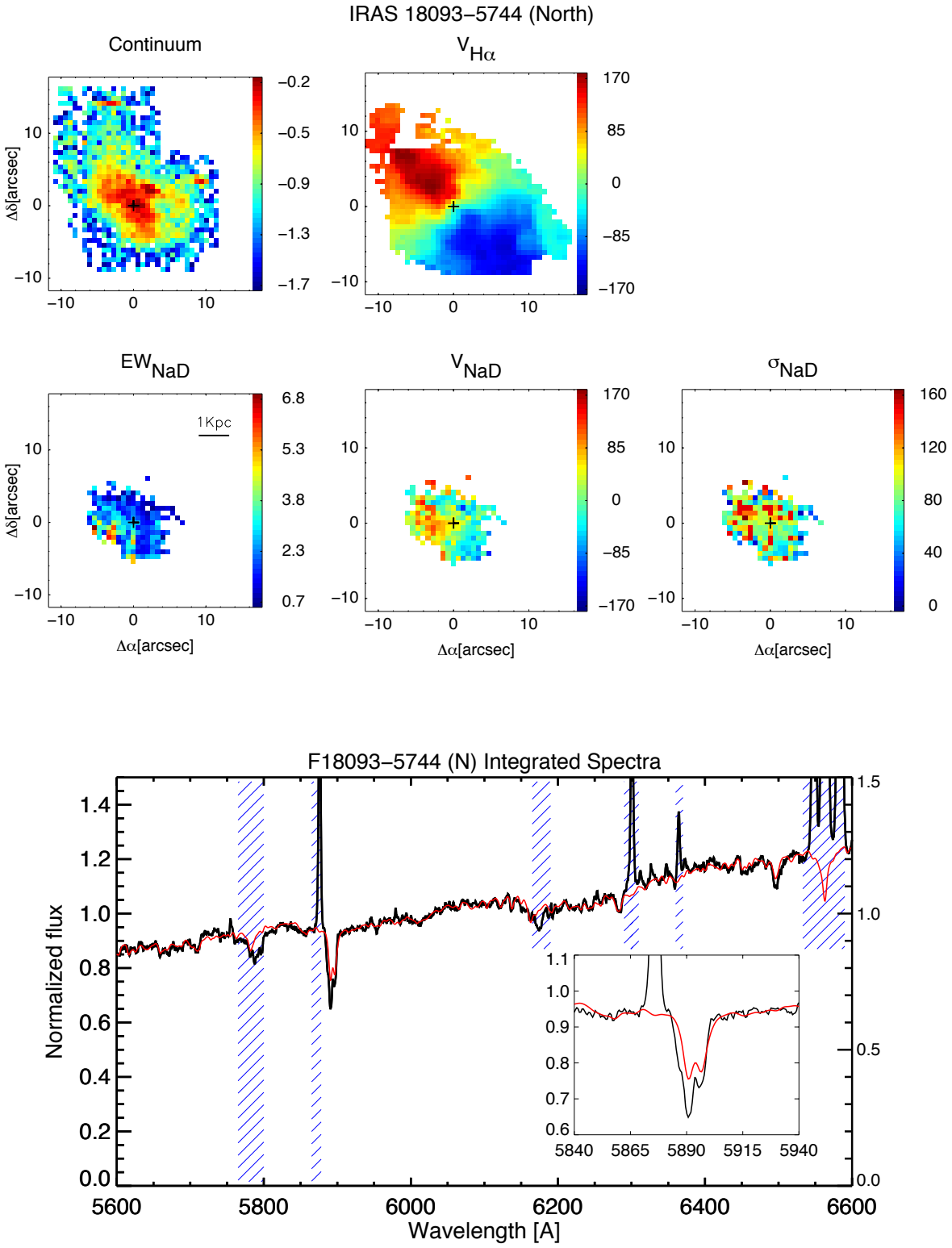

FIGURE A.36: As Fig. A.1 but for IRAS F18093-5744 (N).

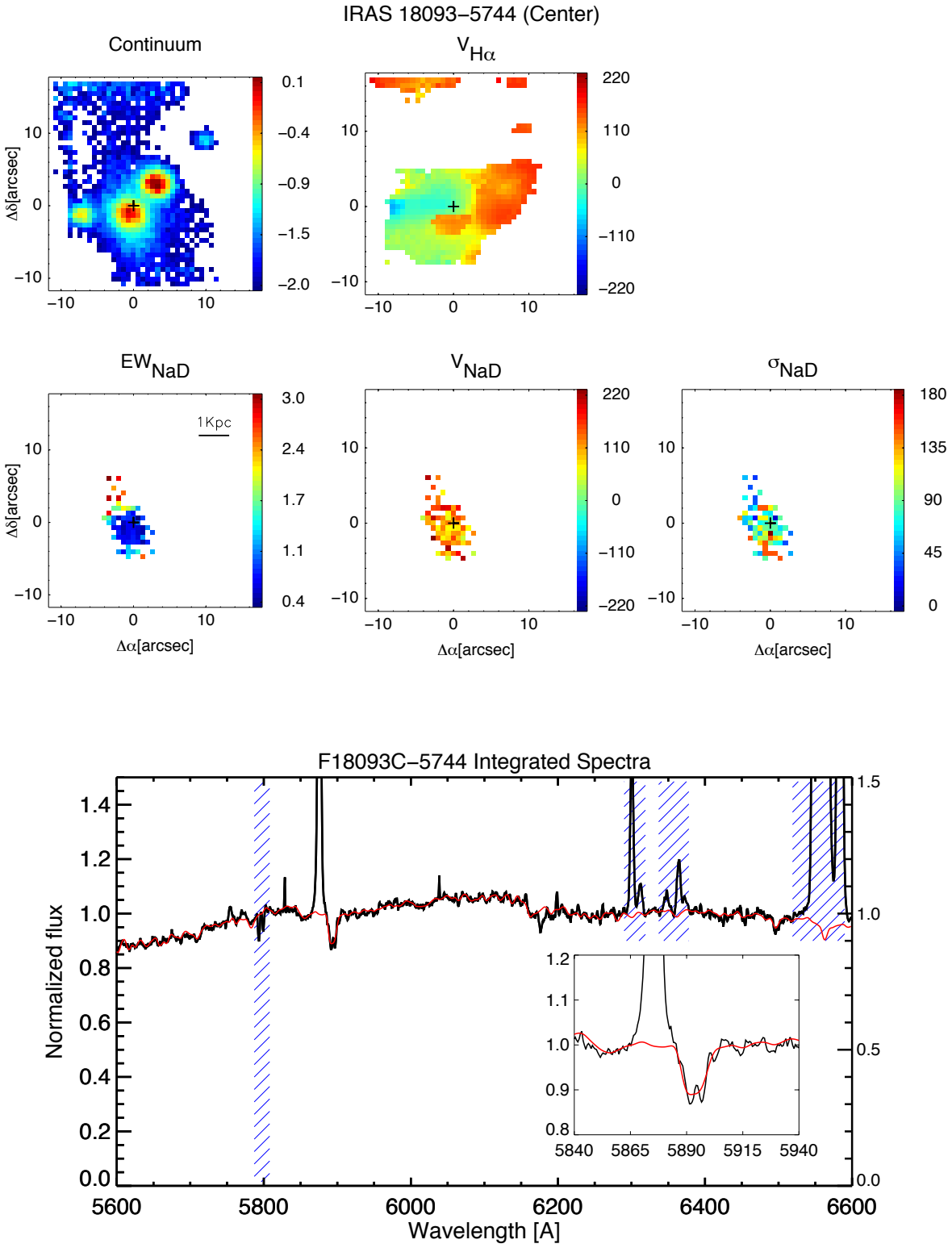

FIGURE A.37: As Fig. A.1 but for IRAS F18093-5744 (C).

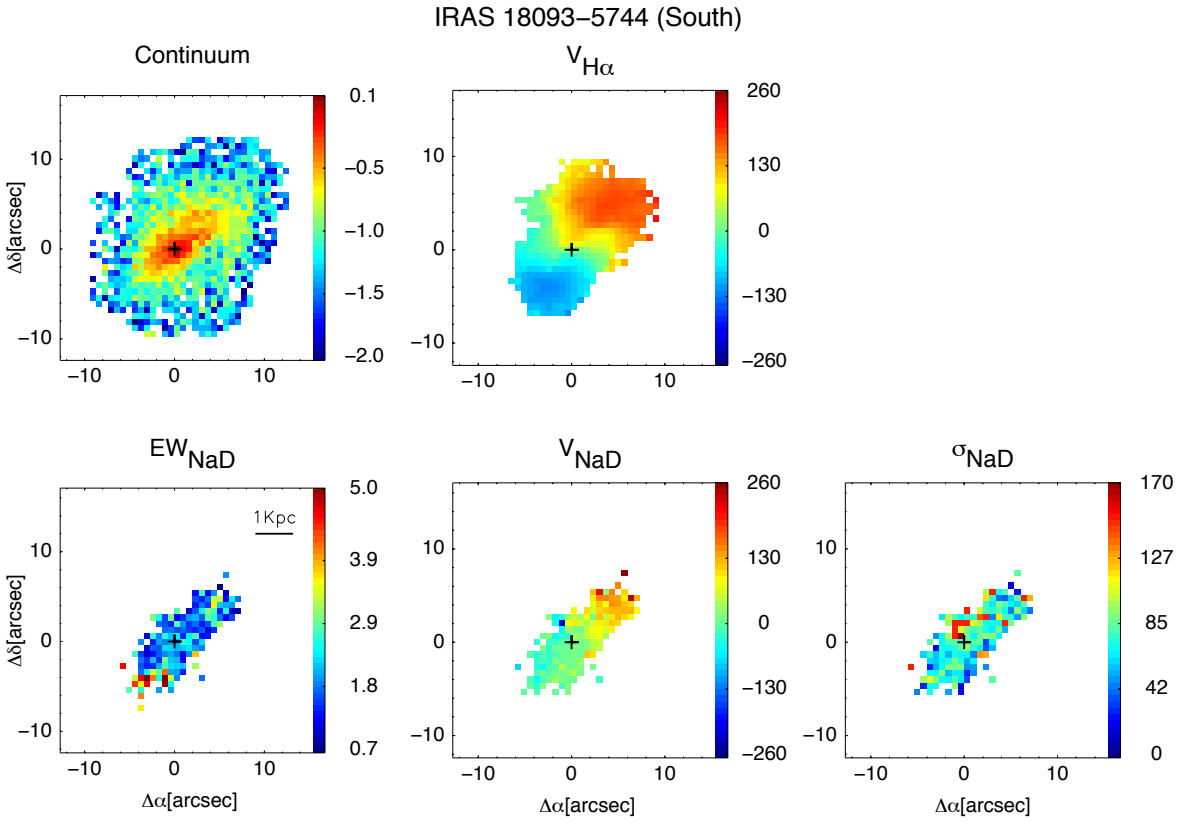

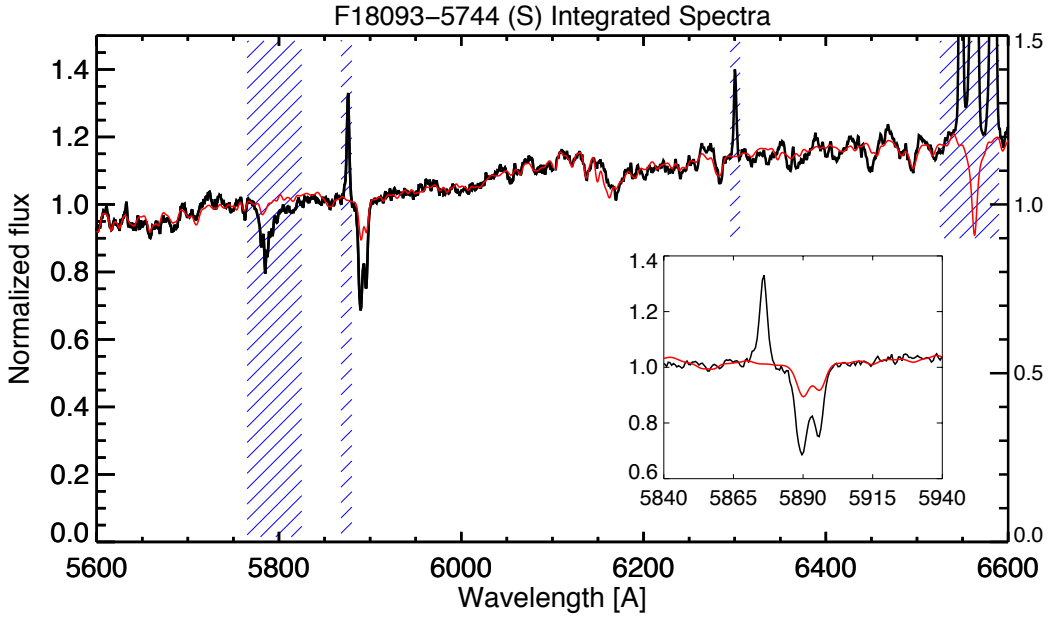

FIGURE A.38: As Fig. A.1 but for IRAS F18093-5744 (S).

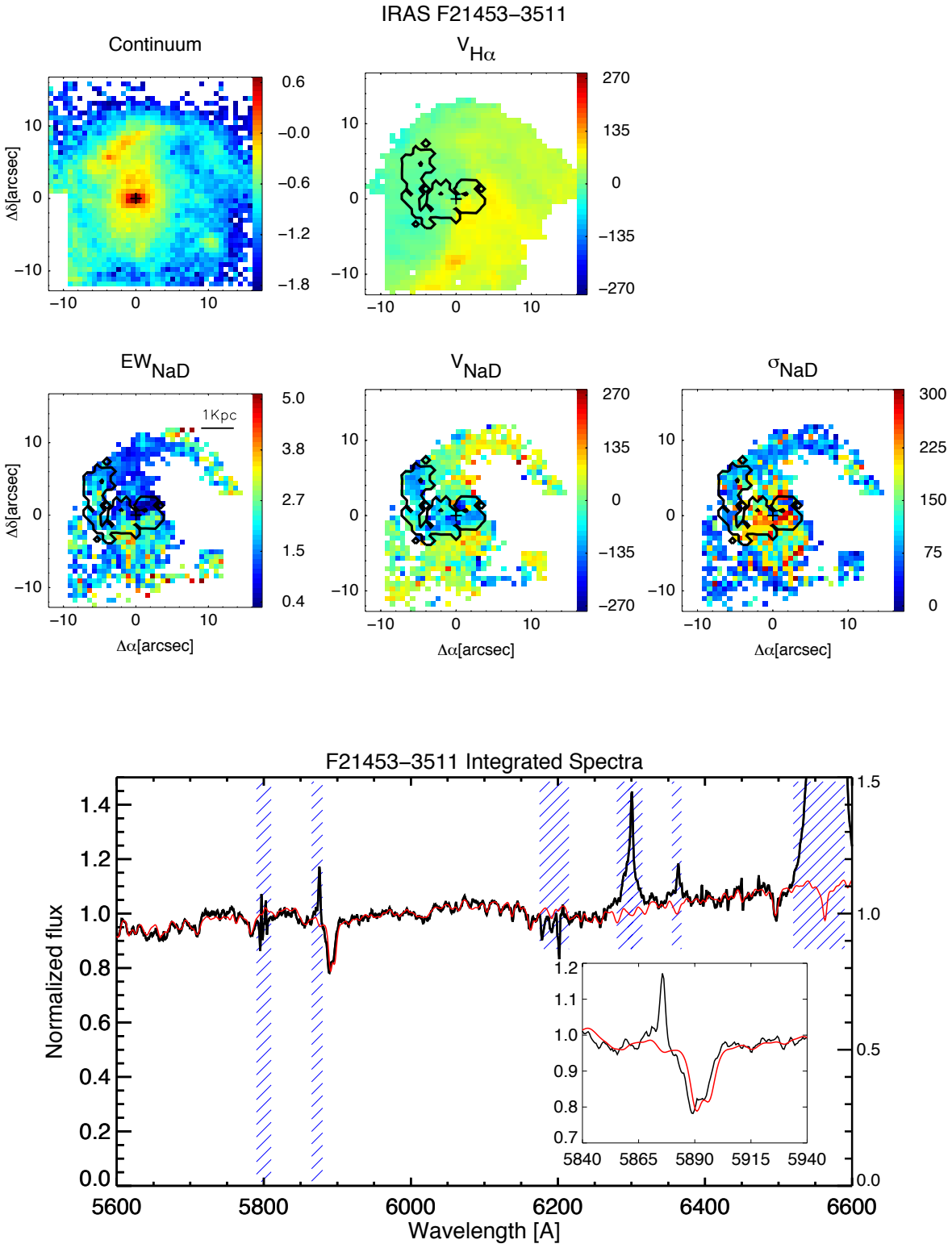

FIGURE A.39: As Fig. A.1 but for IRAS 21453-3511.

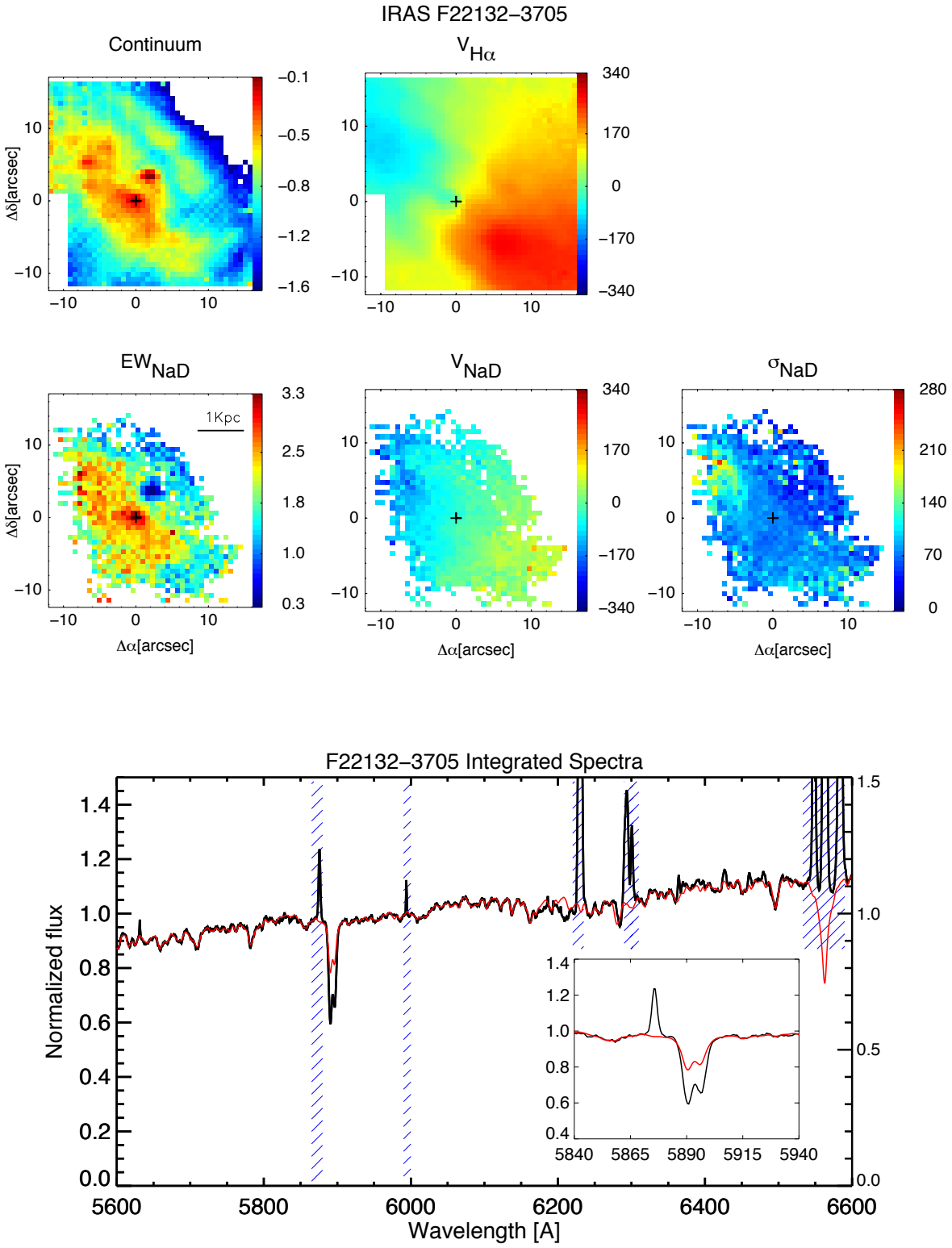

FIGURE A.40: As Fig. A.1 but for IRAS F22132-3705.

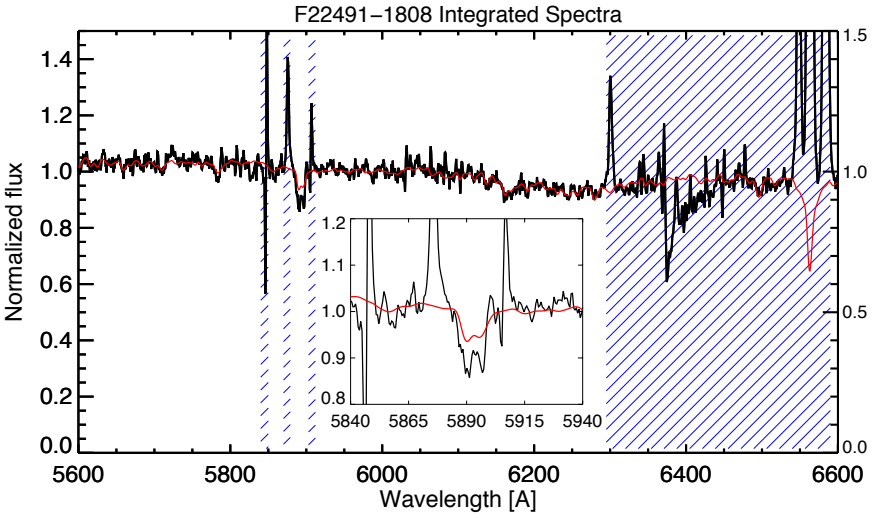

FIGURE A.41: As in the lower panel of Fig. A.1 but for IRAS 22491-1808.

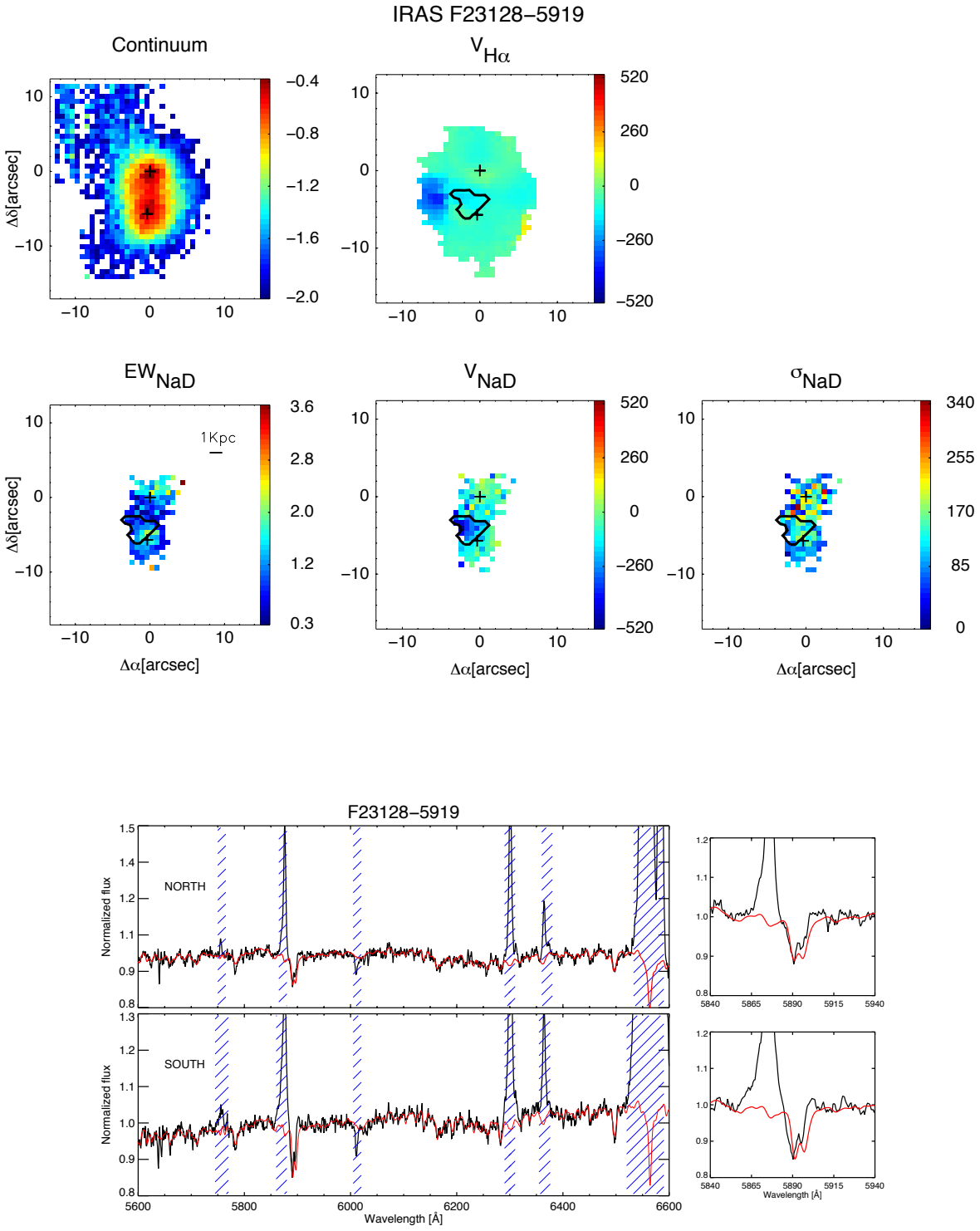

FIGURE A.42: As Fig. A.1 but for IRAS F23128-5919. In this panel the nuclei of both galaxies are marked with a cross.

Appendix B

Comments on the individual galaxies

This appendix is devoted to shortly comment the spatially resolved and/or the integrated characteristics for each galaxy. The LIRG IRAS 11506-3851 is discussed in detail by (Chapt. 4) thus the comments are omitted here.

F01159-4443 (N). The neutral gas kinematics of this galaxy shows deprojected blueshifited velocities (~ 130 kms^{-1}) that are larger than those of the systemic component of the ionized gas at the same location. Therefore, the observed neutral gas velocities cannot be explained with rotation and are interpreted as outflowing.
F01159-4443 (S). This galaxy is not analyzed in this work either with the spatially integrated spectrum or via spatially resolved IFS of NaD because of the low quality of stellar modeling and lack of any clear GW or disk signature, respectively.

F01341-3735 (N). We found a prominent blue wing in the pure-ISM NaD line profile in the spatially integrated spectrum of this LIRG. In the spectral maps, we identified an outflowing neutral gas component with high velocity and velocity dispersion.
F01341-3735 (S). This galaxy was only studied via the integrated spectrum, where the NaD doublet was modeled with a single kinematic component found at the systemic velocity.

F04315-0840. The neutral gas spatial distribution and kinematics of this post-coalescence late-merger starburst LIRG is very different from that of the ionized gas (traced via the Hα narrow component). The neutral gas is mainly seen in the main body of the object, while it is almost absent in the spiral arm. A neutral wind originates from the nucleus toward the southeast with velocity dispersions values higher than 90 kms^{-1}. The blue velocities of the Hα broad component (Bellocchi et al. 2013) spatially overlaps the region where the neutral wind is detected, indicating the presence of a multiphase GW. Interestingly, the velocities of both wind phases are similar at $\sim$ 200-350 kms^{-1}. In the integrated spectrum, we found a blueshifted kinematic component at V $\sim$ 190 kms^{-1} in agreement with our spatially resolved results.

F05189-2524. This merger ULIRG has a very compact nucleus and hosts an AGN that powers the high velocity outflow seen via NaD. The morphology of the outflow could not be constrained well owing to projection effects. A noticeable blue wing is seen in the NaD ISM-absorption line profile in the integrated spectrum, along with the NaD resonant emission line (which is not a common feature of GWs in nearby galaxies) that is studied in detail by (Rupke & Veilleux 2015).

F06035-7102. This galaxy is not analyzed in this work either with the spatially integrated spectrum or via spatially resolved IFS of NaD because of the low quality of stellar modeling and lack of any clear GW or disk signature, respectively.

F06076-2139 (N) and (S). We only study these galaxies via their spatially integrated spectra. In both spectra, the NaD line profile were modeled with one broad and blueshifted kinematical component. However, the complex NaD line profile observed in the spectrum of the northern galaxy likely require more than one (or two) kinematical component(s).

F06206-6315. This ULIRG has two nuclei, which are clearly seen in the near-IR images (Rodríguez-Zaurín et al. 2011) but not in the optical continuum image. The tidal tail, starting in the north and bending toward the southeast, is almost undetected via NaD. While we did not analyze the low S/N integrated spectrum, in 2D, we observed part of the neutral gas as entrained in an AGN-driven outflow. The comparison with the galaxy escape velocity and wind velocities indicates that the neutral gas entrained in the wind is able to escape. A molecular gas outflows, traced by the infrared OH lines, was found by Spoon et al. (2013) at higher observed (terminal) velocity ($\sim 800\,\mathrm{kms}^{-1}$).

F06259-4780 (N). In this galaxy, we detected extended neutral gas that is outflowing nearly everywhere in contrast to what is seen for the ionized gas (narrow component). In addition, neutral and ionized ISM phases also have remarkably different spatial distribution. We identify the GW according to the most blueshifted velocity, the highest velocity dispersion values, and also its direction. Indeed, the outflow is oriented along the minor axis of the rotation seen weakly in the ionized velocity field.
F06259-4780 (C). The 2D-kinematic of the neutral gas in the central galaxy of the system (the southern in Fig. **??**) is classified as rotating disk. This gas is observed in counter-rotation with respect to the ionized disk. This makes this object unique in our sample since, in the nearly all cases, we found slow neutral gas rotation with respect to the ionized gas.
F06259-4780 (S). The southern galaxy of this system is not analyzed in this work. Difficulties in modeling the observed weak NaD absorption in the spatially integrated and spatially resolved data of this galaxy are partially due to its edge-on orientation.

F06295-1735. This LIRG is not analyzed in this work either with the spatially integrated spectrum or via spatially resolved IFS of NaD. The quality of the stellar modeling is low and a large number of spectra in individual spaxels were not suitable for the analysis.

F06592-6313. The integrated spectrum of this LIRG shows a strong NaD absorption in which the stellar contribution is rather low (25%). We modeled the purely ISM NaD line profile with one blueshifted kinematic component. In the spectral maps, toward the south, we also observe strongly blueshifted absorption doublets (with velocities up to 500-600 kms^{-1}), which we interpret as a signature of GW. The broad component of the Hα emission line (Bellocchi et al. 2013), seen with velocities up to 500 kms^{-1}, is rather oriented with the wind well (PA $\sim$ 130

$\circ$

) and partially overlaps the area covered by the neutral wind. However, the overall morphology of the broad Hα component is poorly constrained and it is unclear how it is related to NaD.

F07027-601 (N). The velocity map of this galaxy shows outflowing neutral gas with velocities up to $\sim$ 300 kms^{-1} extended within 1.5 kpc of the nucleus. Despite evidence of an AGN, found by Arribas et al. (2014) according to its optical spectrum, we found no strong evidence that the outflow we detect is boosted by the AGN. The morphology of the outflow could not be constrained well owing to projection effects. Excluding the outflowing gas, the NaD is seen with an irregular spatial distribution, velocity field, and velocity dispersion map. This gas in not-ordered motion could be gas falling back onto the disk in HVCs.
F07027-601 (S). This southern galaxy is an important case to study because its NaD IFS spectra, when fitted with multiple components, provide the possibility of disentangling the ordinary rotation and outflow. One kinematic component was found with rather regular rotation pattern, but lagging with respect to the kinematics of the ionized gas (i.e., Hα-narrow component) with a small positional misalignment. The other (outflowing) kinematic component is evident within $\sim$ 1.3 kpc of the nucleus toward the northeast. This neutral gas component is broad ($\sigma \sim 140\,\mathrm{kms}^{-1}$, on average) and has (observed) velocities within 100-300 kms^{-1}. The morphology of the outflow could not be constrained well owing to projection effects.

F07160-6215. The velocity field of the neutral gas as a disk-like pattern in the main body of this dusty edge-on LIRG as seen for the ionized gas (traced via Hα and Brγ λ2.1655 μm; Bellocchi et al. 2013 and Piqueras López et al. 2012, respectively). The velocity dispersion is almost flat, excluding the region toward the northeast, where a broad and blueshifted NaD component was found and interpreted as a signature of GW. However, no ionized wind-phase counterpart is seen in VIMOS and SINFONI IFS data (Bellocchi et al. 2013; Piqueras López et al. 2012).

08355-4944. This LIRG is not analyzed in this work either with the spatially integrated spectrum or via spatially resolved IFS of NaD. The very weak NaD absorption, seen in both the integrated and the spatially resolved spectra, prevents any robust study.

08424-3130 (N) and (S). These spiral galaxies in interaction are only partially observed in our VIMOS data. For this reason, we did not study these galaxies in detail even though in the northern galaxy,

we detect neutral gas with blueshifted velocities which are higher than those of the ionized gas (i.e., Hα-narrow component) at the same location, which can be interpreted as outflowing.

F08520-6850. This LIRG is not analyzed in this work either with the spatially integrated spectrum or via spatially resolved IFS. The quality of the stellar modeling is low and a large number of spectra in individual spaxels were not suitable for the analysis.

09022-3615. This ULIRG is not analyzed in this work either with the spatially integrated spectrum or via spatially resolved IFS of NaD. The quality of the stellar modeling is low and the spectral maps lack of any clear GW or disk signature.

F09437+0317 (N). Two pointings (i.e., northeast (NE) and northwest (NW); Rodríguez-Zaurín et al. 2011) sample the northern galaxy. However the NW is not useful because of the low S/N of the spectra of the data cube. In the spectral maps obtained from the NE data cube, we observe that the neutral gas disk kinematic shares the same major kinematic axis with the ionized gas rotation, although the neutral gas is found in slower rotation compared to the warm ionized gas (Bellocchi et al. 2013).
F09437+0317 (S). In the southern galaxy (observed with one VIMOS pointing) we observe a shared major kinematic axis and a high kinematical coupling within the neutral and ionized ISM phases. The neutral gas rotation is only slightly slower (of about 40 kms^{-1}, on average) than that measured for the ionized gas at the same distance.

F10015-0614. The NaD-clouds spatial distribution only partially reproduce the spiral structure of this LIRG. No hints of rotation pattern are found in the neutral gas velocity field and velocity dispersion map. On the contrary, we found blueshifted velocities up to 200 kms^{-1} along the kinematic minor axis of the ionized gas rotation. We did not consider as part of the outflow the NaD-clouds toward the north and northeast because of their overlap with the approaching side of the ionized gas rotation pattern. The morphology of the outflow could not be constrained well because of projection effects.

F10038-3338. Our data for this LIRG, show deep, broad, and blueshifted NaD line profiles in the integrated spectrum and spectral maps (toward the northeast). We interpret this feature as a GW.

F10257-4339. This merger LIRG is the nearest object in our VIMOS-IFS survey. The neutral outflow is observed out to distances of 1.4 kpc. We did not consider the NaD-clouds (with negative velocities) toward the north and northwest as part of the outflow, since we observe an irregular and asymmetric NaD line profile in the IFS spectra. We tested two-component modeling, but this modeling gives ambiguous results.

F10409-4556. The observed NaD feature in this LIRG shows generally complex absorption line profiles, best fitted with two absorption doublets. We considered the most negative velocities as part of

the outflow, which have nearly no spatial overlap with the approaching side of the ionized gas rotation. Toward the north, this fast kinematic component associated with a GW dominates the NaD profile. However, the morphology of this outflow could not be constrained well because of the ambiguity in the identification of the region where it is originated. The outflow is also seen via the integrated spectrum.

F10567-4310. The NaD absorption seen in the integrated spectrum and spectra of the IFS cube of this LIRG galaxy is significantly deep and mainly interstellar in origin. Indeed, our stellar continuum modeling indicates a rather low stellar contamination to the NaD doublet (28%). The neutral gas spatial distribution is very compact and the neutral gas velocity field is dominated by a starburst driven GW with outflowing velocity ranging 100 to 300 kms^{-1}. The morphology of the outflow could not be constrained well due to projection effects.

F11255-4120. The observed NaD integrated line-profile in this LIRG show the lowest stellar contamination of the full sample (i.e., 18%). The purely-ISM line profile was modeled with two kinematical components both having blueshifted velocity. Despite of that, the observed NaD line profile in our IFS-data is modeled with one kinematic component well. Our NaD IFS-maps show evidence of a GW, in the inner region (within R > 1.2 kpc), that consist in: large blueshfited velocities (up to 300 kms^{-1}) and high turbulence (σ(NaD) up to 280 kms^{-1}). The morphology of the outflow could not be constrained well owing to projection effects. Weak evidence for an ionized wind counterpart was found (Bellocchi et al. 2013).

F12043-3140 (N). This galaxy is not analyzed in this work. The stellar continuum modeling of the integrated spectrum is rather uncertain. Our spectral maps indicate a generally blueshifted velocity pattern and rather low values for the velocity dispersion and EWs. Therefore, the evidence for claiming a GW detection are weak.

F12043-3140 (S). The absorption due to stars contributes significantly (77%) to the NaD line profile, so the rotation pattern seen in this VIMOS-spectral map might be tracing the stellar kinematics. This result is also supported by the low depth of the absorption found in the EW map. However, additional observations are needed to confirm this interpretation. The 2D neutral gas disk rotation is slower with respect to that of the ionized gas and the major kinematic axes are not aligned well. The high velocity dispersion values seen toward the north are possibly due to additional turbulence this outer region.
Along the southern minor axis there is a region with high blueshifted velocities, and high dispersions that may indicate the presence of an outflow. However, the values of high velocity dispersion are found in just a few spaxels, likely due to low S/N, as the general region has low values. Additionally, in the region of the putative wind, the average value of the residual maps (i.e., V_{NaD}-$V_{H\alpha}$) is slightly lower then the limit we consider. Therefore, we did not include this case from the sample with detected outflows.

F12115-4656. The velocity field is fairly regular with the kinematic center in positional agreement with the continuum and Hα flux peaks. The neutral gas disk is $\sim$45 times thicker than that of the

neutral gas. This LIRG was already studied in great detail by Arribas et al. (2008). We do not excluded the presence of a GW oriented along the kinematic minor axis, but it is not the main feature either in the spectral maps or in the integrated spectrum (where the stellar fraction to the NaD is rather high, 73 %)

F12116-5615. The NaD line profile seen in this LIRG (both in the integrated spectrum and in the spectra of individual spaxels) was fitted with two kinematic components. One kinematical component was found dominated by not-ordered motions and the other by a neutral GW via IFS. The wind is seen almost face-on preventing us from measuring its extent and opening angle. The neutral gas entrained in the wind is likely swept out polluting the IGM. The GW is likely multiphase, since the Hα broad component is seen as outflowing (Bellocchi et al. 2013).

F12596-1529. This LIRG is not analyzed in this work either with the spatially integrated spectrum or via spatially resolved IFS of NaD. The quality of the stellar modeling is low and a large number of spectra in individual spaxels were not suitable for the analysis.
F13001-2339. The ionized gas velocity field and velocity dispersion map (traced via the Hα narrow component) have an irregular pattern and the neutral gas is seen mainly as outflowing. The outflow spatially overlap the region where the ionized gas velocity field has positive velocities. The morphology of the outflow could not be constrained well because of projection effects and the lack of any rotation pattern of reference.

F13229-2934. This LIRG hosts a neutral gas wind detected with both the spatially integrated and spatially resolved spectra. As for the galaxy F04315-0840, an ionized wind counterpart was observed (Bellocchi et al. 2013). This has roughly the same velocities observed in the present neutral gas velocity map. Even though this galaxy hosts an AGN, the comparison of the wind power and kinetic power of the starburst indicate that the multiphase GW is likely driven by SNe.

F14544-4255 (E). We found that the NaD originated in stars gives a modest contribution (41 %) to the integrated line profile for this galaxy, but the modeling is rather uncertain. The neutral gas velocity field is disk-like and the kinematic center seems to be in positional agreement with the continuum peak. The rotation seen for the neutral gas lags compared to that of the ionized gas. For both ISM phases we did not observe a central peak in the velocity dispersion maps (see also Bellocchi et al. 2013); this may indicate that the contribution of the bulge component is negligible.
F14544-4255 (W). The western galaxy has not been classified either in 1D or in 2D. In the spectral maps, the EWs(NaD) are generally low and we found no clear rotation pattern or evidence indicating a GW.

F17138-1017. This LIRG is not analyzed in this work either with the spatially integrated spectrum or via spatially resolved IFS of NaD. The quality of the stellar modeling is low and a large number of

spectra in individual spaxels were not suitable for the analysis.

F18093-5744 (N). The purely ISM NaD profile seen in the integrated spectrum of this galaxy is modeled with one blueshifted kinematic component well. However, in the spectral maps the putative wind (likely seen toward the northeast) has both low velocities and EWs(NaD). This characteristic makes its detection is rather uncertain.
F18093-5744 (C). This galaxy is not analyzed in this work since it was not possible to make a kinematical classification via both the spatially-resolved and spatially-integrated spectroscopy of the NaD absorption.
F18093-5744 (S). The spider pattern seen in the neutral gas velocity field of the galaxy is fairly regular. The rotation is seen for a disk three times thicker and slower with respect to that of the ionized gas. The stellar contamination, estimated with our stellar continuum modeling of the integrated spectrum, is modest (41 %).

F21130-4446. This ULIRG is not analyzed via NaD in this work. The NaD absorption is very weak both in the integrated and spatially resolved spectra.

F21453-3511. In this galaxy, a GW at rather slow velocity is seen emerging from the nucleus. The outflow is also seen via a blue wing in the NaD integrated line profile (despite its strong stellar contamination, i.e., 97%). The morphology of the outflow could not be constrained well because of a patchy distribution of the NaD outflowing clouds and projection effects. Only a weak indication of the presence of an ionized wind was found (Bellocchi et al. 2013). Excluding the region where the wind is detected, the neutral gas velocity field is rather irregular and roughly follows the kinematic of the Hα disk but with strong deviations (up to 150 kms^{-1}).

F22132-3705. The disk-like velocity field is fairly regular with the kinematic center in positional agreement with the continuum and Hα flux peaks. The neutral gas disk is $\sim$20 times thicker than that of the neutral gas. The stellar fraction to the NaD is modest (47 %). The high values found in the velocity dispersion map toward the northeast (particularly evident in the velocity dispersion radial profile) can be explained by either addition turbulence in these outer regions or GW. The evidence for claiming a GW detection however is weak.
F22491-1808. This ULIRG is not analyzed in this work either with the spatially integrated spectrum or via spatially resolved IFS of NaD. The quality of the stellar modeling is low and a large number of spectra in individual spaxels were not suitable for the analysis.

IRAS-F23128-5919 (N) and (S). Despite the high integrated stellar contamination, the NaD velocity field of the two galaxies does not show any ordered rotation pattern typically seen, e.g., the stars. Most of the cold gas associated with this system is outflowing reaching velocities up to 500-600 kms^{-1}. The fast neutral outflowing gas has a conical shape (with the apex in the southern galaxy) as also seen via the Paα and Hα line profiles (Piqueras López et al. 2012; Bellocchi et al. 2013). For this system,

the capability for the wind of polluting the IGM is doubtful because of the inability to estimate the contributions to the velocity field of each individual galaxy reliably (Bellocchi et al. 2013), which leads to additional uncertainties for the calculation of v_{esc}.

List of Figures

List of Tables

Bibliography

Aguirre, A., Hernquist, L., Schaye, J., et al. 2001, ApJ, 561, 521

Aguirre, A. & Schaye, J. 2007, in EAS Publications Series, Vol. 24, EAS Publications Series, ed. E. Emsellem, H. Wozniak, G. Massacrier, J.-F. Gonzalez, J. Devriendt, & N. Champavert, 165–175

Alexander, D. M. & Hickox, R. C. 2012, New A Rev., 56, 93

Alonso-Herrero, A., Pereira-Santaella, M., Rieke, G. H., & Rigopoulou, D. 2012, ApJ, 744, 2

Alonso-Herrero, A., Rieke, G. H., Rieke, M. J., et al. 2006, ApJ, 650, 835

Alonso-Herrero, A., Rieke, G. H., Rieke, M. J., & Kelly, D. M. 2003, AJ, 125, 1210

Anglés-Alcázar, D., Davé, R., Özel, F., & Oppenheimer, B. D. 2014, ApJ, 782, 84

Arribas, S., Carter, D., Cavaller, L., et al. 1998, in Society of Photo-Optical Instrumentation Engineers (SPIE) Conference Series, Vol. 3355, Optical Astronomical Instrumentation, ed. S. D'Odorico, 821–827

Arribas, S., Colina, L., Alonso-Herrero, A., et al. 2012, A&A, 541, A20

Arribas, S., Colina, L., Bellocchi, E., Maiolino, R., & Villar-Martín, M. 2014, A&A, 568, A14

Arribas, S., Colina, L., Monreal-Ibero, A., et al. 2008, A&A, 479, 687

Asmus, D., Hönig, S. F., Gandhi, P., Smette, A., & Duschl, W. J. 2014, MNRAS, 439, 1648

Baan, W. A. & Klöckner, H.-R. 2006, A&A, 449, 559

Bacon, R., Accardo, M., Adjali, L., et al. 2010, in Society of Photo-Optical Instrumentation Engineers (SPIE) Conference Series, Vol. 7735, Society of Photo-Optical Instrumentation Engineers (SPIE) Conference Series, 8

Baldwin, J. A., Phillips, M. M., & Terlevich, R. 1981, PASP, 93, 5

Barai, P., Monaco, P., Murante, G., Ragagnin, A., & Viel, M. 2015, MNRAS, 447, 266

Bauer, M., Pietsch, W., Trinchieri, G., et al. 2007, A&A, 467, 979

Bedregal, A. G., Colina, L., Alonso-Herrero, A., & Arribas, S. 2009, ApJ, 698, 1852

Belfiore, F., Maiolino, R., & Bothwell, M. 2015, ArXiv e-prints

Bell, E. F., McIntosh, D. H., Katz, N., & Weinberg, M. D. 2003, ApJ, 585, L117

Bellocchi, E. 2014, PhD thesis, Universidad Autonóma de Madrid, UAM

Bellocchi, E., Arribas, S., & Colina, L. 2016, ArXiv e-prints

Bellocchi, E., Arribas, S., Colina, L., & Miralles-Caballero, D. 2013, A&A, 557, A59

Binney, J. & Tremaine, S. 2008, Galactic Dynamics: Second Edition (Princeton University Press)

Blain, A. W., Smail, I., Ivison, R. J., Kneib, J.-P., & Frayer, D. T. 2002, Phys. Rep., 369, 111

Bohlin, R. C., Savage, B. D., & Drake, J. F. 1978, ApJ, 224, 132

Bolatto, A. D., Warren, S. R., Leroy, A. K., et al. 2013, Nature, 499, 450

Boomsma, R., Oosterloo, T. A., Fraternali, F., van der Hulst, J. M., & Sancisi, R. 2005, A&A, 431, 65

Boomsma, R., Oosterloo, T. A., Fraternali, F., van der Hulst, J. M., & Sancisi, R. 2008, A&A, 490, 555

Bourne, M. A., Zubovas, K., & Nayakshin, S. 2015, MNRAS, 453, 1829

Brinchmann, J., Charlot, S., White, S. D. M., et al. 2004, MNRAS, 351, 1151

Brooks, A., Governato, F., Booth, C. M., et al. 2006, in Bulletin of the American Astronomical Society, Vol. 38, American Astronomical Society Meeting Abstracts, 925

Bundy, K., Bershady, M. A., Law, D. R., et al. 2015, ApJ, 798, 7

Burke, J. A. 1968, MNRAS, 140, 241

Caldú-Primo, A., Schruba, A., Walter, F., et al. 2013, AJ, 146, 150

Calzetti, D., Armus, L., Bohlin, R. C., et al. 2000, ApJ, 533, 682

Cano-Díaz, M., Maiolino, R., Marconi, A., et al. 2012, A&A, 537, L8

Cappellari, M. & Emsellem, E. 2004, PASP, 116, 138

Caputi, K. I., Lagache, G., Yan, L., et al. 2007, ApJ, 660, 97

Carniani, S., Marconi, A., Maiolino, R., et al. 2015, A&A, 580, A102

Casey, C. M., Narayanan, D., & Cooray, A. 2014, Phys. Rep., 541, 45

Cazzoli, S., Arribas, S., Colina, L., et al. 2014, A&A, 569, A14

Chabrier, G. 2003, PASP, 115, 763

Chen, Y.-M., Tremonti, C. A., Heckman, T. M., et al. 2010, AJ, 140, 445

Chevalier, R. A. & Clegg, A. W. 1985, Nature, 317, 44

Chung, A., Yun, M. S., Naraynan, G., Heyer, M., & Erickson, N. R. 2011, ApJ, 732, L15

Cicone, C., Feruglio, C., Maiolino, R., et al. 2012, A&A, 543, A99

Cicone, C., Maiolino, R., Sturm, E., et al. 2014, A&A, 562, A21

Clemens, M. S., Vega, O., Bressan, A., et al. 2008, A&A, 477, 95

Colina, L., Piqueras López, J., Arribas, S., et al. 2015, A&A, 578, A48

Combes, F., Rex, M., Rawle, T. D., et al. 2012, A&A, 538, L4

Condon, J. J. 1992, ARA&A, 30, 575

Conselice, C. J., Bershady, M. A., Dickinson, M., & Papovich, C. 2003, AJ, 126, 1183

Cooper, J. L., Bicknell, G. V., Sutherland, R. S., & Bland-Hawthorn, J. 2008, ApJ, 674, 157

Costa, T., Sijacki, D., & Haehnelt, M. G. 2014, MNRAS, 444, 2355

Costa, T., Sijacki, D., & Haehnelt, M. G. 2015, MNRAS, 448, L30

Courtes, G. 1982, in Astrophysics and Space Science Library, Vol. 92, IAU Colloq. 67: Instrumentation for Astronomy with Large Optical Telescopes, ed. C. M. Humphries, 123

Courtois, H. M., Tully, R. B., Makarov, D. I., et al. 2011, MNRAS, 414, 2005

Cowie, L. L., Songaila, A., Kim, T.-S., & Hu, E. M. 1995, AJ, 109, 1522

Creasey, P., Theuns, T., & Bower, R. G. 2013, MNRAS, 429, 1922

Cresci, G., Hicks, E. K. S., Genzel, R., et al. 2009, ApJ, 697, 115

Cresci, G., Mainieri, V., Brusa, M., et al. 2015, ApJ, 799, 82

Croom, S. M., Lawrence, J. S., Bland-Hawthorn, J., et al. 2012, MNRAS, 421, 872

Croton, D. J., Springel, V., White, S. D. M., et al. 2006, MNRAS, 365, 11

Daddi, E., Dickinson, M., Morrison, G., et al. 2007, ApJ, 670, 156

Dadina, M. 2007, A&A, 461, 1209

Dale, D. A., Roussel, H., Contursi, A., et al. 2004, ApJ, 601, 813

Dale, D. A., Sheth, K., Helou, G., Regan, M. W., & Hüttemeister, S. 2005, AJ, 129, 2197

Dannerbauer, H., Rigopoulou, D., Lutz, D., et al. 2005, A&A, 441, 999

Davé, R., Finlator, K., & Oppenheimer, B. D. 2012, MNRAS, 421, 98

Davies, R. & Kasper, M. 2012, ARA&A, 50, 305

Davies, R. I. 2007, MNRAS, 375, 1099

Davis, T. A., Krajnović, D., McDermid, R. M., et al. 2012, MNRAS, 426, 1574

Dawson, S., Spinrad, H., Stern, D., et al. 2002, ApJ, 570, 92

de Bruyne, V., Vauterin, P., de Rijcke, S., & Dejonghe, H. 2003, MNRAS, 339, 215

de Vaucouleurs, G., de Vaucouleurs, A., Corwin, Jr., H. G., et al. 1991, Third Reference Catalogue of Bright Galaxies. Volume I: Explanations and references. Volume II: Data for galaxies between 0^h and 12^h. Volume III: Data for galaxies between 12^h and 24^h. (ADS)

Di Teodoro, E. M. & Fraternali, F. 2015, MNRAS, 451, 3021

Díaz-Santos, T., Charmandaris, V., Armus, L., et al. 2011, ApJ, 741, 32

Dixon, T. G. & Joseph, R. D. 2011, ApJ, 740, 99

Draine, B. T. 2011, Physics of the Interstellar and Intergalactic Medium

Dutton, A. A. & van den Bosch, F. C. 2009, MNRAS, 396, 141

Eisenhauer, F., Abuter, R., Bickert, K., et al. 2003, in Society of Photo-Optical Instrumentation Engineers (SPIE) Conference Series, Vol. 4841, Instrument Design and Performance for Optical/Infrared Ground-based Telescopes, ed. M. Iye & A. F. M. Moorwood, 1548–1561

Elbaz, D., Daddi, E., Le Borgne, D., et al. 2007, A&A, 468, 33

Elbaz, D., Dickinson, M., Hwang, H. S., et al. 2011, A&A, 533, A119

Epinat, B., Amram, P., Balkowski, C., & Marcelin, M. 2010, MNRAS, 401, 2113

Erb, D. K. 2015, Nature, 523, 169

Erb, D. K., Quider, A. M., Henry, A. L., & Martin, C. L. 2012, ApJ, 759, 26

Fabian, A. C. 2012, ARA&A, 50, 455

Farrah, D., Afonso, J., Efstathiou, A., et al. 2003, MNRAS, 343, 585

Feruglio, C., Maiolino, R., Piconcelli, E., et al. 2010, A&A, 518, L155

Flores, H., Hammer, F., Puech, M., Amram, P., & Balkowski, C. 2006, A&A, 455, 107

Förster Schreiber, N. M., Genzel, R., Bouché, N., et al. 2009, ApJ, 706, 1364

Förster Schreiber, N. M., Genzel, R., Newman, S. F., et al. 2014, ApJ, 787, 38

Förster Schreiber, N. M., Shapley, A. E., Genzel, R., et al. 2011, ApJ, 739, 45

Fraternali, F. & Binney, J. J. 2008, MNRAS, 386, 935

Fraternali, F., Oosterloo, T. A., Sancisi, R., & Swaters, R. 2005, in ASP Conf. Ser., Vol. 331, Extra-Planar Gas, ed. R. Braun, 239

Fraternali, F., van Moorsel, G., Sancisi, R., & Oosterloo, T. 2002, AJ, 123, 3124

Fujita, A., Martin, C. L., Mac Low, M.-M., New, K. C. B., & Weaver, R. 2009, ApJ, 698, 693

Gallagher, J. S., Yoast-Hull, T. M., & Zweibel, E. G. 2014, in IAU Symposium, Vol. 303, IAU Symposium, ed. L. O. Sjouwerman, C. C. Lang, & J. Ott, 61–65

García-Burillo, S., Combes, F., Usero, A., et al. 2014, A&A, 567, A125

García-Lorenzo, B., Márquez, I., Barrera-Ballesteros, J. K., et al. 2015, A&A, 573, A59
Garzilli, A., Theuns, T., & Schaye, J. 2015, MNRAS, 450, 1465
Genzel, R., Burkert, A., Bouché, N., et al. 2008, ApJ, 687, 59
Genzel, R., Förster Schreiber, N. M., Rosario, D., et al. 2014, ApJ, 796, 7
Genzel, R., Newman, S., Jones, T., et al. 2011, ApJ, 733, 101
Gerhard, O. E. 1993, MNRAS, 265, 213
Green, A. W., Glazebrook, K., McGregor, P. J., et al. 2014, MNRAS, 437, 1070
Greve, T. R., Bertoldi, F., Smail, I., et al. 2005, MNRAS, 359, 1165
Habart, E., Boulanger, F., Verstraete, L., Walmsley, C. M., & Pineau des Forêts, G. 2004, A&A, 414, 531
Hamann, F., Barlow, T. A., Junkkarinen, V., & Burbidge, E. M. 1997, ApJ, 478, 80
Harrison, C. M., Alexander, D. M., Swinbank, A. M., et al. 2012, MNRAS, 426, 1073
Heckman, T. M. 2002, in Astronomical Society of the Pacific Conference Series, Vol. 254, Extragalactic Gas at Low Redshift, ed. J. S. Mulchaey & J. T. Stocke, 292
Heckman, T. M., Armus, L., & Miley, G. K. 1987, AJ, 93, 276
Heckman, T. M., Armus, L., & Miley, G. K. 1990, ApJS, 74, 833
Heckman, T. M., Lehnert, M. D., Strickland, D. K., & Armus, L. 2000, ApJS, 129, 493
Hill, M. J. & Zakamska, N. L. 2014, MNRAS, 439, 2701
Hinshaw, G., Larson, D., Komatsu, E., et al. 2013, ApJS, 208, 19
Hopkins, P. F., Cox, T. J., Kereš, D., & Hernquist, L. 2008, ApJS, 175, 390
Hopkins, P. F., Hernquist, L., Cox, T. J., et al. 2006, ApJS, 163, 1
Houck, J. R., Schneider, D. P., Danielson, G. E., et al. 1985, ApJ, 290, L5
Huang, Z. P., Thuan, T. X., Chevalier, R. A., Condon, J. J., & Yin, Q. F. 1994, ApJ, 424, 114
Huchra, J., Davis, M., Latham, D., & Tonry, J. 1983, ApJS, 52, 89
Imanishi, M. & Terashima, Y. 2004, AJ, 127, 758
Ishibashi, W. & Fabian, A. C. 2012, MNRAS, 427, 2998
Iwasawa, K., Sanders, D. B., Teng, S. H., et al. 2011, A&A, 529, A106
Jacoby, G. H., Hunter, D. A., & Christian, C. A. 1984, ApJS, 56, 257
Jiménez-Bailón, E., Loiseau, N., Guainazzi, M., et al. 2007, A&A, 469, 881
Jiménez-Vicente, J., Castillo-Morales, A., Mediavilla, E., & Battaner, E. 2007, MNRAS, 382, L16
Keller, B. W., Wadsley, J., & Couchman, H. M. P. 2015, ArXiv e-prints
Kennicutt, R. C. & Evans, N. J. 2012, ARA&A, 50, 531
Kennicutt, Jr., R. C. 1998, ARA&A, 36, 189
Kennicutt, Jr., R. C., Tamblyn, P., & Congdon, C. E. 1994, ApJ, 435, 22
Kewley, L. J., Groves, B., Kauffmann, G., & Heckman, T. 2006, MNRAS, 372, 961
Kilerci Eser, E., Goto, T., & Doi, Y. 2014, ApJ, 797, 54
Kilerci Eser, E., Vestergaard, M., Peterson, B. M., Denney, K. D., & Bentz, M. C. 2015, ApJ, 801, 8
Kim, D.-C., Veilleux, S., & Sanders, D. B. 1998, ApJ, 508, 627
King, A. & Pounds, K. 2015, ARA&A, 53, 115
Kormendy, J. & Ho, L. C. 2013, ARA&A, 51, 511
Krug, H. B., Rupke, D. S. N., & Veilleux, S. 2010, ApJ, 708, 1145

Labrie, K. & Pritchet, C. J. 2006, ApJS, 166, 188

Lagache, G., Puget, J.-L., & Dole, H. 2005, ARA&A, 43, 727

Landt, H., Bentz, M. C., Ward, M. J., et al. 2008, ApJS, 174, 282

Larkin, J. E., Armus, L., Knop, R. A., Soifer, B. T., & Matthews, K. 1998, ApJS, 114, 59

Le, H. A. N., Kang, W., Pak, S., et al. 2011, ArXiv e-prints

Le Fèvre, O., Saisse, M., Mancini, D., et al. 2003, in Society of Photo-Optical Instrumentation Engineers (SPIE) Conference Series, Vol. 4841, Instrument Design and Performance for Optical/Infrared Ground-based Telescopes, ed. M. Iye & A. F. M. Moorwood, 1670–1681

Le Floc'h, E., Papovich, C., Dole, H., et al. 2005, ApJ, 632, 169

Lehnert, M. D., Heckman, T. M., & Weaver, K. A. 1999, ApJ, 523, 575

Leitherer, C., Schaerer, D., Goldader, J. D., et al. 1999, ApJS, 123, 3

Leitner, S. N. & Kravtsov, A. V. 2011, ApJ, 734, 48

Levesque, E. M. & Leitherer, C. 2013, ApJ, 779, 170

Lonsdale, C. J., Farrah, D., & Smith, H. E. 2006, Ultraluminous Infrared Galaxies, ed. J. W. Mason, 285

Luhman, M. L., Satyapal, S., Fischer, J., et al. 2003, ApJ, 594, 758

Lynd, C. R. & Sandage, A. R. 1963, ApJ, 137, 1005

Maiolino, R., Gallerani, S., Neri, R., et al. 2012, MNRAS, 425, L66

Maiolino, R., Krabbe, A., Thatte, N., & Genzel, R. 1998, ApJ, 493, 650

Maíz-Apellániz, J. 2004, PASP, 116, 859

Malin, D. & Hadley, B. 1997, PASA, 14, 52

Mannucci, F., Cresci, G., Maiolino, R., Marconi, A., & Gnerucci, A. 2010, MNRAS, 408, 2115

Marasco, A., Fraternali, F., & Binney, J. J. 2012, MNRAS, 419, 1107

Markwardt, C. B. 2009, in Astronomical Society of the Pacific Conference Series, Vol. 411, Astronomical Data Analysis Software and Systems XVIII, ed. D. A. Bohlender, D. Durand, & P. Dowler, 251

Martin, C. L. 1999, ApJ, 513, 156

Martin, C. L. 2005, ApJ, 621, 227

Martin, C. L. 2006, ApJ, 647, 222

Martin, C. L., Shapley, A. E., Coil, A. L., et al. 2012, ApJ, 760, 127

Martin, C. L., Shapley, A. E., Coil, A. L., et al. 2013, ApJ, 770, 41

McNamara, B. R. & Nulsen, P. E. J. 2007, ARA&A, 45, 117

Melioli, C., Brighenti, F., D'Ercole, A., & de Gouveia Dal Pino, E. M. 2008, MNRAS, 388, 573

Merritt, D. 1997, AJ, 114, 228

Monreal-Ibero, A., Arribas, S., Colina, L., et al. 2010, A&A, 517, A28

Moshir, M., Kopman, G., & Conrow, T. A. O. 1992, IRAS Faint Source Survey, Explanatory supplement version 2 (California Institute of Technology)

Moster, B. P., Somerville, R. S., Maulbetsch, C., et al. 2010, ApJ, 710, 903

Moustakas, J., Coil, A. L., Aird, J., et al. 2013, ApJ, 767, 50

Müller-Sánchez, F., Prieto, M. A., Hicks, E. K. S., et al. 2011, ApJ, 739, 69

Murray, N., Martin, C. L., Quataert, E., & Thompson, T. A. 2007, ApJ, 660, 211

Narayanan, D., Cox, T. J., Kelly, B., et al. 2008, ApJS, 176, 331
Narayanan, D., Hamann, F., Barlow, T., et al. 2004, ApJ, 601, 715
Nardini, E., Risaliti, G., Salvati, M., et al. 2009, MNRAS, 399, 1373
Nardini, E., Risaliti, G., Watabe, Y., Salvati, M., & Sani, E. 2010, MNRAS, 405, 2505
Navarro, J. F. & Steinmetz, M. 2000, ApJ, 538, 477
Nelson, D., Pillepich, A., Genel, S., et al. 2015, Astronomy and Computing, 13, 12
Neri, R., Genzel, R., Ivison, R. J., et al. 2003, ApJ, 597, L113
Netzer, H. & Turner, T. J. 1997, ApJ, 488, 694
Newman, S. F., Genzel, R., Förster-Schreiber, N. M., et al. 2012, ApJ, 761, 43
Noeske, K. G., Weiner, B. J., Faber, S. M., et al. 2007, ApJ, 660, L43
Obreja, A., Brook, C. B., Stinson, G., et al. 2014, MNRAS, 442, 1794
Oosterloo, T., Fraternali, F., & Sancisi, R. 2007, AJ, 134, 1019
Papadopoulos, P. P., van der Werf, P. P., Xilouris, E. M., et al. 2012, MNRAS, 426, 2601
Pereira-Santaella, M., Alonso-Herrero, A., Rieke, G. H., et al. 2010, ApJS, 188, 447
Perez-Olea, D. E. & Colina, L. 1995, MNRAS, 277, 857
Pettini, M., Rix, S. A., Steidel, C. C., et al. 2002, ApJ, 569, 742
Pietsch, W., Vogler, A., Klein, U., & Zinnecker, H. 2000, A&A, 360, 24
Piqueras López, J., Colina, L., Arribas, S., & Alonso-Herrero, A. 2013, A&A, 553, A85
Piqueras López, J., Colina, L., Arribas, S., Alonso-Herrero, A., & Bedregal, A. G. 2012, A&A, 546, A64
Ptak, A., Heckman, T., Levenson, N. A., Weaver, K., & Strickland, D. 2003, ApJ, 592, 782
Rasera, Y. & Teyssier, R. 2006, A&A, 445, 1
Riffel, R., Rodríguez-Ardila, A., Aleman, I., et al. 2013, MNRAS, 430, 2002
Risaliti, G., Gilli, R., Maiolino, R., & Salvati, M. 2000, A&A, 357, 13
Robishaw, T., Quataert, E., & Heiles, C. 2008, ApJ, 680, 981
Rodighiero, G., Daddi, E., Baronchelli, I., et al. 2011, ApJ, 739, L40
Rodríguez-Zaurín, J., Arribas, S., Monreal-Ibero, A., et al. 2011, A&A, 527, A60
Rosales-Ortega, F. F. 2011, New A, 16, 220
Rosales-Ortega, F. F., Arribas, S., & Colina, L. 2012, A&A, 539, A73
Roth, M. M., Kelz, A., Fechner, T., et al. 2005, PASP, 117, 620
Rubin, K. H. R., Weiner, B. J., Koo, D. C., et al. 2010, ApJ, 719, 1503
Rujopakarn, W. 2012, PhD thesis, The University of Arizona
Rujopakarn, W., Rieke, G. H., Eisenstein, D. J., & Juneau, S. 2011, ApJ, 726, 93
Rupke, D. S., Veilleux, S., & Sanders, D. B. 2002, ApJ, 570, 588
Rupke, D. S., Veilleux, S., & Sanders, D. B. 2005a, ApJ, 632, 751
Rupke, D. S., Veilleux, S., & Sanders, D. B. 2005b, ApJS, 160, 87
Rupke, D. S., Veilleux, S., & Sanders, D. B. 2005c, ApJS, 160, 115
Rupke, D. S. N. & Veilleux, S. 2011, ApJ, 729, L27
Rupke, D. S. N. & Veilleux, S. 2013, ApJ, 768, 75
Rupke, D. S. N. & Veilleux, S. 2015, ApJ, 801, 126
Sánchez, S. F., Kennicutt, R. C., Gil de Paz, A., et al. 2012, A&A, 538, A8

Sánchez, S. F., Rosales-Ortega, F. F., Iglesias-Páramo, J., et al. 2014, A&A, 563, A49
Sánchez Almeida, J., Elmegreen, B. G., Muñoz-Tuñón, C., & Elmegreen, D. M. 2014, A&A Rev., 22, 71
Sánchez-Blázquez, P., Rosales-Ortega, F. F., Méndez-Abreu, J., et al. 2014, A&A, 570, A6
Sandage, A. 1986, A&A, 161, 89
Sanders, D. B., Mazzarella, J. M., Kim, D.-C., Surace, J. A., & Soifer, B. T. 2003, AJ, 126, 1607
Sanders, D. B. & Mirabel, I. F. 1996, ARA&A, 34, 749
Sato, T., Martin, C. L., Noeske, K. G., Koo, D. C., & Lotz, J. M. 2009, ApJ, 696, 214
Schechter, P. 1976, ApJ, 203, 297
Schwartz, C. M. & Martin, C. L. 2004, ApJ, 610, 201
Segers, M. C., Crain, R. A., Schaye, J., et al. 2016, MNRAS, 456, 1235
Shapley, A. E., Steidel, C. C., Pettini, M., & Adelberger, K. L. 2003, ApJ, 588, 65
Shih, H.-Y. & Rupke, D. S. N. 2010, ApJ, 724, 1430
Silk, J. 2001, MNRAS, 324, 313
Silk, J. 2003, MNRAS, 343, 249
Silk, J. & Mamon, G. A. 2012, Research in Astronomy and Astrophysics, 12, 917
Silk, J. & Rees, M. J. 1998, A&A, 331, L1
Smartt, S. J. 2009, ARA&A, 47, 63
Soifer, B. T., Sanders, D. B., Madore, B. F., et al. 1987, ApJ, 320, 238
Somerville, R. S. & Davé, R. 2015, ARA&A, 53, 51
Somerville, R. S., Hopkins, P. F., Cox, T. J., Robertson, B. E., & Hernquist, L. 2008, MNRAS, 391, 481
Soto, K. T. & Martin, C. L. 2012, ApJS, 203, 3
Sparre, M., Hayward, C. C., Springel, V., et al. 2015, MNRAS, 447, 3548
Spitoni, E., Calura, F., Matteucci, F., & Recchi, S. 2010, A&A, 514, A73
Spitoni, E., Matteucci, F., & Marcon-Uchida, M. M. 2013, A&A, 551, A123
Spitzer, L. 1978, Physical processes in the interstellar medium (New York Wiley-Interscience)
Spoon, H. W. W., Farrah, D., Lebouteiller, V., et al. 2013, ApJ, 775, 127
Springel, V. & Hernquist, L. 2003, MNRAS, 339, 289
Springel, V., White, S. D. M., Jenkins, A., et al. 2005, Nature, 435, 629
Steidel, C. C., Erb, D. K., Shapley, A. E., et al. 2010, ApJ, 717, 289
Stott, J. P., Swinbank, A. M., Johnson, H. L., et al. 2016, MNRAS, 457, 1888
Strickland, D. K. & Heckman, T. M. 2009, ApJ, 697, 2030
Strickland, D. K. & Stevens, I. R. 2000, MNRAS, 314, 511
Sturm, E., González-Alfonso, E., Veilleux, S., et al. 2011, ApJ, 733, L16
Sun, A.-L., Greene, J. E., Zakamska, N. L., & Nesvadba, N. P. H. 2014, ApJ, 790, 160
Surace, J. A. & Sanders, D. B. 2000, AJ, 120, 604
Surace, J. A., Sanders, D. B., & Mazzarella, J. M. 2004, AJ, 127, 3235
Tacconi, L. J., Neri, R., Chapman, S. C., et al. 2006, ApJ, 640, 228
Taylor, P. & Kobayashi, C. 2015, ArXiv e-prints
Thean, A., Pedlar, A., Kukula, M. J., Baum, S. A., & O'Dea, C. P. 2000, MNRAS, 314, 573

Toyouchi, D. & Chiba, M. 2015, ApJ, 810, 18
Treister, E., Urry, C. M., Schawinski, K., Cardamone, C. N., & Sanders, D. B. 2010, ApJ, 722, L238
Tremonti, C. A., Heckman, T. M., Kauffmann, G., et al. 2004, ApJ, 613, 898
Tripp, T. M., Meiring, J. D., Prochaska, J. X., et al. 2011, Science, 334, 952
Turatto, M., Benetti, S., & Cappellaro, E. 2003, in From Twilight to Highlight: The Physics of Supernovae, ed. W. Hillebrandt & B. Leibundgut, 200
Valdes, F., Gupta, R., Rose, J. A., Singh, H. P., & Bell, D. J. 2004, ApJS, 152, 251
Valiante, E., Lutz, D., Sturm, E., Genzel, R., & Chapin, E. L. 2009, ApJ, 701, 1814
van den Broek, A. C., van Driel, W., de Jong, T., et al. 1991, A&AS, 91, 61
van der Burg, R. F. J., Hoekstra, H., Muzzin, A., et al. 2015, A&A, 577, A19
van der Marel, R. P. & Franx, M. 1993, ApJ, 407, 525
Vanzella, E., Giavalisco, M., Dickinson, M., et al. 2009, ApJ, 695, 1163
Vasiliev, E. O., Nath, B. B., & Shchekinov, Y. 2015, MNRAS, 446, 1703
Veilleux, S., Cecil, G., & Bland-Hawthorn, J. 2005, ARA&A, 43, 769
Veilleux, S., Kim, D.-C., & Sanders, D. B. 1999, ApJ, 522, 113
Veilleux, S., Kim, D.-C., & Sanders, D. B. 2002, ApJS, 143, 315
Veilleux, S., Kim, D.-C., Sanders, D. B., Mazzarella, J. M., & Soifer, B. T. 1995, ApJS, 98, 171
Veilleux, S., Meléndez, M., Sturm, E., et al. 2013, ApJ, 776, 27
Veilleux, S., Rupke, D. S. N., Kim, D.-C., et al. 2009, ApJS, 182, 628
Villar Martín, M., Emonts, B., Humphrey, A., Cabrera Lavers, A., & Binette, L. 2014, MNRAS, 440, 3202
von Glasow, W., Krause, M. G. H., Sommer-Larsen, J., & Burkert, A. 2013, MNRAS, 434, 1151
Wagner, A. Y., Bicknell, G. V., Umemura, M., Sutherland, R. S., & Silk, J. 2015, ArXiv e-prints
Walter, F., Weiss, A., & Scoville, N. 2002, ApJ, 580, L21
Weiner, B. J. 2009, in American Institute of Physics Conference Series, Vol. 1201, American Institute of Physics Conference Series, ed. S. Heinz & E. Wilcots, 142–145
Weller, J., Ostriker, J. P., Bode, P., & Shaw, L. 2005, MNRAS, 364, 823
Westmoquette, M. S., Clements, D. L., Bendo, G. J., & Khan, S. A. 2012, MNRAS, 424, 416
Westmoquette, M. S., Smith, L. J., & Gallagher, III, J. S. 2011, MNRAS, 414, 3719
Whitaker, K. E., van Dokkum, P. G., Brammer, G., & Franx, M. 2012, ApJ, 754, L29
Wilson, C. D., Petitpas, G. R., Iono, D., et al. 2008, ApJS, 178, 189
Winge, C., Riffel, R. A., & Storchi-Bergmann, T. 2009, ApJS, 185, 186
Wisnioski, E., Förster Schreiber, N. M., Wuyts, S., et al. 2015, ApJ, 799, 209
Wright, E. L. 2006, PASP, 118, 1711
Wuyts, S., Förster Schreiber, N. M., van der Wel, A., et al. 2011, ApJ, 742, 96
York, D. G., Adelman, J., Anderson, Jr., J. E., et al. 2000, AJ, 120, 1579
Yuan, T.-T., Kewley, L. J., & Sanders, D. B. 2010, ApJ, 709, 884
Zahid, H. J., Dima, G. I., Kewley, L. J., Erb, D. K., & Davé, R. 2012, ApJ, 757, 54
Zanichelli, A., Garilli, B., Scodeggio, M., et al. 2005, PASP, 117, 1271
Zubovas, K., Nayakshin, S., Sazonov, S., & Sunyaev, R. 2013, MNRAS, 431, 793